TUM School of Engineering and Design

State of health estimation for lithium-ion batteries

Julius Schmitt, M.Sc.

Vollständiger Abdruck der von der TUM School of Engineering and Design der Technischen Universität München zur Erlangung des akademischen Grades eines

Doktors der Ingenieurwissenschaften (Dr.-Ing.)

genehmigten Dissertation.

Vorsitz:		Prof. Dr. Christoph Goebel
Prüfer*innen der Dissertation:	1.	Prof. Dr.-Ing. Andreas Jossen
	2.	Prof. Dr. Dirk Uwe Sauer

Die Dissertation wurde am 22. Dezember 2022 bei der Technischen Universität München eingereicht und durch die TUM School of Engineering and Design am 10. April 2023 angenommen.

Abstract

Lithium-ion batteries degrade during operation and storage. This leads to a decrease in the energy and power that can be delivered by battery systems. Monitoring of the degradation is an important task for battery management systems (BMSs), as accurate estimates on the state of health (SOH) of the battery are needed in order to guarantee the reliable operation of battery-powered systems. In addition to this, methods to derive information on the battery degradation from the measurement data recorded by the BMS during regular operation could enable the analysis of the impact of operating conditions on battery degradation without the need for extensive laboratory experiments.

In this thesis, two methods for the estimation of the SOH of lithium-ion batteries are presented. In the first method, the shape of the voltage curve that can be measured during partial constant current charging phases is used to determine the degradation modes that have occurred during battery aging. With this method, accurate estimates on the remaining cell capacity can be obtained from partial charging processes at current rates of up to approximately C/4, if the state of charge (SOC) window between 10% and 80% is contained in the measured charging curves. In addition to this, if lower currents are used, the method also allows to estimate the loss of active material at the individual electrodes based on partial charging processes. The method is independent of the estimation of the SOC and no prior information on the progress of battery aging is needed.

The method is based on a mechanistic model describing the electrical behavior of lithium-ion cells during aging. The invariance of the shape of the half-cell open-circuit potential (OCP) curves of electrode materials during aging is a central hypothesis for this type of models. In this thesis, this hypothesis is experimentally investigated for two state-of-the-art electrode materials. It is found, that the shape of the half-cell OCP curve of NMC-811 does not change significantly during cycle aging while the shape of the OCP curve of silicon-graphite changes. This change is probably due to a decrease in the relative capacity contribution of the silicon because of a faster degradation of the silicon in comparison to the graphite.

It is further shown that neglecting these changes on the half-cell level leads to an underestimation of the loss of active anode material, an overestimation of the loss of cathode material, and an overestimation of the loss of lithium inventory for the investigated cell type, if the degradation modes are determined based on full-cell open-circuit (OCV) curves. The errors are in the order of a few percentage points. In order to consider changes in the shape of the half-cell OCP curve of silicon-graphite, the half-cell OCP curve is described by a blend electrode model. The mechanistic cell model is thus expanded to the component level. This model extension allows the estimation of the remaining capacity fraction provided by the silicon based on full-cell charging curves measured at a low current.

The second method for SOH estimation presented in this thesis is based on the correlation between the increase in the gas pressure inside the case of prismatic lithium-ion cells and the decrease in the cell capacity. This correlation was empirically observed in an aging study that is presented in this thesis. In addition to this, results on the dependence of the gas pressure inside prismatic lithium-ion cells on the SOC and the temperature are presented.

Kurzfassung

Lithium-Ionen-Batterien altern im Laufe des Betriebs und während Lagerzeiten. Hierdurch verringern sich die Energie und die Leistung, die von Batteriesystemen zur Verfügung gestellt werden können. Die Überwachung dieser Alterung ist eine wichtige Aufgabe von Batteriemanagementsystemen, da eine genaue Schätzung des Gesundheitszustandes (engl. *state of health*, SOH) der Batterie für einen zuverlässigen Betrieb von batteriebetriebenen Anwendungen notwendig ist. Methoden zur Bestimmung der Batteriealterung aus während des regulären Betriebs erfassten Messdaten könnten außerdem dazu eingesetzt werden, den Einfluss der Betriebsbedingungen auf die Batteriealterung basierend auf Felddaten zu untersuchen.

Im Rahmen dieser Arbeit wurden zwei Methoden zur SOH-Bestimmung von Lithium-Ionen-Batterien entwickelt. Die erste Methode besteht darin, die auftretenden Degradationsmoden anhand der Form der während Teilladevorgängen gemessenen Spannungskurven zu bestimmen. Mit dieser Methode kann die verbleibende Zellkapazität mit hoher Genauigkeit, basierend auf Teilladekurven, die mit Ladestromraten von bis zu ca. C/4 aufgezeichnet wurden, bestimmt werden. Eine Voraussetzung dafür ist, dass der Ladezustandsbereich zwischen 10 % und 80 % in der Ladekurve enthalten ist. Für den Fall, dass niedrigere Stromraten verwendet werden, erlaubt die Methode zusätzlich die Abschätzung des Aktivmaterialverlusts der einzelnen Elektroden. Die Methode funktioniert unabhängig von einer etwaigen Ladezustandsschätzung und es werden keine im Vorfeld gewonnenen Informationen über den Verlauf der Batteriealterung benötigt.

Die Methode basiert auf einem mechanistischen Zellmodell, welches das elektrische Verhalten von Lithium-Ionen-Zellen im Verlauf der Alterung beschreibt. Es ist eine zentrale Annahme in dieser Art von Modellen, dass sich die Form der Halbzell-Ruhepotentialkennlinien (engl. *open-circuit potential curves*, OCP-Kurven) mit der Zellalterung nicht verändert. In dieser Arbeit wird diese Annahme für zwei dem Stand der Technik entsprechenden Elektrodenmaterialien experimentell überprüft. Es wird gezeigt, dass sich die Form der OCP-Kurve von NMC-811 während der Alterung nicht signifikant ändert. Die Form der OCP-Kurve von Silizium-Graphit weist hingegen deutliche Änderungen im Verlauf der Alterung auf. Diese Änderungen werden von einer Abnahme des relativen Beitrags des Siliziums zur Elektrodenkapazität, ausgelöst durch eine schnellere Alterung des Siliziums im Vergleich zum Graphit, hervorgerufen.

Des Weiteren wird gezeigt, dass für den untersuchten Zelltyp die Vernachlässigung dieser Änderungen auf der Halbzellebene zu einer Unterschätzung des Anodenaktivmaterialverlusts, einer Überschätzung des Kathodenaktivmaterialverlusts sowie einer Überschätzung des Verlusts von zyklisierbarem Lithium führt, wenn die Degradationsmoden basierend auf Vollzell-Ruhespannungskurven bestimmt werden. Die Abweichungen sind in der Größenordnung einiger Prozentpunkte. Um die Änderungen der Form der Halbzell-OCP-Kurve von Silizium-Graphit zu berücksichtigen, kann die Halbzell-OCP-Kurve durch ein Mischelektrodenmodell beschrieben werden. Das mechanistische Zellmodell wird hierdurch auf die Elektrodenkomponentenebene erweitert. Diese Modellerweiterung ermöglicht die Abschätzung des verbleibenden Kapazitätsanteils, der durch das Silizium bereitgestellt wird, basierend auf mit geringem Strom gemessen Vollzell-Ladekurven.

Die zweite in dieser Arbeit vorgestellte Methode zur SOH-Schätzung basiert auf der Korrelation zwis-

chen dem Anstieg des Gasdrucks innerhalb des Gehäuses prismatischer Zellen und der Kapazitätsabnahme der Zellen während zyklischer Alterung. Diese Korrelation wurde im Rahmen einer in dieser Arbeit gezeigten Alterungsstudie beobachtet. Außerdem werden Ergebnisse zur Abhängigkeit des Gasdrucks von Ladezustand und Temperatur gezeigt.

Contents

List of figures

List of tables

Abbreviations

Please note that the list below is based on the main part of this thesis and does not fully cover the abbreviations used in the included research papers.

BEV . . . . . battery electric vehicle
BMS . . . . . battery managment system

CC . . . . . constant current
CCCV . . . . . constant current constant voltage
CEI . . . . . cathode electrolyte interface
CV . . . . . constant voltage

DC . . . . . direct current
DM . . . . . degradation mode
DMA . . . . . degradation mode analysis
DMC . . . . . dimethyl carbonate
DOD . . . . . depth of discharge
DV . . . . . differential voltage
DVA . . . . . differential voltage analysis

ECM . . . . . equivalent-circuit model
EFC . . . . . equivalent full cycle
EIS . . . . . electrochemical impedance spectroscopy
EOC . . . . . end of charge
EOD . . . . . end of discharge
EU . . . . . European Union
EV . . . . . electric vehicle

FOI . . . . . feature of interest

GA . . . . . genetic algorithm

HF . . . . . hydrofluoric acid

IC . . . . . incremental capacity
ICA . . . . . incremantal capacity analysis
IP . . . . . interior-point

LAM . . . . . loss of active material

LAM_{an} . . . . . loss of active material at the anode
LAM_{cat} . . . . . loss of active material at the cathode
LCO . . . . . lithium cobalt oxide
LFP . . . . . lithium iron phosphate
LLI . . . . . loss of lithium inventory
LM . . . . . Levenberg-Marquardt
LMO . . . . . lithium managanese oxide
LSS . . . . . large-scale storage system
LSTM . . . . . long and short term memory
LUT . . . . . look up table

MC . . . . . Monte-Carlo
MJ1 . . . . . INR18650-MJ1
MSMR . . . . . multiple-species multiple-reaction

NCA . . . . . nickel cobalt aluminum oxide
NLLS . . . . . non-linear least squares
NMC . . . . . nickel manganese cobalt oxide
NN . . . . . neuronal Network

OCP . . . . . half-cell open-circuit potential
OCV . . . . . full-cell open-circuit voltage

PHEV . . . . . plug-in hybrid electric vehicle
PS . . . . . pattern search
pSEI . . . . . positive solid electrolyte interface
PSO . . . . . particle swarm optimzation
PV . . . . . photovoltaic

RMSE . . . . . root-mean-square error
RUL . . . . . remaining useful lifetime

SEI . . . . . solid electrolyte interface
SiC . . . . . silicon-graphite
SOC . . . . . state of charge
SOH . . . . . state of health
SQP . . . . . sequential quadratic programming
SSE . . . . . sum of squared error
SVR . . . . . support vector regression

TM . . . . . transition metal

Formula symbols

Please note that the list below is based on the main part of this thesis and does not fully cover the formula symbols used in the included research papers.

α_{an} . . . . . anode scaling factor
α_{cat} . . . . . cathode scaling factor

β_{an} . . . . . anode offset
β_{cat} . . . . . cathode offset

C_2 . . . . . capacitance modeling dynamic overpotentials in F
C_{act} . . . . . actual (remaining) full-cell capacity in Ah
C_{an} . . . . . anode capacity in Ah
$C_{\mathrm{an,ini}}$ . . . . . initial anode capacity in Ah
C_{cat} . . . . . cathode capacity in Ah
$C_{\mathrm{cat,ini}}$ . . . . . initial cathode capacity in Ah
$C_{\Delta\mathrm{Int}}$ . . . . . differential intercalation capacity of a blend electrode in $\mathrm{As\,V^{-1}}$
$C_{\Delta\mathrm{Int}i}$ . . . . . differential intercalation capacity of electrode component i in $\mathrm{As\,V^{-1}}$
C_{ini} . . . . . initial cell capacity in Ah
C_{lit} . . . . . lithium inventory in Ah
$C_{\mathrm{lit,ini}}$ . . . . . initial lithium inventory in Ah
C_{loss} . . . . . capacity loss in Ah
$C_{\mathrm{loss,cal}}$ . . . . . calendaric capacity loss in Ah
$C_{\mathrm{loss,cyc}}$ . . . . . cyclic capacity loss in Ah

DOD . . . . . depth of discharge

F . . . . . Faraday constant, $9.648533212331001 84{\cdot}10^4\,\mathrm{C\,mol^{-1}}$

G . . . . . Gibbs free energy in $\mathrm{J\,mol^{-1}}$
γ . . . . . activity coefficient
γ_i . . . . . active mass scaling factor of component i

H . . . . . enthalpy in $\mathrm{J\,mol^{-1}}$

LAM_{an} . . . . . loss of active material at the anode
LAM_{cat} . . . . . loss of active material at the cathode
LLI . . . . . loss of lithium inventory

m . . . . . molality of lithium-ions at electrode surface in $\mathrm{mol\,kg^{-1}}$

μ . . . . . electrochemical potential in $\mathrm{J\,mol^{-1}}$
μ^{Θ} . . . . . electrochemical potential at standard conditions in $\mathrm{J\,mol^{-1}}$
μ_{an} . . . . . electrochemical potential of lithium in the anode in $\mathrm{J\,mol^{-1}}$
μ_{cat} . . . . . electrochemical potential of lithium in the cathode in $\mathrm{J\,mol^{-1}}$
μ_{ref} . . . . . electrochemical potential of a reference electrode in $\mathrm{J\,mol^{-1}}$

n . . . . . number of electrons transferred per reaction
n_{G} . . . . . amount of gas in mol

Ω . . . . . search space for alignment parameters
ω_j . . . . . degree of disorder of the intercalation reaction of gallery j

p . . . . . internal gas pressure in kPa

Q . . . . . charge throughput in Ah
Q_{blend} . . . . . charge of blend electrode in As
Q_{tot} . . . . . total charge throughput in Ah

R . . . . . universal gas constant, $8.31446261815324\,\mathrm{J\,K^{-1}\,mol^{-1}}$
R_1 . . . . . resistance modeling instantaneous overpotentials in Ω
R_2 . . . . . resistance modeling dynamic overpotentials in Ω

S . . . . . entropy in in $\mathrm{J\,mol^{-1}\,K^{-1}}$
SOC . . . . . state of charge
SOH . . . . . state of health

T . . . . . absolute temperature in K
θ . . . . . alignment parameters

U_{an} . . . . . open-circuit potential of the anode vs. $\mathrm{Li/Li^+}$ in V
U_{cat} . . . . . open-circuit potential of the cathode vs. $\mathrm{Li/Li^+}$ in V
U_{comp1} . . . . . open-circuit potential of electrode component 1 vs. $\mathrm{Li/Li^+}$ in V
U_{comp2} . . . . . open-circuit potential of electrode component 2 vs. $\mathrm{Li/Li^+}$ in V
U_j . . . . . open-circuit potential of the jth gallery in V
U_j^0 . . . . . concentration-independent standard potential in V
U_{max} . . . . . upper cut-off voltage in V
U_{min} . . . . . lower cut-off voltage in V
U_{OCP} . . . . . (half-cell) open-circuit potential vs. $\mathrm{Li/Li^+}$ in V
U_{OCV} . . . . . (full-cell) open-circuit voltage in V
$U_{\mathrm{OCV,meas}}$ . . . . measured full-cell open-circuit voltage in V
$U_{\mathrm{OCV,model}}$ . . . . simulated full-cell open-circuit voltage in V

V . . . . . free volume inside cell case in $\mathrm{m^3}$

x . . . . . lithiation degree of an electrode
x_{an} . . . . . electrode state of charge of the anode

x_{cat}	electrode state of charge of the cathode
x_{comp1}	state of charge of electrode component 1
x_{comp2}	state of charge of electrode component 2
X_{full}	full-cell state of charge range available for curve alignment
x_{full}	full-cell state of charge
$x_{\mathrm{full,i}}$	state of charge interpolation points for full-cell open-circuit voltage curve reconstruction
X_j	number of lithiation host sites of gallery j
x_j	fraction of filled host sites of gallery j
z	aging-model power law parameter

1 Introduction

1.1 The significance of battery electric storage for the energy transition

The transition of the global economy and society towards carbon neutrality is one of the major challenges of our age. In the 2015 Paris Agreement, the Conference of the Parties to the United Nations Framework Convention on Climate Change agreed on the common goal to hold the increase in the global average temperature to well below 2 °C above pre-industrial levels and to pursue efforts to limit the temperature increase to 1.5 °C as this would significantly reduce the risks and impacts of climate change [1]. In order to achieve this goal, the European Union (EU) and its member states have declared to target a reduction of 55% in greenhouse gas emissions by 2030 compared to 1990 [2] and to reach a climate-neutral EU by 2050 [3]. This ambitious endeavor will only be successful if substantial progress can be reached in all economic sectors including energy production, industry and transport. The EU has therefore set the target of a 32.5% improvement in the efficiency of its primary and final energy consumption by 2030 compared to a historic baseline [4] and to reach a contribution of at least 32% of renewable energy in the final energy consumption by 2030 [5]. Even more ambitious goals are currently discussed on the European level [6].

In the transport sector an average reduction of the CO_2 emissions per kilometer from passenger cars sold in the EU by 37.5% from 2021 levels by 2030 has been agreed on [7]. The most important strategy for the reduction of the greenhouse gas emissions in the transport sector is the stepwise replacement of cars with an internal combustion engine by electric cars, including battery electric vehicles (BEVs) and plug-in hybrid electric vehicles (PHEVs). During the last decade, there has been a continuous increase in the number of annual new electric car registrations as well as in the share of electric vehicles in total new car registrations in the EU [8], as shown in figure 1.1. In 2021, BEVs already accounted for 9.0 % and PHEVs for 8.8 % of the total new car registrations [8]. This trend is expected to continue during the next years [9] and the EU aspires that zero- and low-emission vehicles should constitute a share of at least 35 % of new passenger cars in 2030 [7]. Following the current negotiations on the European level, these goals might even get drastically tightened in the near future, culminating in a CO_2 reduction goal of 100 % for new passenger vehicles registered in the EU from 2035 onward [10].
As of today, lithium-ion batteries are the primarily used energy storage technology for electric vehicles [11]. In comparison to other battery technologies, they have an exceptionally high gravimetric energy density of about 250 $\mathrm{Wh\,kg^{-1}}$ [12]. Also prices for lithium-ion batteries have fallen dramatically during the last decade to reach about 130 $\mathrm{\$\,kWh^{-1}}$ [12]. The lithium-ion battery pack is a key component of today's electric vehicles and constitutes a significant share of the total production costs of a BEV.

Besides their high significance for the electrification of the transport sector, lithium-ion batteries are also expected to play a major role in the transformation of the energy sector. The increase in the share of renewable energy sources, which are fluctuating in their nature, will require an electricity

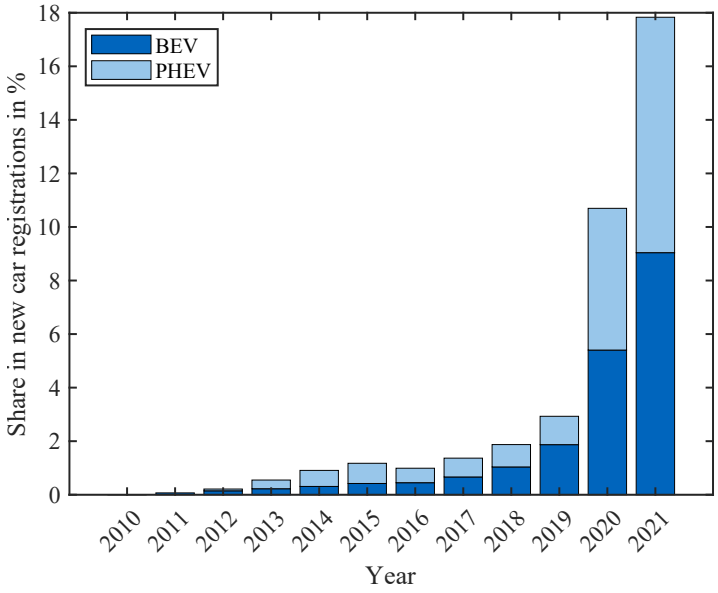

Figure 1.1: Share of electric vehicles in new car registrations in the EU between 2010 and 2021. Based on data from [8].

system with greater flexibility [13; 14]. Stationary energy storage systems using lithium-ion batteries are predicted to provide part of this flexibility [13; 14]. The services which can be offered by these systems to compensate for the fluctuations of renewable energy sources include frequency regulation, electric supply capacity reserves and renewable capacity firming [13]. In addition to this, battery electric storage systems are anticipated to be used at large scale to increase the local self-consumption of decentralized energy generation [13; 15]. The most important application of this type will probably be time shifting of the electricity produced by photovoltaic (PV) systems from daytime to the evening and night [13]. The increase in the cumulated capacity of stationary large-scale storage systems (LSSs) based on lithium-ion batteries installed in Germany is shown in figure 1.2. LSSs are defined as projects with a storage capacity $\geq 1\,\mathrm{MWh}$ and/or a nominal power output of $\geq 1\,\mathrm{MW}$ here [15].

Due to their significance for the decarbonization of the transport sector as well as for stabilizing the supply of electrical energy in a grid with a high share of fluctuating renewable sources, lithium-ion batteries are a key technology for the transition towards a carbon-neutral future. In order to facilitate an even broader use of this technology, it is important to better understand how lithium-ion batteries perform in applications throughout their life cycle, which usually spans multiple years for electric vehicles and stationary storage systems. Being able to monitor and predict the energy and power that can be delivered by a lithium-ion battery pack is an essential requirement both for the development of safe and reliable battery-powered systems as well as for optimizing the operation strategy of the systems.

1.2 Introduction to battery degradation and state of health estimation

Lithium-ion batteries degrade during usage and time [17; 18]. This leads to a decrease in the usable energy and power and eventually to the end of the usable lifetime of a battery [19]. In the field of

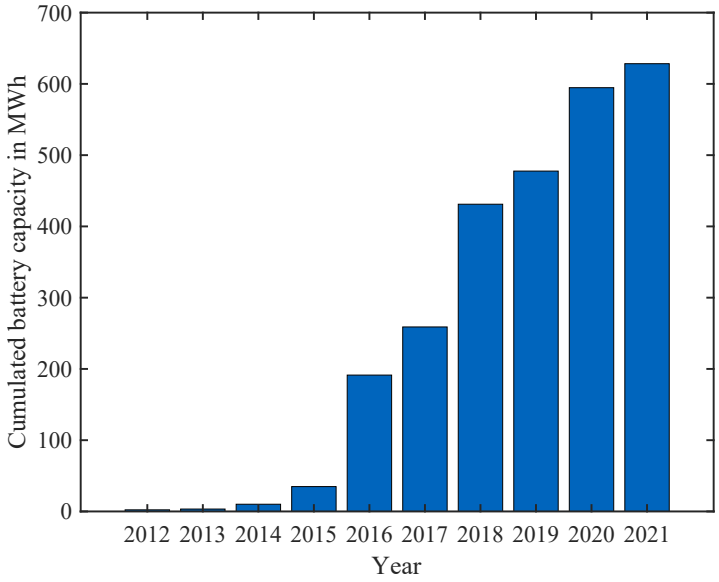

Figure 1.2: Cumulated capacity of large-scale storage systems based on lithium-ion batteries in Germany between 2012 and 2021. Based on data from [15; 16].

battery degradation research, there are three main topics, which are described in the following:

1. Understanding and modeling the mechanisms of battery degradation

Since the commercialization of lithium-ion batteries, a lot of research has been dedicated to deepen the understanding of the fundamental physical and chemical mechanisms that cause the degradation effects observable on cell and system level [17; 18; 20]. Still, the degradation mechanisms occurring in lithium-ion batteries and their interplay are highly complex and not fully understood on a microscopic level until today. It is therefore not yet possible to predict battery degradation of a certain system based on the material and design parameters using first-principle models.

2. Empirical modeling of degradation effects

The prediction of battery degradation as a function of operating conditions is highly important in an application context, for example to provide a reasonable warranty for a battery-powered product, to calculate the economic feasibility of stationary energy storage projects, to optimize the operation strategy in order to enhance the lifetime of an application or to design a system for which a certain lifetime of the battery is crucial, e.g., during space missions [21]. Due to the lack of fundamental understanding of the degradation mechanisms, empirical models are mostly used to describe and simulate the degradation of battery cells and systems [19]. These empirical aging models are parameterized based on aging tests conducted in the laboratory. This approach is time and cost intensive and it is a tremendous effort to test the degradation of a certain type of battery cell under all relevant combinations of operating conditions. In addition to this, the conditions in laboratory experiments usually differ from the conditions in the application [19]. This limits the transfer from the degradation observed in laboratory experiments to the application. Due to these shortcomings, it would be highly beneficial to develop methods that allow the parametrization of empirical aging models based on data that is recorded directly in the application and under operating conditions. This approach would have the advantage that battery aging under all relevant operating conditions could be monitored without the

need for costly and time consuming tests in the laboratory. The insights on the aging behavior of a certain type of system could then be used to optimize the operating strategy of such systems in the future.

3. Quantification of degradation effects during operation

The third important research goal is the development of methods that allow the quantification of battery degradation throughout the lifetime of a system [22–24]. This task, which is often called state of health (SOH) estimation, is usually performed by the battery managment system (BMS) of a battery system. Accurate determination of the remaining energy and power that can be provided by a battery is crucial in many applications, for example to estimate the remaining range of an electric vehicle or the energy that can be provided by a stationary storage system. Precise and robust SOH estimation is a key requirement for the reliability of many battery-powered applications. It can also be used to determine the residual value of a system which is important for example when a system is resold. In addition to this, accurate methods for SOH estimation are also a prerequisite to enable the parametrization of empirical aging models based on field data.
A vast number of methods for SOH estimation for lithium-ion batteries has been presented in the literature [22–24]. The methods can be classified into three main categories concerning the input data that is used:

- Aging model-based SOH estimation: The SOH is estimated by monitoring the operation conditions of the battery, and then translating the operation history into an estimate for the SOH using a pre-parametrized empirical aging model.
- Feature correlation-based SOH estimation: A correlation between a feature that is measurable during battery operation and the SOH is established empirically. Whenever the feature can be measured during operation, the correlation is used to estimate the SOH. This category includes most methods using machine learning techniques.
- Physical model-based SOH estimation: The physical behavior of the battery, e.g. in the electrical domain, is described by a model. The model parameters contain the SOH or quantities that allow the calculation of the SOH. The model parameters are updated during battery operation based on measurement data.

While all three approaches have their individual advantages, only the last category enables the parametrization of aging models based on field data. The physical model-based approach has also the great advantage that no aging experiments conducted in the laboratory are needed for algorithm development, except for testing and validation purposes.

The three research goals in the field of battery degradation research are closely linked to each other: Fundamental understanding of battery degradation mechanisms is the basis for physical model-based SOH estimation. It can also motivate the selection of features for feature correlation-based SOH estimation and the structure of empirical aging models. Empirical aging models are the basis for aging model-based SOH estimation and physical model-based SOH estimation is a requirement for field data based aging model parametrization. The interconnections between the different topics in the field of battery degradation research are presented in figure 1.3.

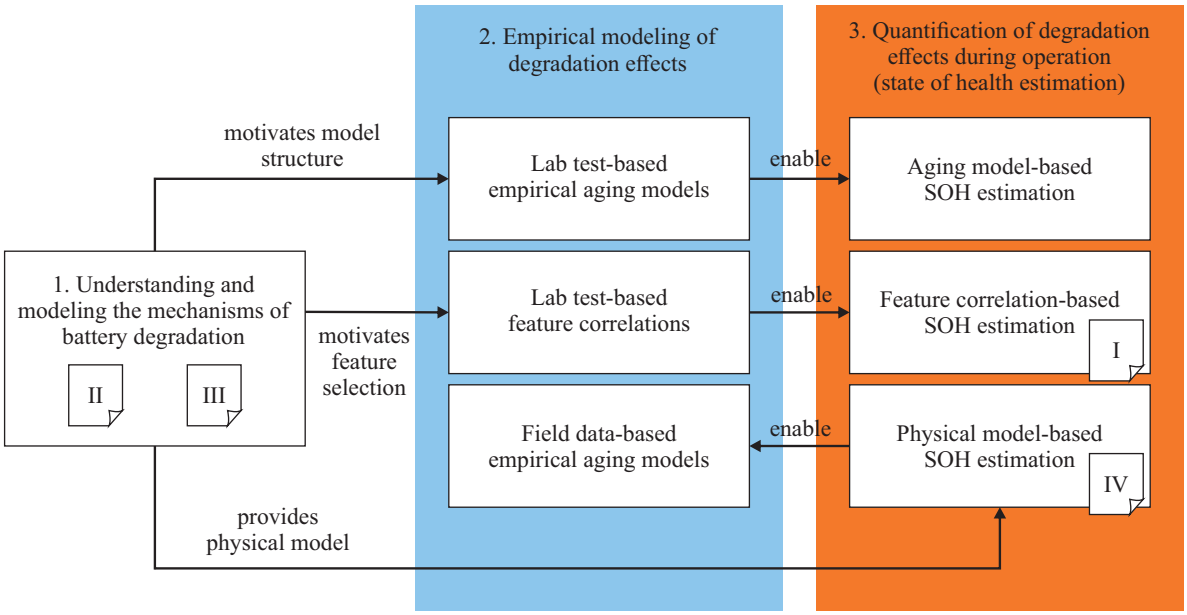

Figure 1.3: Research topics in the fields of battery degradation research. The studies presented in the scope of this thesis are represented by sheets with Roman numerals which are associated with the research topic they are mainly contributing to.

1.3 Scope and structure of this work

The individual studies presented in the scope of this thesis are classified into the context of the field of research in figure 1.3. As described in the previous section, accurate and robust SOH estimation for lithium-ion batteries is important for the reliable operation of battery systems. The main goal of this work is the development of two novel methods for SOH estimation for lithium-ion batteries. The first method investigated in the scope of this work is a feature correlation-based method in which the correlation between the increase in the gas pressure inside a prismatic lithium-ion cell and the decrease in the cell capacity during cycle aging is used to estimate the SOH (Study I). The second method is physical model-based. The concept of this method is to use the voltage curve measured during CC charging phases to determine the remaining capacities of the individual electrodes and the electrode balancing and thus to estimate the remaining cell capacity (Study IV). This second method is based on the mechanistic cell model introduced by Dubarry et al. [25]. This modeling approach associates changes in the full-cell open-circuit voltage (OCV) curve of lithium-ion cells with clusters of degradation mechanisms, so called degradation modes, that have occurred during aging. It is a central hypothesis of the mechanistic modeling approach that the shape of the half-cell open-circuit potential (OCP) curves of the electrodes does not change during aging [26]. In the scope of this thesis, it is investigated, whether this aging-invariance can also be assumed for cells with silicon-graphite (SiC) as anode material (Study II + III), which can be regarded as a preliminary step for Study IV. Apart from this, this investigation also contributes to a better understanding and modeling of the degradation of SiC, which could also be useful in other contexts.

The remaining part of this work is structured as follows: the fundamentals of lithium-ion batteries with emphasis on the OCV and the mechanical behavior, are presented in section 2.1. An overview on the current understanding of battery degradation on different levels of abstraction is given in section

2.2. In section 2.3, an overview on the definitions and requirements for SOH estimation as well as a literature review on methods for SOH estimation are presented.
In the main part of this work, four research articles are presented: in chapter 3, the aforementioned method for SOH estimation based on internal gas pressure measurements is presented (Study I). In chapter 4, results on the aging-invariance of half-cell OCP curves are presented. This includes experimental results on the change in the shape of the half-cell OCP curves of SiC and nickel manganese cobalt oxide (NMC)-811 during cycle aging (Study II), presented in section 4.1. Results on the impact of these changes on the shape of the full-cell OCV curve (Study III) are presented in section 4.2. In chapter 5, the method for SOH estimation based on charging curves is presented (Study IV). The key results of all studies contained in this thesis are collectively discussed and a general conclusion is drawn in chapter 6. Finally, an outlook on possible future research directions is given in this chapter. The structure of this thesis is graphically illustrated in figure 1.4.

Chapter 1: Introduction

Chapter 2: Aging of lithium-ion batteries and state of health estimation

Chapter 3: Measurement of internal gas pressure for state of health estimation

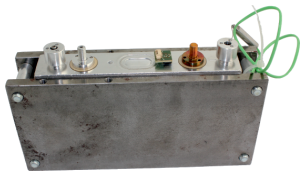

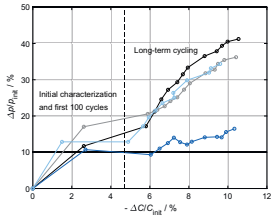

Study I: Measurement of gas pressure inside large-format prismatic lithium-ion cells during operation and cycle aging

Chapter 4: Change in the shape of the open-circuit potential curve during cycle aging

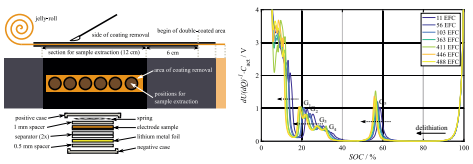

Study II: Change in the half-cell open-circuit potential curves of silicon–graphite and nickel-rich lithium nickel manganese cobalt oxide during cycle aging

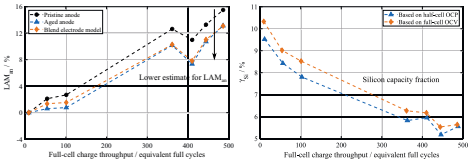

Study III: Determination of degradation modes of lithium-ion batteries considering aging-induced changes in the half-cell open-circuit potential curve of silicon–graphite

Chapter 5: State of health estimation based on partial charging curves

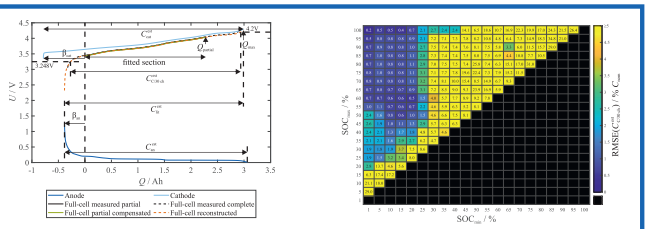

Study IV: Capacity and degradation mode estimation for lithium-ion batteries based on partial charging curves at different current rates

Chapter 6: Discussion, conclusion and outlook

Figure 1.4: Structure of this thesis.

2 Aging of lithium-ion batteries and state of health estimation

2.1 Fundamentals of lithium-ion batteries

In this section, different topics related to lithium-ion batteries, which are necessary for the understanding of the main part of this thesis, are presented.

2.1.1 Components and working principle

A lithium-ion cell is an electrochemical cell that contains two electrodes and an electrolyte [27]. The components and the working principle of lithium-ion cells are schematically shown in figure 2.1. During charging and discharging of lithium-ion cells, lithium cations intercalate and deintercalate into/from the electrodes, which can be described as a spatially separated redox reaction [28]. The most common active material for lithium-ion negative electrodes is graphite [27] and the half-cell reactions at this electrode are described [29] by

$$\mathrm{Li}_x\mathrm{C}_6 \rightleftharpoons x\,\mathrm{Li}^+ + x\,\mathrm{e}^- + \mathrm{C}_6. \tag{2.1}$$

During discharging of the full-cell, the reaction direction goes from the left to the right as lithium-ions deintercalate from the graphite and the graphite electrode gets oxidized. The generated lithium-ions are then transported to the positive electrode via the electrolyte while the released electrons go through the external electric circuit and can be used to do work. At the positive electrode, lithium-ions are inserted into the host structure. The positive electrode host structures of the cells investigated in this work are layered transition metal oxides and the half-cell reactions at this type of positive electrodes are simplified described by

$$\mathrm{Li}_{1-x}\mathrm{MO}_2 + x\,\mathrm{Li}^+ + x\,\mathrm{e}^- \rightleftharpoons \mathrm{LiMO}_2 \tag{2.2}$$

where M represents a combination of Ni, Mn and Co. The reaction direction during discharging of the full-cell goes from the left to the right as the positive electrode gets reduced. The complete full-cell reactions at both electrodes can then be simplified described [30] by

$$\mathrm{Li}_x\mathrm{C}_6 + \mathrm{Li}_{1-x}\mathrm{MO}_2 \rightleftharpoons \mathrm{C}_6 + \mathrm{LiMO}_2. \tag{2.3}$$

Lithium-ion cells can be reversibly charged and discharged and therefore both electrodes can be reduced or oxidized depending on the reaction direction. For the nomenclature of the electrodes, the discharging case is defined as standard and the negative electrode which gets oxidized in this case is called anode while the positive electrode which gets reduced is called cathode [30]. This definition is also used throughout this thesis.

In order to enable controlled charging and discharging of the cell, both electrodes need to be ionically connected by an electrolyte, which is typically a mixture of organic solvents in which a lithium salt is dissolved [27]. At the same time, the electrodes need to be electrically separated which is accomplished by a porous separator in between the electrodes [27]. The separator is soaked with electrolyte and allows transport of lithium-ions while it prevents the contact and electrical shorts between the electrodes. Conductive materials like carbon black and binders are typically added to the electrode active materials in order to increase the electrical conductivity and structural stability of the electrodes [27]. The electrode slurries are coated onto metal foils which serve as current collectors and which are connected to the cell terminals. Copper is used for the anode current collector while aluminum is used for the cathode current collector [31]. The components of the cell are contained either inside a hard metallic case (cylindrical cells, prismatic cells, and coin-cells) or inside a flexible metallic composite foil (pouch cells) [31]. In the following, some background information on the anode material types used in the cells that are investigated in the main part of this work (chapter 3-5) is provided.

Graphite Graphite is a carbonaceous material with a layered structure [32]. Lithium can intercalate in between the carbon layers to form lithium-graphite intercalation compounds. At ambient pressure, a maximum of one lithium atom per six carbon atoms can intercalate ($x \leq 1$ in Li_xC_6) [32], which results in a theoretical gravimetric capacity of $372\,mAh\,g^{-1}$ [33]. At low lithiation, lithium is not inserted in between all the graphene layers but there are periodically unoccupied layer gaps. Thus, during lithiation and delithiation of graphite, different phases, so-called stages, form in the graphite [34; 35]. The staging is a thermodynamic phenomenon that is related to the energy necessary for broadening the van der Waals gap between two graphene layers [36] and the repulsive interactions between the intercalated lithium-ions, which makes few but highly occupied van der Waals gaps energetically favored [32]. The number of graphene layers in between layers that are filled with lithium atoms decreases during lithiation and increases during delithiation. The stages are usually referred to by the number of graphite layers between two lithium layers. In some cases, partly lithiated stages are energetically favorable, they are usually marked with an additional 'L' (for liquid-like) [34; 37]. The concept of graphite stages is schematically shown in figure 2.2. The following stages are reported in the literature

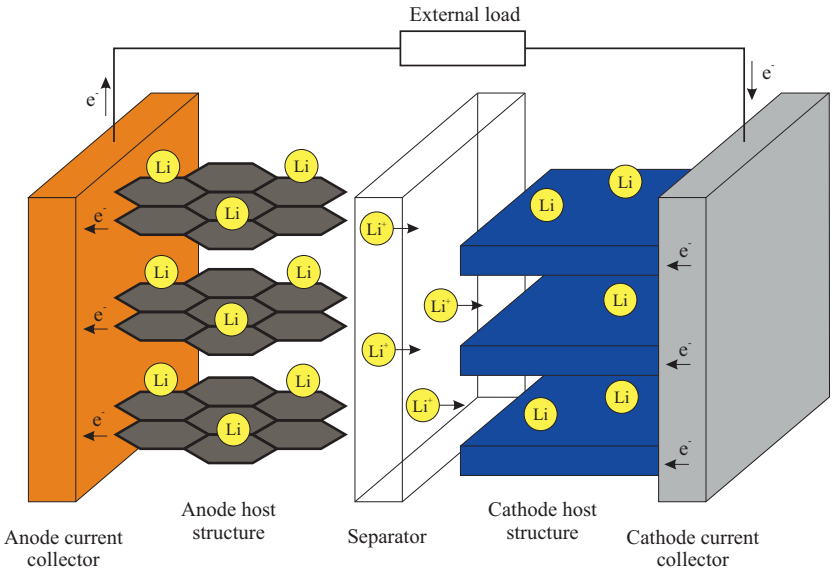

Figure 2.1: Components and working principle of a lithium-ion cell during discharging.

[34; 37–40] where x refers to the degree of lithiation in Li_xC_6: Stage 1 (LiC_6, $x = 1$), stage 2 (LiC_{12}, $x = 0.5$), stage 2L ($x \approx 0.25$), stage 3 (LiC_{27}, $x \approx 0.22$), stage 4 (LiC_{36}, $x \approx 0.17$), and a dilute stage 1L (LiC_{72}, $x \approx 0.083$). The differentiation and exact crystallographic description of the lowly-lithiated phases ($x < 0.5$) is still subject to ongoing research [35; 36]. Graphite is used as anode active material in the cells that are investigated in the study on internal gas pressure measurements for SOH estimation, which is presented in chapter 3.

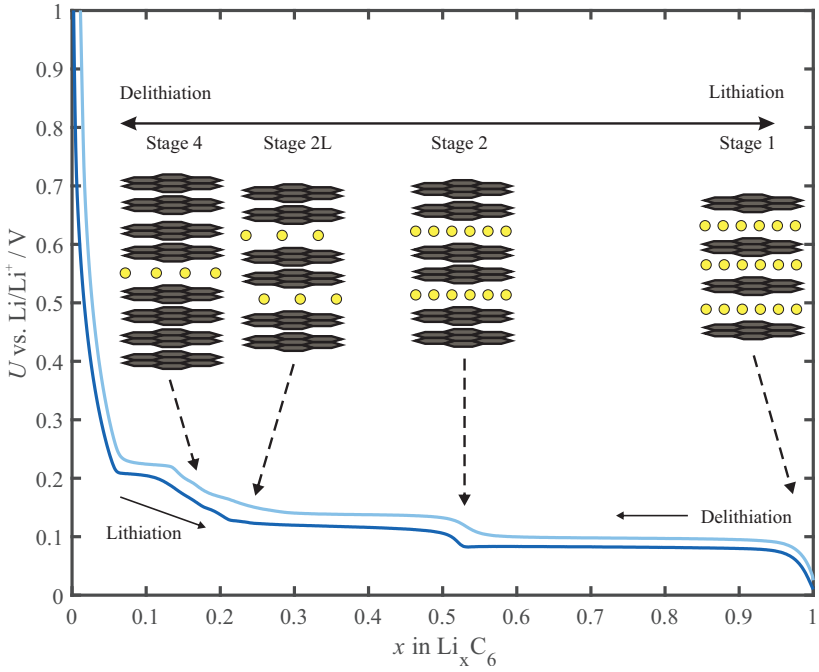

Figure 2.2: OCP of graphite during lithiation and delithiation. The regions of the OCP curves with large slope are associated with lithiation stages of graphite. The structure of selected graphite stages is schematically presented.

Silicon-graphite Due to its high theoretical gravimetric capacity of $3572\,\mathrm{mAh\,g^{-1}}$ [41] and its low electrochemical potential, silicon is a promising negative electrode material for lithium-ion cells [42]. In contrast to the intercalation-type reaction between graphite and lithium-ions, the electrochemical reaction between silicon and lithium-ions is an alloying reaction [42]. Silicon exhibits a pronounced expansion of up to 400 % upon lithiation [43], which is a challenge for the cycle stability of this material. A strategy to combine the high capacity of silicon with the cycle stability of graphite is to use blends of silicon and graphite as anode material. The overall gravimetric capacity of the electrode can be significantly increased by adding comparably small amounts of silicon to the graphite [44], while still decent cycle stability is retained [45]. The commercial cells used for the studies presented in chapter 4 and 5 have SiC anodes [45–50].

2.1.2 Open-circuit voltage models

Full-cell OCV curves and half-cell OCP curves are investigated in chapters 4 and 5 in the main part of this thesis. In the following, the theoretical background on models for the full-cell OCV and the half-cell OCP is presented.

Fundamentals The following description of the fundamentals of the OCV is based on [28]. The driving force behind the Faradaic reactions in a lithium-ion cell is the difference between the electrochemical potentials of the reactive species, i.e., the lithium atoms, in the electrodes. The electrochemical potential of a species in a phase is a thermodynamic quantity that depends on the temperature, pressure, chemical composition and electrical state of the phase. The change in energy per electrochemical redox reaction in a lithium-ion cell is given by the change in Gibbs free energy

$$\Delta G = \mu_{\mathrm{cat}} - \mu_{\mathrm{an}} \tag{2.4}$$

where G is Gibbs free energy, μ_{cat} is the electrochemical potential of lithium in the cathode and μ_{an} is the electrochemical potential of lithium in the anode. According to the aforementioned convention, the electric potential of the electrode defined as anode is more negative, and therefore its electrochemical potential is higher. If the two electrodes are electrically connected via an external circuit, electrons will spontaneously flow from the anode to the cathode while the same number of lithium-cations will be transferred from the anode to the cathode. The change in Gibbs free energy is negative in this case as it is a spontaneous reaction by which energy is released from the system. This energy can be used to do work in the external circuit and the difference in electrochemical potential between the electrodes is the theoretical maximum for the electrical work that can be done per reaction.

The electrochemical potential (μ) of lithium at the surface of intercalation electrodes depends mainly on the chemical composition of the electrode, including the degree of lithiation at the surface, and, to a lesser extent, on the temperature (T) and the molality (m) of lithium-ions in the electrolyte at the surface which can be described by

$$\mu = \mu^{\ominus} + RT \ln(m\gamma) \tag{2.5}$$

where γ is the activity coefficient, $\mu^{\ominus}$ is the electrochemical potential at standard conditions and R is the universal gas constant.

The change in Gibbs free energy per reaction is related to the electrical voltage U_{OCV} that can be measured between the two electrodes of a lithium-ion cell at thermodynamic equilibrium according to

$$\Delta G = -nFU_{\mathrm{OCV}}, \tag{2.6}$$

where $n = 1$ is the number of electrons transferred per reaction and F is Faraday's constant. This voltage is called (full-cell) OCV. Thus, the OCV of a lithium-ion full-cell depends on the electrochemical potentials of both electrodes. Similar to this, the difference in the electrochemical potential of lithium in one of the electrodes to the electrochemical potential of lithium in a reference electrode is linked to the (half-cell) OCP (U_{OCP}), which is equal to the voltage that can be measured between the lithium intercalation electrode and an ionically connected reference electrode via

$$\mu - \mu_{\mathrm{ref}} = -nFU_{\mathrm{OCP}}. \tag{2.7}$$

This relation allows the description of the electrochemical potential of an intercalation electrode at equilibrium conditions by a measurable electrical voltage. The common reference for the electrochemical potential of lithium in intercalation electrodes is the electrochemical potential of lithium in a metallic lithium electrode ($\mathrm{Li/Li^+}$), which is always higher than the electrochemical potential in an intercalation electrode at equilibrium. In this work, OCP refers to the electric potential of a half-cell

under equilibrium conditions where Li/Li^+ is used as reference, while OCV refers to the voltage between the electrodes of a full-cell at equilibrium conditions. The OCP between the anode and a lithium metal reference is denoted as U_{an} and the OCP between the cathode and a lithium metal reference is denoted as U_{cat} in this thesis. For practical reasons, the use of electrochemical potentials is avoided in most approaches for modeling the physical behavior of lithium-ion cells and the thermodynamic properties of electrode materials at equilibrium are directly described by the half-cell OCP with respect to lithium metal.

The relation between the half-cell OCP of the electrodes vs. Li/Li^+ and the full-cell OCV can be derived by using the equality between equation 2.4 and equation 2.6

$$-nFU_{OCV} = \mu_{cat} - \mu_{an}, \tag{2.8}$$

adding $\mu_{ref} - \mu_{ref} = 0$ to the right side of the equation

$$-nFU_{OCV} = (\mu_{cat} - \mu_{ref}) - (\mu_{an} - \mu_{ref}), \tag{2.9}$$

using equation 2.7 at the right side of the equation for both cathode and anode

$$-nFU_{OCV} = -nFU_{cat} - (-nFU_{an}), \tag{2.10}$$

and finally canceling the constants

$$U_{OCV} = U_{cat} - U_{an}. \tag{2.11}$$

The full-cell OCV is therefore simply described by the difference between the electrical half-cell OCP of the cathode and the electrical half-cell OCP of the anode, both with respect to Li/Li^+ or any other chosen reference.

The electrochemical potential of lithium intercalation electrodes significantly depends on the lithiation degree of the electrode. The half-cell OCP of the electrodes therefore changes during lithiation/delithiation. In the modeling frameworks which model the behaviour of lithium-ion cells on the electrode or half-cell level, this is represented by implementing the OCP of the individual electrodes as functions of lithiation degree, so called half-cell OCP curves. Examples for this are electrochemical Newman-type p2D models [49] or the mechanistic model introduced by Dubarray et al. [25]. In more practically-oriented models that only model physical quantities on the full-cell level, the half-cell origin of the full-cell OCV is often neglected and the full-cell OCV curve, i.e., the relationship between full-cell OCV and full-cell state of charge (SOC), is directly used as model parameter [51]. A description of the cell voltage at thermodynamic equilibrium is a fundamental part of every model for the electrical behaviour of a lithium-ion cell and it is also needed for most physical model-based methods for SOH estimation. In the following, an overview on approaches for modeling the half-cell OCP curve and the full-cell OCV curve is given.

Dependence of the half-cell OCP on the lithiation degree The OCP of a lithium intercalation electrode as a function of the lithiation degree is defined by the thermodynamic properties of the electrode material. The process of lithium intercalation is generally not uniform due to the complex interactions of intercalated lithium atoms and the host structure [52]. The lithiation/delithiation of graphite fol-

lows the staging process described in section 2.1.1, during which different phases of lithiated graphite with individual structural and thermodynamic properties are formed. At certain lithiation degrees the graphite is almost exclusively in one phase. In these single-phase regions, the graphite intercalation compound is described as a solid solution and the OCP varies strongly with the lithiation degree, as the filling fraction of the lithiated layers continuously changes [52]. Between the single-phase regions, the coexistence of two adjacent phases is thermodynamically favorable. In these two-phase transition regions, the chemical composition of the two phases does not change significantly, but the ratio in which the two phases are present in the electrode changes. In these regions, the chemical potential of both phases is the same at equilibrium and exhibits only minor change as long as both phases coexist. This results in a plateau of the OCP curve in this region [52]. The intercalation process of typical cathode materials like transition metal layered oxides also takes place as a series of two-phase transitions between a number of different phases of lithium intercalation compounds. For example, NMC-811, the cathode material that is used in the commercial cell investigated in chapters 4-5, forms three different hexagonal and one monoclinic phases during lithiation/delithiation [53; 54].

There are thermodynamic models based on the description of Gibbs free energy of an intercalation material, so called phase-field models, that allow the prediction of phases, phase-transition regions and also the OCP curve [52; 55]. The objective of such models is rather to provide a framework for the theoretical understanding of the processes occurring during lithium intercalation/deintercalation than to quantitatively predict the OCP curve of a certain material.
In contrast to this, there are also models which do not establish a relation between the fundamental material thermodynamics and the OCP curve of an electrode, but which describe the OCP curve based on empirically determined parameters. A commonly used model of this type is the multiple-species multiple-reaction (MSMR) model [56–60]. In this model, an electrochemical potential and an associated OCP is assigned to the possible intercalation sites for the lithium-ions. There are j types of intercalation sites with different energy, which are sometimes called galleries [60]. j also corresponds to the number of voltage plateaus of the OCP curve. The OCP of a specific gallery U_j is calculated as

$$U_j = U_j^0 + \frac{\omega_j}{F/(RT)} \ln\left(\frac{X_j - x_j}{x_j}\right) \tag{2.12}$$

where U_j^0 is the lithium concentration-independent standard electrode potential of this gallery. X_j is the number of lithiation host sites of the gallery divided by the total number of host sites of the material and x_j is the fraction of the filled host sites of this gallery. ω_j is a unitless parameter that describes the degree of disorder of the intercalation reaction of gallery j. At equilibrium, the OCP of all galleries is equal and corresponds to the half-cell OCP ($U_j = U_{\mathrm{OCP}} \forall j$). By solving equation 2.12 for x_j and summing up over all galleries ($\sum_j x_j = x$), an expression for the overall lithiation degree of the electrode (x) can be obtained

$$x = \sum_j \frac{X_j}{1 + \exp[\frac{F}{RT\omega_j}(U_{\mathrm{OCP}} - U_j^0)]}. \tag{2.13}$$

Equation 2.13 is then the model description for the OCP curve and the model can be parametrized by fitting this equation to a measured half-cell OCP curve. The model is then parameterized by the number of galleries j and the three parameters U_j^0, ω_j and X_j for every gallery [57; 60]. Due to its generic formulation, the MSMR model can be used to model the OCP curve of graphite [56–60], the OCP curve of cathodes materials that are lithiated/delithiated via two-phase transition reactions [57;

59; 60] and even to model the OCP curve of substitution-alloy materials such as lithiated silicon [58]. There are also other thermodynamics-motivated models that describe the shape of an experimentally determined OCP curve, e.g. the Redlich-Kister model [61; 62] or a model based on an expansion of the Nernst equation by terms describing the interactions associated with the staging phenomena [63].

Due to the fact that first-principles thermodynamic models can not predict the OCP curve of lithium intercalation electrodes with the necessary accuracy until now, the OCP curve of a specific electrode material is usually obtained experimentally [49] regardless of whether it is then described by the MSMR model, fitted by a simpler analytical equation or directly implemented into a cell model as a lookup table. Common methods for measuring half-cell OCP curves are described in 2.1.3.

The OCP curve generally differs during lithiation and delithiation [57; 64; 65]. This phenomenon is called voltage hysteresis. It is caused by the fact that different thermodynamically stable electrode configurations with the same lithiation degree can be reached via the lithiation and the delithiation reaction [65]. Individual OCP curves for the lithiation and the delithiation direction are therefore often used in electrical cell models [66].

Temperature dependence of the half-cell OCP curve The part of the electrochemical potential that is independent from the concentration of lithium-ions on the electrode surface (see equation 2.5) also depends on the temperature because of the thermodynamic definition of Gibbs free energy. The change in Gibbs free energy per reaction is described by

$$\Delta G = \Delta H - T\Delta S \tag{2.14}$$

where H is the enthalpy and S the entropy of the system [28]. Thus, the OCP curve is temperature-dependent [60]. The change in entropy upon lithiation/delithiation depends on the lithiation degree and can be determined by measuring the OCP at a certain lithiation degree during a change in temperature [67]

$$\Delta S(x) = nF\frac{dU_{\mathrm{OCP}}(x)}{dT}. \tag{2.15}$$

Blend electrode open-circuit potential The OCP curve of a blend electrode material, such as silicon-graphite, depends on the thermodynamic properties and thus on the OCP curves of its components. Schmidt et al. proposed a model to describe the OCP curve of blend electrodes [68], which is used to describe the OCP of SiC electrodes in chapter 4.2. In this model, the differential intercalation capacity (in $\mathrm{As\,V^{-1}}$) at voltage U ($C_{\Delta\mathrm{Int}}(U)$) is described as

$$C_{\Delta\mathrm{Int}}(U) = \gamma_1 \cdot C_{\Delta\mathrm{Int1}}(U) + \gamma_2 \cdot C_{\Delta\mathrm{Int2}}(U) \tag{2.16}$$

where $C_{\Delta\mathrm{Int}i}$ is the differential intercalation capacity of the ith component (in $\mathrm{As\,V^{-1}}$) and γ_i are factors to scale the active masses of the components. The blend OCP curve is obtained by integrating equation 2.16

$$Q_{\mathrm{blend}}(U_{\mathrm{OCP}}) = \int_{U_{\mathrm{OCP}}}^{U_{\mathrm{max}}} C_{\Delta\mathrm{Int}}(U)dU \tag{2.17}$$

to obtain a description for the charge of the intercalated lithium at a certain OCP ($Q_{\mathrm{blend}}(U)$), and then taking the inverse

$$U_{\mathrm{OCP}}(Q_{\mathrm{blend}}) = f^{-1}(Q_{\mathrm{blend}}(U_{\mathrm{OCP}})). \tag{2.18}$$

In this way, the capacity contributions of both components at a certain voltage are added up and the blend OCP curve is obtained. The parameters γ_i are obtained by fitting equation 2.18 to a measured blend OCP curve. The concept of blending the component OCP curves is schematically displayed in figure 2.3. The half-cell OCPs of the two electrode components are denoted as U_{comp1} and U_{comp2}. The component specific SOCs are denoted as x_{comp1} and x_{comp2}. This model was experimentally validated for blends of nickel cobalt aluminum oxide (NCA) and lithium managanese oxide (LMO) with different mass fractions [68]. The same approach was used by Jung for modeling NMC/LMO as well as graphite/soft carbon blend OCP curves [69]. Anseán et al. modeled the blend electrode OCP of SiC using this approach [70]. The modeling approach is limited to near equilibrium scenarios in which the current through the cell is negligible. If higher current are passing through the cell, the overpotentials, which could be generally different for the individual electrode components, need to be considered [68]. More complex blend electrode models are used to capture the inhomogeneous lithiation/delithiation of silicon and graphite at higher current rates [66; 69].
Due to the difference in the OCP curves of silicon and graphite, the silicon is primarily lithiated at the beginning of the lithiation of SiC while the graphite is mainly lithiated later at lower half-cell potentials. During delithiation, the graphite is preferably delithiated before the silicon is delithiated [71]. The OCP curve of silicon has a pronounced hysteresis [72; 73] which needs to be considered in a blend electrode OCP model. For example, different component OCP curves for lithiation and delithiation can be used [66].

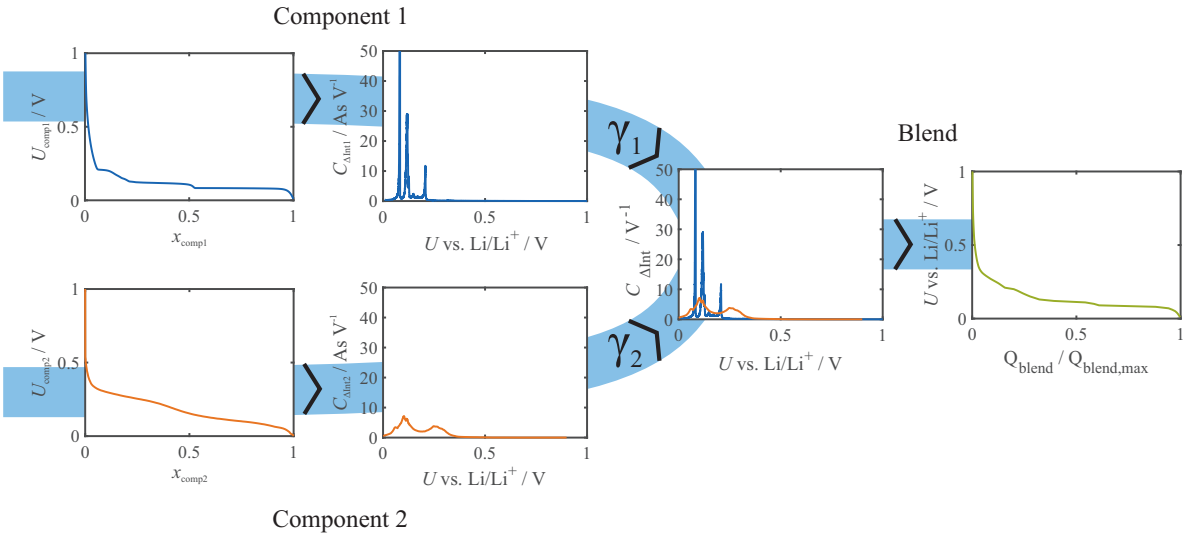

Figure 2.3: Blend OCP model presented by Schmidt et al. [68]. Data for graphite (component 1) [46] and silicon (component 2) [74] is shown.

Full-cell OCV curve models According to equation 2.11, the full-cell OCV curve, i.e., the OCV as a function of full-cell SOC (x_{full}) can be calculated as the difference between the half-cell OCP curves as

$$U_{\mathrm{OCV}}(x_{\mathrm{full}}) = U_{\mathrm{cat}}(x_{\mathrm{cat}}) - U_{\mathrm{an}}(x_{\mathrm{an}}) \tag{2.19}$$

where U_{cat} and U_{an} are functions of the electrode SOCs x_{cat} and x_{an} [25; 75]. The full-cell SOC range is defined in between the lower and the upper cut-off voltage of the full-cell. Due to practical reasons, most cathode materials can not be fully delithiated as explained in section 2.1.3. Thus, the electrode SOC range is defined by the part of an electrode capacity that can be reversibly lithiated and delithiated [60]. In this work, $x_{\mathrm{an}} = 0$ corresponds to the state where the anode is at the upper half-cell cut-off voltage (delithiated) while $x_{\mathrm{an}} = 1$ corresponds to the state in which the anode is at the lower half-cell cut-off voltage (lithiated). $x_{\mathrm{cat}} = 0$ corresponds to the state in which the cathode is at the upper half-cell cut-off voltage (delithiated) and $x_{\mathrm{cat}} = 1$ corresponds to the state in which the cathode is at the lower half-cell cut-off voltage (lithiated). The relationship between the full-cell SOC and the electrode SOCs is defined by the capacitive and stoichiometric balancing of the electrodes.
The electrode balancing can be determined by shifting and scaling the half-cell OCP curves in a way that their difference matches the measured full-cell OCV curve as shown in figure 2.4. To do this, the half-cell OCP curves get linearly scaled on the SOC-axis by α_{an} and α_{cat} respectively. α_{an} and α_{cat} therefore denote the factor by which each reversibly usable electrode capacity exceeds the full-cell capacity. The relative position of the half-cell OCP curves on the SOC-axis is determined by an offset β_{an} and β_{cat} with respect to the starting point of the full-cell OCV curve, i.e., $x_{\mathrm{full}} = 0$. The shifting and scaling of the half-cell OCP curves resembles a transformation of the electrode SOC into the corresponding full-cell SOC. For the anode, this transformation is described by

$$x_{\mathrm{full}} = x_{\mathrm{an}} \cdot \alpha_{\mathrm{an}} + \beta_{\mathrm{an}} \tag{2.20}$$

while for the cathode it is described by

$$x_{\mathrm{full}} = (1 - x_{\mathrm{cat}}) \cdot \alpha_{\mathrm{cat}} + \beta_{\mathrm{cat}}. \tag{2.21}$$

Solving equation 2.20 for x_{an} and equation 2.21 for x_{cat} and inserting them into equation 2.19 results in a model description of the full-cell OCV curve as a function of full-cell SOC

$$U_{\mathrm{OCV}}(x_{\mathrm{full}}) = U_{\mathrm{cat}}(1 - (x_{\mathrm{full}} - \beta_{\mathrm{cat}})/\alpha_{\mathrm{cat}}) - U_{\mathrm{an}}((x_{\mathrm{full}} - \beta_{\mathrm{an}})/\alpha_{\mathrm{an}}). \tag{2.22}$$

The electrode balancing is therefore completely described by the the four alignment parameters α_{an}, α_{cat}, β_{an} and β_{cat} [25]. This OCV model is the basis for the mechanistic cell model described in section 2.2.2 and which is used in the studies presented in section 4.2 and chapter 5 in the main part of this thesis.

In many cell models that are used for state estimation, measured full-cell OCV curves are directly implemented as lookup tables [51; 64; 76; 77] without considering the OCP of the half-cells and the electrode balancing. Measured full-cell OCV curves are also sometimes fitted with mathematical model equations that are not physically motivated but which resemble a memory-optimized implementation of the OCV curve using a limited number of parameters. Possible model equations include polynomial and exponential models [78; 79]. The MSMR model approach can also be applied to describe full-cell OCV curves. In this case, the individual phases are not assigned to a specific electrode [75].

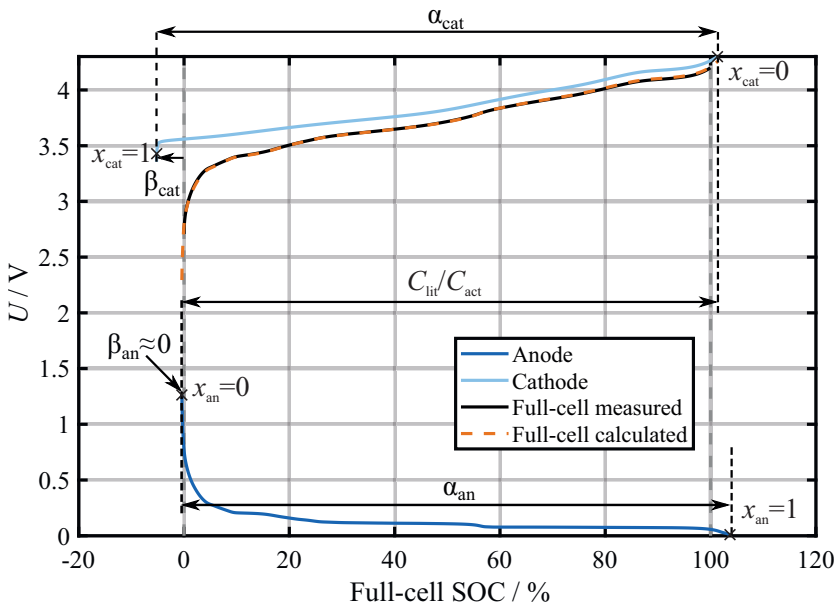

Figure 2.4: Full-cell OCV curve as difference between half-cell OCP curves. Figure based on [47].

2.1.3 Methods for measuring the open-circuit voltage

Measurements of full-cell OCV curves and half-cell OCP curves are described in the main part of this thesis. In this section, an overview on the methods for such measurements is provided.

Measurement of full-cell OCV curves The two established methods for determining the OCV curve of a full-cell are described in the following.

The OCV of a cell is defined as the voltage that can be measured between the terminals when the cell is in an equilibrium state. A common method for measuring the OCV of a cell is therefore to bring the cell to a certain SOC, let it rest under open-circuit conditions, and then measure the terminal voltage after relaxation [36; 57; 65; 77; 80–82]. This method is referred to as incremental OCV measurement [80]. Complete equilibrium can never be reached as there are continuous side reactions like self-discharge or processes associated with calendar aging even at open-circuit conditions [83]. A quasi-equilibrium state is therefore usually defined to be reached if the change in terminal voltage during a certain time is below a threshold. The relaxation time after which this equilibrium is reached is different for individual cell types and also depends on the SOC, the temperature and the current that was applied before the relaxation period. The duration of the relaxation period is usually in the order of a few hours [65; 80; 81]. The complete measurement procedure consists of fully charging or discharging the cell first, followed by alternating phases of CC discharging/charging and relaxation [81].

The second established method to measure the OCV of a lithium-ion cell is to measure the terminal voltage during constant low-current charging or discharging between the lower and upper cut-off voltage. This method is sometimes called quasi-stationary OCV measurement. The idea behind this approach is that if a small enough current is used to charge or discharge the cell, the deviation of the terminal voltage from the OCV is negligibly small. On the one hand, this approach has two main advantages over the relaxation based method: firstly, it is usually much faster, and secondly, the resolution in the SOC dimension is theoretically only limited by the maximum sampling rate of

the testing instrument and the available memory for data storage. On the other hand, the voltage measured at a certain SOC usually differs from the value obtained via a relaxation measurement with long relaxation time, especially if comparably high current rates are used. Even when low current rates are used, there is still some deviation from the OCV measured after relaxation as the cell is not completely at rest during the measurement [77]. Typical current rates for quasi-stationary OCV measurements range from C/10 [81] over C/20 [84–86], C/25 [87; 88] and C/30[49; 60] to C/50 [89]. Some authors encourage to conduct an extended constant voltage (CV) or dither phase before the CC phase in order to make sure that the electrodes are at a well defined stoichiometry at the beginning of the test [60]. Besides the limitations of this method, it is still preferably applied if the measurement data is to be analyzed via differential voltage analysis (DVA), incremantal capacity analysis (ICA) [81] or degradation mode analysis (DMA) (see section 2.2.3) because quasi-continuous voltage data over the whole SOC range can be obtained. Dubarry et al. recommend to sample the quasi-OCV curve with a resolution of approximately 1 mV if it is intended to be used for DVA or ICA [90].

Measurement of the half-cell OCP curves The OCP curves of electrodes can not be retrieved from the full-cell OCV but must be measured individually for the electrodes [60]. There are two approaches for accessing the OCP vs Li/Li^+ of individual electrodes. One method is to insert a reference electrode into a full-cell that allows the independent measurement of the electrode potentials [91]. This approach is comparably complex and has the disadvantage that only the part of the half-cell OCP accessible in the voltage operation window of the full-cell can be measured. The second, and more frequently used method, is to build half-cells containing an electrode sample as working electrode and lithium metal foil as counter electrode. Half-cells are often built as coin-cells [57; 85; 88; 92], typically in the 2032 coin-cell format [49; 60; 93]. Also, cells that include a lithium metal reference electrode in addition to the lithium counter electrode [94] and pouch cells [95] are sometimes used.

If the electrode material of a commercial cell for which the OCP is to be measured is not available, e.g. as sheets, the first step is to open up the cell and to extract samples from the electrodes. The cells are usually discharged until the lower-cut off voltage [94] and then opened in a glove box under argon atmosphere [60; 93] in order to prevent reactions of the electrodes with moisture. If the current collectors are coated with active material on both sides, the active material has to be removed on one side prior to the sample extraction. This is done by mechanical scraping often in combination with using a solvent [57; 60; 93; 94]. Sometimes, the electrode sheets are additionally washed with dimethyl carbonate (DMC) which influences the shape of the measured OCP curve [94]. Afterwards, the electrode samples can be extracted from the electrode sheet or jelly roll by using a circular punch [57; 60; 93]. The half-cell assembly is also performed inside the glove box. A typical half-cell coin-cell stack is shown in figure 2.5.

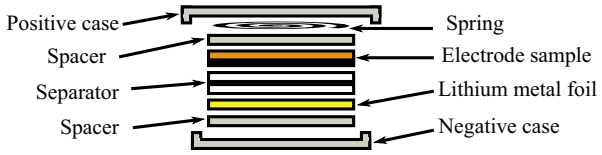

Figure 2.5: Half-cell coin-cell stack as used in [46].

The measurement method is the same as for full-cell OCV measurements, i.e., the half-cell OCP is measured either by bringing the electrode to different lithiation degrees and measuring the voltage vs.

Li/Li^+ after a relaxation period [57; 82] or as the voltage recorded during a quasi-stationary low-current lithiation or delithiation process whereby the latter approach is more frequently used. To measure the quasi-stationary OCP curve, the half-cell is first charged or discharged to the respective cut-off voltage vs. Li/Li^+. In some studies, an additional CV phase or dither profile [60] is applied after reaching the cut-off voltage. The cell is then fully discharged or charged until the opposite cut-off voltage is reached [60]. The current rates used for the CC charging and discharging range from C/20 [86; 92; 95; 96] over C/25 [97; 98], C/30 [60], C/33 [93] to C/100 [49]. The voltage limits for cycling the half-cells have to be selected carefully in order to prevent harmful side reactions. Graphite and SiC should not be lithiated below 0 V vs. Li/Li^+ to prevent lithium plating. Positive electrode materials should not be lithiated to low potentials either to prevent high material stress and cracking [60]. During delithiation, copper corrosion which occurs above about 3 V vs. Li/Li^+ for most electrolytes should be avoided for the anode samples [60]. The positive electrodes might experience a structural breakdown and also electrolyte decomposition may occur at voltages above 4.3 V vs. Li/Li^+ [60]. Cut-off voltages used in the literature for quasi-stationary half-cell OCP measurements are listed in table 2.1.

Table 2.1: Cut-off voltages for half-cell OCP curve measurements.

Electrode material	U_{min} / V	U_{max} / V	Reference
Graphite	0.01	1.5	[60]
Graphite	0.05	2.0	[86]
Graphite	0.005	1.2	[95]
Graphite	0.01	1.5	[93]
Graphite	0.01	1.5	[88]
Graphite	0.05	2	[96]
SiC	0.01	1.7	[49]
NMC (unknown composition)	2.1	4.3	[60]
NMC (unknown composition)	3.0	4.35	[86]
Lithium cobalt oxide (LCO)	3.5	4.35	[95]
NMC/LCO blend	2.5	4.3	[93]
NMC/LCO blend	3.0	4.3	[88]
NMC-811	3.0	4.3	[49]
NMC-523	3.0	4.35	[96]
NMC-811	3.0	4.4	[92]
NMC-111	3.0	4.4	[92]

As for full-cell OCV measurements, a disadvantage of quasi-stationary OCP measurements is that there is always some overpotential as the cell is not in an equilibrium state [60]. Trying to compensate for these overpotentials is difficult, as the resistances leading to these overpotentials are SOC dependent [60]. Apart from this, Lu et al. describe three additional problems occurring during the measurement of quasi-stationary OCP curves [60]:

The "missing-data problem" consists in the fact that the stoichiometric range that is accessible during low-current lithiation differs from the range that is accessible during low-current delithiation if the half-cell is brought to a specified stoichiometry prior to the test using an extended CV phase or dither profile. This is caused by the rapid impedance increase when approaching a completely lithiated or delithiated state.

The second problem is the "inaccessible-lithium problem", which means that a practical lithium intercalation electrode can not be fully lithiated or delithiated in an experiment due to restriction of the voltage range because of the considerations described above. This results in the fact, that some

regions of the OCP curve are not obtainable during experiments and that the measurable electrode SOC does not directly correspond with the absolute stoichiometry needed for most physico-chemical models. A transformation from apparent electrode SOC to absolute electrode lithiation is thus needed for these models. This transformation can be realized by associating characteristic points in the OCP curve with absolute lithium concentrations [49].
The last problem Lu et al. address is the "data-quality problem", which means that the experimental data obtained during quasi-stationary OCP measurements is noisy because of the limited voltage quantification of the test system and statistical fluctuations during the experiment. This is problematic if the data is to be analyzed via ICA. The last two problems are not specific to quasi-stationary OCP measurements but also occur during stationary OCP measurements.

2.1.4 Mechanical behaviour

The lithiation and delithiation of common electrode materials used in lithium-ion cells leads to changes in their mechanical and geometric properties. The consequences of this effect on the gas pressure inside the case of prismatic cells is investigated in chapter 3 of this work. The theoretical background on this topic is described in the following.

Reversible volume change of negative electrodes Graphite anodes expand during lithiation and contract during delithiation [35; 99]. The volume change is not linear with the lithiation degree but differs for the different graphite stages. In the region where the dilute graphite stages 4L-2L are formed, the volume changes more rapid with lithiation degree compared to the region of the stage 2L-2 phase transition [35; 100]. During the 2-1 phase transition, the volume change upon change in lithiation is again more pronounced [35; 100; 101]. A total volume change of 13.2 % is reported for the graphite unit cell upon lithiation from C_6 to LiC_6 [35]. The electrode thickness is reported to increase by 7 % during lithiation [101].
Pure silicon exhibits a much larger expansion of up to 400 % upon lithiation [43]. Blend electrodes containing both silicon and graphite exhibit less pronounced volume change upon lithiation and delithiation [44]. The thickness change of SiC blend electrodes increases linearly with the increase in silicon content [44].

Reversible volume change of positive electrodes In comparison to the graphite-based anode materials, layered metal oxide-based cathode materials show a smaller volume change upon lithiation and delithiation [102; 103]. The volume of NMC-111 decreases only by less than 2 % until a lithiation degree of 1/3 is reached [102–104]. During complete delithiation, which is usually avoided during operation, values between 3-5 % have been reported for the decrease in volume in comparison to the fully lithiated state [102–104]. A similar behaviour is also found for nickel-rich NMC-811: the decrease in volume during delithiation is small until a lithiation degree of about 30 % is reached. This is followed by a collapse of the interlayer spacing and an associated volume decrease during complete delithiation [105].

Cell level volume changes The way how volume change on the electrode level translates to volume and thickness changes on the cell level depends on the cell design and the external mechanical conditions under which the cells are operated. The cell level thickness change of pouch cells that are operated

without external mechanical constraints can be measured with a dilatometer [100; 106]. The associated non-linear volume change of the different graphite stages during lithiation and delithiation can be observed in the cell level thickness change [100].
Pouch cells that are mechanically constrained during operation, which is often the case in applications, can not expand freely during lithiation. In this case, the stack stress between cell and constraint fixture, which can be measured by a load cell, increases reversibly during charging of the cell [107]. In addition to the reversible change in cell thickness or stack stress, the cell thickness or stack stress irreversibly increases during long-term cycling which is associated to solid electrolyte interface (SEI) growth and irreversible changes in the electrode structure [107; 108]. For cells with a rigid case, the volume change of the electrodes can result in a strain of the casing, which has been reported for coin-cells [109] and cylindrical cells [110; 111].

Internal gas pressure Lithium-ion cells with a rigid case usually contain some free volume on top of the electrode stack or jelly-roll that is filled with gases. The gas pressure inside lithium-ion cells with rigid case also changes depending on the SOC due to the volume change of the electrodes [35; 112; 113]. The system can be described by the ideal gas law

$$p \cdot V = n_{\mathrm{G}} \cdot R \cdot T \tag{2.23}$$

where p is the pressure inside the cell case, V is the free volume and n_{G} is the amount (moles) of gas in the volume [112]. The measurable gas pressure is therefore influenced by V which depends on the electrode expansion and the temperature [113]. In addition, the internal gas pressure can increase due to gas formation which is discussed in section 2.2.1.

2.2 Aging of lithium-ion batteries

In the main part of this thesis, different topics concerning the degradation of lithium-ion batteries are investigated. In this section, an overview on the current understanding of the degradation of lithium-ion batteries is thus provided.
The degradation of lithium-ion batteries can be described on three levels of abstraction: The most detailed level are degradation mechanisms that describe the physical and chemical processes occurring within the cell during aging on a microscopic level. The degradation mechanisms are often clustered according to the cell component they are affecting, but also according to their impact on the thermodynamic and kinetic behavior of the cell. These clusters are called degradation modes. They form the second level of abstraction. The degradation modes finally result in degradation effects that are observable on the cell level [18; 19; 97; 114]. The connection between degradation mechanisms, degradation modes and degradation effects is schematically shown in figure 2.6. In this section, an overview on the topic of lithium-ion cell degradation spanning these three levels of abstraction is provided. In addition, a detailed literature review on methods for the diagnosis of battery degradation based on quasi-stationary OCV curves is provided in section 2.2.3, as such methods are applied and advanced in the main part of this thesis.

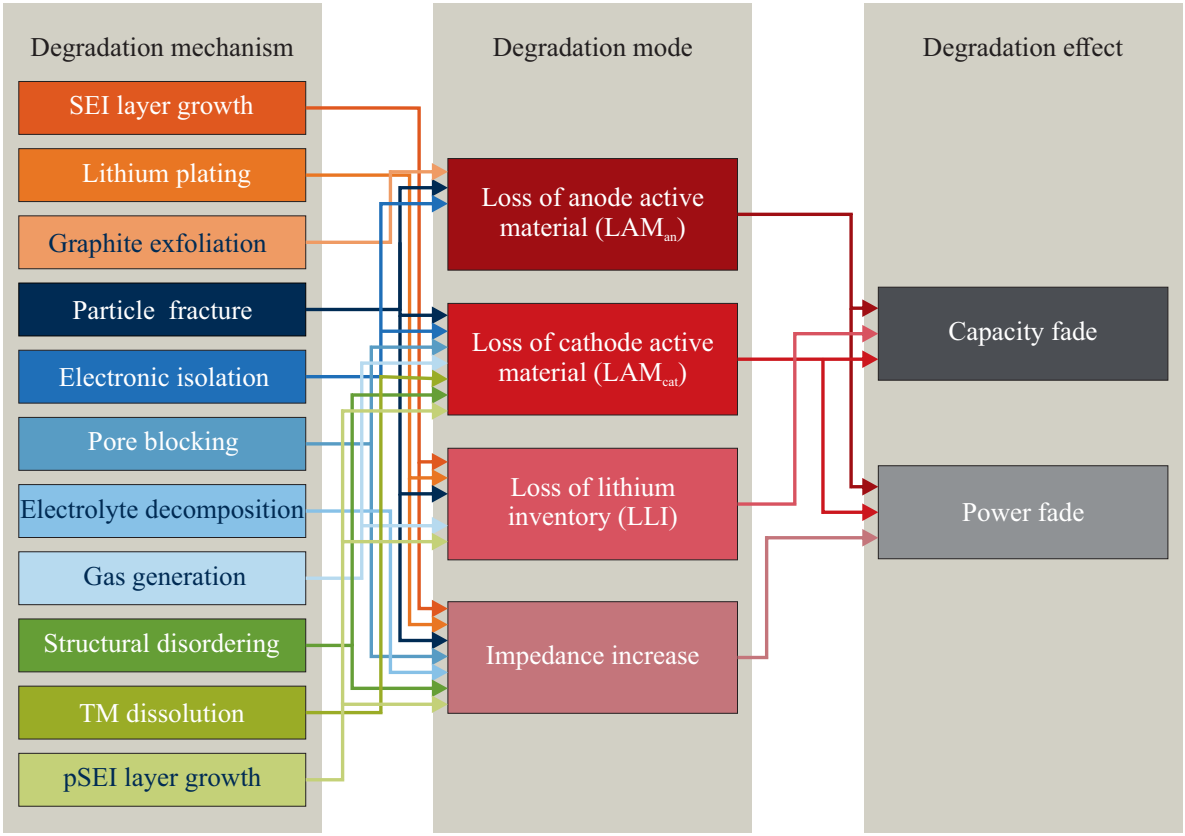

Figure 2.6: Schematic overview on degradation of lithium-ion batteries on three levels of abstraction. Commonly assumed correlations between degradation mechanisms and degradation modes, as well as between degradation modes and degradation effects are shown based on [18–20; 97; 114].

2.2.1 Degradation mechanisms

The most important degradation mechanisms and concepts for modeling degradation mechanisms are presented in this section, but not all mechanisms described in the literature can be described in the scope of this work. More detailed reviews on degradation mechanisms can be found in [17; 18; 20].

Anode degradation mechanisms An important degradation mechanism occurring on the anode is the growth of the SEI layer. During the formation of a lithium-ion cell, an SEI layer is formed on graphite and lithium metal anodes because common electrolytes are not stable at the low potentials these anode are operated at [17]. The SEI layer should be ionically conductive in order to allow lithiation/delithiation of the anode material, but at the same time it should be electrically isolating to prevent further electrolyte reduction. Still, an ongoing growth of the SEI during aging is often observed [18]. SEI layer growth may also lead to pore blockage which subsequently can increase the risk of lithium plating [115]. The SEI layer growth is also reported to lead to an irreversible expansion of graphite-based anodes [99]. SEI growth leads to loss of lithium inventory (LLI) as cyclable lithium is trapped in the SEI. It also results in an increase in impedance [18].
Another important degradation mechanism that occurs on both electrodes is particle cracking due to the expansion/contraction of the electrode material during lithiation/delithiation (see section 2.1.4). Particle cracking can lead to a loss in the electronic and ionic conductivity, the formation of isolated islands and thus evoke loss of active material (LAM) and increase in impedance [18]. In the case of the anode, particle cracking can also lead to a fracturing of the SEI which results in the formation of additional SEI on the freshly exposed particle surfaces. This is sometimes called SEI repair [116]. Enhanced particle cracking is observed for silicon containing anodes due to the large volume change of silicon upon lithiation/delithiation [18].
If the potential at the anode surface is below 0 V vs. Li/Li^+, lithium-ions can form metallic lithium instead of intercalating into the anode material, which is called lithium plating [117]. Lithium plating can have a thermodynamic origin if the anode is already fully lithiated, as well as a kinetic origin, if 0 V vs. Li/Li^+ is reached due to a large overpotential at high current rates or at low temperatures [18; 118]. Lithium plating results in LLI as the plated lithium can undergo subsequent side reactions to form SEI or if the plated lithium gets electrically isolated [18].

Cathode degradation mechanisms As for the anode, cathode materials can suffer from particle cracking [116]. Apart from this, the degradation mechanisms occurring at the cathode strongly depend on the material composition. The following degradation mechanisms are reported for NMC materials, which are investigated in the main part of this thesis. Lattice oxygen can get oxidized resulting in a dissolution of transition metals (TMs) [119]. TM dissolution can also be triggered by acidic species such as hydrofluoric acid (HF) that are formed from traces of moisture. Ni^{2+} can be dissolved in the electrolyte leading to a decomposition of electrolyte. Dissolved TM ions can form a surface layer on the cathode referred to as positive solid electrolyte interface (pSEI) or cathode electrolyte interface (CEI). Ni^{2+} and Li^+ can also switch their positions (site exchange) in the crystal of NMC. All of these mechanisms lead to LAM and an increase in impedance [18].
Another important degradation mechanism for nickel-rich NMC during prolonged cycling is the formation of a resistive, electrochemically inactive layer on the surface of the primary particles [120–122], which is also referred to as phase change [18]. As some of the active material is irreversible transformed into this inactive surface layer, the overall electrode capacity decreases [120]. In addition to this, the formation of the surface layer leads to a severe increase in the charge transfer resistance [120; 121].

This leads to a higher overpotential during cycling, which can result in a gradual decrease of the usable electrode SOC window if fixed currents and voltage limits are used [120]. The formation of the surface layer is reported to be at least partly driven by cracking of the secondary particles which leads to the exposure of additional primary particle surfaces to the electrolyte [121] and furthermore causes an increase in the cell impedance due to a reduction of the electrical connection of the primary particles [50]. Another degradation mechanism for nickel-rich NMC is the formation of an additional fatigued bulk phase in the delithiated state. This phase can only be partly delithiated during regular cycling conditions due to kinetic limitations [121; 122].

Gassing Some of the degradation mechanisms that occur during operation [123] and storage [113] of lithium-ion batteries involve gas formation. This is relevant for this work as a correlation between the internal gas pressure inside prismatic cells and the remaining cell capacity is investigated in chapter 3. For unconstrained pouch cells, the gas formation results in a volume expansion of the cell [124; 125]. For cells with a rigid case, the gas formation results in an increase in the internal gas pressure, which can be described by an increase in the gas amount n_G in the ideal gas equation (equation 2.23). The gassing is reported to occur mainly on the negative electrode where electrolyte compounds react with lithium containing compounds during SEI formation [113; 126; 127]. The gassing is therefore especially pronounced during the first cycles [128]. The gas species that are produced can contain CO [123], CO_2 [123], CH_4 [123], C_2H_4 [123; 127], C_2H_6 [123; 127] and C_3H_8 [123]. The amount of gas is influenced by the used additives [127]. Reactions with trace water also have been reported to lead to the formation of CO_2 [127] or H_2 [113]. The reaction of electrolyte compounds with Li_2CO_3 or LiOH at the positive electrode surface can result in the formation of CO_2 [124] and the release of O_2 from the cathode crystal lattice has been reported for NMC materials [54].
The amount of gas production is often reported to correlate with the capacity fade during cycle aging [113; 123; 126; 129]. The gases that are formed during side reactions might even enhance future capacity loss [130]. The gas formation during cycle aging is reported to be less pronounced for cells containing lithium iron phosphate (LFP) as cathode active material [131].

In order to obtain a better understanding of the interactions between different degradation mechanisms and to enable the prediction of cell degradation under different operating conditions with reduced parametrization effort, physico-chemical aging models that explicitly model individual degradation mechanisms have been developed. In a recent work by O'Kane et al., the degradation mechanisms SEI layer growth, lithium plating, particle fracture and LAM are added to a Doyle-Fuller-Newman model [132]. Keil and Jossen presented a p2D model including SEI formation as well as reversible and irreversible lithium plating and stripping [133]. More examples for physics-based aging models can be found in [134; 135]. An overview on the state of the art of physico-chemical degradation modeling is given in [18].

2.2.2 Degradation modes

Battery aging is a complex process consisting of many single mechanisms as described in section 2.2.1. Direct observation of individual degradation mechanisms during observation is difficult [18]. In addition, a bottom-up physical explanation of aging based on single effects on the micro scale might not be able to capture battery aging as a whole, as also effects in the meso and macro scale have a huge influence on the aging which can not be covered by the microscopic models [97]. One possibility to

reduce the complexity in describing cell aging is to investigate so called degradation modes that are clusters of degradation mechanisms that can be differentiated based on full-cell measurements [18; 25; 97].

The main degradation modes are loss of active material at the anode ($\mathrm{LAM_{an}}$), loss of active material at the cathode ($\mathrm{LAM_{cat}}$) and LLI. LAM includes all degradation mechanisms that lead to a reduction in the lithiation capacity of an electrode. LLI describes all mechanisms that result in a reduction of the amount of cyclable lithium. Some authors consider stoichiometric drift, i.e., a change in electrode balancing as a separate degradation mode [18] but this can also be regarded as a consequence of the other aforementioned degradation modes. Apart from these degradation modes that affect the thermodynamic behavior, i.e., the shape of the OCV curve, there is also a change in the dynamic behavior of the cell associated with degradation. This can be collectively described by the degradation mode impedance increase [18].

The model for the full-cell OCV curve described in section 2.1.2 can be used to link the change in the full-cell OCV curve during aging with these degradation modes (DMs). A graphical illustration of the effect of the individual DMs on the full-cell OCV curve is provided in figure 2.7. In figure 2.7a the full-cell OCV curve and the half-cell OCP curves of a pristine cell are shown. The capacities of the electrodes and the capacity associated with the lithium inventory of the cell are also schematically depicted as bars.
The scaling factors of the individual half-cell OCP curves (α_{an} and α_{cat}) describe the individual electrode capacities in terms of the actual full-cell capacity. The absolute electrode capacity can be obtained by multiplying the scaling factors with the actual full-cell capacity C_{act}

$$C_{\mathrm{an}} = \alpha_{\mathrm{an}} \cdot C_{\mathrm{act}}, \tag{2.24}$$

$$C_{\mathrm{cat}} = \alpha_{\mathrm{cat}} \cdot C_{\mathrm{act}}. \tag{2.25}$$

The LAM is then calculated as the relative loss in electrode capacity, i.e., for the anode

$$LAM_{\mathrm{an}} = \frac{(C_{\mathrm{an,ini}} - C_{\mathrm{an}})}{C_{\mathrm{an,ini}}}, \tag{2.26}$$

where $C_{\mathrm{an,ini}}$ denotes the anode capacity of the pristine cell. Similar for the cathode

$$LAM_{\mathrm{cat}} = \frac{(C_{\mathrm{cat,ini}} - C_{\mathrm{cat}})}{C_{\mathrm{cat,ini}}} \tag{2.27}$$

applies, where $C_{\mathrm{cat,ini}}$ is the pristine cathode capacity. $\mathrm{LAM_{an}}$ results in a shrinking of the half-cell OCP curve of the anode as shown in figure 2.7c. If the lost material is assumed to be in a delithiated state, $\mathrm{LAM_{an}}$ is modeled by a linear scaling of the anode OCP curve with the left (delithiated) end point kept fixed. The resulting full-cell OCV curve is shown as a saturated curve in this figure. The reduction of C_{an} and the resulting reduction of the capacity that can be accessed inside the full-cell voltage limits (C_{act}) is also schematically illustrated. In this example, $\mathrm{LAM_{an}}$ has the effect that the cell, which was initially limited by the cathode at the end of charge (EOC), is now limited by the anode at EOC and a portion of the cathode capacity and the lithium inventory at high cell voltages can not be accessed anymore.
Analogously, $\mathrm{LAM_{cat}}$ leads to a shrinking of the cathode OCP curve as shown in figure 2.7d. If the lost material is assumed to be in a delithiated state, $\mathrm{LAM_{cat}}$ is modeled as a linear scaling of the cathode

OCP curve with the right (delithiated) end point kept fixed. Also here, the resulting full-cell OCV curve is represented by a saturated line and the effect on the usable full-cell capacity is schematically shown. In this example, the full-cell, which was initially limited by the anode capacity at end of discharge (EOD) is now limited by the cathode at EOD and a portion of the anode capacity and the lithium inventory at low full-cell voltages can not be accessed anymore.

The lithium inventory C_{lit} is the lithium that is available for delithiation in both electrodes [136]. It can be calculated as the sum of the amount of lithium that can be delithiated from the cathode and the amount of lithium that can be delithiated from the anode until the upper voltage limit of the respective electrode is reached. This quantity is related to the alignment parameters [47] according to

$$C_{\mathrm{lit}} = (\alpha_{\mathrm{cat}} + \beta_{\mathrm{cat}} - \beta_{\mathrm{an}}) \cdot C_{\mathrm{act}} \tag{2.28}$$

as illustrated in figure 2.4. It should be noted here that the signs of β_{cat} and β_{an} are negative. The LLI is defined as

$$LLI = \frac{(C_{\mathrm{lit,ini}} - C_{\mathrm{lit}})}{C_{\mathrm{lit,ini}}} \tag{2.29}$$

where $C_{\mathrm{lit,ini}}$ is the lithium inventory in the pristine state. LLI results in a relative shift of the positions of the half-cell OCP curves as shown in figure 2.7b. LLI can be modeled as a right shift of the anode OCP curve. The resulting full-cell OCV curve is shown as a saturated line. In the schematic illustration of the component capacities, it can be seen that the pure LLI simulated in this example would result in inaccessible capacity reserves in both electrodes and thus to a reduction of the usable full-cell capacity.

This concept of degradation modes, i.e., the linkage between clusters of degradation mechanisms and a characteristic change in the electrical behavior of a lithium-ion cell, was introduced by Dubarry et al. in 2012 [25]. The concept for describing cell degradation and the associated electrical cell model is also referred to as the mechanistic cell model or the mechanistic modeling approach [26]. The concept provides a component-specific description of degradation as had been contained in earlier electrochemical models [137; 138], but its complexity is much lower. The concept of degradation modes has been used in studies with focus on different aspects since then [26]: due to the reduced complexity, the degradation modes can be easily determined from full-cell quasi-stationary OCV curve measurements, which lead to a widespread use of DMA as a diagnostic method [68; 84; 85; 96; 98; 116; 139–146] (see 2.2.3).
The concept of degradation modes has also frequently been used in the prognostic direction to simulate the performance of cells during aging [147–150]. The mechanistic modeling framework was also used to generate large synthetic datasets of voltage vs. capacity curves that can be used to train diagnostic algorithms based on statistical or deep learning methods [151]. A review of applications and extension of the concept of degradation modes and the associated modeling framework is provided in [26].
In some studies, it is differentiated whether the LAM occurs while the electrode is in a lithiated or a delithiated state. Depending on the lithiation state, the end of the half-cell OCP curve associated with the delithiated or the lithiated state is used as origin of the scaling of the half-cell OCP curve associated with the LAM [25]. This differentiation can be used in prognostic models to simulate the effect of LAM at different lithiation states on the evolution of the full-cell OCV curve [25; 147; 149; 152]. In the following, some aspects concerning the mechanistic modeling approach are discussed in more detail.

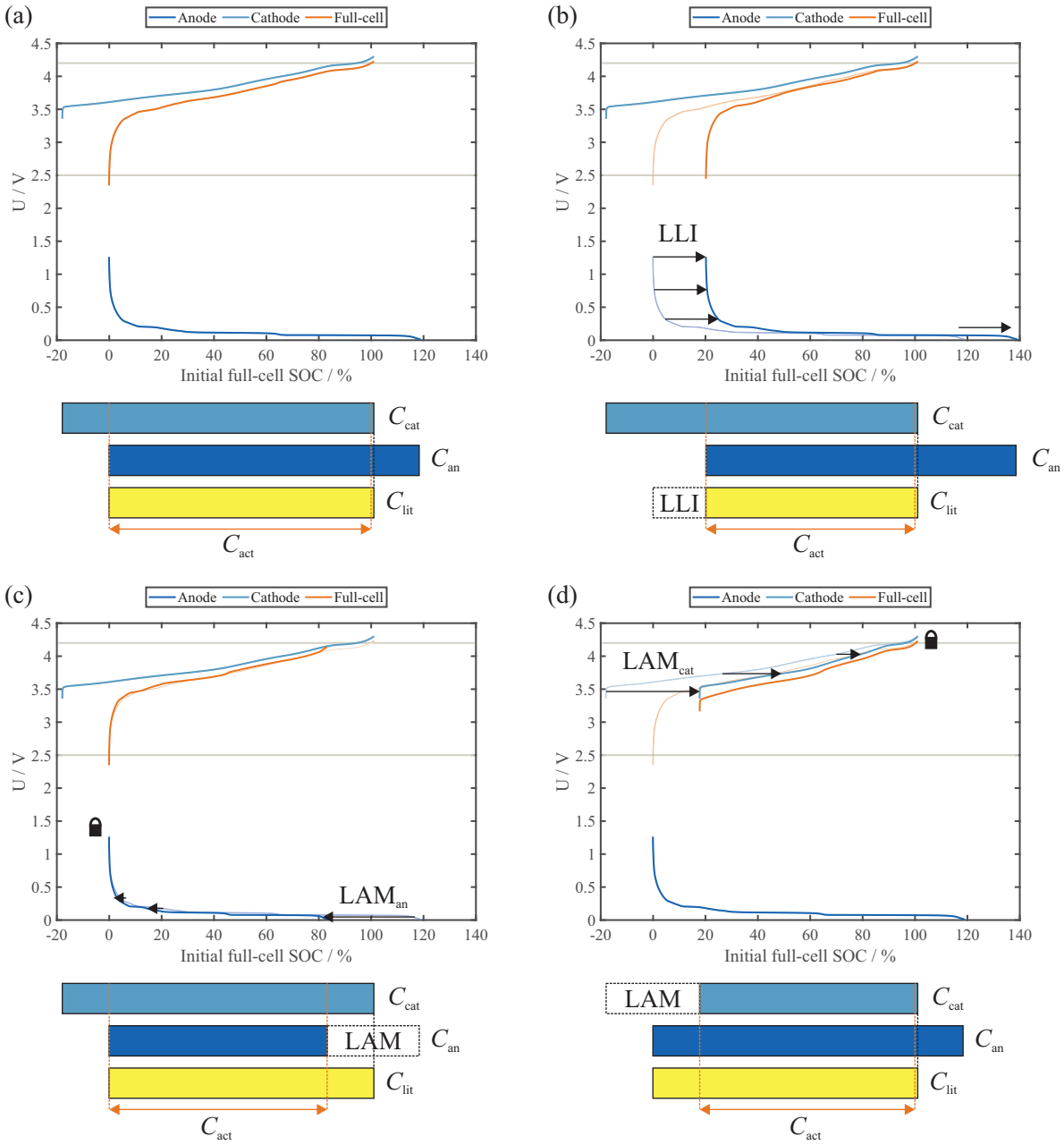

Figure 2.7: Impact of the degradation modes on the full-cell OCV curve based on [25; 97]: (a) No degradation, (b) LLI, (c) LAM_{an}, (d) LAM_{cat}. For each scenario, the shifting and scaling of the half-cell OCP curves and the resulting full-cell OCV curve is shown. The initial full- and half-cell curves are shown as light-colored lines in (b-d). The voltage plotted on the Y-axis is vs. Li/Li^+ for the half-cell curves. A schematic representation of the utilization of the electrode capacities and the lithium inventory is additionally shown for each scenario.

Representation of cell dynamics Apart from LAM and LLI, which impact the cell capacity and the cell voltage at quasi-equilibrium conditions, some degradation mechanisms also alter the overpotential that occurs when a non-negligible current is flowing through the cell. In the original modeling framework presented by Dubarry et al. an approach for modeling the overpotential on electrode level throughout aging is described [25]. This is done by modeling each electrode as a simple equivalent-circuit model (ECM) consisting of an electrode SOC-dependent voltage source that resembles the half-cell OCP, a resistor that resembles all quasi-instantaneous overpotentials (R_1) and an RC-circuit (R_2, C_2) to model overpotentials with non-negligible time constants as shown in figure 2.8. They parameterize this model based on half-cell lithiation/delithiation curves measured at different current rates. Aging-induced changes in the electrode resistance and kinetics can then be simulated by altering the value of the passive ECM elements. Aging-related changes in electrode kinetics can also be simulated by altering the effective current rate at the electrodes [25]. The changes in the cell dynamics leading to increased overpotentials and finally a decrease in the power that can be delivered by a cell can also be defined as additional degradation modes. Until now, there is no established definition and nomenclature for this type of degradation modes.
From the representation in figure 2.8 it becomes clear, that the mechanistic cell model is an ECM in which phenomena on the half-cell level and their evolution during aging are modeled. In cases in which overpotentials are neglected, e.g. in low-current scenarios, the ECM only contains the two voltage sources representing the half-cell OCPs.

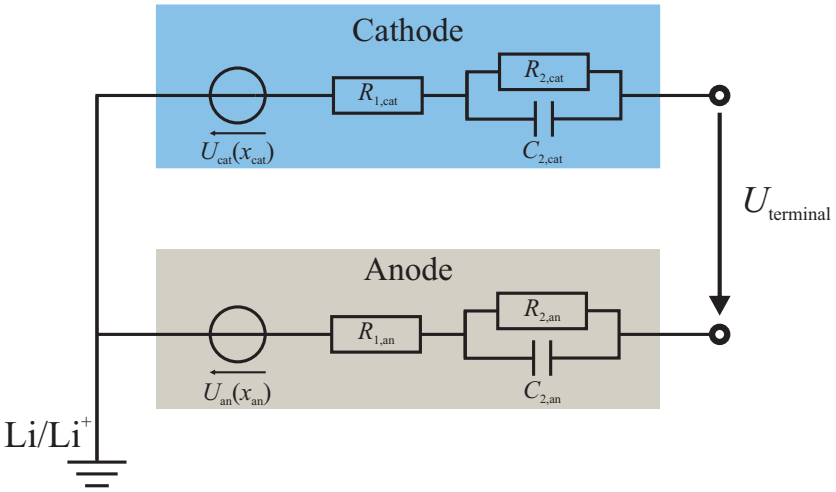

Figure 2.8: Mechanistic full-cell model with half-cell sub-models. The subscript "cat" denotes that an element models the overpotential at the cathode. The subscript "an" denotes that an element models the overpotential at the anode.

Experimental confirmation and limitations of the concept of degradation modes The validity of the concept of degradation modes has been experimentally investigated: Schmidt et al. prepared full-cells where they artificially introduced LLI and $\mathrm{LAM_{cat}}$ by using different amounts (areas) of active material to simulate LAM or electrodes harvested from cells at different SOC to simulate loss of active lithium [68]. The full-cell OCV curves of these manipulated cells showed the features that were expected from the model, which experimentally confirms the validity of the modeling approach. Similar results were later also presented by Birkl et al., who additionally confirmed the validity of the modeling approach for $\mathrm{LAM_{an}}$ [97].
Validation of the LAM calculated from full-cell measurements via measuring the capacity of harvested

electrode samples is difficult: Sieg et al. reported that the LAM_{an} calculated from the capacity loss measured for harvested graphite samples was smaller than the LAM_{an} expected from the full-cell OCV curve [153]. They assume that accessible anode material decreases because the anode gets partly covered by a surface layer. This apparent LAM is reverted during electrode sample harvesting, as the surface layer sticks to the separator and is therefore removed in the half-cell configuration. The conditions during the half-cell measurement thus significantly differ from the conditions in the full-cell. Also, Coron et al. found that the measured half-cell capacity of a harvested samples from an aged anode was larger than what had been expected based on the full-cell OCV [154]. Their explanation for this is that the anode degrades inhomogeneously and the samples were extracted from a comparably less degraded area. The degradation modes that can be determined from full-cell measurements are thus limited to resemble an average degradation over the respective electrode and spatial inhomogeneity of degradation is not modeled with this approach.

Aging-invariance of the OCP curve It is a central hypothesis in most studies using the mechanistic modeling approach that the shape of the half-cell OCP curves stays constant during aging. This assumption is motivated by the fact that in theory the OCP at a certain lithiation degree is a property that results from the thermodynamics of the intercalation material which should not change if the structure of the material stays the same. This is why LAM is usually modeled as a linear scaling of the half-cell OCP curves without changing the shape of the curve.
There is only a limited number of studies investigating this aspect experimentally by cycling full-cells and characterizing electrode samples harvested from the aged cells: Liu et al. measured the OCP curves of LFP and graphite samples harvested from aged full-cells. They did not find significant changes in the curve shape compared to the pristine state [155]. Bloom et al. found minor aging-induced differences in the OCP curve shape of graphite, which they associated with co-intercalation of the solvent [156]. Larger changes in the OCP curve shape have been found for blend anodes consisting of graphite and silicon. They are associated with a faster degradation of the silicon in comparison to the graphite [41; 50; 157]. The change in the capacity contribution of the components of a blend electrode can be captured by a blend electrode model as described in section 2.1.2. Modeling of blend electrodes by two half-cell ECMs connected in parallel, which is conceptually equivalent to the blend electrode model proposed by Schmidt et al. [68], was also proposed by Dubarry et al. [25]. A model in which two electrochemically active anode components are considered is shown in figure 2.9. Similarly, a core-shell behavior can be modeled by a serial connection of half-cell ECMs [25]. Also the formation of new phases such as oxide surface layers or plated lithium can be modeled with this framework by additional electrode components connected in parallel. This type of blend electrode model has been used to simulate the full-cell OCV curves of cells with SiC anodes assuming individual rates for the LAM of graphite and silicon [70].

The evolution of the OCP curve of cathode materials has also been investigated: Li et al. showed that no additional phases are observable in the half-cell OCP curves of aged NMC-811 [50]. Also Jung et al. reported that the OCP curve of NMC-811 does not change significantly during cycle aging [92], if it has not been exposed to air prior to the cycling. Lee et al. found that the full-cell OCV curve can be fit more accurately by two half-cell OCP curves, if the shape of the half-cell OCP curve of a NMC cathode is adapted during aging [85]. As possible reasons for the change in the OCP curve of NMC they suggest transition-metal dissolution, structural disordering of the electrode and surface film modification. Jia et al. showed that the full-cell OCV curve can be reconstructed with higher accuracy if half-cell OCP curve measured for aged half-cells are used [96].

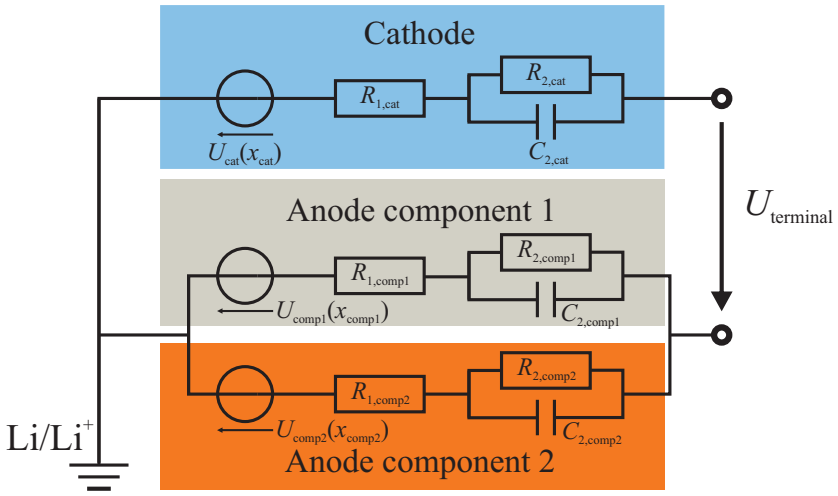

Figure 2.9: Mechanistic full-cell model with half-cell and electrode component sub-models. The subscript "cat" denotes that an element models the overpotential at the cathode. The subscript "comp1" denotes that an element models the overpotential at anode component 1. The subscript "comp2" denotes that an element models the overpotential at anode component 2.

Another origin for an apparent change in the shape of the OCP curve is increased spatial inhomogeneity of the lithiation degree in the electrodes. Fath et al. modeled the OCP curve of inhomogeneously lithiated electrodes as the average of several OCP curves that are constructed slightly shifted against each other on the SOC-axis [146]. Schindler et al. proposed to model inhomogeneous electrode aging by using an SOC-dependent scaling factor for the alignment of the half-cell OCP curves [144].

Degradation mode-based aging models In some studies, the empirically determined relationship between individual degradation modes and stress factors during aging is described by model equations. This approach is conceptually similar to the well established empirical aging models on full-cell level described in section 2.2.4. Honkura et al. determined the degradation modes $\mathrm{LAM_{an}}$, $\mathrm{LAM_{cat}}$ and LLI during calendar aging and found that while the LLI followed a square root of time dependence, the LAM of both electrodes can be better described by an exponential function of time [158]. They extrapolated the progression of the individual degradation modes to predict the full-cell capacity fade and found that this approach yields more accurate results than the classical square root of time model for calendar aging. A similar method was later presented by Downey et al. who modeled the LAM to follow an exponential function of time and the relative shift between the electrode half-cell curves to have a square root of time dependence during cycle aging [159]. In a simulation study they showed that their approach yields a more accurate prediction of the remaining useful lifetime (RUL) in comparison to a capacity-based approach. Lui et al. experimentally determined the degradation modes based on low-current charging curves measured at different aging stages during cycle aging [89]. They extrapolated the observed degradation trends using exponential and power-law model equations and showed that this extrapolation enables an accurate prediction of the capacity fade if the operating conditions are kept constant.

2.2.3 Diagnostic methods based on open-circuit voltage curves

As described in section 2.2.2, LAM and LLI are linked to a characteristic change in the shape of the full-cell OCV of lithium-ion cells. Because of this, measurements of the quasi-stationary OCV curve obtained at different states during aging are often used to analyze and quantify the degradation modes that have occurred in lithium-ion cells. Three types of diagnostic methods based on OCV curve measurements can be differentiated. They are presented in this section.

Differential voltage analysis The differential voltage analysis was established for lithium-ion cells by Bloom et al. in 2004 [160]. As described in section 2.1.2, during the lithiation/delithiation of common electrode materials, different phases of partly lithiated host material are formed in a sequence of two-phase transitions. The slope of the half-cell OCP is comparably small during these two-phase transitions while it is larger at lithiation degrees in between the two-phase transitions where the electrode consists almost exclusively of one phase. This phenomenon can be visualized by plotting the first derivative (dU/dQ) of a quasi-stationary OCV curve as a function of SOC [160]. The dU/dQ-axis is often normalized by multiplication with the cell capacity [156; 160]. Peaks in this differential voltage (DV) plot correspond to single phases while valleys correspond to two-phase transitions. The method can be applied both to full-cell and half-cell voltage curves [156]. If it is applied to full-cell OCV curves, the phases and two-phase transitions of both half-cells are superimposed.
DVA can be applied to qualitatively analyze the charging/discharging behavior of lithium-ion cells [161]. This also includes the estimation of the lithiation degree of the electrodes [101; 162–164] and the capacity contribution of blend electrode components [165]. The distance between characteristic DV curve features can be used to determine the capacity of one of the electrodes [83; 153; 162; 166; 167] or of blend electrode components [166]. Under the assumption of an aging-invariant OCP curve shape, the distances between DV features can also be used to determine the LAM of individual electrodes during aging. A broadening of the DV peaks is associated with an increase in the spatial inhomogeneity of the lithiation degree during charging/discharging [153].
The association of the peaks with one of the half-cells is generally done manually based on the general knowledge on the shape of the half-cell OCP curve of the respective electrode material [155; 161; 166]. In order to eliminate the influence of measurement noise, which would be amplified by the differentiation and result in high peaks in the DV plot, measured quasi-stationary OCV curves are sometimes filtered before they are differentiated in the scope of the DVA [156]. A thorough discussion of the DVA method can be found in [168].

Incremental capacity analysis The non-linear slope of the OCV curve can also be analyzed by calculating the local antiderivative (dQ/dU) and plotting it as a function of terminal voltage [25; 70; 81; 91; 140; 147; 169]. This method is called incremantal capacity analysis. In contrast to the DVA, the peaks correspond to two-phase transitions while the valleys correspond to single phase configurations in this representation. Constant offsets in the absolute OCV curve translate into a shift of the incremental capacity (IC) curve on the voltage axes.
A change in the absolute OCV curve associated with a degradation mode also leads to a change in the shape of the IC curve. Characteristic features, so called feature of interest (FOI), of the IC curve are thus often used as indicators for the degradation modes or as indicators for the overall cell capacity [70; 147; 170–172]. An overview of such methods for SOH estimation is provided in section 2.3.2. The mechanistic modeling approach described in section 2.2.2 can also be used to simulate the IC curve for

different assumptions for the degradation modes [70; 90; 147; 170; 172]. The results of such simulations can then be compared to experimentally determined IC curves to associate changes in the IC curve with degradation modes.
Numerically, the IC is often calculated simply as finite differences ($\Delta Q/\Delta U$ at terminal voltage U) [81]. The value for ΔU is typically in the order of 5 mV [81]. Lu et al. suggested to process the raw data by applying a "histogram counting" method in which stoichiometric equidistant data samples inside a certain voltage range are counted to calculate the IC with reduced noise [60]. A similar filter method for the calculation of IC curves, which is called Level Evaluation Analysis (LEAN), was proposed by Feng et al. [173]. Dubarry et al. recommend to take the average of a low-current charging and discharging quasi-stationary OCV curves as basis for DVA and ICA as overpotentials can be mainly eliminated this way [90]. A review on methodical aspects of the ICA is given in [168; 174].

Full-cell OCV curve alignment According to the mechanistic model described in section 2.2.2, the information on the capacities and the balancing of the electrodes is contained in the full-cell OCV curve. Thus, a set of plausible alignment parameters can be obtained if a simulated full-cell OCV curve matching the measured full-cell OCV curve can be found. An OCV curve can be simulated according to equation 2.22 by calculating

$$U_{\mathrm{OCV,model}}(x_{\mathrm{full}}, \theta) = U_{\mathrm{cat}}(1 - (x_{\mathrm{full}} - \beta_{\mathrm{cat}})/\alpha_{\mathrm{cat}}) - U_{\mathrm{an}}((x_{\mathrm{full}} - \beta_{\mathrm{an}})/\alpha_{\mathrm{an}}) \tag{2.30}$$

for different values of $x_{\mathrm{full}} \in X_{\mathrm{full}}$ where X_{full} is the SOC range in which the measured full-cell OCV curve is available. E.g. $X_{\mathrm{full}} = [0, 1]$ if the OCV curve is measured over the complete SOC range. θ is a vector that contains the alignment parameters

$$\theta = [\alpha_{\mathrm{an}}, \alpha_{\mathrm{cat}}, \beta_{\mathrm{an}}, \beta_{\mathrm{cat}}]. \tag{2.31}$$

The variation of the alignment parameters that is executed in order to find a plausible solution set for θ can be graphically described as shifting and scaling of the half-cell OCP curves until their difference matches the measured full-cell OCV curve. This curve alignment can be executed manually [49; 89]. To facilitate the manual alignment, the DV curves or the IC curves, in which the characteristic features are more pronounced, can be aligned instead of the absolute OCV curves [49; 89].

More reproducible results for the alignment parameters and in general also a more accurate reconstruction of the OCV curve can be obtained if the variation of the alignment parameters is not executed manually but automatically using an optimization algorithm. Automatized alignment of measured full-cell OCV curves has been used as a diagnostic method for degradation mode analysis by many authors during the last decade [75; 84–86; 89; 93; 96–98; 139; 140; 145; 146]. Automated curve alignment eliminates the bias introduced by the manual alignment and the automation aspect is also a prerequisite for implementing such a method in an application context. The optimization problem can generally be formulated as

$$\arg\min_{\theta \in \Omega} f(\theta) \tag{2.32}$$

$$\text{subject to:} \quad g(\theta) = 0 \tag{2.33}$$

$$h(\theta) \leq 0 \tag{2.34}$$

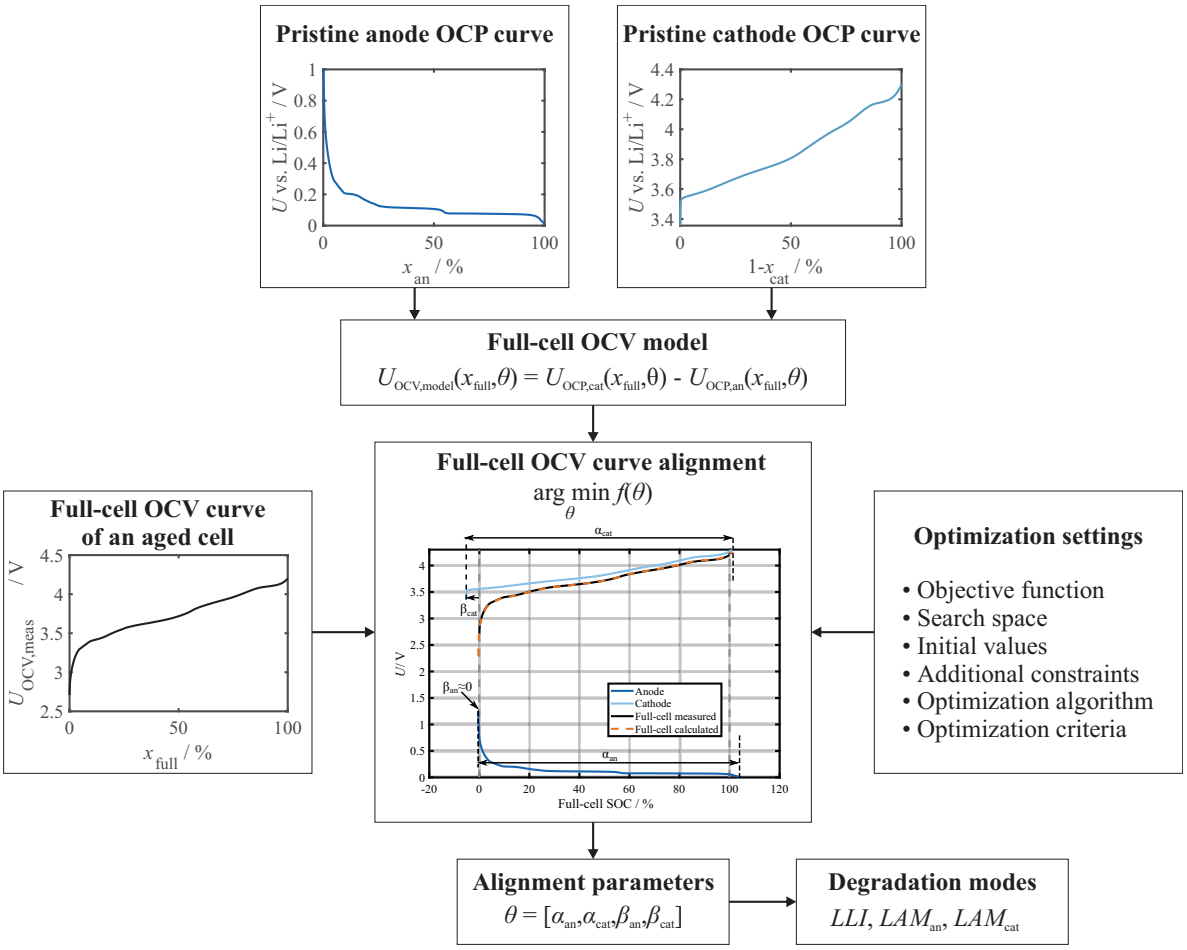

Figure 2.10: Schematic representation of the method of full-cell OCV curve alignment.

where $f(\theta)$ is the objective function, which is generally a non-linear function of the alignment parameters and Ω is the search space for alignment parameters. $g(\theta)$ and $h(\theta)$ are non-linear functions that are used to define additional constraints on the solution space. The method of degradation mode analysis based on automated full-cell OCV curve alignment including the necessary inputs and the obtained outputs is schematically shown in figure 2.10.

There are multiple settings that influence the robustness and also the computational effort of the optimization procedure:

- Objective function: there are several options for the objective function that is used to describe the degree of matching between the simulated and the measured full-cell OCV curve. A commonly used function is the sum of squared errors (SSEs) between the simulated and the measured curve [85; 136]

$$f(\theta) = \sum_i \left(U_{\mathrm{OCV,model}}(x_{\mathrm{full,i}},\theta) - U_{\mathrm{OCV,meas}}(x_{\mathrm{full,i}})\right)^2, \tag{2.35}$$

  where $U_{\mathrm{OCV,meas}}(x_{\mathrm{full}})$ is the measured full-cell OCV as a function of full-cell SOC and $x_{\mathrm{full,i}}$ is a set of, typically equally spaced [175], interpolation points on the SOC-axis covering the SOC range of the measured full-cell OCV. This objective function makes sure that the absolute OCV curves match and that larger local deviations are penalized by taking the squared difference.

Alternatively, the root-mean-square error (RMSE) of the absolute OCV curves is often used as objective function to achieve these goals [84; 86; 96; 98; 140; 141; 145; 175–179]. Another option is to minimize the squared difference of the DV curves that can be calculated from the measured and simulated OCV curves [144; 180]. The objective function is then defined as

$$f(\theta) = \sum_i \left(\frac{dU_{\mathrm{OCV,model}}(x_{\mathrm{full,i}}, \theta)}{dx_{\mathrm{full}}}\Big|_{x_{\mathrm{full,i}}} - \frac{dU_{\mathrm{OCV,meas}}(x_{\mathrm{full,i}})}{dx_{\mathrm{full}}}\Big|_{x_{\mathrm{full,i}}} \right)^2, \tag{2.36}$$

i.e., the sum of the squared differences of the local slope of the measured and simulated OCV curve at a set of, typically equally spaced [145], interpolation points. This objective function emphasizes the alignment of the features in DV curve which corresponds to aligning the positions where the different phase transitions of the electrodes are assumed. Constant offsets that could be introduced by SOC-independent overpotentials both in the half-cell and the full-cell curves are neglected with this objective function. Using DV-based objective function can be advantageous as it emphasizes the alignment of the phases and phase-transitions which better resembles the concept behind the mechanistic model for near equilibrium conditions. Using a DV-based objective function is also supposed to reduce the ambiguity of the results [158].
Objective functions based on comparing the IC curves [75] and objective functions that are weighted sums of the aforementioned functions have also been proposed by some authors [75; 86; 146; 181]. As of now, there is no consensus on the optimal objective function for OCV curve alignment in the literature.

- Search space: the search space Ω should be chosen as narrow as possible in order to avoid physically not plausible results for θ, but at the same time it should be chosen as wide as necessary in order to avoid the results to be determined by the selection of the search space. β_{an} and β_{cat} should be restricted to negative values as the half-cell curves are always left-shifted in comparison to the full-cell OCV curve. For cells that are limited by the anode capacity at the EOD, which is mostly the case, β_{an} should be close to zero. α_{an} and α_{cat} need to be greater than or equal to 1 as the full-cell capacity can never exceed the lowest half-cell capacity. In studies that investigate the evolution of degradation modes during cell aging, the search space is often defined to allow a certain relative variation of the individual alignment parameters based on the best fit that is determined for the preceding aging state [86]. Some authors restrict the search space even more rigorously based on physical considerations, e.g. by requiring at least a certain anode excess at EOC [86].

- Initial values: a physical plausible set of initial values should be chosen in order to achieve a fast convergence of the optimization and also to avoid results that correspond to a local minimum of the objective function. Using the best fit obtained for the preceding aging state as initial parameters is suggested by some authors [86]. In some studies, the optimization is run multiple times with different sets of initial values to avoid the results to correspond to a local minimum [85; 98].

- Additional constraints: Additional constraints can be used to avoid physically non-plausible results. An example constraint for the case in which a simulated OCV curve is aligned to a measured complete quasi-stationary charging curve would be

$$U_{\mathrm{OCV,model}}(x_{\mathrm{full,max}}, \theta) \geq U_{\mathrm{max}}, \tag{2.37}$$

where $x_{\text{full,max}}$ is the largest SOC value for which the curve is measured and U_{max} is the upper cut-off voltage used for the charging process. This constraint forces the right side of the simulated OCV curve to cover at least the upper cut-off voltage for the operation of the full-cell. Similarly, the modeled OCV at 100 % SOC can be forced to be equal to the upper-cut off voltage [136].

- Optimization algorithm: The following algorithms have been used in the literature to find a solution for the optimization problem: interior-point (IP) algorithm [145], Levenberg-Marquardt (LM) algorithm [182], non-linear least squares (NLLS) optimization [183], sequential quadratic programming (SQP) techniques [85], the genetic algorithm (GA) [93; 140; 175; 177], particle swarm optimzation (PSO) [96; 139; 141; 176], the Monte-Carlo (MC) algorithm, and a pattern search (PS) algorithm [146]. In many studies the selected algorithm is also not reported on (see table 2.2).

- Optimization criteria: the optimization is regarded to have converged if certain optimization criteria are fulfilled. The selection of these criteria can influence the results that are obtained by the optimization in principle. Still, this topic is not covered in most studies reporting on degradation mode analysis via OCV curve fitting. RMSEs between the simulated and the measured OCV curve in the order of a few mV have been reported in the literature [57; 96; 140; 141; 145; 183].

An overview on studies in which degradation modes are analyzed based on automated fitting of OCV curves is provided in table 2.2. It can be seen that in most studies, low-current ($\leq$C/20) charging or discharging curves are used as input and aging-invariance of the half-cell OCP curves is assumed.

In some models a differentiation between the loss of cyclable lithium caused by loss of lithiated active material and the loss of cyclable lithium caused by stoichiometric drift (also known as electrode slippage) due to lithium consuming side reactions is made [25]. The loss of lithiated active material, which can be simulated by scaling the half-cell curve fixed at the lithiated end, leads to the same change in the shape of the full-cell OCV curve as a combination of the loss of delithiated active material and LLI, which can be simulated by scaling the half-cell curve fixed at the delithiated end and subsequent shifting of the curve. The two effects can thus not be differentiated based on the final full-cell OCV curve [81; 88; 93; 144; 170].

The model used to simulate the full-cell OCV curve can be extended to cover additional effects, e.g., a term describing the overpotential can be introduced [86; 93; 140]. Additional model parameters describing the cell impedance are then obtained by optimization alongside the aforementioned alignment parameters [86; 140]. Another extension of the method is to use a model for the lithiation inhomogeneity (see section 2.2.2), and to obtain the degree of inhomogeneity as an additional optimization parameter [93; 146]. The method can also be extended by using simulated OCP curves obtained with a blend electrode model (see section 2.2.2). This allows to estimate the capacity contribution of individual electrode components based on the full-cell OCV curve. This was shown for the first time for SiC blend anodes in the study presented in section 4.2 of this work. The same approach was also recently used by Kirkaldy et al. to obtain results on the impact of the SOC window used for cycling on the component specific degradation of silicon [81]. A similar approach was used by Ando et al. to separate the LAM of NMC and LMO contained in a blend cathode [184]. A change in the shape of the half-cell OCP curves has also been considered by Jia et al. by using half-cell OCP curves measured

for aged electrode material to fit the full-cell OCV curves of aged cells. They reported that the fit accuracy can be increased this way [96]. Lee et al. assumed a change in the curve shape of NMC and expanded the method by calculating a new OCP curve for the NMC cathode, if the fitting accuracy of the full-cell OCV curves drops below a certain threshold [85].

Table 2.2: Optimization settings used for full-cell OCV curve alignment and investigated cell chemistry in different studies.

Reference	Year	Cell chemistry	Current rate	Direction	Objective fct.	Algorithm	Add. fit para.	OCP change
Honkura et al. [180]	2008		C/25	dch.	SSE DV			no
Honkura et al. [158]	2011		C/25	dch.	DV-based			no
Fathi et al. [185]	2014	LCO/G	C/50	ch.	DV-based			no
Han et al. [140]	2014	NMC/LTO, LFP/G	C/3	ch.	RMSE OCV	GA	resistance	no
Wang et al. [182]	2014	NMC-111-LMO/G	C/25	dch.	OCV-based	LM		no
Ouyang et al. [176]	2015	LFP/G	C/20	ch.	RMSE OCV	PSO	resistance	no
Ouyang et al. [175]	2016	LFP/G, LMO-NMC/G	C/3	dch.	RMSE OCV	GA	resistance	no
Yan et al. [177]	2016	LMO/G, NMC/LTO	1C	ch.	RMSE OCV	GA	resistance	no
Birkl et al. [98]	2017	LCO-NCO/G	C/25	dch.	RMSE OCV	fmincon*		no
Lu et al. [183]	2017	NMC/G	C/25	dch.	OCV-based	NLLS	overpotential	no
Schindler et al. [144]	2017	LFP/G	C/20		SSE DV			yes
Ando et al. [184]	2018	NMC-532-LMO/G	C/20		DV-based		NMC/LMO masses	yes
Gao et al. [139]	2018	NMC/G	C/20		OCV-based	PSO		no
Hahn et al. [181]	2018	NMC-111/G	C/10	dch.	DV- & OCV-based			no
Ma et al. [141]	2018	NMC-111-LMO/G	C/20		RMSE OCV	PSO	resistance	no
Fath et al. [146]	2019	NMC-622/G	C/10	dch.	OCV-, DV-, IC-based	PS	inhomogeneity	no
Gantenbein et al. [186]	2019	NCA/G	C/10	dch.	OCV-based			no
Gao et al. [84]	2019		C/20		RMSE OCV			no
Rumberg et al. [178]	2019	NMC-622/G	incremental		RMSE OCV			no
Dose et al. [187]	2020	NMC-811/G	C/20	ch.	DV-based			no
Jia et al. [96]	2020	NMC-532/G	C/20	ch.	RMSE OCV	PSO		yes
Lee et al. [136]	2020	NMC/G	C/20	dch.	SSE OCV			no
Lee et al. [85]	2020	NMC/G	C/20	dch.	SSE OCV	SQP		yes
Pan et al. [179]	2020	LFP/G	C/25	dch.	RMSE OCV	MC	resistance	no
Lu et al. [75]	2021	NMC/G	C/30		OCV- & IC-based	fmincon*		no
Mbeya et al. [188]	2021	LFP/G	C/25	avg.	OCV-based	NLLS		no
Tian et al. [145]	2021	LCO-NCO/G	C/20	ch.	RMSE OCV	IP		no
Yang et al. [86]	2021	NMC/G	C/20	ch.	RMSE OCV	globalsearch*	resistance	no
Chen et al. [93]	2022	NMC-111-LCO/G	C/33	dch.	DV/IC peaks**	GA		no

* MATLAB function name ** DV/IC peak positions and capacity G = Graphite

2.2.4 Degradation effects on the cell level

The most important effects of the degradation mechanisms on the macroscopic cell level are capacity fade and an overall resistance increase which leads to a reduction of the power that can be provided by the cell. Capacity fade can be caused both by LAM and by LLI. It should be noted, that these degradation modes sometimes do not directly lead to capacity fade. This is the case when lithium inventory or electrode capacity that does not contribute to the cell capacity in the full-cell operating range is lost. Power fade can be caused by LAM at both electrodes as well as by impedance increase [18–20; 97; 114]. The capacity accessible under typical operation conditions also decreases as the cell resistance increases as the voltage limits are reached earlier during charging or discharging. The two degradation effects are thus closely connected with each other.

There are many studies in which cell level degradation effects are investigated. They are often described using comparably simple analytical equations [19]. This types of aging models are called empirical aging models, as there is no direct link between a first-principles description of individual degradation mechanisms and the equations that are used to describe the degradation effects on the cell level. Still, the selection of the model equations is often motivated by assumptions on the underlying degradation mechanisms, which is why these models are sometimes also referred to as semi-empirical aging models. The main aim of these models is to allow the prediction of cell degradation under different operating conditions, which is needed in the scope of system design and optimization of operation strategies [19]. Most empirical aging models presented in the literature concentrate on describing the remaining capacity or the capacity fade as a function of stress factors, but there are also studies in which the change in cell impedance during aging is analyzed [189; 190]. The scope of empirical aging models is typically limited to the main part of a cells lifetime before any mechanisms leading to rapid capacity fade [191; 192] occur. In most empirical aging-models, calendar and cycle aging contribute to the total aging in a purely summative way [190; 193] described by

$$C_{\mathrm{loss}} = C_{\mathrm{loss,cal}} + C_{\mathrm{loss,cyc}}, \tag{2.38}$$

where C_{loss} is the total capacity loss, $C_{\mathrm{loss,cal}}$ the part of the capacity loss caused by calendar aging and $C_{\mathrm{loss,cyc}}$ the part of the capacity loss caused by cycle aging. For the parametrization of a cycle aging model, simulated values for the calendar aging part of the aging have to be subtracted from the measurement results to obtain the pure cycle aging part [190; 193]. The capacity fade during calendar aging is often modeled by an equation of the form

$$C_{\mathrm{loss,cal}} = f(T, SOC) \cdot t^z \tag{2.39}$$

where the exponential factor z describes the impact of storage time on the capacity fade. A value of 0.5 is often chosen for z [193; 194] based on the consideration that the capacity fade during calendar aging is mainly caused by SEI formation, which is a self-inhibiting process [195]. The function $f(T, SOC)$ describes the impact of temperature and SOC on the rate of calendar capacity fade. Empirical models for cycle aging are usually functions of the total charge throughput, as it is assumed that the additional degradation caused by the cycling scales with this quantity. Similar to the calendar aging models, the impact of charge throughput is often modeled by a power-law dependence [19]

$$C_{\mathrm{loss,cyc}} = f(T, SOC, DOD, I) \cdot {Q_{\mathrm{tot}}}^z. \tag{2.40}$$

Here, the function $f(T, SOC, DOD, I)$ describes the impact of the stress factors on the rate of cycle aging. In contrast to calendar aging, SOC stands for the mean SOC of the cycling window. The depth of discharge (DOD) of the cycling window as well as the current rate are additional stress factor that are often assumed to influence the rate of cycle aging. Sometimes the current rate during charging and discharging are treated individually [193]. Cycle aging models are often more complex than models for calendar aging, because a strong interaction between the stress factors is assumed [193]. A detailed review on the current state of empirical aging modeling on the cell level is given in [19].

2.3 State of health estimation

In the main part of this thesis, two novel methods for SOH estimation of lithium-ion batteries are presented. In this section, a general introduction to the topic of SOH estimation and a review on methods for SOH estimation that have been proposed in the literature are provided.

2.3.1 Definitions, general approaches, requirements and validation

Definitions of the state of health In the context of lithium-ion batteries, the term SOH denotes an abstract quantity that describes the condition of a battery cell or system regarding its degradation. There is no standardized definition of the state of health in the literature [22]. The most common definitions are related to the degradation effects observable on cell level (see section 2.2.4). In many contexts, the SOH is defined as the ratio between the actual, i.e., remaining, cell capacity C_{act} and the initial cell capacity C_{ini} [108; 196–200]:

$$SOH = \frac{C_{\mathrm{act}}}{C_{\mathrm{ini}}}. \tag{2.41}$$

The nominal capacity is also often used for the denominator in equation 2.41 instead of the initial capacity. In order to obtain a complete and exact definition, equation 2.41 needs to be complemented by the test conditions that are used to measure C_{act} and C_{ini}. These test conditions are also not standardized in the literature, which has the consequence that there is a multiplicity of possible definitions, even if only capacity-based SOH definitions are considered. In most studies, where SOH is used as a quantitative parameter, an exact definition is provided specifically for the respective study.
Other common definitions for the SOH are based on the increase of the overall internal resistance of a battery, which can limit the power that can be delivered by the battery [22]. Also this category of SOH definitions contains a multiplicity of variants that are differentiated by the way the internal resistance is measured. If, for example, a direct current (DC) current pulse is used to determine the internal resistance, measurements at different SOCs, temperatures and with different pulse duration will lead to different resistance values and thus to different values for an resistance-based SOH.

This indeterminacy of the term SOH makes it difficult to compare the results from different studies and also to clearly define the scope and goal of methods for SOH estimation, as this term can refer to multiple different estimation objectives. The complexity can be significantly reduced by treating SOH estimation as an application driven task: depending on the application-specific requirements, an individual definition for the SOH should be used. If, for example, the remaining capacity under typical discharging conditions is of interest in a specific application context, a quantity defined this way should form the basis for the definition of the SOH for this application context. In the scope of SOH estimation method development, a quantity that is expected to be relevant in an application context should be used as basis for the definition of the SOH. Even if the exact requirements on the estimated quantity differ in another application context, e.g., if the remaining discharging capacity at a different current rate or temperature is required, methods can often be adapted to this specific goal.

In this work, the scope of SOH estimation is narrowed to the determination of the remaining cell capacity. In the remaining part of this section, the term SOH refers to a quantity based on the remaining cell capacity, such as defined in equation 2.41, without further specifications, in order to allow a comparison between different studies on an abstract level.

General approaches for SOH estimation Following this narrowed definition of SOH, SOH estimation refers to a method that allows the estimation of the actual capacity of a battery cell or system. In principle, the actual capacity could also be directly measured by performing a full charging/discharging cycle with accurate current measurement. In most practical applications, this is either technically not possible or at least unfavorable due to the effort and temporary unavailability of the system. As already briefly introduced in section 1.2, on a very abstract level, there are three approaches for SOH estimation which are denoted as aging model-based, feature correlation-based and physical model-based in this work. The abstract concepts behind these three approaches are schematically represented in figure 2.11 and discussed in the following. An overview on concrete methods for SOH estimation described in the literature is provided in section 2.3.2.

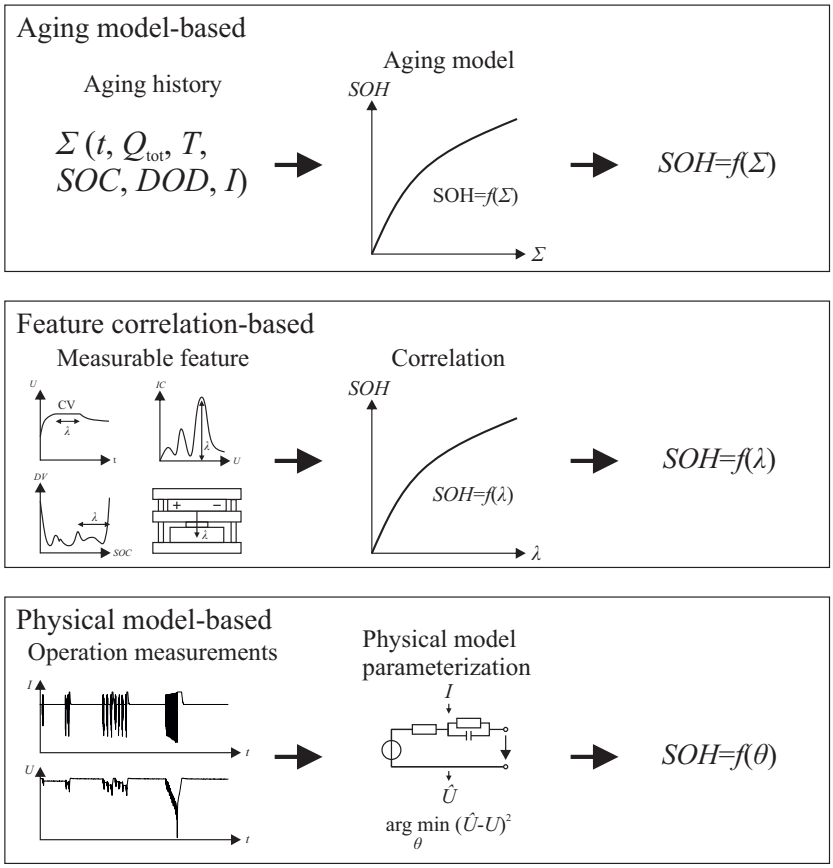

Figure 2.11: Schematic representation of the three general approaches for SOH estimation. Σ denotes an abstract, potentially aggregated, representation of a cells aging history. λ represents any kind of feature that can be measured directly or indirectly during the lifetime of a battery. θ denotes a vector containing the free model parameters of the physical model used to describe the cell behaviour in a certain context.

In **aging model-based** SOH estimation methods, an aging model, i.e., a known correlation between the operation history and the remaining capacity that can be expected, is used to determine the SOH [198; 199; 201]. The conditions under which the cell or system is operated are tracked throughout its lifetime. The aging model can then be used to obtain an estimate on the remaining capacity based on the tracked operation history, whenever needed.
The challenge for this type of SOH estimation methods consists in the development and parametrization of an accurate aging model for the cell or system. In general, the capacity fade depends non-linearly on a variety of stress factors [19]. These dependencies need to be represented to obtain an accurate and universally applicable aging model, which leads to a large parametrization effort. Another drawback is that the aging tests needed for parametrizing the aging model, which can last for several years, need to be completed before an algorithm for SOH estimation based on the aging model can be implemented in a BMS. Aging-model based SOH estimation methods are only applicable to the analysis of field data if an aging model is available for the cell or system under investigation.

Feature correlation-based SOH estimation methods are based on a known correlation between a feature that is measurable during battery operation and the remaining capacity. The measurable feature can for example be the duration of the CV phase of the charging procedure [202; 203], the height or position of a peak in the IC or DV spectrum of the cell [204], or the stack stress measured for a constrained cell [108]. Whenever this feature is measured during operation, the correlation can be used to obtain an estimate on the SOH. The method for SOH estimation based on internal gas pressure measurement presented in chapter 3 belongs to this category as well as most SOH estimation methods using machine learning techniques.
The challenge for this type of SOH estimation methods consists in the identification of the feature to SOH correlation. The correlation needs to be valid for all relevant aging conditions, which is difficult to prove in laboratory studies. As for the aging model-based methods, the correlation needs to be parameterized via lengthy aging experiments before the method can be applied. Another drawback is that in the application, SOH estimation is only possible in situations in which the feature can be measured.

The **physical model-based** SOH estimation methods rely on a mathematical model that describes the physical behaviour of a cell or system in a certain context. The model is defined by its structure, which needs to be determined beforehand, but the model parameters do not need to be known beforehand. Both the model input and the model output need to be quantities that are measurable during operation. A common example for such a model is an electrical ECM that relates current as model input to the terminal voltage as model output [205–207]. During operation, the model inputs are measured and the model output is calculated assuming an initial guess for the model parameters. The difference between the simulated and the measured model output is an indicator for the correctness of the model parameters used for the simulation. Then, optimization or model identification methods are used to adapt the model parameters to minimize the difference between the simulated and the measured model output. The model is thus parameterized based on measurement data obtained during operation. In a last step, the actual capacity, which is either an explicit model parameter or a quantity that can be calculated using the now parameterized model is determined. The method for SOH estimation based on reconstructing the OCV curve from partial charging curves presented in chapter 5 is a contribution to this category of methods.
The main challenge for physical model-based SOH estimation methods is the identification of a model

structure that accurately describes the behaviour of the cell or system throughout aging under all relevant conditions. Another challenge is the development of efficient algorithms for the model parameter estimation. With methods of this type, SOH estimation is only possible in situations where suitable input and output data for parametrizing the model can be measured. Another problem is that with increasing number of free model parameters, the obtained results can become ambiguous as different sets of model parameters lead to a minimization of the difference between input and output.

Requirements and validation The requirements for SOH estimation methods are specific to the individual application. It is therefore difficult to quantify the general performance of a specific method. The accuracy obtained for the estimation of the remaining capacity in a certain scenario is often used as an indicator for the performance of a method, but this is only one aspect that needs to be addressed. Other dimensions of the requirements on SOH estimation methods are:

- Parametrization effort: in a practical context, a key requirement is often set by the available resources and data. If, for example, the SOH is to be determined based on field data from a system for which no aging model or correlation between a specific feature and the SOH is available, aging model-based and feature correlation-based models are not applicable. The need and effort for model parametrization can thus be defined as an additional evaluation criterion for SOH estimation methods.

- Feature observability: feature correlation-based methods and physical model-based methods are only applicable in situations where the relevant feature or model input/output is measurable. A concrete method can thus only be applied if this situation occurs with the necessary frequency during operation. The frequency of the occurrence of such relevant situations can be defined as another, application-specific evaluation criterion for SOH estimation methods.

- Aging path universality: another important aspect is whether a method performs well for cells aged under different conditions, which is often neglected in the literature. This is important as different aging conditions might trigger different degradation mechanisms that result in a different evolution of the features used for SOH estimation.

- Transferability to other cell types: most methods for SOH estimation presented in the literature are developed for one specific cell type. The transferability to another cell types is an important aspect for the wider applicability of an SOH estimation method.

- Robustness: finally, also the robustness of the methods, i.e., whether the results are influenced by external factors that are not explicitly considered by the method should be considered. This includes for example, if the temperature at which a feature used in a feature correlation-based method is measured influences the estimated SOH.

The discussion of these additional aspects is typically outside the scope of studies presenting methods for SOH estimation. Thus, also the validation of SOH estimation methods is mostly restricted to the quantification of the capacity estimation accuracy for a certain scenario. This approach is justified in a proof-of-concept stage, as long as it can be assumed that the scenario used for algorithm validation is

realistic for some kind of application. A review on approaches for validating SOH estimation methods is provided in the following. Four different approaches for SOH estimation algorithm validation can be found in the literature. The constant current (CC) discharging capacity directly measured in temporal proximity to the validation period is used as reference by most authors.

One option is to apply the SOH estimation algorithm to measurement data recorded during cell aging. Some authors apply constant current constant voltage (CCCV) cycling for cell aging and use the data of the cycling as algorithm input [202; 203; 208–222]. This has the advantage that a reference CC discharge capacity is measured at each cycle. On the other hand, continuous CCCV cycling does not occur in most real application. The applicability of the algorithm to real operation data is therefore not shown. Many studies that use this kind of algorithm validation do not use original measurement data but apply their algorithms to publicly available datasets [203; 209–212; 220; 222]. An overview on such datasets is provided in [223]. Other authors use aging data where a profile typical for the dynamic operation during battery discharging in an electric vehicle (EV) is combined with CCCV charging [224–227]. In this case, capacity measurements during periodic checkups are used as reference. Most of the times, full cycles [224; 225; 227] or at least very large SOC windows (>80%) are used for these cycling experiments. Long pauses during the discharging are not implemented and the general cycling to pause ratio is much higher than in a real EV application. Both of these aspects lead to significant differences between the data that would be available in a real application and the data that is used for algorithm validation. There are some studies where more realistic varying conditions are used for algorithm validation [201; 228–230]. Still, only very short rest times are implemented in these studies compared to the typical use profile of a BEV.

The second widely used option is to apply the algorithms to comparably short validation tests periods representing a use case, which are typically not longer than a few hours. The tests are typically part of the periodic characterization procedures during long-term aging experiments and a capacity measured before or after the validation test is used as reference [231–239]. The advantage of this method is that the profile used for algorithm validation, which should be as close to the application profile as possible, is independent of the aging profile. In this way, the cell aging can be accelerated by rapid cycling or high temperatures, while the test data recorded for algorithm validation is still close to the data available in an application. An example for such a validation test is to completely discharge a fully charged cell with an EV driving profile [231]. There are also some studies in which special profiles that enhance the observability of the feature used by the algorithm, are applied as part of the regular characterization routine and used for algorithm validation [240–242]. For example, the validation profile can contain low-current charging periods to enhance the visibility of DVA peaks [240]. Another special case of this option is found in some studies focused on methods for model identification: here, short periods of dynamic cell operation are used to demonstrate the performance of the model identification algorithm at one single aging state and no aging is applied at all [225; 243–247].

A third option is to use measurement data recorded during cell aging at real time during operation. This data can either be obtained in long-term laboratory tests [200; 248] or recorded in a real applications in the field [198; 199; 249]. This approach of course yields the most realistic data for algorithm validation, but it is associated with huge effort. This is why there are only a few studies using this option so far. It can be expected that algorithm validation based on field data will gain more popularity in the future, as the technology for cloud-based recording of operation data improves.

The last option is to follow a model in the loop approach and use simulated data for algorithm validation. In this case, an accurate cell model containing all relevant aging effects is needed. Application scenarios like EV driving profiles are used to simulate the terminal voltage, current and temperature during operation for cells at different aging states [205; 245; 250]. Sometimes, hardware-related restrictions like sensor inaccuracy or signal delays are also considered in such simulations [205]. This approach is fast and yields reproducible results. The challenge is here to obtain a cell aging model containing all relevant aging effects that can occur under all aging conditions.

Studies describing aging model-based SOH estimation algorithms and feature correlation-based SOH estimation algorithms mostly do not contain any formal validation of the algorithm, but are limited to discussing the accuracy of the analyzed correlation.

2.3.2 Methods for state of health estimation

The overview on methods for SOH estimation for lithium-ion batteries presented in this section aims to provide examples for the most important conceptual approaches rather than to include all available studies on this topic. Systematic reviews on methods for SOH estimation can be found in [22–24].

Aging model-based methods A large number of studies presenting empirical aging models has been presented in recent years. A comprehensive review of these studies can be found for example in [19]. In principle, every aging model can be used for aging model-based SOH estimation, but this scope of application is not explicitly mentioned in most studies describing aging models. The following types of aging models have been explicitly proposed to be used for SOH estimation:

- Empirical aging model: Hamar et al. presented an empirical aging model (see section 2.2.4) that shows a good correlation between the operation history of EVs operated in the field and accurate capacity measurements recorded at certain points in time [198].

- Support vector regression: Nuhic et al. proposed an algorithm that uses support vector regression (SVR) to model the relation between SOH and operation history [201].

- Neuronal network: in addition to the analytical empirical model, Hamar et al. also presented an aging model in the form of a neuronal Network (NN) [198]. Their validation results show a higher accuracy of the NN model in comparison to the analytical model. He et al. proposed an aging-model described by a long and short term memory (LSTM) NN that maps operation history to residual capacity [199]. They validated their method with field data of EVs from which they also extract the ground truth used for the model parametrization.

Feature correlation-based methods The following features have been shown to correlate with the SOH and could thus be used for SOH estimation. This list is not conclusive, but it provides an overview on the most common concepts for feature correlation-based SOH estimation:

- IC curve FOIs: many authors described a correlation between characteristic features of the IC curve (see 2.2.3), so called feature of interests (FOIs), and the SOH [87; 170; 197; 204; 251].

The most common FOIs are the peak height, peak position and peak area of the IC spectrum. Sometimes, also a combination of several FOIs is used. Dubarry et al. suggested to simulate the quasi-stationary OCV curves of a cell suffering from different combinations of degradation modes [170]. Afterwards, multiple features of the IC curves such as peak positions, voltage at the edges of the spectrum, peak half-width, voltage variation, peak intensity or intensity variation can be analyzed for their correlation with degradation modes. A multi-dimensional look up table (LUT) correlating a selected combination of FOIs with the degradation modes can then be created. In this way, the degradation modes can be retrieved if the combination of FOIs is observed. As the remaining capacity can be calculated based on the degradation modes, this also resembles a method for SOH estimation. Simulating battery degradation using the mechanistic model allows to establish the correlation between IC FOIs and SOH without the necessity of long and tedious aging experiments [118].

- DV curve FOIs: similar to the correlation between IC FOI and SOH, also features of the DV curve (see 2.2.3) such as the position or height of DV peaks and valleys are found to correlate with SOH and can thus be used for SOH estimation [204; 208].

- Shape of charging/discharging curves: also charging or discharging curves themselves contain characteristic information that can be correlated with SOH without the need of calculating the DV or IC first. Park et al. presented a correlation between an aging parameter that is based on the shape of the CC discharging curve and the SOH [196]. Richardson et al. showed that there is a correlation between the shape of partial CC charging and discharging curves with the SOH [252]. Shen et al. proposed an algorithm that correlates the current and voltage measurements during complete and partial CCCV charging with the SOH using a deep convolutional NN [253]. Li et al. proposed an algorithm based on random forest regression using partial CC charging curves as input [219]. Yang et al. proposed to use a combination of manually selected features of the charging curve (time in CC phase, time in CV phase, slope at end of CC phase and slope at lower SOC) [203]. Guo et al. used a relevance vector machine to correlate charging curve features with the SOH [254].

- Duration of CV phase: the duration of CV phases at the same voltage and with the same cut-off current is reported to correlate with the SOH and can thus be used for SOH estimation [202; 203].

- Current decay during CV phase: also the time constant of the current decay during CV charging has been shown to strongly correlate with SOH [202; 255].

- Relaxation after CCCV charging: voltage measurements from the relaxation phase after a CCCV charging process can be correlated with the SOH using machine learning techniques [256].

- OCV curve shape: Ma et al. presented a method in which the OCV curve is first extracted from dynamic discharge data and then fit by a model equation. The combined fit parameters of this equation correlate with the SOH [238].

- Internal resistance: a correlation between the internal resistance measured with a DC current pulse and the remaining capacity has been described [257]. A problem of using this correlation

for SOH estimation is that the ratio of relative capacity fade and relative impedance increase is generally different for different aging conditions [257]. Cai et al. presented a correlation between characteristic points of DC current pulses with SOH modeled by a support vector regression model that could be used for SOH estimation [200].

- Electrochemical impedance spectrum: a correlation between ECM parameters obtained by fitting electrochemical impedance spectroscopy (EIS) spectra and SOH has been proposed for SOH estimation [233].

- Mechanical quantities: some of the mechanical parameters that can in principle be measured during operation of lithium-ion cells correlate with the SOH and have thus been proposed as features for SOH estimation. Cannarella et al. presented a correlation between cell stack stress and SOH [108]. Other studies present correlations between features of ultrasonic waves that are transmitted through lithium-ion cells and SOH [258]. A major problem with these methods is that mechanical properties are also dependent on SOC and temperature, which needs to be considered in an algorithm for SOH estimation. Another drawback of these models is the additional effort that results from the necessity of additional sensors. The method for SOH estimation based on measurements of the internal gas pressure inside prismatic cells presented in chapter 3 of this work is a novel contribution to this type of methods for SOH estimation.

- Entropy: Wu et al. showed that there is a correlation between the temperature evolution during CC charging of an LCO-NCA/graphite cell and the SOH [259].

- Cumulative balancing charge: Zilberman et al. showed that there is a correlation between the cumulative balancing charges in a pack of serially connected cells that are cycle aged and the difference between the individual cell capacities [161]. This could help to determine the SOH of individual cells connected in series.

Physical model-based methods The key elements of physical model-based methods are the physical model and the algorithm used for online model parametrization. In the following list, the most common types of physical models used for SOH estimation are presented:

- Coulomb counting: The simplest method for physical model-based SOH estimation is based on Coulomb counting. The capacity can be determined if the charge throughput balance during a certain period of charging or discharging is divided by the change in SOC:

$$C_{\mathrm{act}} = \frac{\Delta Q}{\Delta SOC}. \tag{2.42}$$

  The only model parameter in this case is the battery capacity and the model is described by

$$\Delta SOC = \frac{\Delta Q}{C_{\mathrm{act}}}, \tag{2.43}$$

  where ΔQ can be regarded as the model input and ΔSOC as the model output. If the ΔSOC calculated by the Coulomb counting model does not correspond with the ΔSOC that is calculated based on the difference between the SOC before and after the operation phase, the assumed

battery capacity needs to be updated. There are two main challenges for this method: first, ΔQ hast to be measured with high accuracy. Second, a reliable method to determine the difference in SOC before and after the operation period that is independent of Coulomb counting is needed. Voltage-based SOC estimation is mainly used for this task, but this is problematic, as the relationship between SOC and voltage, i.e., the OCV curve, also changes with cell degradation. It has been proposed to mitigate this problem by using a suitable voltage window whose relative contribution towards the complete capacity does not change significantly during aging [260; 261]. Another option is to apply Coulomb counting only to a certain SOC window in which the main portion of degradation is expected, and which is defined by the position of DV peaks [262]. Besides the mentioned drawbacks, Coulomb counting-based SOH estimation can yield sufficient results in many applications and is often chosen because of the simplicity of the method.

- Equivalent circuit model: ECMs are often used to describe the electrical behaviour of lithium-ion cells and systems. The model input is usually the current and often additionally the temperature. The model output is typically the terminal voltage. A typical ECM for a lithium-ion battery consists of a voltage source modeling the OCV as a function of SOC, a serial resistance modeling the ohmic internal resistance and one or several RC-circuits modeling overpotentials that exhibit a transient behaviour. The most important model element for the SOH estimation is the OCV. One option is to use an OCV curve that is externally determined during initial model parametrization and to regard the shape of the OCV curve to be invariant during aging. In this case the only free model parameter describing the static part of the model is the cell capacity. This approach is used in many SOH estimation algorithms based on Kalman filter techniques [205; 206]. Other studies consider a change in the shape of the OCV curve, which more realistically resembles the actual physical behaviour of aged cells. In these models, the OCV curve is implemented as an analytical equation that includes parameters that are obtained via model identification based on operation data throughout aging [249; 263]. The equations describing the OCV curve do not explicitly consider the half-cell origin of the full-cell OCV curve.
  Different algorithms have been used in the literature for online parametrization of ECMs with the aim of SOH estimation. This includes the Big-Bang Big-Crunch algorithm [249], different types of Kalman filters [205–207], least squares optimization [264; 265] and a combination between Extended Kalman Filter, recursive least squares optimization and a parameter varying approach [263].

- Mechanistic cell model: The mechanistic cell model described in section 2.2.2 is a special case of an ECM, in which the half-cell origin of the full-cell OCV curve is explicitly modeled and associated with degradation modes. Using full-cell OCV curve alignment (see section 2.2.3) is typically used to parameterize this type of model. The same approach has also been proposed as a method for SOH estimation. The model input is here the charge throughput during CC charging or discharging and the model output is the terminal voltage. Two aspects need to be considered to apply this method, which was originally developed for the analysis of complete low-current CC charging and discharging curves, to data frequently observable in applications: first, complete charging or discharging phases are rarely observed in many applications. It would therefore be beneficial if the method could also be applied to partial charging or discharging curves. Second, in the case in which CC charging is applied, the current is typically in a range where the overpotential cannot be neglected and the charging curve does not resemble a quasi-

stationary state. These aspects have been recently investigated by some authors:
Yang et al. showed that accurate SOH estimation based on partial charging curves measured at a current rate of C/3 is possible with this method, if the overpotential is compensated by a resistance term and if the available SOC window includes at least the range between 20-70 % [86]. Lee et al. investigated the theoretical estimation uncertainty of the alignment parameters based on partial OCV curves [136]. They found that the analytical error bound decreases with increasing size of the SOC window and that the inclusion of regions with a high voltage slope improves the estimation accuracy. Dey et al. proposed an algorithm for the identification of a half-cell-based model using dynamic input data [266]. Marongiu et al. showed that accurate SOH estimation for a LFP/graphite cell is possible if the length of the upper two full-cell OCV plateaus is observable [142; 143]. This detection of the voltage plateau length represents a slightly different approach than the pure OCV curve alignment. Higher current rate input has also been investigated by Lu et al. who compensated the overpotential during CC phases by a linearly SOC-dependent resistance term [75]. The algorithm presented in chapter 5 of this work comprises another contribution to this type of SOH estimation methods.

- Physico-chemical models: reduced order physico-chemical models can also be parameterized based on voltage and current measurements obtained during operation and then be used to calculate the SOH. For example, Bartlett et al. proposed to parameterize a single-particle model based on operation data using an Extended Kalman Filter, a Kalman smoother and a particle filter [230]. Online parametrization of a single-particle models was also proposed by other authors [267; 268].

3 Measurement of internal gas pressure for state of health estimation

In the scope of the study presented in this chapter, a novel method for SOH estimation based on measurements of the gas pressure inside prismatic lithium-ion cells is described.
The physical quantities that are measured by a BMS, which form the basis for SOH estimation, are usually limited to voltage, current and temperature. The available information on the battery can be enhanced by using sensors that measure additional physical parameters of the cell during operation. This additional information could in principle be used to improve the safety monitoring or the state estimation, including SOH estimation, performed by the BMS. This concept was investigated in the scope of the joint research project *Multifunktionale intelligente Batterie Zelle* (multi-functional smart battery cell) funded by the German Federal Ministry of Education (grant number 03XP0027G), which was partly carried out at the Chair for Electrical Energy Storage Technology at the Technical University of Munich.
In the scope of this project, prismatic lithium-ion cells in the PHEV2 format with integrated and attached sensors were manufactured and tested. The active anode material of the cells was graphite. NMC-111 was used as active cathode material. The cells were equipped with a reference electrode and a thermocouple inside the cell case. Outside the cell, a gas pressure sensor was glued on top of a small hole in the top cover plate of the cell. The article titled *Measurement of gas pressure inside large-format prismatic lithium-ion cells during operation and cycle aging*, which is presented in this chapter, describes and discusses the results of measurements of the gas pressure inside the case of the aforementioned sensor-equipped lithium-ion cells.

In the scope of this article, the influence of changes in SOC and temperature on the gas pressure inside the cells as well as changes during long-term cycling are investigated. One general result of this study is that long-term monitoring of the gas pressure inside the case of a prismatic cell is feasible with a miniaturized commercially available pressure sensor and does not lead to premature battery failure or accelerated aging. This finding is a novelty, as measurements of the internal gas pressure of lithium-ion cells had previously only been reported for smaller cells [269; 270] or using large-scale laboratory equipment [35; 112; 113; 123; 126; 131].
The gas pressure exhibits a reversible, non-linear dependence on SOC that is most probably due to a change in the free volume inside the cell case caused by the expansion and contraction of the electrodes during lithiation and delithiation (see section 2.1.4). The absolute change between the fully discharged and fully charged state is approximately 3 kPa for the investigated cells. Three regions with different pressure change upon SOC variation can be distinguished during charging and discharging. At SOC below approximately 35 %, the pressure exhibits a comparably strong increase with SOC, which is due to the pronounced expansion of the graphite anode during lithiation as long as the graphite is in the dilute stages (4L-2L). In the middle SOC region (approximately 35-73 %SOC), where the graphite is in the stage 2L-stage 2 phase transition, the gas pressure slightly decreases with increasing SOC. This is probably due to the contraction of the cathode that dominates the overall change in the free volume

in this SOC region where the graphite anode exhibits only a small increase upon lithiation. In the upper SOC region above 73 %, the pressure aging increases with the SOC due to the expansion of the graphite.
It is found that the internal gas pressure reversibly and non-linearly increases with increasing temperature. For an ideal gas, a linear correlation with temperature would be expected from the general gas equation (equation 2.23). A probable cause for the additional pressure increase at elevated temperature is an increase in the partial gas pressure of electrolyte components.
During long-term cycling, the gas pressure irreversibly increases. This is most probably mainly due to the evolution of gas during side reactions (see section 2.2.1). The gas pressure rapidly increases during the first 100 equivalent full cycles (EFCs) and exhibits a slower increase afterwards. Cycle aging at 10 °C and 25 °C is investigated in the scope of the study but no impact of the ambient temperature during cycling on the capacity fade or irreversible pressure change is observed. There is a comparably large variation in the absolute gas pressure both at the begin of life as well as during the cycling for the individual cells. This is probably due to manufacturing tolerances as the cells are custom built prototypes. Still, the investigated cells show an approximately linear correlation between relative increase in pressure and decrease in capacity during cycling after 100 EFC.

The correlation between capacity fade and internal gas pressure found in the scope of this study could be used to estimate the SOH based on gas pressure measurements. The concept of such an algorithm for SOH estimation as well as the necessary steps during algorithm development are outlined in the presented article. The proposed algorithm can be categorized as feature correlation-based SOH estimation (see section 2.3.2). SOH estimation following the proposed concept could for example be applied in addition to other methods that are based on voltage, current and temperature, in order to implement a second method for SOH estimation with true redundancy. Apart from this application, the general understanding on the impact of SOC, temperature and cycle aging upon the gas pressure inside the case of a prismatic cell derived in the presented study, might also be valuable in the scope of mechanical cell and pack design.

The detection of safety critical events is another possible scope of application for monitoring the internal gas pressure of battery cells which is not discussed in the presented article. Results on this topic that were also obtained in the scope of the project *Multifunktionale intelligente Batterie Zelle* were presented as part of a poster contribution titled *In-situ measurement of gas pressure inside prismatic lithium ion cells during operation and abuse scenarios* at Batterieforum Deutschland in 2019.

Publication notes

The article titled *Measurement of gas pressure inside large-format prismatic lithium-ion cells during operation and cycle aging* is presented in the following. The article was published in the Journal of Power Sources [271]. Parts of the results have been presented as poster contributions titled *In-situ measurement of gas pressure inside prismatic lithium ion cells during operation and abuse scenarios* (Batterieforum Deutschland, Berlin, 2019), *Change of Gas Pressure inside Prismatic Lithium Ion Cells during Aging* (Advanced Battery Power, Aachen, 2019) and *Influence of State of Charge, Temperature and Aging on the Gas Pressure inside Prismatic Lithium Ion Cells* (Batterieforum Deutschland, Berlin, 2020).

Author contribution

The concept of the study was developed by Julius Schmitt supported by discussions with Benjamin Kraft and Jan Philipp Schmidt. The experimental design was developed by Julius Schmitt. Julius Schmitt carried out the experiments. The experimental data was analyzed and visualized by Julius Schmitt. Benjamin Kraft and Betina Meir provided additional experimental data recorded at their laboratory that is not presented in the article but which was used for validation of the presented results. Klaus Elian, David Ensling and Goran Keser provided the sensor-equipped battery cells that were used in the study. Andreas Jossen supervised the research project as well as the scientific work presented in the article. The manuscript was written by Julius Schmitt and was edited by all authors. All authors discussed the data and commented on the results.

Measurement of gas pressure inside large-format prismatic lithium-ion cells during operation and cycle aging

Julius Schmitt, Benjamin Kraft, Jan Philipp Schmidt, Betina Meir, Klaus Elian, David Ensling, Goran Keser and Andreas Jossen.

Journal of Power Sources 478 (2020), p. 228661, DOI: 10.1016/j.jpowsour.2020.228661

Permanent weblink:
https://doi.org/10.1016/j.jpowsour.2020.228661

Journal of Power Sources 478 (2020) 228661

Contents lists available at ScienceDirect

Journal of Power Sources

journal homepage: www.elsevier.com/locate/jpowsour

Measurement of gas pressure inside large-format prismatic lithium-ion cells during operation and cycle aging

Julius Schmitt [a,*], Benjamin Kraft [b], Jan Philipp Schmidt [c], Betina Meir [b], Klaus Elian [d], David Ensling [e], Goran Keser [d], Andreas Jossen [a]

[a] Technical University of Munich, Institute for Electrical Energy Storage Technology, Arcisstraße 21, 80333, Munich, Germany
[b] VARTA Storage GmbH, Nürnberger Straße 65, 86720, Nördlingen, Germany
[c] Bayerische Motorenwerke AG, Petuelring 130, 80788, Munich, Germany
[d] Infineon Technologies AG, Am Campeon 1-15, 85579, Neubiberg, Germany
[e] VARTA Microbattery GmbH, VARTA-Platz 1, 73479, Ellwangen, Germany

HIGHLIGHTS

- Gas pressure in prismatic lithium-ion cells is measured with an attached sensor.
- Measurement of gas pressure during long-term cycling is feasible for large cells.
- Change in electrode volumes, depending on lithiation, affects internal pressure.
- Dependence of internal pressure on temperature is investigated.
- Pressure increase during cycling correlates with capacity decrease.

GRAPHICAL ABSTRACT

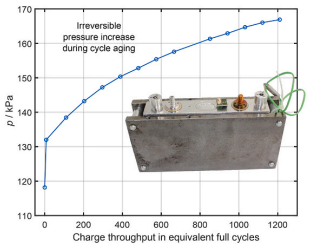

ARTICLE INFO

Keywords:
Lithium-ion battery
Internal gas pressure
Cycle aging
Gassing
State estimation
Graphite

ABSTRACT

In this study we investigate the influence of the state of charge (SOC), temperature and aging on the gas pressure inside prismatic lithium-ion cells with a $LiNi_{1/3}Mn_{1/3}Co_{1/3}O_2$ cathode and a graphite anode. The internal gas pressure inside lithium-ion cells has so far been only investigated for small cells using large-size laboratory measurement equipment. We show for the first time that measuring the internal gas pressure is also possible for large-format prismatic cells and by using miniaturized pressure sensors that can be integrated into a battery pack. We also show that this measurement method enables the monitoring of the gas pressure during long-term cycling without leading to premature battery failure or accelerated aging. The gas pressure depends on the SOC in a non-linear way. This is caused by the dependence of the electrode volumes on the degree of lithiation. The gas pressure also correlates non-linearly with temperature, and the magnitude of temperature dependence increases with aging. During long-term cycling, the pressure irreversibly increases, which is most likely due mainly to gas formation. The increase in pressure correlates with a loss of capacity, which basically qualifies internal gas pressure for an indicator for state of health.

* Corresponding author.
E-mail address: julius.schmitt@tum.de (J. Schmitt).

https://doi.org/10.1016/j.jpowsour.2020.228661
Received 31 March 2020; Received in revised form 7 June 2020; Accepted 13 July 2020
Available online 1 September 2020

1. Introduction

The gas pressure inside prismatic lithium-ion cells is a physical cell parameter which has to be considered during cell design. The vent, in particular, must be constructed in a way that it will open at a defined internal pressure during abuse cases, and not during regular operation or as a result of pressure increase during cell aging. In addition to its relevance for cell design, gas pressure inside the case of prismatic or cylindrical cells could also provide an additional source of information about the state of the battery, enabling advanced state estimation. This would require the measurement of the gas pressure during operation.

According to the general gas equation (1), the pressure p inside a closed volume V depends on the amount (moles) of gas n in the volume and the absolute temperature T. R is the ideal gas constant.

$$p \cdot V = n \cdot R \cdot T \quad (1)$$

The general gas equation refers to a hypothetical ideal gas but is also often a good approximation for the behavior of real gases. Applying this approximation, the gas pressure inside a battery cell with a rigid case depends on the amount of gas in the cell, the free volume inside the cell case, and the temperature. The gas pressure inside lithium-ion cells has been reported to be affected by the following effects:

1 Production of gas during formation and aging [1–5].
2 Reversible changes of electrode volume during intercalation and deintercalation of lithium, resulting in a change of free volume inside the cell [4,6].

A number of authors have reported experiments where the gas pressure inside lithium-ion batteries has been monitored during operation. Matasso et al. constructed a test chamber for examining the pressure and gas formation of cylindric lithium-ion batteries [1,2,6,7]. In their test setup, the pressure release cap was removed from the batteries and they were transferred into the test chamber, which was subsequently sealed. Over the course of 250 cycles, an increase of gas pressure was observed for a cell with a lithium cobalt oxide cathode [1]. The rate of pressure increase per cycle decreased during cell aging, which the authors interpreted as a change in the primary effects leading to the pressure increase. They also analyzed - using gas chromatograph mass spectrometry - the gas inside the cell after the cycling, and identified CO, CO_2, CH_4, C_2H_4, C_2H_6 and C_3H_8 as components of the gas. Taking into account results from the post-mortem scanning electron microscopy analysis, they concluded that the processes causing the production of these gases are not related to the type of cathode material. They also reported that higher cycling rates lead to a higher rate of pressure increase [2]. No significant gas evolution was observed between the 5th and 100th cycle for a lithium iron phosphate (LFP) cell [7]. Concerning the influence of the state of charge (SOC), they found that the pressure during low-rate cycling of an LFP/graphite cell is lower after discharge compared with the charged state [6]. Schiele et al. [3] developed a multichannel pressure-measurement system for observing the pressure inside small, self-built electrochemical cells. They used this method in combination with differential electrochemical mass spectroscopy, in order to gain insights into the gas evolution and the reactions taking place inside different types of lithium-ion cells. They found that gas is formed during the formation cycle and that the amount of gas produced is higher at elevated temperatures. The loss of capacity during the formation phase also correlates with the pressure increase due to gassing [3]. Schweidler et al. used the same setup and measured the pressure of the gas volume at the top part of a lithium titanate oxide (LTO)/graphite cell during cycling [4]. By subtracting the pressure increase due to gassing and assuming no volume change in the LTO, the pressure change due to the change in the volume of graphite was calculated, and shown to be in good accordance with the results obtained from their X-ray diffraction measurements of the lithiation-dependent volume change of graphite. Lanz et al. [5] constructed an electrochemical cell with a built-in pressure transmitter to study the oxygen release at elevated cell potentials. Park et al. [8] used a 18650-type cell with a pressure sensor containing an electrode jelly roll, filler and electrolyte, in order to study the influence of surface modifications on the oxygen release of high-voltage oxide cathodes at high potentials. Measurements of internal gas pressure have also been reported for other cell chemistries, including nickel-metal hydride [9,10] and lithium-sulfur [11].

Apart from the studies where gas pressure is explicitly measured, there are many studies of the fundamental effects causing gassing inside lithium-ion batteries during formation and aging, without an explicit focus on pressure measurements. Production of C_2H_4, CO, CO_2 and H_2 during the formation of lithium nickel manganese cobalt oxide (NMC)/graphite cells has been reported [12]. C_2H_4 is formed as a product of the ethylene carbonate (EC) reduction at the anode when the solid electrolyte interface (SEI) is formed. The H_2 formed during formation cycles originates from the reduction of traces of water at the anode. It is also assumed that protic electrolyte oxidation species are transferred from the cathode to the anode where they are subsequently reduced, releasing additional H_2 even after the initial traces of water have been removed by reduction [12]. The gas formation of $LiNi_{0.4}Mn_{0.4}Co_{0.2}O_2$/graphite pouch bag cells during formation was found to occur mainly during two distinct steps, one at 3.7 V cell voltage and one at 4.3 V [13]. It was also shown that the gases evolving during cycle aging do influence the further aging of the cells, as they can take part in chemical reactions [14]. At elevated temperatures, EC is reported to chemically react with traces of H_2O, thus releasing CO_2 [15]. Other authors found that at elevated temperatures CO is produced by reactions with the cathode material, while CO_2 is mainly produced by reactions with the free lithium compounds Li_2CO_3 and LiOH which are also found in the cathodes [16]. Additional gas formation is reported for high cell potentials which are usually avoided during normal operation. Starting at a cell voltage of 4.6 V, lattice oxygen is released from NMC leading to a decomposition of EC accompanied by the production of CO and CO_2 [17].

Measurements of gas pressure inside lithium-ion batteries have mainly been reported for small cells [5,8] or using special experimental setups containing electrochemical cells [1–4,6,7]. The methods for measuring the internal gas pressure of lithium-ion cells described in the literature are useful to investigate fundamental electrochemical processes but are not suitable for on-board monitoring of the internal gas pressure in an application, which is possible with the method presented in this work. In this study the integration of a pressure sensor attached to a large-format cell, and the resulting measurements of internal cell pressure, are described for the first time. We show that measuring the gas pressure is feasible with a commercially available sensor, which essentially enables the industrialization of the presented method for on-board monitoring. The used sensor could also be integrated into a battery pack because of its small size. The methods presented in the literature either use a much larger sensor or result in a significant change in the free volume that is accessible by the gas. Changes in the free volume accessible by the gas do not occur with the method presented in this work. This is advantageous because the operating conditions are then not altered compared to a regular cell in an application. The method for measuring the internal gas pressure presented in this work also shows excellent long-term stability and does not lead to premature battery failure or accelerated aging, which enables its use throughout the whole lifetime of a battery pack. To the authors' knowledge, this is the first time, a method for measuring the internal gas pressure inside lithium-ion cells fulfilling these requirements is presented.

We present and discuss pressure measurements during the cycle aging of a large-format lithium-ion cell for over 1100 equivalent full cycles for the first time. We show that similar observations to those reported in the literature for small cells can be made with large-format prismatic cells. In addition to the influence of the SOC and aging on the cell pressure, we present and discuss measurements of cell pressure at different temperatures, which has not been subject to much

investigation to date. Based on our results, we finally draw conclusions about the chances and limitations of using pressure measurement for battery state estimation.

2. Experimental

2.1. Custom-built cells with pressure sensor

In order to monitor the gas pressure inside lithium-ion cells during operation, custom-built prismatic cells were equipped with pressure sensors. The cells were manufactured by VARTA Microbattery GmbH (Germany). The positive electrodes consisted of lithium nickel manganese cobalt oxide ($LiNi_{1/3}Mn_{1/3}Co_{1/3}O_2$, NMC-111) and polyvinylidene fluoride (PVDF, < 5 % wt) as the binder, coated on an aluminum current collector. The negative electrodes consisted of refined natural graphite, and both carboxymethyl cellulose (CMC) and styrene-butadiene rubber (SBR) as binders (total < 5 % wt), coated on a copper current collector. A separator with ceramic coating was used. The cells contained EC, dimethyl carbonate (DMC), and ethyl methyl carbonate (EMC) in similar proportions as the electrolyte, and $LiPF_6$ as the conducting salt. Vinylene carbonate (VC, < 5 % wt) was used as an additive.

The cells were of PHEV2 format (outer dimensions of 91 mm × 148 mm × 26.5 mm) and had a nominal capacity of 34 Ah. C-rates and equivalent full cycles (EFC) used in this study are always given with respect to this value. The cells were clamped between two steel plates (8 mm thickness) at a distance of 26.5 mm using spacers and fixed by screws in order to prevent deformation of the cell case through electrode swelling, and to apply similar conditions to those seen in typical applications. A photograph of one of the cells in between the plates is shown in Fig. 1. The results presented in this publication are based on experiments with four cells of this type, which are referred to as A to D.

For sensing the gas pressure inside the cell case, SP40 pressure sensors from Infineon Technology AG (Germany) were used. The integrated sensor package contains a pressure-sensitive membrane which lies beneath an opening in the sensor package. The membrane deforms upon variation in pressure of the volume of gas in contact with the opening of the package, enabling the gas pressure to be measured. It provides on-chip temperature compensation and analog-to-digital conversion. The sensors were soldered on small circuit boards with buffer capacitors and a standard plug for communication. The top cover plate of each battery case had an additional small opening. A pressure sensor on the circuit board was glued over this opening using a high-performance industrial adhesive. Afterwards, the cover plate with the sensor was mounted on the cell case. In this way, the membrane of the sensor was brought into contact with the volume of space in the battery head. Subsequently, the cell was filled with electrolyte and underwent formation. As displayed in Fig. 1, the custom-built cells also contained an internal thermocouple and a reference electrode inside the jelly roll, as additional sensing elements. The results of the measurements with these devices will be addressed in a following publication. Due to the small size of the reference electrode and the thermocouple it is not assumed that they have an influence on the general behavior of the cell.

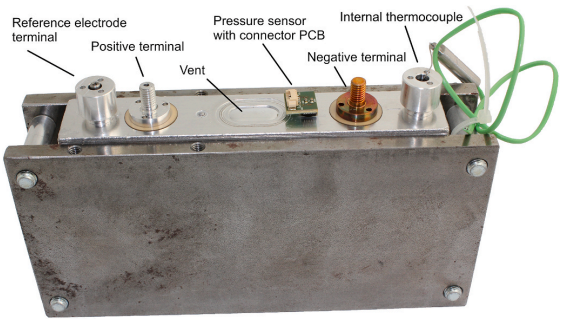

Fig. 1. Custom-built prismatic lithium-ion cell clamped between two steel plates. On top of the cell, the terminals, the vent, the attached pressure sensor with connector printed circuit board, the terminal for a reference electrode and the lead-through for an internal thermocouple are visible.

2.2. Setup and instrumentation

All tests were carried out at controlled ambient temperature inside MK53 climatic chambers from Binder GmbH (Germany). A XCTS battery test system from Basytec GmbH (Germany) with a voltage/current measurement uncertainty of 1mV/100 mA was used for electrochemical cycling and characterization. Temperature sensors were attached to the negative cell terminals to measure the outer cell temperature during testing.

2.3. Test overview and initial characterization

An overview of the experiments carried out during this study is given in Fig. 2. At the beginning of the experiments, as an initial characterization, all cells were tested with the procedures described in Table 1. Afterwards, the cells were repeatedly cycled for 100 cycles, then electrochemically characterized and subsequently exposed to a temperature profile. These three steps were repeated thirteen times, resulting in an overall testing time of 360 days. Details of the individual testing procedures are given below. Whenever the cells were set to a certain voltage before or after a test, this was done at 25 °C using 1C constant current - constant voltage (CCCV) charging/discharging until $|I| < 0.02$C.

2.4. Electrochemical characterization

The electrochemical characterization procedure consisted of charging and discharging cycles with different current rates, followed by a low-current, quasi-stationary open-circuit voltage (OCV) measurement at 0.05C. The quasi-stationary OCV measurement was used for capacity measurement and to correlate pressure changes during charging and discharging, using differential voltage analysis (DVA). Finally, the cells were discharged to 3.7 V and both a charging and a discharging pulse were applied. The detailed test parameters are listed in Table 2. If not otherwise stated, the procedure was applied at 25 °C. The procedure was always preceded by a rest period of at least 6 h at the set temperature. Typical voltage and current measurements during the characterization procedure are shown in Fig. 2 (b). The characterization procedure after the eight cycling period was interrupted due to a technical problem. The results from this characterization are therefore excluded from the discussion for all cells.

2.5. Galvanostatic intermittent titration technique with pressure sensing

Cell open-circuit voltage and gas pressure at rest were measured at different SOCs using the galvanostatic intermittent titration technique (GITT) in order to analyze the influence of the SOC on gas pressure at equilibrium conditions. The experiments were carried out at 25 °C. The cells were first charged with $I = 1$C CCCV until $U = 4.1$ V; $I < 0.02$C. Subsequently, they were kept under open-circuit conditions for 6 h. Afterwards, a 10 s discharging pulse of 1C was applied, followed by one more minute of rest. Finally, 1.7 Ah of charge (corresponding to approximately 5 % of the cell capacity) were drawn from cells by constant current (CC) discharging at 0.2C. These steps were repeated until the terminal voltage reached 2.5 V. Then the same procedure was applied in the charging direction, ending with a CCCV charging phase (until $U = 4.1$ V; $I < 0.02$C). This procedure was conducted during the initial characterization and after the cycling.

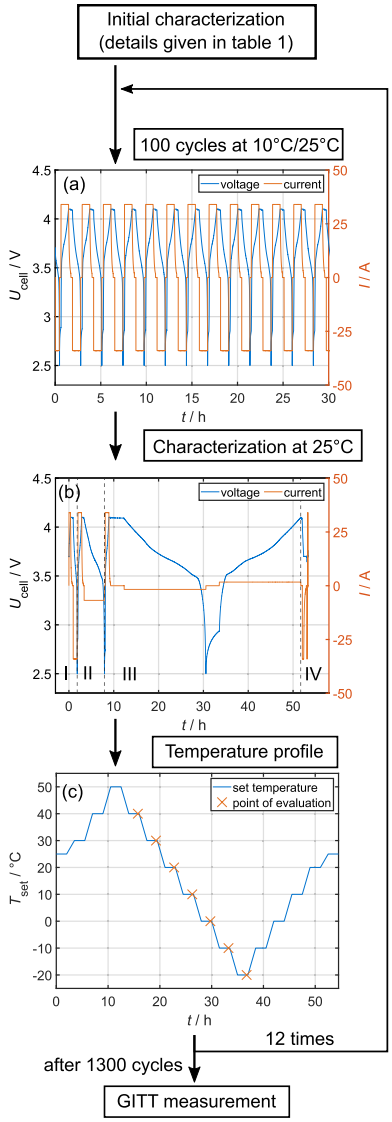

Fig. 2. Overview of the tests carried out in this study: (a) Cell voltage and current during a cycling period (only a section of a cycling period is shown). (b) Cell voltage and current during electrochemical characterization - the marked sections are (I) 1C/1C cycle, (II) 1C/0.2C cycle, (III) 0.05C/0.05C cycle and (IV) discharging the cell to 3.7 V and applying current pulses. (c) Set temperature during the temperature profile procedure with marked points in time where the gas pressure is evaluated.

2.6. Cycling

Each cycling period consisted of 100 cycles, where the cells were CC discharged with 1C until $U = 2.5$ V and afterwards CCCV charged with 1C until $U = 4.1$ V and $I < 0.05$C. There were 10 min of rest time in between charging and discharging. At the end of the procedure, the cells were discharged to $U = 3.7$ V. Cell A and cell B were cycled at a temperature of 25 °C. Cell C and cell D were cycled at 10 °C. The cells were kept at the set temperature for at least 6 h before the cycling was started. The voltage and current during a section of a cycling period are shown in Fig. 2(a).

Table 1
Procedures applied during the initial characterization with experimental conditions.

Procedure	U_{cell}	ϑ
Electrochemical characterization	–	25 °C
Electrochemical characterization	–	10 °C
Temperature profile	3.7 V	–
Temperature profile	4.1 V	–
Temperature profile	3.3 V	–
Electrochemical characterization	–	25 °C
Galvanostatic intermittent titration technique	–	25 °C
Temperature profile	3.7 V	–

Table 2
Steps of the electrochemical characterization procedure.

Step	Parameter	Termination
CCCV Charge	$I = 1$C; $U = 4.1$ V	$I < 0.02$C
Pause	–	$t > 10$ min
CC Discharge	$I = 1$C	$U < 2.5$ V
Pause	–	$t > 10$ min
CCCV Charge	$I = 1$C; $U = 4.1$ V	$I < 0.02$C
Pause	–	$t > 10$ min
CC Discharge	$I = 0.2$C	$U < 2.5$ V
Pause	–	$t > 10$ min
CCCV Charge	$I = 1$C; $U = 4.1$ V	$I < 0.02$C
Pause	–	$t > 3$ h
CC Discharge (quasi-stationary OCV)	$I = 0.05$C	$U < 2.5$ V
Pause	–	$t > 3$ h
CC Charge (quasi-stationary OCV)	$I = 0.05$C	$U > 4.1$ V
Pause	–	$t > 10$ min
CCCV Charge	$I = 1$C; $U = 4.1$ V	$I < 0.02$C
Pause	–	$t > 10$ min
CCCV Discharge	$I = 1$C; $U = 3.7$ V	$I < 0.02$C
Pause	–	$t > 10$ min
CC Discharge (pulse)	$I = 1$C	$t > 20$ s
Pause	–	$t > 10$ min
CC Charge (pulse)	$I = 1$C	$t > 20$ s

2.7. Temperature profiles

During the temperature profiles, the cells were kept under open-circuit conditions while the temperature inside the climatic camber was set according to the following profile in order to study the influence of temperature on internal cell pressure. Each set temperature level was reached by a linear ramp of 1.5 h duration, and then kept for 2 h. The set temperatures were $\vartheta_{set} = \{ 25, 30, 40, 50, 40, 30, 20, 10, 0, -10, -20, -10, 0, 10, 20, 25\}$C. The set temperature during the procedure is shown in Fig. 2(c).

3. Results and discussion

3.1. Dependence of pressure on state of charge

The results of the GITT tests, where the gas pressure is measured at stationary conditions at different SOCs, are used to study the influence of the SOC on internal gas pressure. During the GITT tests performed as part of the initial characterization, an irreversible pressure rise due to gas formation or an irreversible change in electrode volume is likely to occur, as is discussed below in section 3.3. After cycling the cells for approximately one year, a significant irreversible pressure rise during the test with a duration of approximately 220 h can be excluded.

Therefore, the results of the GITT tests performed after cycling the cells are used for the analysis of pressure dependence on the SOC.

In Fig. 3 the change in internal cell pressure of cell A during the charging phase of the GITT measurement after cycling for 1215 equivalent full cycles at 25 °C is displayed. The difference in pressure at different SOCs is plotted against the pressure at 0 % SOC. The influence of differences in temperature can be excluded because of the long relaxation time at each SOC.

The internal gas pressure at stationary conditions exhibits a non-linear dependence on the SOC. There are three regions in the SOC range with different correlation between pressure and SOC change. In the lower SOC region (SOC < 36 %) the pressure strongly increases with increasing SOC. In the middle SOC range, the cell pressure slightly decreases with increasing SOC. In the upper SOC range (SOC > 72 %), the pressure again increases with increasing SOC.

The gas pressure inside the case of lithium-ion cells can basically be described by the ideal gas equation (1). The temperature of the system at the points of evaluation during the GITT measurement is constant and therefore can be excluded from being the cause of the change in pressure. The influence of the formation of additional gas during one cycle can be estimated from the results of the cycle aging experiments presented in section 3.3. During the last 89 equivalent full cycles before the GITT measurement, the internal pressure of cell A increases by only 0.87 kPa. The pressure increase per equivalent full cycle in this late stage of cycle life is therefore below 0.01 kPa assuming a linear approximation. The irreversible pressure increase is thus negligible compared to the reversible pressure change depicted in Fig. 3. There are also no reports of reversible gas formation/consumption depending on the SOC in the literature. This means that only a change in the free volume can lead to the change in pressure observed during the GITT measurement. We conclude that the change of pressure upon SOC variation is evoked by a change in the free volume inside the cell case. The free volume inside the cell case depends on the expansion of both the anode and the cathode, while the total volume inside the case stays constant, as a deformation of the rigid cell case is prevented by two steel plates bracing the cell.

Graphite exhibits a pronounced volume change during intercalation and deintercalation of lithium-ions. The change of the crystal structure of graphite during lithiation is a non-homogeneous process, whereby there are different phases inside the crystal depending on the degree of lithiation [18]. At low levels of lithiation, there are dilute, liquid-like phases usually referred to as 1L (lithium is randomly distributed in the graphite) [18], 4L, 3L and 2L, whereby the number refers to the number of unoccupied graphene layers in between partly lithiated graphene layers [19]. At higher degrees of lithiation, the dense, completely filled stages 2 (LiC_{12}) and stage 1 (LiC_6) [18] form. Graphite half cells significantly increase their volume until stage 2 starts to form [4,20]. The exact separation and description of the dilute graphite stages is still under discussion [21]. Therefore, graphite stages up to 2L are referred to as *dilute* and are not further distinguished within this study as they show an almost uniform volume increase during lithiation [4]. There is only a small volume increase in graphite during the dilute-2 phase transition, where both dilute phases and stage 2 coexist. During the 2-1 phase transition at high levels of lithiation, there is again a strong increase in unit cell volume of graphite [4,20,22]. The total unit cell volume change in between C_6 and LiC_6 is reported to be 13.2 % [4] while electrode thickness has been reported to vary by 7 % [22].

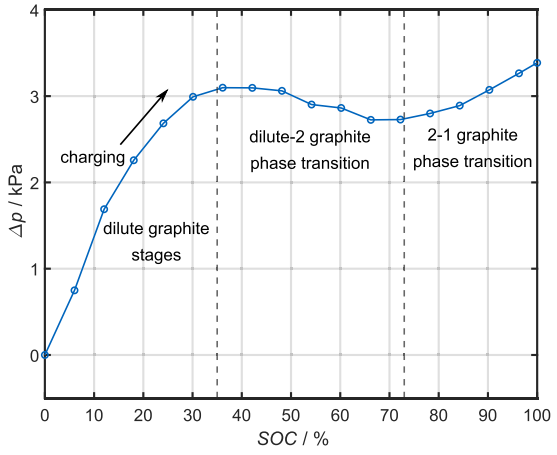

Fig. 3. Change of internal pressure of cell A during charging phase of GITT measurement after cycling for 1215 equivalent full cycles at 25 °C. The pressure difference of stationary pressures at different SOCs compared to the pressure at 0 % SOC is shown.

The unit cell volume of NMC-111 decreases during delithiation (charging the full cell). The decrease in unit cell volume during delithiation is small until a lithiation degree of about 30 % is reached [23–25]. The SOC dependence of gas pressure displayed in Fig. 3 is most likely due to the combination of the volume change at both electrodes. The pronounced increase in pressure during an SOC increase in the lower SOC range is presumably caused by the strong expansion of graphite during the filling of the dilute stages exceeding the shrinking of the cathode. In the middle SOC range, the graphite is in the dilute-2 phase transition regime where its volume stays almost constant during lithiation. The overall pressure decrease during charging is most likely dominated here by the decrease in cathode volume as discussed below. The increase in pressure during the SOC increase in the upper SOC range is presumably due to the pronounced increase in graphite volume while the graphite is in the 2-1 phase transition regime, which again exceeds the decrease in the cathode volume during delithiation. This qualitative form of dependence between internal cell pressure and SOC is observed for all investigated cells.

The same qualitative results regarding the SOC dependence of gas pressure are obtained when the change in gas pressure during the quasi-stationary OCV measurements - conducted as part of the characterization procedure at fixed intervals during cycle aging - are analyzed. The internal gas pressure during the quasi-stationary OCV measurements at all aging states is shown in Fig. 4(a and b).

In addition to this, the differential voltage change during discharging and charging is displayed in Fig. 4(c and d) so as to enable the further investigation of the correlation between pressure change and graphite staging. Differential voltage analysis can be used to analyze phase transitions of graphite [22]. SOC levels where one electrode consists of only one single phase (graphite stage) are observable as peaks in the DVA diagram. In between these peaks, the electrodes are in a phase transition where two phases of lithiation coexist. Both during charging and discharging, there is a pronounced peak in the $dU/dSOC$ curve in between 70 % and 80 % SOC. This peak corresponds to the SOC level where the graphite is in stage 2 (LiC_{12}). The location of stage 2 graphite peaks in the DVA diagrams in 4 (c,d) correspond well with the local minima of the pressure curves in 4 (a,b). At higher SOCs, the graphite is in the 2-1 phase transition; at lower SOCs, it is in the dilute-2 phase transition.

The different dilute stages are not clearly distinguishable in the DVA, but the onset of the dilute-2 phase transition is expected at a lithiation of 25 % [4,18,26]. Two distinct features of the differential voltage during charging depicted in Fig. 4(d) can be used to determine the lithiation degree of the graphite as a function of full cell SOC: The stage 2 peak (LiC_{12}) at 73 % SOC corresponds to a lithiation of the graphite of 50 % [27]. The distinct peak at 21 % is identified with stage 4 (LiC_{36}) and corresponds to a graphite lithiation of 16 % [27]. According to this correlation, a graphite lithiation of 25 % is reached at 35 % SOC. This corresponds well with the position of the local pressure maximum in Fig. 4(a and b). The local maximum of the pressure curve during charging is at a slightly higher SOC than for discharging, which might be

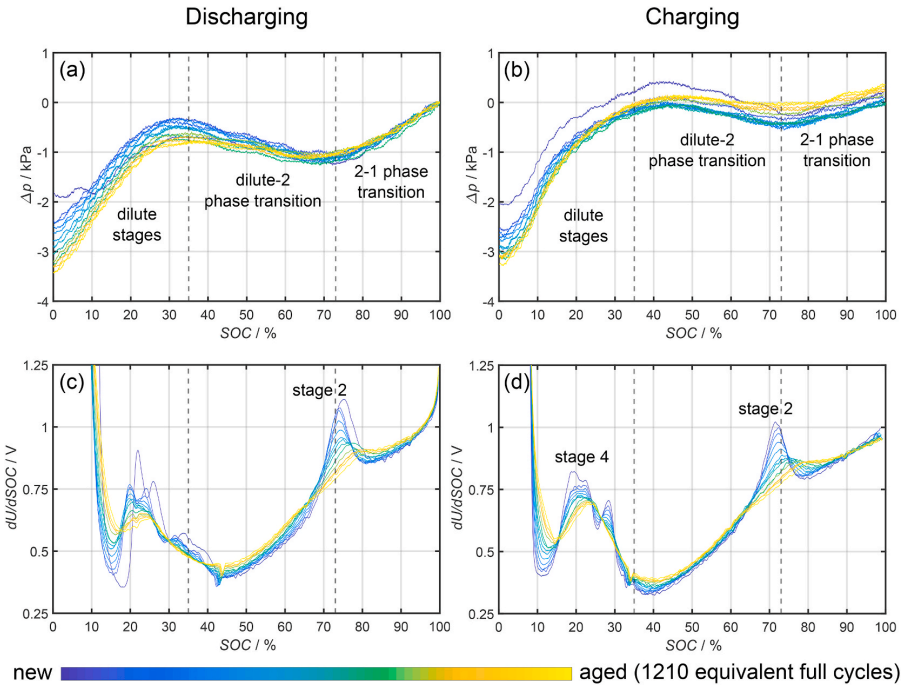

Fig. 4. Pressure and differential voltage during quasi-stationary OCV measurements as part of the characterization procedure of cell A at different aging states up to 1210 equivalent full cycles. The SOC for the different aging stages is calculated considering the actual capacity at the individual aging stage. (a) Pressure during discharging (difference compared to pressure at the beginning of discharging). (b) Pressure during charging (difference compared to pressure at the beginning of discharging). (c) Differential voltage during discharging. (d) Differential voltage during charging. The raw data of both pressure measurement and DVA has been smoothed using a moving average filter.

due to the fact that the cell is not at equilibrium conditions during the experiment. Similar forms of gas pressure dependence on SOC have been reported in the literature [6].

The correspondence between SOC and graphite lithiation established via DVA can also be used to carry out an assessment of the change in electrode volumes in the SOC range, where a decrease in pressure is observed during the GITT depicted in Fig. 3. The pressure decreases during charging in between 42.1 % SOC and 66.2 % SOC, which corresponds to an increase in graphite lithiation from 29.8 % to 45.6 %. During this change in lithiation, the average graphene inter-layer spacing is supposed to only increases by 0.29 % [28]. The relative volume increase can be assumed to be the same because the in-plane volume change of graphite is negligible compared to the volume change along the c-axis [26]. Knowing the lithiation of the graphite at these two SOC points also allows to calculate the cathode potential by adding the anode potential to the terminal voltage of the cell after relaxation. The full cell rest voltages at 42.1 % SOC and 66.2 % SOC are 3.677 V and 3.803 V respectively. The anode potential at the calculated levels of lithiation are 0.089 V and 0.076 V [28]. This means that the cathode potential increases from 3.766 V to 3.879 V. In this voltage range, the cathode volume is supposed to decrease by 0.327 $Å^3$ or 0.33 % [29]. The shrinking of the cathode thus exceeds the swelling of the graphite in the middle SOC range.

Fig. 4 also displays the progression of both pressure and differential voltage, depending on the aging state of the cell. The absolute pressure difference between the fully charged and the fully discharged state increases during aging. This can be explained by an irreversible increase in the amount of gas in the cell, or by irreversible electrode swelling, as will be discussed in section 3.3. The irreversible increase in the amount of gas or the irreversible increase in electrode volume presumably leads to a higher sensitivity of the pressure to changes in the free volume, according to the ideal gas equation. Apart from this, there are no significant changes in the form of the pressure curve during aging.

3.2. *Dependence of pressure on temperature*

In this section the results of pressure measurements during the temperature profiles applied at regular intervals throughout cycle aging are presented and discussed. In order to use pressure measurements for SOC or state of health (SOH) estimation, the influence of temperature changes on gas pressure during operation has to be separated from other effects. Therefore, knowledge of the influence of temperature on internal gas pressure is crucial for state estimation using internal gas pressure.

A linear dependence of gas pressure on temperature is expected from the ideal gas equation (1). In Fig. 5(a) the internal pressure of cell A measured during temperature profiles is plotted against the temperature at the cell surface. Only the data points during the cooling phase of the temperature profile are considered, in order to provide a similar temperature history for all data points. This procedure is necessary because the cell pressure does not completely reach stationary conditions during the 2 h of rest time at each set temperature, even while the temperature measured at the cell surface reaches steady values. The points in time that are used for the analysis are displayed in Fig. 2(c). The pressure inside the cell displayed in Fig. 5(a) is higher at elevated temperatures for all aging states, as is to be expected according to the ideal gas equation. The absolute values of pressure at all temperatures increase during aging, which will be discussed in section 3.3.

In Fig. 5(b) the difference quotients $\Delta p/\Delta T$ during the cooling phase are plotted as an approximation of the local slope of the curves in Fig. 5

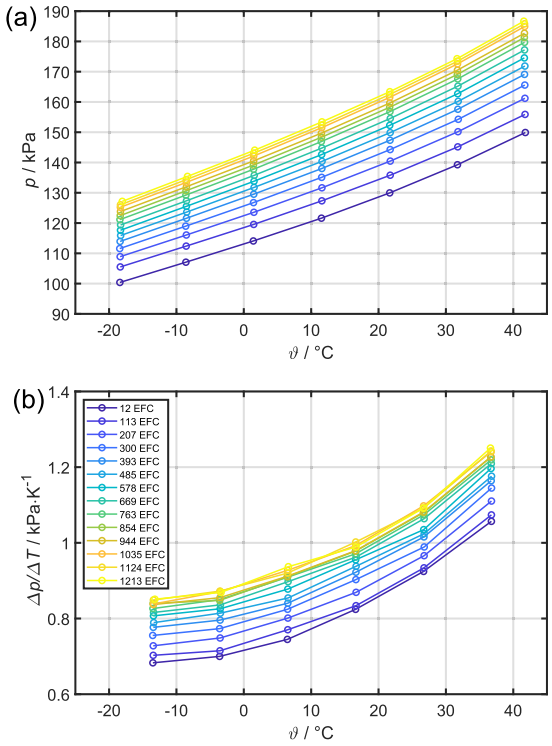

Fig. 5. Results of temperature profiles at different aging stages (number of equivalent full cycles (EFC) indicated in the legend) for cell A: (a) Pressure at stationary temperatures during the cooling phase of temperature profiles. (b) Local gradient of pressure change with temperature change (difference quotient) with the mean of two adjacent temperature measurements on the x-axis.

(a). The mean temperature of each two data points used to calculate the difference quotients is plotted on the x-axis. As shown in Fig. 5(b), the gradient of the correspondence between pressure and temperature is higher at elevated temperatures. The measurement data can therefore not be explained solely by a linear relationship between the two quantities, which would be expected from the gas equation. One effect that might be the cause of this non-linearity is the non-linear temperature dependence of the vapor pressure of the electrolyte, whose partial pressure also contributes to the total gas pressure [30]. In the investigated temperature range, pure DMC is reported to have vapor pressure of several kPa which would have a significant impact on the total pressure [31]. Another finding is that the slope of pressure change upon temperature variation increases during aging for the whole temperature range. This effect can be explained by an additional amount of gas in the cell, or by irreversible electrode swelling, as will be discussed in section 3.3. This might lead to a higher sensitivity of pressure to temperature change, according to the gas equation (1).

3.3. Irreversible pressure increase during cycle aging

Besides the reversible changes in gas pressure dependent on the SOC and temperature, the gas pressure irreversibly increases during cycle aging. In Fig. 6 the pressure of cell A in between cycle 100 and 200 is plotted as a typical example for the progression of pressure during cycling periods. At the beginning of each period, the pressure significantly increases by about 5 kPa and then shows a repeating pattern around a mean value for each cycle. The initial pressure increase is caused by the elevated battery temperature during cycling. The

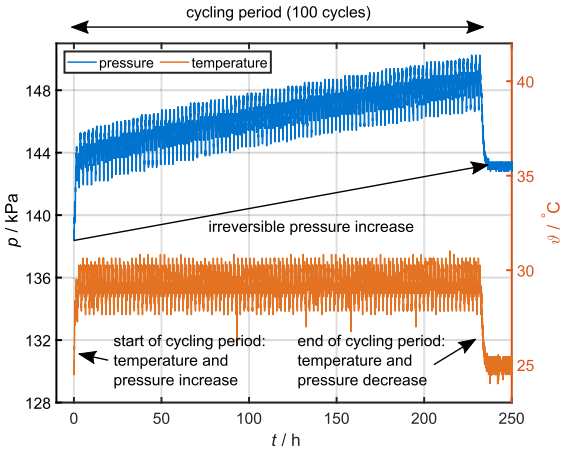

Fig. 6. Internal gas pressure of cell A during cycling at ambient temperature of 25 °C for the second period (cycle 100 to 200). At the end of the experiment there are several hours of rest under open-circuit conditions.

repeating pattern results from a superposition of temperature changes during the different phases of cycling, and changes in the overall electrode volume dependent on the SOC, as discussed in section 3.1.

In the course of a period of 100 cycles, the mean value of the periodic pattern of pressure increases. The window in which the temperature fluctuates during cycling stays the same after the second cycle, as shown in Fig. 6. Therefore, a long-term increase in temperature can be excluded as a cause of the pressure increase. When the cycling ends, the cell temperature approaches ambient temperature, and both cell temperature and pressure reach stable values after a couple of hours. The pressure at equilibrium conditions following the cycling is higher than before the cycling period, which means that the pressure irreversibly increases during cycling. The irreversible increase in gas pressure is probably mainly caused by an increase in the amount of gas inside the cell, as will be discussed below.

In Fig. 7(a) the cell capacity of the four investigated cells measured during the 0.05C CC discharging phase of the electrochemical characterization procedure at 25 °C is plotted against the charge throughput in equivalent full cycles. Low-current discharging is used for capacity measurement, in order to minimize the influence of impedance change on capacity measurement. All four cells show a decreasing trend in capacity. The rate of capacity decrease is large during the initial characterization (between the first and the second data point) and during the first cycling period (between the second and the third data point). In the remaining part of the cycling, the capacity decreases in an approximately linear fashion with regard to charge throughput.

Capacity progression during the main part of cycle life of lithium-ion cells with the same electrode materials as used in this study have been described as linear with regard to charge throughput, until the onset of accelerated aging at the end of the cell's cycle lifetime [32,33]. The approximately linear capacity decrease found during the main part of cycle aging in our measurements is therefore in accordance with the literature. No accelerated capacity fade at later aging states is observed in our experimental data, because the cells are only cycled until a capacity fade of up to 11 % where accelerated aging is not yet expected. The rate of capacity decrease does not depend on the ambient temperature during cycling. There are studies where a stronger capacity decrease is reported for very low (0 °C and below) and very high (40 °C and above) temperatures compared to the capacity decrease at mild temperatures in between these extremes for both cycle aging [32,34,35] and calendar aging [36,37]. The absence of temperature dependence of capacity fade in our experimental data is probably due to the fact that

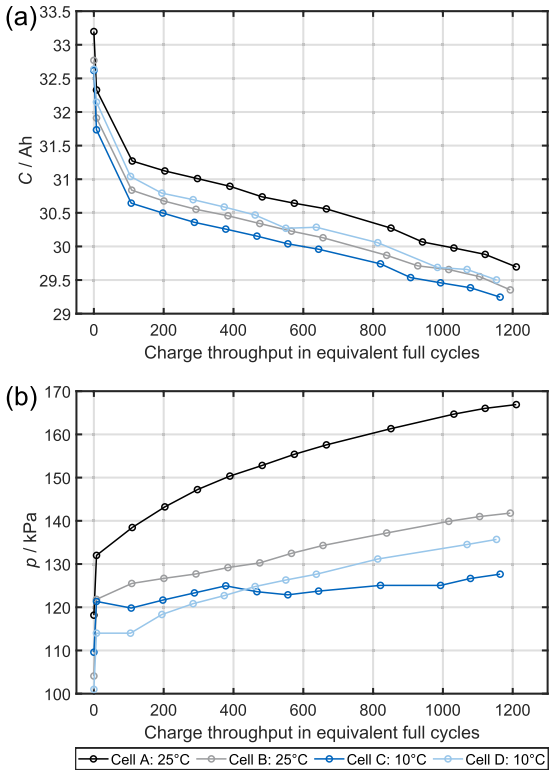

Fig. 7. (a) Capacity during 0.05C CC discharging phase of the electrochemical characterizations and (b) gas pressure inside the cells at the beginning of the electrochemical characterization periods at 3.7 V and 25 °C, both plotted versus charge throughput. The first data point of each graph refers to the pristine cell, the second data point to the status after the initial characterization, and the following data points to the recurring characterizations during cycle aging.

both temperatures applied during cycling are inside the optimal temperature window for this cell, and that no aging mechanisms caused by extremely low or high temperatures are triggered.

The gas pressure inside the cells at the beginning of each electrochemical characterization period at 25 °C is shown in Fig. 7(b). The mean value during a time period of 60 s at the beginning of the characterization procedure, where the cells have reached equilibrium conditions, is shown. All cells show a general trend towards rising pressure during cycling.

We assume that this irreversible increase in gas pressure is mainly caused by an increase in the amount of gas inside the cell. Gassing has been reported to be the main effect leading to an increase in pressure inside lithium-ion cells in literature [1–5]. Another effect which might contribute to the long-term increase of gas pressure is an irreversible increase in electrode volumes. During regular operation, the SEI on the graphite anode continuously grows, which might lead to an irreversible expansion of this cell component [38,39]. The magnitude of the irreversible overall thickness increase for cells with graphite anodes during long-term cycling is reported to be in the order of the reversible thickness change due to lithium intercalation [40,41]. If a similar behavior is assumed for the cells under investigation in our study, the magnitude of the contribution of irreversible electrode swelling towards the increase in pressure is similar to the magnitude of pressure differences due to reversible electrode swelling. The contribution of irreversible electrode swelling is therefore most probably in the order of a few kPa. As the total increase of pressure is in the order of tens of kPa, the contribution of irreversible electrode swelling is most probably small compared to the contribution of gassing. Irreversible lithium plating is also known to result in the irreversible expansion of NMC/graphite pouch cells [42,43] and to lead to the formation of comparably thick surface layers on the anode [44]. This could also affect long-term pressure progression, but we do not expect plating to occur during our experiments, because of the mild temperatures and low current rates applied during cycling.

A pronounced pressure increase in between the first and the second characterization can be observed for all cells in Fig. 7(b). The cells experienced a small amount of cycling in between these two measurements. In addition to that, they were exposed to three temperature profiles at different states of charge. The pressure increase can be attributed to the cycling during the first electrochemical characterization procedure at 25 °C and the electrochemical characterization procedure at 10 °C. This is assumed because the pressure values after the characterization procedure at 10 °C almost reach the values of the beginning of the second characterization procedure at 25 °C (second data point in Fig. 7(b)). The temperature profiles - including charging and discharging the cells to specific voltage levels - seem to have a minor impact on gassing. Strong gassing during the first formation cycle has been reported in literature [5,45]. Our results suggest that this pronounced gassing also continues for up to 7 more cycles after the formation cycle. Another possible explanation for the strong pressure increase during the first 7 cycles is the irreversible expansion of the graphite. Comparably strong irreversible graphite expansion during the first cycle has been reported in literature [20,39,46]. Reasons for this irreversible expansion are particle rearrangement [20] and solvent cointercalation during initial SEI formation [47].

When the pressure before and after the first cycling period is compared, the individual cells display varying behavior. This is probably due to tolerances in the cell manufacturing process. The pressure in cell A and B (both cycled at 25 °C) increases during the first cycling period. The pressure in cell D stays the same while the pressure in cell C even decreases. The pressure in cell C also decreases at later points during cycling, but still shows a trend towards long-term pressure increase. Apart from this, the pressure in the other cells continuously increases after the first cycling period. The rate of pressure increase falls with cycling for cell A. Similar behavior was reported in literature [1,2]. The pressure in cell B and D increases in an approximately linear fashion during cycling.

Similar to the rate of capacity decrease, the rate of pressure increase seems to be independent of the temperature during cycling. This suggests that the same aging mechanisms are dominant at both cycling temperatures. It should be noted, that there is a significant difference in the absolute value of pressure increase, even for cells cycled under the same condition. This might be due to differences in the free volume inside the custom-built cells, and could disguise differences in gas production depending on the ambient temperature during cycling. Differences in between the individual cells are probably also the cause for the differences in initial cell pressure at the beginning of the experiments.

In Fig. 8 the relative pressure increase is plotted against the relative capacity decrease. Two aging phases can be distinguished. In the first phase, corresponding to the initial characterization and the first cycling period, there is both a strong capacity loss and a significant pressure increase. As discussed before, this can be ascribed to ongoing formation processes. Beginning with the second cycling period, the two presented quantities exhibit an approximately linear correlation similar to results in the literature [1]. While all tested cells show the aforementioned correlation, the gradient of pressure increase with capacity loss differs between the cells. Differences in initial free volume are the most probable reason for this.

The correlation between the increase in gas pressure and capacity loss basically enables the usage of pressure measurements for SOH determination. A prerequisite to use measurements of the internal gas pressure for SOH estimation is that all cells of the same type show the

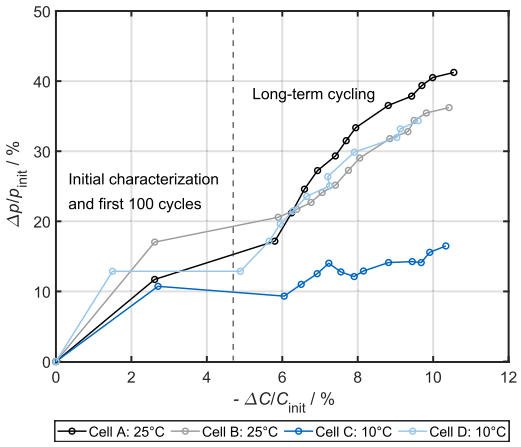

Fig. 8. The relative difference between pressure at the beginning of each electrochemical characterization and the pressure at the beginning of the first electrochemical characterization at 25 °C (pressure increase) plotted against the relative difference between capacity measured during the 0.05C CC discharging phase of each electrochemical characterization and the capacity measured during the first characterization (capacity loss).

same correlation between the increase in gas pressure and capacity loss. Further tests with cells that are manufactured with a higher degree of automation are necessary in order to evaluate if this prerequisite is fulfilled for commercial cells. We suggest the following approach for developing an algorithm that uses measurements of internal gas pressure for the estimation of the remaining cell capacity: First, the correlation between internal pressure increase and capacity decrease is determined through aging experiments in the laboratory in a similar way as presented in this work. Afterwards, the following algorithm could be implemented in the battery management system: Whenever the battery pack is at rest and thermal equilibrium conditions have approximately been reached, the internal gas pressure is measured. Then, influences of temperature and SOC on the gas pressure are considered by applying corrections to determine the gas pressure at the reference temperature and reference SOC, where the correlation between gas pressure and capacity has been recorded. In a last step, the predefined correlation between pressure and capacity is used to calculate the remaining capacity from the corrected gas pressure value.

4. Conclusion

As a key result of this study, we showed that measuring the internal gas pressure of large-format, prismatic lithium-ion cells with a built-in sensor over several hundreds of cycles is possible. Our results confirm the observations regarding pressure dependence on the SOC and aging in the literature, and show that they are transferable to large-format cells.

We found a non-linear relationship between the gas pressure inside prismatic lithium-ion cells with $LiNi_{1/3}Mn_{1/3}Co_{1/3}O_2$ cathodes and graphite anodes and the SOC. This effect is most likely due to the dependence of the volumes of the electrodes on the degree of lithiation. The difference in cell pressure between the fully charged and fully discharged state for the investigated prismatic cells of format PHEV2 is in the order of 3 kPa. In principle, this would qualify the gas pressure for an indicator for SOC estimation. A fundamental problem hindering the development of such methods is that the relationship between pressure and SOC is not monotone over the whole SOC range. Instead, the gas pressure over SOC curve has a local maximum in between 30 % and 40 % SOC and a local minimum in between 70 % and 80 % SOC, where the graphite anode is in stage 2. The methods would therefore be limited to the low SOC range where the pressure shows a monotone change with regard to the SOC.

Another main finding is that the gas pressure inside the cells has a non-linear relationship with temperature. The main part of the temperature dependence can be explained by the linear relationship between pressure and temperature according to the general gas equation. The deviations from the linear relationship are most likely caused by the temperature dependence of electrolyte vapor pressure. The influence of temperature on cell pressure, considering typical temperature fluctuations occurring in the battery packs of electric vehicles of several 10 K, would exceed the influence of the SOC on internal gas pressure by at least one order of magnitude. In order to achieve gas-pressure-measurement-based SOC estimation for such operating conditions, the influence of temperature needs to be compensated for, which requires a model description of the temperature dependence of pressure which is valid for all aging stages. The development of such models should be the subject of further research.

During long-term cycling, we observed an irreversible increase in gas pressure inside the cells over more than 1100 equivalent full cycles. The increase in gas pressure during cycle aging correlates with the loss of cell capacity after 100 cycles, when formation processes have completely decayed. For the remaining lifetime of the cell, the gas pressure therefore basically qualifies for an indicator for SOH estimation. A requirement for such estimation methods would be that all cells of the same type show the same rate of pressure increase upon capacity decrease. The influence of different aging conditions and calendar aging on pressure progression will be studied in our future research.

CRediT authorship contribution statement

Julius Schmitt: Conceptualization, Methodology, Validation, Formal analysis, Investigation, Writing - original draft, Writing - review & editing, Visualization. **Benjamin Kraft:** Conceptualization, Validation, Writing - review & editing. **Jan Philipp Schmidt:** Conceptualization, Writing - review & editing. **Betina Meir:** Validation, Writing - review & editing. **Klaus Elian:** Resources, Writing - review & editing. **David Ensling:** Resources, Writing - review & editing. **Goran Keser:** Resources, Writing - review & editing. **Andreas Jossen:** Writing - review & editing, Supervision, Project administration, Funding acquisition.

Declaration of competing interest

The authors declare that they have no known competing financial interests or personal relationships that could have appeared to influence the work reported in this paper.

Acknowledgments

This work was supported by the German Federal Ministry of Education and Research (grant number 03XP0027G). The responsibility for this publication lies with the authors.

References

[1] A. Matasso, D. Wong, D. Wetz, F. Liu, Correlation of bulk internal pressure rise and capacity degradation of commercial LiCoO2 cells, J. Electrochem. Soc. 161 (14) (2014) A2031–A2035, https://doi.org/10.1149/2.0221414jes.
[2] A. Matasso, D. Wong, D. Wetz, F. Liu, Effects of high-rate cycling on the bulk internal pressure rise and capacity degradation of commercial LiCoO2 cells, J. Electrochem. Soc. 162 (6) (2015) A885–A891, https://doi.org/10.1149/2.0461506jes.
[3] A. Schiele, T. Hatsukade, B.B. Berkes, P. Hartmann, T. Brezesinski, J. Janek, High-throughput in situ pressure analysis of lithium-ion batteries, Anal. Chem. 89 (15) (2017) 8122–8128, https://doi.org/10.1021/acs.analchem.7b01760.
[4] S. Schweidler, L. de Biasi, A. Schiele, P. Hartmann, T. Brezesinski, J. Janek, Volume changes of graphite anodes revisited: a combined operando X-ray diffraction and in situ pressure analysis study, J. Phys. Chem. C 122 (16) (2018) 8829–8835, https://doi.org/10.1021/acs.jpcc.8b01873.

[5] P. Lanz, H. Sommer, M. Schulz-Dobrick, P. Novák, Oxygen release from high-energy xLi2MnO3·(1−x)LiMO2 (M=Mn, Ni, Co): electrochemical, differential electrochemical mass spectrometric, in situ pressure, and in situ temperature characterization, Electrochim. Acta 93 (2013) 114–119, https://doi.org/10.1016/j.electacta.2013.01.105.
[6] A. Matasso, D. Wetz, F. Liu, The effects of internal pressure evolution on the aging of commercial Li-ion cells, J. Electrochem. Soc. 162 (1) (2015) A92–A97, https://doi.org/10.1149/2.0611501jes.
[7] A. Matasso, D. Wetz, F. Liu, The effects of internal pressure evolution on the aging of commercial Li-ion cells, ECS Trans. 58 (46) (2014) 37–44, https://doi.org/10.1149/05846.0037ecst.
[8] M.-S. Park, J.-W. Lee, W. Choi, D. Im, S.-G. Doo, K.-S. Park, On the surface modifications of high-voltage oxide cathodes for lithium-ion batteries: new insight and significant safety improvement, J. Mater. Chem. 20 (34) (2010) 7208–7213, https://doi.org/10.1039/c0jm00617c.
[9] D.J. Cuscueta, H.R. Salva, A.A. Ghilarducci, Inner pressure characterization of a sealed nickel-metal hydride cell, J. Power Sources 196 (8) (2011) 4067–4071, https://doi.org/10.1016/j.jpowsour.2010.11.131.
[10] J. Zhang, G. Shao, W. Guo, Y. Lou, B. Xia, Estimating the state of charge of MH-Ni batteries by measuring their stable internal pressure, J. Power Sources 343 (2017) 183–187, https://doi.org/10.1016/j.jpowsour.2017.01.031.
[11] A. Jozwiuk, B.B. Berkes, T. Weiß, H. Sommer, J. Janek, T. Brezesinski, The critical role of lithium nitrate in the gas evolution of lithium–sulfur batteries, Energy Environ. Sci. 9 (8) (2016) 2603–2608, https://doi.org/10.1039/C6EE00789A.
[12] M. Metzger, B. Strehle, S. Solchenbach, H.A. Gasteiger, Origin of H 2 evolution in LIBs: H 2 O reduction vs. Electrolyte oxidation, J. Electrochem. Soc. 163 (5) (2016) A798–A809, https://doi.org/10.1149/2.1151605jes.
[13] J. Self, C.P. Aiken, R. Petibon, J.R. Dahn, Survey of gas expansion in Li-ion NMC pouch cells, J. Electrochem. Soc. 162 (6) (2015) A796–A802, https://doi.org/10.1149/2.0081506jes.
[14] Y. Ma, L. Feng, C.-Y. Tang, J.-H. Ouyang, S.J. Dillon, Effects of commonly evolved solid-electrolyte-interphase (SEI) reaction product gases on the cycle life of Li-ion full cells, J. Electrochem. Soc. 165 (13) (2018) A3084–A3094, https://doi.org/10.1149/2.0691813jes.
[15] M. Metzger, B. Strehle, S. Solchenbach, H.A. Gasteiger, Hydrolysis of ethylene carbonate with water and hydroxide under battery operating conditions, J. Electrochem. Soc. 163 (7) (2016) A1219–A1225, https://doi.org/10.1149/2.0411607jes.
[16] Y. Kim, Mechanism of gas evolution from the cathode of lithium-ion batteries at the initial stage of high-temperature storage, J. Mater. Sci. 48 (24) (2013) 8547–8551, https://doi.org/10.1007/s10853-013-7673-2.
[17] R. Jung, M. Metzger, F. Maglia, C. Stinner, H.A. Gasteiger, Oxygen release and its effect on the cycling stability of LiNi x Mn y Co z O 2 (NMC) cathode materials for Li-ion batteries, J. Electrochem. Soc. 164 (7) (2017) A1361–A1377, https://doi.org/10.1149/2.0021707jes.
[18] J.R. Dahn, Phase diagram of LixC6, Phys. Rev. B 44 (17) (1991) 9170–9177, https://doi.org/10.1103/PhysRevB.44.9170.
[19] M. Heß, P. Novák, Shrinking annuli mechanism and stage-dependent rate capability of thin-layer graphite electrodes for lithium-ion batteries, Electrochim. Acta 106 (2013) 149–158, https://doi.org/10.1016/j.electacta.2013.05.056.
[20] M. Bauer, M. Wachtler, H. Stöwe, J.V. Persson, M.A. Danzer, Understanding the dilation and dilation relaxation behavior of graphite-based lithium-ion cells, J. Power Sources 317 (2016) 93–102, https://doi.org/10.1016/j.jpowsour.2016.03.078.
[21] A. Senyshyn, O. Dolotko, M.J. Mühlbauer, K. Nikolowski, H. Fuess, H. Ehrenberg, Lithium intercalation into graphitic carbons revisited: experimental evidence for twisted bilayer behavior, J. Electrochem. Soc. 160 (5) (2013) A3198–A3205, https://doi.org/10.1149/2.031305jes.
[22] B. Rieger, S. Schlueter, S.V. Erhard, J. Schmalz, G. Reinhart, A. Jossen, Multi-scale investigation of thickness changes in a commercial pouch type lithium-ion battery, J. Energy Storage 6 (2016) 213–221, https://doi.org/10.1016/j.est.2016.01.006.
[23] Y. Koyama, I. Tanaka, H. Adachi, Y. Makimura, T. Ohzuku, Crystal and electronic structures of superstructural Li1−x[Co1/3Ni1/3Mn1/3]O2 (0≤x≤1), J. Power Sources 119–121 (2003) 644–648, https://doi.org/10.1016/S0378-7753(03)00194-0.
[24] W.-S. Yoon, K.Y. Chung, J. McBreen, X.-Q. Yang, A comparative study on structural changes of LiCo1/3Ni1/3Mn1/3O2 and LiNi0.8Co0.15Al0.05O2 during first charge using in situ XRD, Electrochem. Commun. 8 (8) (2006) 1257–1262, https://doi.org/10.1016/j.elecom.2006.06.005.
[25] N. Yabuuchi, Y. Makimura, T. Ohzuku, Solid-state chemistry and electrochemistry of LiCo1/3Ni1/3Mn1/3O2 for advanced lithium-ion batteries, J. Power Sources 154 (4) (2007) A314, https://doi.org/10.1149/1.2455585.
[26] D. Billaud, F.X. Henry, M. Lelaurain, P. Willmann, Revisited structures of dense and dilute stage II lithium-graphite intercalation compounds, J. Phys. Chem. Solid. 57 (6–8) (1996) 775–781, https://doi.org/10.1016/0022-3697(95)00348-7.
[27] D. Allart, M. Montaru, H. Gualous, Model of lithium intercalation into graphite by potentiometric analysis with equilibrium and entropy change curves of graphite electrode, J. Electrochem. Soc. 165 (2) (2018) A380–A387, https://doi.org/10.1149/2.1251802jes.
[28] H. He, C. Huang, C.-W. Luo, J.-J. Liu, Z.-S. Chao, Dynamic study of Li intercalation into graphite by in situ high energy synchrotron XRD, Electrochim. Acta 92 (2013) 148–152, https://doi.org/10.1016/j.electacta.2012.12.135.
[29] L. de Biasi, A.O. Kondrakov, H. Geßwein, T. Brezesinski, P. Hartmann, J. Janek, Between Scylla and charybdis: balancing among structural stability and energy density of layered NCM cathode materials for advanced lithium-ion batteries, J. Phys. Chem. C 121 (47) (2017) 26163–26171, https://doi.org/10.1021/acs.jpcc.7b06363.
[30] P.T. Coman, S. Mátéfi-Tempfli, C.T. Veje, R.E. White, Modeling vaporization, gas generation and venting in Li-ion battery cells with a dimethyl carbonate electrolyte, J. Electrochem. Soc. 164 (9) (2017) A1858–A1865, https://doi.org/10.1149/2.0631709jes.
[31] W.V. Steele, R.D. Chirico, S.E. Knipmeyer, A. Nguyen, Vapor pressure, heat capacity, and density along the saturation line, measurements for cyclohexanol, 2-Cyclohexen-1-one, 1,2-dichloropropane, 1,4-di- tert -butylbenzene, (±)-2-Ethylhexanoic acid, 2-(methylamino)ethanol, perfluoro- n -heptane, and sulfolane, J. Chem. Eng. Data 42 (6) (1997) 1021–1036, https://doi.org/10.1021/je9701036.
[32] A. Maheshwari, M. Heck, M. Santarelli, Cycle aging studies of lithium nickel manganese cobalt oxide-based batteries using electrochemical impedance spectroscopy, Electrochim. Acta 273 (2018) 335–348, https://doi.org/10.1016/j.electacta.2018.04.045.
[33] S.F. Schuster, T. Bach, E. Fleder, J. Müller, M. Brand, G. Sextl, A. Jossen, Nonlinear aging characteristics of lithium-ion cells under different operational conditions, J. Energy Storage 1 (2015) 44–53, https://doi.org/10.1016/j.est.2015.05.003.
[34] J. Schmalstieg, S. Käbitz, M. Ecker, D.U. Sauer, A holistic aging model for Li (NiMnCo)O2 based 18650 lithium-ion batteries, J. Power Sources 257 (2014) 325–334, https://doi.org/10.1016/j.jpowsour.2014.02.012.
[35] T. Waldmann, M. Wilka, M. Kasper, M. Fleischhammer, M. Wohlfahrt-Mehrens, Temperature dependent ageing mechanisms in Lithium-ion batteries – a Post-Mortem study, J. Power Sources 262 (2014) 129–135, https://doi.org/10.1016/j.jpowsour.2014.03.112.
[36] J. Schmitt, A. Maheshwari, M. Heck, S. Lux, M. Vetter, Impedance change and capacity fade of lithium nickel manganese cobalt oxide-based batteries during calendar aging, J. Power Sources 353 (2017) 183–194, https://doi.org/10.1016/j.jpowsour.2017.03.090.
[37] P. Keil, S.F. Schuster, J. Wilhelm, J. Travi, A. Hauser, R.C. Karl, A. Jossen, Calendar aging of lithium-ion batteries, J. Electrochem. Soc. 163 (9) (2016) A1872–A1880, https://doi.org/10.1149/2.0411609jes.
[38] E.M.C. Jones, Ö.Ö. Çapraz, S.R. White, N.R. Sottos, Reversible and irreversible deformation mechanisms of composite graphite electrodes in lithium-ion batteries, J. Electrochem. Soc. 163 (9) (2016) A1965–A1974, https://doi.org/10.1149/2.0751609jes.
[39] J. Sturm, F.B. Spingler, B. Rieger, A. Rheinfeld, A. Jossen, Non-destructive detection of local aging in lithium-ion pouch cells by multi-directional laser scanning, J. Electrochem. Soc. 164 (7) (2017) A1342–A1351, https://doi.org/10.1149/2.0161707jes.
[40] J.H. Lee, H.M. Lee, S. Ahn, Battery dimensional changes occurring during charge/discharge cycles—thin rectangular lithium ion and polymer cells, J. Power Sources 119–121 (2003) 833–837, https://doi.org/10.1016/S0378-7753(03)00281-7.
[41] J. Cannarella, C.B. Arnold, Stress evolution and capacity fade in constrained lithium-ion pouch cells, J. Power Sources 245 (2014) 745–751, https://doi.org/10.1016/j.jpowsour.2013.06.165.
[42] B. Bitzer, A. Gruhle, A new method for detecting lithium plating by measuring the cell thickness, J. Power Sources 262 (2014) 297–302, https://doi.org/10.1016/j.jpowsour.2014.03.142.
[43] F.B. Spingler, W. Wittmann, J. Sturm, B. Rieger, A. Jossen, Optimum fast charging of lithium-ion pouch cells based on local volume expansion criteria, J. Power Sources 393 (2018) 152–160, https://doi.org/10.1016/j.jpowsour.2018.04.095.
[44] B. Rieger, S.F. Schuster, S.V. Erhard, P.J. Osswald, A. Rheinfeld, C. Willmann, A. Jossen, Multi-directional laser scanning as innovative method to detect local cell damage during fast charging of lithium-ion cells, J. Energy Storage 8 (2016) 1–5, https://doi.org/10.1016/j.est.2016.09.002.
[45] C.P. Aiken, J. Xia, D.Y. Wang, D.A. Stevens, S. Trussler, J.R. Dahn, An apparatus for the study of in situ gas evolution in Li-ion pouch cells, J. Electrochem. Soc. 161 (10) (2014) A1548–A1554, https://doi.org/10.1149/2.0151410jes.
[46] D. Sauerteig, S. Ivanov, H. Reinshagen, A. Bund, Reversible and irreversible dilation of lithium-ion battery electrodes investigated by in-situ dilatometry, J. Power Sources 342 (2017) 939–946, https://doi.org/10.1016/j.jpowsour.2016.12.121.
[47] J.O. Besenhard, M. Winter, J. Yang, W. Biberacher, Filming mechanism of lithium-carbon anodes in organic and inorganic electrolytes, J. Power Sources 54 (2) (1995) 228–231, https://doi.org/10.1016/0378-7753(94)02073-C.

4 Change in the shape of the open-circuit potential curve during cycle aging

The full-cell OCV curve is a fundamental model parameter for most methods for physical model-based SOH estimation (see section 2.3.2). It is also an important parameter for many models that are used to describe the electrical behavior of lithium-ion cells. The shape of the full-cell OCV curve changes during cell aging, which is a challenge for physical model-based SOH estimation. The change in the shape of the OCV curve needs to be considered in the models in order to provide accurate SOH estimates throughout aging.

The most popular way to model the change in the shape of the OCV curve of lithium-ion full-cells is the mechanistic modeling approach introduced by Dubarry et al. [25], which is described in section 2.2.2. In this modeling framework, the change in the shape of the full-cell OCV curve during aging is described by the degradation modes LAM_{an}, LAM_{cat} and LLI. The full-cell OCV curve of an aged cell can then be calculated based on the degradation modes and the shape of the half-cell OCP curves. For most electrode materials including graphite and most commonly used cathode materials, it is assumed, that the shape of the OCP curve, i.e., the relationship between lithiation degree of the electrode and its OCP, does not change during aging [26]. Thus, the half-cell OCP curve of pristine electrode material is used to calculate the full-cell OCV curves of aged cells. In the scope of this work, it is investigated, whether this hypothesis is also valid for blend electrodes containing both graphite and silicon, as well as for nickel-rich NMC-811. In this chapter, the results of the experimental investigation on the half-cell level are presented in section 4.1. In section 4.2 the consequences of the change in the shape of the half-cell OCP of SiC on the change in the shape of the full-cell OCV curve during aging are analyzed.

4.1 Aging-induced change in the shape of half-cell open-circuit potential curves

In the study presented in this section, the half-cell OCP curves of SiC and NMC-811 during cycle aging are investigated. Commercially available full-cells of the type INR18650-MJ1 built by LG Chem were cycled using CCCV charging and CC discharging at 25°C. This cell type was chosen for this study as it resembles a state-of-the-art high energy cell with a silicon-containing anode. The cycling was stopped after a different number of cycles for the individual cells, in order to obtain cells at different aging states. After the cycling had been stopped, the cells were opened under Argon atmosphere inside a glove box and several samples were extracted from both electrodes. Half-cells in the CR2032 coin-cell format containing a harvested electrode sample as working electrode and lithium metal foil as counter electrode were built subsequently. The half-cells were then cycled with a low current of approximately C/90 to obtain the quasi-stationary OCP curve of the electrode materials. In this way, the OCP curves of SiC and NMC-811 at different aging states were recorded.
The shape of the recorded OCP curves was generally similar for electrode samples extracted from the same full-cell. An exception to this is the low lithiated region of SiC during lithiation, where large deviations between the samples are found. A probable reason for this is inhomogeneity in the silicon distribution over the electrode sheet. Averaged OCP curves were used for the following analysis of the change in OCP curve shape during aging, in order to reduce the influence of uncontrollable differences in the coin-cell manufacturing process and to consider the inhomogeneity over the electrode sheet at least to some degree.
The half-cell OCP curves at different aging states are analyzed by direct comparison as well as by DVA and ICA. It is found that the shape of the OCP curve of SiC significantly changes during aging. The DV peaks corresponding to graphite stages shift to lower electrode SOC during aging and a smaller fraction of the electrode capacity is accessed at high electrode potentials. These findings are interpreted to be caused by a decrease in the electrode capacity fraction that is provided by the silicon. It is concluded that both graphite and silicon degrade during cycling, but the rate of capacity decrease is higher for the silicon, which leads to a change in the relative capacity contributions of both components. The changes in the OCP curve shape are more pronounced during delithiation, which is probably due to the hysteresis of the silicon.
No significant change in the shape of the OCP curve of NMC-811 during aging is found. Even though there is some variation between the DV and IC of the OCP curves at different aging stages, the differences do no exhibit a trend with aging and are probably due to uncontrollable influences of the electrode harvesting or coin-cell preparation process.
These results are relevant for modeling lithium-ion cells with SiC anodes during aging, as well as for physical model-based state estimation for this type of cells. In order to accurately model the change in the full-cell OCV curve of SiC containing cells during cycle aging, not only the changes in the overall electrode capacities and the electrode balancing, but also changes in the shape of the half-cell OCP curve should be considered. The results of this study help to better understand the aging of SiC blend anodes, which differs from the aging of classical graphite electrodes. The impact of the changes in the SiC half-cell OCP curve on the full-cell OCV curve were investigated in a subsequent study that is presented in section 4.2.

Publication notes

The article titled *Change in the half-cell open-circuit potential curves of silicon–graphite and nickel-rich lithium nickel manganese cobalt oxide during cycle aging* is presented in the following. The article was published in the Journal of Power Sources [46]. Parts of the results have been presented as an online presentation titled *Experimental investigation of the aging invariance of electrode open circuit voltage curves* in the scope of the Advanced Battery Power conference in April 2021.

Author contribution

The concept of the study was developed by Julius Schmitt and Markus Schindler. The experimental design was developed by Julius Schmitt and Markus Schindler. Markus Schindler conducted the experiments on full-cell level. Julius Schmitt and Markus Schindler carried out the cell openings, electrode harvesting, coin-cell manufacturing and measurements on half-cell level. The experimental data was analyzed and visualized by Julius Schmitt. Andreas Jossen supervised the related research projects as well as the scientific work presented in the article. The manuscript was written by Julius Schmitt and was edited by all authors. All authors discussed the data and commented on the results.

Change in the half-cell open-circuit potential curves of silicon–graphite and nickel-rich lithium nickel manganese cobalt oxide during cycle aging

Julius Schmitt, Markus Schindler and Andreas Jossen.

Journal of Power Sources 506 (1) (2021), p. 230240, DOI: 10.1016/j.jpowsour.2021.230240

Permanent weblink:
https://doi.org/10.1016/j.jpowsour.2021.230240

Journal of Power Sources 506 (2021) 230240

Contents lists available at ScienceDirect

Journal of Power Sources

journal homepage: www.elsevier.com/locate/jpowsour

Change in the half-cell open-circuit potential curves of silicon–graphite and nickel-rich lithium nickel manganese cobalt oxide during cycle aging

Julius Schmitt [a,*], Markus Schindler [a], Andreas Jossen [a,b]

[a] Technical University of Munich (TUM), Institute for Electrical Energy Storage Technology (EES), Arcisstraße 21, 80333 Munich, Germany
[b] Technical University of Munich (TUM), Munich School of Engineering (MSE), Lichtenbergstraße 4a, 85748 Garching, Germany

HIGHLIGHTS

- Half-cell OCP of Si-graphite and NMC-811 is measured at different aging stages.
- Several samples per electrode enable OCP averaging and quantification of deviations.
- The shape of the Si-graphite OCP curve changes during cycle aging.
- Change in Si-graphite OCP is due to reduced contribution of Si to electrode capacity.
- The shape of the NMC-811 OCP curve stays similar during cycle aging.

ARTICLE INFO

Keywords:
Lithium-ion battery
Cycle aging
Half-cell open-circuit potential
silicon–graphite
NMC-811

ABSTRACT

The relationship between the degree of lithiation and open-circuit potential (OCP) of the half-cells of lithium-ion batteries is mostly regarded to be invariant during battery aging. In electrical cell modeling, the OCP curve of aged half-cells is therefore usually obtained by linear scaling of OCP curves measured for pristine electrodes. In this study, the aging invariance of the shape of both half-cell OCP curves of a commercial NMC-811/silicon–graphite cell is investigated experimentally. Full-cells are cycled until different degradation levels are reached. Subsequently, several electrode samples are extracted and the OCP of both electrodes is measured using coin-cells containing electrode samples as working electrode and lithium metal foil as counter electrode. Changes in half-cell OCP are analyzed using differential voltage analysis and incremental capacity analysis. The OCP of the NMC-811 does not change with aging, while the OCP of silicon–graphite exhibits changes which are mainly due to a decrease in the relative capacity contribution of the silicon. The main consequence of our findings is, that changes in the shape of the OCP curve of silicon–graphite during cycle aging should be considered in electrical battery models which are used for full-cell aging diagnostics and state estimation algorithms in battery management systems.

1. Introduction

Degradation processes occurring in lithium-ion batteries during operation and storage result in a reduction of the available energy and power that can be delivered by the battery [1–9]. In addition to this, the degradation also leads to a significant change in the relationship between open-circuit potential (OCP) and state of charge (SOC), which has been the subject of many studies mainly motivated by two aspects: Firstly, monitoring this change can be used as a non-destructive method to investigate the occurrence of different degradation mechanisms [2,7,8,10–15] and to enable more sophisticated state of health (SOH) estimation [16]. When it is possible to assign degradation to a single electrode, the SOH can be defined and monitored on the electrode level eventually enabling advanced control algorithms for optimized cell operation [17]. Secondly, knowing the relationship between OCP and SOC with high accuracy during the whole lifetime of a battery is a prerequisite for many methods of state estimation [18–20]. Therefore, a lot of research has been devoted to the development of methods for adjusting the OCP to SOC relationship during battery aging [11,13,21–23].

A common approach reducing the complexity in describing cell aging is to cluster individual aging mechanisms that lead to the same characteristic changes in cell OCP to so called degradation modes [11,13,14,21,24]. The most important degradation modes are loss of lithium

* Corresponding author.
E-mail address: julius.schmitt@tum.de (J. Schmitt).

https://doi.org/10.1016/j.jpowsour.2021.230240
Received 6 April 2021; Received in revised form 2 June 2021; Accepted 1 July 2021

inventory (LLI), loss of anode active material (LAM_A) and loss of cathode active material (LAM_C) [11,24]. In a full-cell OCP model consisting of two half-cell OCP curves, LLI results in a shift of the relative position of the anode half-cell curve compared to the cathode half-cell curve [11,24]. LAM is usually treated as a linear scaling of the individual half-cell curves resembling the fact that the individual electrodes can store less lithium but otherwise do not change their properties. The point of the curve which is fixed during this scaling depends on whether degradation occurs while the electrode is lithiated or delithiated [11,24]. This general framework of describing battery degradation via aging modes resulting in a superposition of shifting and linear scaling of half-cell OCP curves has been used in many studies as a tool to extract information on degradation mechanisms from full-cell quasi-stationary OCP curves [2,7,11,13,14,21,24]. It has also be used to simulate the change in OCP during aging [25].

In all of these studies, the shape of the half-cell OCP curves is assumed to be invariant during aging and therefore the aged half-cell OCP is calculated by linear scaling of the pristine half-cell OCP curve. There are only few studies investigating this assumption experimentally: Schmidt et al. showed that the predicted change in full-cell OCP due to LLI and LAM_C can be experimentally validated if these aging modes are artificially evoked during cell preparation [26]. Later, Birkl et al. presented an experimental validation also for the other aging modes using electrode sample manipulation [24].

The effect of cycle aging on the shape of half-cell OCP curves has also been investigated by cycling full-cells and characterizing electrode samples harvested from the aged cells [10,12,27–29]. Only minor deviations in the shape of the OCP curve have been reported for graphite anodes [10,12]. However, much larger alterations of the OCP curve shape have been found for blend anodes consisting of graphite and silicon. These alterations of the curve shape are associated with a faster degradation of the silicon in comparison to the graphite [27–29]. Anseán et al. recently presented a method to construct the OCP of blended silicon–graphite (SiG) electrodes based on the OCP curves of their components [30].

There are only few studies where a change in the shape of the NMC OCP curve during full-cell cycling is investigated experimentally [29,31–33]. Lee et al. presented an algorithm to extract the half-cell OCP curves from full-cell low-current charging data and showed that adapting the shape of the cathode OCP curve for aged cells leads to an improvement in the accuracy of the full-cell OCP which they reconstructed from the half-cell OCP curves [22].

The aim of this study is to experimentally investigate changes in the shape of the electrode OCP curves of blended silicon–graphite anodes and NMC-811 cathodes during cycle aging. We therefore cycle commercial cylindrical cells containing these electrode materials and open them at different aging stages to harvest electrode samples. By cycling the electrodes in the full-cell configuration, we ensure that the electrode degradation occurs in a setting similar to an application. We finally measure the half-cell OCP of the harvested samples in coin-cell configuration vs. lithium metal foil.

Our work is distinguished to former studies in two aspects: Firstly, we perform electrode characterization at multiple aging stages allowing an analysis of the change in half-cell OCP as a function of full-cell charge throughput, i.e., number of equivalent full cycles in full-cell configuration. Secondly, we base our results on measurements of several electrode samples taken from one electrode. This allows us to give an estimation of the accuracy of the method, reduces the influence of uncontrollable processes during sample extraction and coin-cell manufacturing, and provides a possibility to take into account spatial inhomogeneity of the electrodes [34,35].

2. Experimental

2.1. Investigated cells

In this study, commercially available cylindrical cells of the type INR18650-MJ1 from LG Chem were investigated. The cells have a nominal minimum capacity of 3.35 Ah according to the manufacturer. C-rates used to operate full-cells are always given with respect to this capacity in this work. Sturm et al. showed that the cathode of this high-energy cells is based on nickel-rich NMC-811 while the anode is based on a combination of graphite and silicon with a silicon fraction of ca. 3.5 wt.% [36]. Based on the dimensions of the double-side coated electrodes of this cell, which are 5.8×61.5 cm [36], the nominal areal capacity of the electrodes corresponds to 4.7 mAh /cm^2 per side. This cell type was chosen for this study because it contains state-of the-art electrode materials and the process for extracting electrode samples and manufacturing coin-cells using electrode material from this cell type has been optimized previously at our institute [36].

2.2. Cycle aging and electrochemical characterization of cylindrical full-cells

After delivery, all cells were initially tested according to a series of procedures, internally standardized at our institute [37–39]. This standardized initial characterization is conducted to gain information on the long-term development of cell parameters of this type of commercial cells [37]. Eight cells were randomly chosen for the experiments which are presented in this study. They are referred to as cell #1–8.

A schematic overview of the experimental procedure excluding the initial characterization is shown in Fig. 1(a). An HRT-M10 battery test system from Battery Dynamics (Germany) was used for characterizing and cycling the full-cells. The cells were kept at 25 °C inside an MK53 climatic chamber from BINDER (Germany) during the experiments. The voltage limits recommended by the cell manufacturer, i.e., $U_{min} = 2.5$ V and $U_{max} = 4.2$ V, were used for all tests. First, a capacity checkup consisting of two CCCV cycles ($I_{dch} = 0.2$ C, $I_{ch} = 0.5$ C, $I_{cutoff} = 50$ mA for both charging and discharging) was conducted. Then, a low-current CCCV cycle to determine the quasi-stationary OCP was applied. The current for both charging and discharging was set to 0.033 C, the cut-off current was 0.001 C and a 6 h pause followed each CV phase. Cells #2–8 were then cycled for up to 550 cycles consisting of 1 C CC discharge and 0.5 C CCCV charge steps with $I_{cutoff} = 0.03$ C. A pause of 30 min duration followed each discharge and charge step. The cycling was terminated after a different number of cycles for each cell (see Table 1) in order to have cells at different aging stages for the following characterization procedures and the subsequent electrode sample extraction. The individual number of cycles was defined for each cell at the beginning of the cycling period and was not influenced by the aging progress an individual cell exhibited during the cycling period.

After the cycling, another quasi-stationary OCP measurement and a galvanostatic titration technique (GITT) measurement were conducted. For cells #2, 3, and 4 there was an additional capacity checkup before the quasi-stationary OCP measurement after the cycling period, which was not applied to the other cells. Finally, the cells were CCCV discharged to 3 V with 0.5 C and $I_{cutoff} = 0.115$ C and then opened.

Cell #1 was used as a reference in this study. After the initial characterization described in [37], it was subject to five CC cycles and two CCCV cycles according to the specifications presented in [37]. It was then characterized using the same procedures as the other cells (capacity checkup, quasi-stationary OCP measurement, GITT). Subsequently, it was discharged and opened without any further cycling.

The total charge throughput until the opening of the cells $Q_{opening}$ is used as a measure for the aging stress applied to the cells. It is given in equivalent full cycles (EFC) with one EFC corresponding to a charge throughput of twice the nominal capacity, equivalent to

Table 1
Overview of parameters of the investigated cells. Cycles corresponds to the number of nominal cycles applied during the cycling period. For cell #1 only one quasi-stationary OCP measurement was conducted in full-cell configuration, therefore C_{EOL} is equal to C_{BOL}.

Cell #	Cycles	$Q_{opening}$/EFC	C_{BOL}/Ah	C_{EOL}/Ah	SOH_{EOL}/%
1	0	11.2	3.4139	3.4139	100
2	50	56.0	3.4715	3.3636	96.9
3	100	103.1	3.4809	3.3218	95.4
4	200	195.4	3.4815	3.2556	93.5
5	400	363.1	3.4856	3.0704	88.1
6	450	411.4	3.4936	3.1139	89.1
7	500	445.5	3.4913	3.0602	87.7
8	550	487.5	3.4885	2.9974	85.9

charging and discharging the cell by the nominal capacity. For the cell under investigation with a nominal capacity of 3.35 Ah, this means that one EFC equals 6.7 Ah. The charge throughput during the standard initial characterization is excluded for the calculation of $Q_{opening}$.

2.3. Cell opening and manufacturing of coin-cells

After being discharged to 3 V, the cells were opened inside an Argon-filled glove box (M. Braun Inertgas-Systeme, Germany). The electrodes were partially unrolled and the section between 6 cm and 18 cm measured from the beginning of the double-side coated area at the outer end of the electrode jelly-roll was cut out. A schematic side view and a top view of a harvested silicon–graphite electrode are shown in Figs. 1(b) and 1(c) to illustrate the position on the jelly-roll where the samples were extracted. The same position was chosen for sample extraction on the cathode but with the difference that there was no single-coated area at the outer end of the jelly-roll. The electrode sections were then fixed on a glass plate using adhesive tape as suggested in the literature [40] with the originally inward facing side (in the rolled up configuration) now being on top. The coating on the side now facing the top was removed by both mechanical abrasion using a scalpel and applying a solvent. Diethyl carbonate (DEC, 99 %, Merck) was used as solvent to remove anode coating while N-methyl-2-pyrrolidone (NMP, 99.5%, Sigma-Aldrich) was used to remove the cathode coating. Subsequently, six circular samples with 14 mm diameter were punched from the middle of the electrode section.

Half-cells in the CR2032 coin-cell format with lithium metal foil as anode were built with the SiG samples under Argon atmosphere following the procedure presented in [36]. Inside the housing the cells contained a stack consisting of a 0.5 mm aluminum spacer, a circular piece of lithium metal foil (15.6 mm diameter, 250 µm thickness), two glass fiber separators (16 mm diameter, 260 µm thickness each, VWR, type 691) filled with 90 µl of 1 M $LiPF_6$ in 3:7 (wt:wt) ethylene carbonate (EC)/ethyl methyl carbonate (EMC) electrolyte (LP57, 99.9%, Solvionic, France), a SiG sample, a 1 mm aluminum spacer, and a spring. A schematic of the coin-cell stack is shown in Fig. 1(d).

The cathode samples were wetted under vacuum in a pressure chamber (Harro Höflinger Verpackungsmaschinen, Germany) within the glove box as suggested by Sturm et al. [36] in order to properly fill the low porous electrode with electrolyte. The pressure profile shown in Table 2 was used for the wetting process. Afterwards, half-cells in coin-cell format were built with the cathode samples following the same procedure as for the anode samples with the exception that only 70 µl of LP57 were added.

2.4. Characterization of coin-cells

The coin-cells were put into a climatic chamber at 25 °C and connected to a CTS battery test system from Basytec (Germany). First, the cells were kept at open-circuit conditions for 12 h to allow the electrolyte to fully soak into the separator disks and electrode samples. Afterwards, the quasi-stationary OCP was obtained by cycling the coin-cells at low-current rates. First, the cells were discharged (lithiation of the harvested electrode sample) with a current of 160 µA until the lower cut-off voltage was reached. Afterwards, they were fully charged (delithiation of the harvested sample) with a current of 80 µA until the upper cut-off voltage was reached and subsequently fully discharged with a current of 80 µA until the lower cut-off voltage was reached again. The last two steps were repeated once to have two full cycles in total after the initial discharge step. Based on the nominal areal capacity and the electrode sample area of 1.54 cm^2, the coin-cell capacity is estimated to be 7.2 mAh. The current therefore corresponds to a current rate of approximately C/90. The coin-cells containing NMC-811 were cycled between 3.0 V and 4.3 V, the coin-cells containing SiG between 0.01 V and 1.7 V. Due to a technical problem, the half-cell measurements with the samples taken from cell #4 were not carried out correctly. These measurements are therefore exclude from the analysis.

3. Results and discussion

3.1. Full-cell degradation during cycling

In Table 1 an overview on the parameters of the individual full-cells is given including the total charge throughput $Q_{opening}$ the cells have experienced until they were opened. The capacity measured during the quasi-stationary OCP measurement (CCCV discharging) conducted at begin of life (BOL) C_{BOL} is also listed in Table 1. C_{BOL} of cell #1 is slightly smaller than the mean C_{BOL} of the other cells although it comes from the same production batch. This is probably due to two reasons: Firstly, the cell experienced some additional cycling compared to the other cells corresponding to 6.9 equivalent full cycles before the characterization was conducted. Secondly, the tests with cell #1 were conducted 205 days after the beginning of the tests with the other cells. Therefore, there might be some additional calendar aging affecting cell #1 even though it was stored at 4 °C during this time.

The capacity of cells #2 to 8 decreases during the cycling period as depicted in Fig. 2 where the CC discharge capacity extracted during the single cycles is plotted as a function of the charge throughput during cycling $C_{cycling}$. The rate of capacity decrease does not stay constant for the individual cells during the whole cycling period but changes during aging even though the experimental conditions stay the same. Despite the fact that the cells show no significant difference in capacity at BOL and are exposed to the same aging conditions, their capacities exhibit an increasing spread during aging as the individual cell capacities decrease at different rates. Production related differences inside the cells leading to an intrinsic difference in their aging behavior are the most probable reason for this. Production related differences in the calendar aging rate have been reported for this cell type before [38].

The SOH of the cells determined during the quasi-stationary OCP measurement at the end of life (EOL) just prior to the cell opening is lower for cells that have been cycled for a larger number of cycles as depicted in Table 1. The SOH is here defined as the ratio between the CCCV discharge capacity during the quasi-stationary OCP measurement after the cycling period C_{EOL} (also shown in Table 1) and the CCCV discharge capacity during the quasi-stationary OCP measurement before the cycling period C_{BOL}. The only exception to this trend is cell #5 which has a lower SOH at EOL than cell #6 even though it experienced less cycling. As discussed before, this is probably due to production related differences in the cells leading to different individual aging behavior. Despite these differences in individual aging behavior, the differences in SOH after the cycling period show that the cells are aged to different degrees at the point of cell opening. Therefore the electrodes should also be in different aging states, thus allowing an analysis of the influence of cycle aging on the open-circuit potential curve of the electrodes.

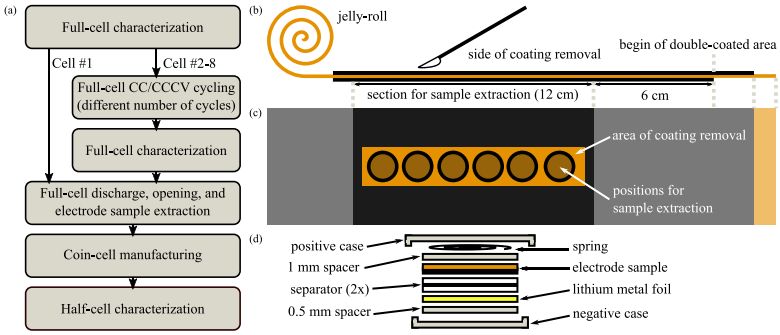

Fig. 1. (a) Overview on the experimental procedure. (b) Schematic side view of a harvested silicon–graphite electrode. (c) Schematic top view of a harvested silicon–graphite electrode. (d) Schematic side view of a coin-cell stack.

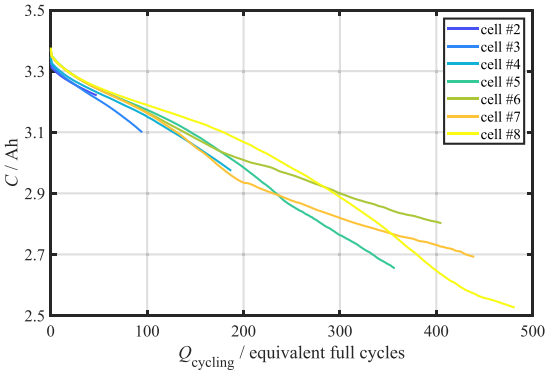

Fig. 2. Development of the full-cell discharge capacity during the cycling period (1 C CC discharging and 0.5 C CCCV charging at 25 °C) as function of the charge throughput during the cycling period.

Table 2
Pressure profile used for wetting the cathode samples.

Step	Pressure/mbar	Duration/s
Vacuum I	12	10
Release I	60	10
Vacuum II	22	20
Release II	80	10
Vacuum III	32	10
Wetting	32	1

3.2. Reproducibility of half-cell open-circuit potential measurements using coin-cells

The quasi-stationary OCP curves obtained from several coin-cells built with material from the same electrode exhibit certain differences between each other. There are probably two main reasons for these differences. Firstly, it might be possible that the electrode is inhomogeneous [35] to some degree and therefore the individual samples taken from one electrode also differ to some degree. Secondly, the manual handling steps during sample extraction and coin-cell preparation could introduce small differences between the individual coin-cells even if all steps were carried out with high thoroughness.

A quantitative measure for the differences between the OCP curves obtained from the coin-cells built from one electrode can be defined as the mean standard deviation over the whole SOC range σ_{OCP}, which is calculated according to

$$\sigma_{OCP} = \frac{1}{N_{step}} \cdot \sum_{i=1}^{N_{step}} \sqrt{\frac{1}{N_{coin}-1} \sum_{j=1}^{N_{coin}} (U_{ij} - \overline{U}_i)^2} \quad (1)$$

where N_{step} is the number of equally spaced points of the SOC range at which the measured curves are interpolated for comparison (here $N_{step} = 2800$), N_{coin} is the number of working coin-cells built from one electrode of the full-cell, U_{ij} is the quasi-stationary OCP of the jth coin-cell at the ith SOC interpolation point and $\overline{U}_i$ is the arithmetic mean of the OCP at the ith SOC interpolation point of the coin-cells built from the same electrode. In Table 3 σ_{OCP} is listed for all sets of coin-cells for the first and second low-current charging and discharging step. The sets of coin-cells used for this analysis consist of different numbers of coin-cells, which are also listed in Table 3, because some of the coin-cells did not work properly and were therefore excluded.

The mean σ_{OCP} is lower for the first quasi-stationary cycle iteration for both electrode types and current directions as indicated in Table 3. The shape of the quasi-stationary OCP obtained during the first and the second low-current cycle is similar for most coin-cells. We draw the conclusion that the first cycle is better suited to analyze the change in electrode OCP due to the following reasons: Firstly, the influence of additional degradation in the coin-cell configuration during the OCP measurement, which takes approximately eight days per cycle, is minimized. Secondly, the lower mean σ_{OCP} obtained during the first cycle indicates a higher reproducibility of the results. Therefore, we use only the OCP curves obtained during the first low-current cycle applied to the coin-cells for the further analysis in the scope of this study. Besides that, we want to emphasize that the σ_{OCP} values shown in Table 3 do not exhibit a trend during the progress of the full-cell cycling which shows that our method is suitable to measure the half-cell OCP of both pristine and aged cells.

For the analysis of the change in the shape of the electrode OCP curves, averaged quasi-stationary OCP curves are used in the following sections. For the averaging, the quasi-stationary OCP curves measured for the individual coin-cells built from one electrode are linearly interpolated at 2800 equally spaced SOC points and the arithmetic mean of all curves is treated as the averaged OCP at this SOC. The aim of this averaging is to reduce the influence of non-controllable, statistical variations induced by the manual coin-cell manufacturing and thereby enhancing the reproducibility of the averaged results. In addition to that, by using averaged OCP curves, possible inhomogeneity in radial direction of the jelly-roll is considered at least to some extent and therefore the averaged results might resemble the actual situation in a large size electrode better than just looking at the results obtained from one comparably small fraction of the electrode. Contrariwise, it has to be stated that due to the averaging, the sharpness of voltage steps observed in the curve is reduced but which might actually resemble the OCP curve of an inhomogeneous electrode [35].

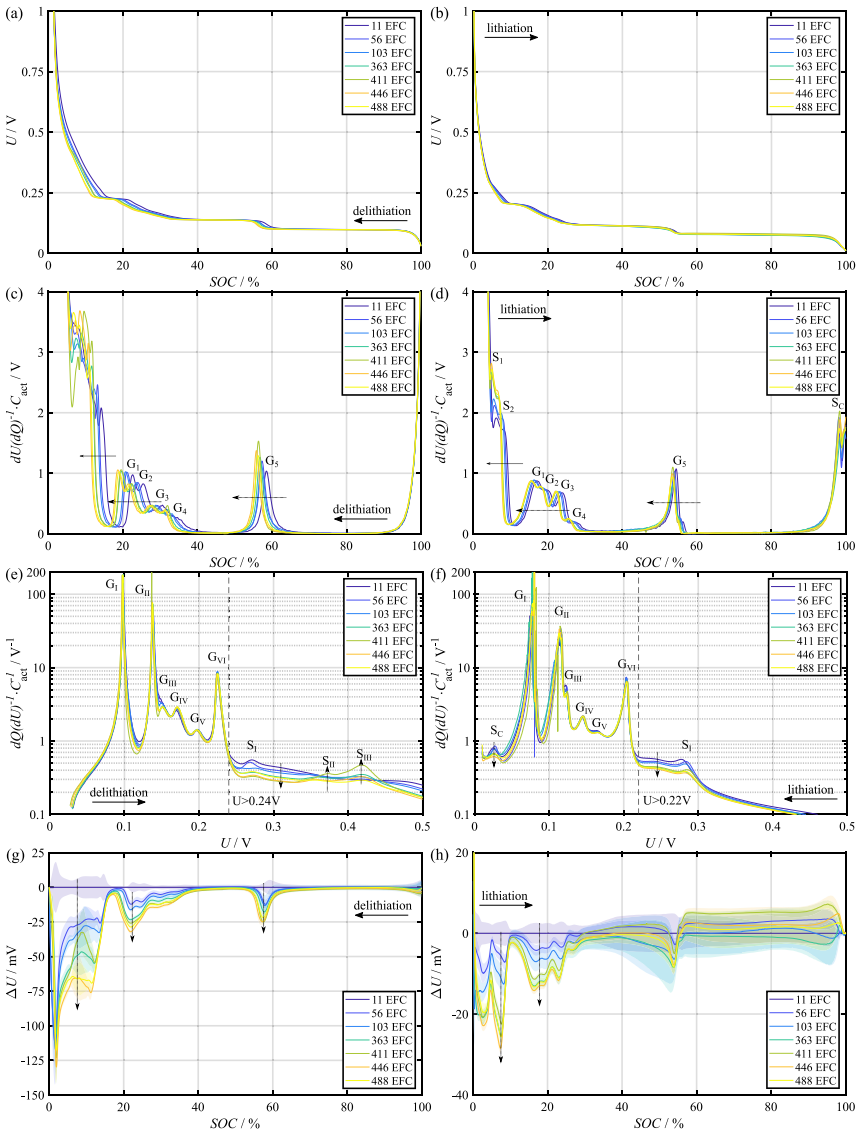

Fig. 3. First row: Mean quasi-stationary OCP vs. Li/Li^+ during (a) delithiation and (b) lithiation of the silicon–graphite samples extracted from full-cells that have been cycled for the number of equivalent full cycles indicated in the legend. Second row: Differential voltage during (c) delithiation and (d) lithiation of the silicon–graphite samples calculated based on the averaged OCP curves. The differential voltage values are normalized by multiplying with the actual capacity during the respective (dis-)charging step C_{act} and smoothed using a moving average filter. Third row: Incremental capacity during (e) delithiation and (f) lithiation of the silicon–graphite samples calculated based on the averaged OCP curves and plotted against cell voltage vs. Li/Li^+. The incremental capacity values are normalized by multiplying with the inverse of the actual capacity during the respective (dis-)charging step C_{act} and smoothed using a moving average filter. Fourth row: Difference between mean OCP of aged silicon–graphite samples and mean OCP of pristine silicon–graphite samples during (g) delithiation and (h) lithiation. The standard deviation between the OCP of the single samples harvested from the same electrode is shown as shaded area.

3.3. Change in the silicon–graphite delithiation open-circuit potential curve during cycle aging

In Figs. 3(a) and 3(b) the mean voltage curves obtained during the first delithiation and lithiation step applied to the coin-cells containing SiG samples from full-cells at different aging stages are displayed. The electrode SOC plotted on the *x*-axis is based on the actual coin-cell capacity at the respective aging stage. The shape of the voltage curves and their change is analyzed using differential voltage analysis (DVA), which is commonly used to identify phase transitions during delithiation and lithiation of electrodes [9,12,41]. The differential voltage (DV) as a function of the electrode SOC is displayed in Fig. 3(c) for delithiation and in Fig. 3(d) for lithiation of the SiG. The DV is normalized by multiplying by the actual coin-cell capacity C_{act} during the (dis-)charge step.

During the (de-)lithiation of graphite, different crystallographic phases, so-called stages, form in the graphite [42–47]. The central peak G_5 in Fig. 3(c) is located at SOC = 58.5% for cell #1 (11 EFC)

Table 3
Mean standard deviation of the OCP of the coin-cells built from one electrode over the whole SOC range (σ_{OCP}) measured during the first and the second low-current CC charging and discharging step.

Electrode	SiG					NMC-811				
Full-cell #	N_{coin}	σ_{OCP} 1st ch./mV	σ_{OCP} 2nd ch./mV	σ_{OCP} 1st dch./mV	σ_{OCP} 2nd dch./mV	N_{coin}	σ_{OCP} 1st ch./mV	σ_{OCP} 2nd ch./mV	σ_{OCP} 1st dch./mV	σ_{OCP} 2nd dch./mV
1	5	2.7	2.9	3.0	3.5	6	2.3	1.7	2.8	3.0
2	6	3.1	2.5	1.7	0.8	6	2.5	5.4	4.9	9.8
3	6	3.2	2.9	4.4	3.5	6	5.7	13.8	9.4	54.5
5	4	2.5	1.9	3.4	3.0	3	4.0	13.4	9.2	52.3
6	4	1.8	3.5	0.6	3.6	4	8.7	2.5	9.1	8.6
7	6	1.9	2.7	2.7	3.3	5	2.2	2.7	7.5	9.9
8	6	2.3	3.1	3.0	3.4	6	1.1	1.0	2.2	2.0
Mean	5.3	2.5	2.8	2.7	3.0	5.1	3.8	5.8	6.4	20.0

and corresponds to graphite stage 2. This graphite stage corresponds to a lithiation degree of the graphite of 50% [42]. The fact that the peak is at a higher electrode SOC than 50 % is due to the fact that the silicon significantly contributes to the total electrode capacity but is not significantly delithiated in the SOC range above peak G_5. The potential of silicon exhibits a steep increase right at the beginning of the delithiation and therefore significant lithium extraction from silicon only takes place at potentials higher than approximately 0.22 V [48,49]. The main voltage plateaus of graphite are at lower voltages [42,49] which has the effect that mainly graphite is delithiated until the cell potential reaches approximately 0.22 V [49]. Therefore, the charge extracted until graphite stage 2 is reached is mainly drawn from the graphite. Peak G_5 tends to appear at lower SOC with increasing number of full-cell cycles. This is probably due to a decrease in the relative contribution of the silicon to the overall electrode capacity during aging [28,48]. The peaks G_1–G_4 correspond to lower lithiated graphite stages. Peak G_1 corresponds to graphite stage 4 which is expected at a graphite lithiation degree of 17% [41] while the corresponding peak appears at a higher electrode SOC because of the contribution of the silicon to the electrode capacity. Peak G_1 corresponds to a cell voltage of 0.211 V for the pristine anode samples. Therefore, significant delithiation of silicon should mainly take place below this peak. All peaks G_1–G_4 exhibit a shift to lower SOC for aged cells. The reason for this shift is most probably the same as for the shift of peak G_5, i.e., a reduced contribution from the silicon to the overall electrode capacity [28,48] which is accessed at low electrode SOC. Reduced silicon capacity is probably also the reason for the left-shift of the steep ascend to the left of the DV valley corresponding to the graphite voltage plateau (stage 4-1L phase transition) [44,49] around SOC = 15–20%. At low SOC there are local peaks corresponding to silicon phases. A detailed analysis of the progression of these peaks during aging is not possible because the curves shown in Fig. 3(c) appear to be blurred at SOC < 13% for the aged cells, which is probably due to the different delithiation behavior of the individual electrode samples in this SOC region, which is discussed later.

In addition to the DVA, the delithiation of the SiG samples is analyzed via incremental capacity analysis (ICA). Incremental capacity (IC) during delithiation, normalized by multiplying with the inverse of the actual capacity extracted during the delithiation step C_{act}, is plotted as a function of half-cell voltage (vs. Li/Li^+) in Fig. 3(e). In this representation, the peaks correspond to voltage plateaus which indicate phase transitions. Peaks G_I to G_{VI} correspond to phase transitions of the graphite [44]. In the voltage region up to 0.240 V, there are only minor differences between the curves obtained at different aging stages. Especially the main graphite transition peaks G_I around 0.098 V, G_{II} around 0.138 V, and G_{VI} around 0.225 V are approximately at the same voltages for different aging states. This indicates that the same graphite stages are formed during delithiation independent of electrode degradation.

There are up to three more peaks at higher potentials (S_I–S_{III}), which correspond to phase transitions during the delithiation of silicon [27,50–52]. The main change in the IC curves is that the normalized IC in the silicon-dominated voltage regime above 0.24 V generally decreases with aging. This sign of a decrease in the relative capacity contribution of the silicon underlines the results from the DVA. The decrease in the relative contribution of silicon to the electrode capacity is estimated by the change in the capacity fraction accessed above 0.24 V during delithiation. A similar approach was presented by Klett et al. [48]. In Fig. 4 the fraction of the capacity accessed above 0.24 V during delithiation is shown for different aging stages. 0.24 V is above the highest graphite voltage plateau, therefore silicon delithiation should dominate the capacity accessed above this voltage. The fraction of the capacity accessed above 0.24 V decreases from 15.1% to 11.7% which is a decrease by 22.7%.

Contrary to this general trend, peaks S_{II} and S_{III}, which are at 0.37 V and 0.42 V, are more pronounced for some of the aged cells. Here, it has to be considered that there are significant differences between the individual coin-cells built from one electrode.

The individual SiG samples show significant differences in their voltage curves in the SOC region below approximately 15 % during delithiation. As an example of the differences in delithiation curves, the voltage curves of the coin-cells built from cell #7 (446 EFC) are shown in Fig. 5(a). The voltage curves in Fig. 5(a) lie closely together for most parts of the delithiation, proofing the high reproducibility of the measurement. Contrary to this, in the SOC region between 5% and 12%, there are comparably large differences between the coin-cell voltages reaching up to 38 mV. The shown example is representative for the finding that silicon-related features in the quasi-stationary OCP curves during delithiation in this SOC region are pronounced to different degrees for different samples. We interpret this as a sign of the inhomogeneity of the SiG electrode. This inhomogeneity is also the cause for the blurring of the DV curves in the low SOC region during delithiation shown in Fig. 3(c).

There are also qualitative differences between the delithiation IC curves of individual samples. The shape of the IC curve above 0.24 V can be divided into two categories referred to as ‘type A’ and ‘type B’ for the individual coin-cells. Representative curves are shown in Fig. 5(b). IC curves of type A have a distinct sharp peak around 0.27 V and a very broad peak between 0.40 V and 0.45 V. IC curves of type B exhibit three sharp peaks at 0.27 V, 0.37 V and 0.42 V respectively. In the literature, two IC peaks corresponding to phase transitions during delithiation of silicon have been reported: One around 0.27 V [27,51,52] and another one between 0.4 V and 0.5 V [27,51,52].

The fraction of coin-cells exhibiting an IC curve of type A decreases with aging, which is shown in Fig. 5(c). Correspondingly, the fraction of cells exhibiting IC curves of type B with sharp peaks at 0.37 V and 0.42 V increases. This results in an overall increase in height for the IC peaks S_{II} and S_{III} based on the averaged delithiation curves in Fig. 3(e).

To understand the processes occurring during the delithiation of silicon shown in Fig. 3(e) and to give a possible explanation for the increase of peak S_{III}, knowledge about the phase constitution of the lithiated silicon at the beginning of the delithiation is crucial. Most of the samples exhibit an IC peak below 0.05 V during the very first lithiation step directly after the coin-cell assembly, preceding the delithiation shown in Fig. 3(e). This is an indicator for the formation of crystalline c-$Li_{15}Si_4$ [50]. The fraction of working coin-cells at a certain aging stage

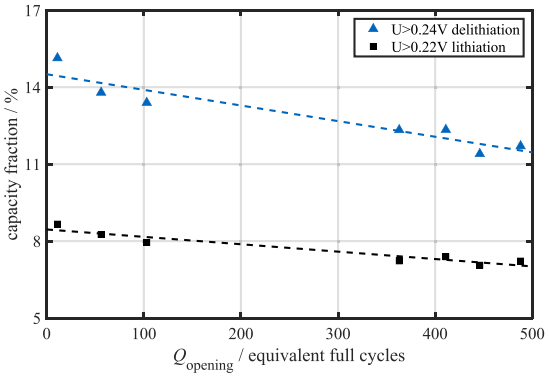

Fig. 4. Fraction of the capacity of silicon–graphite samples which is accessed above 0.24 V (vs. Li/Li$^+$) during delithiation and above 0.22 V during lithiation based on averaged quasi-stationary (de-)lithiation curves measured for samples harvested from full-cells which have experienced a different total charge throughput before cell opening $Q_{opening}$.

exhibiting this peak is shown in Fig. 5(c). We therefore assume that most of the samples contain crystalline c-$Li_{15}Si_4$ at the beginning of the delithiation step shown in Fig. 3(e).

Following the model for the delithiation of c-$Li_{15}Si_4$ presented by Jiang et al. [53], amorphous a-Li_xSi is formed as an intermediate phase during the delithiation of c-$Li_{15}Si_4$. The fraction of a-Li_xSi formed as an intermediate phase is higher if more free surface of silicon is exposed, because the surface energy barrier of the electrochemical amorphization of c-$Li_{15}Si_4$ is lower [53]. The IC peak S_{III} in Fig. 3(e) can be associated with lithium extraction during the phase transition from a-Li_xSi to a-Si [51]. Therefore, the overall increase of peak S_{III} in Fig. 3(e) might possibly be linked to an increase in the relative amount of a-Li_xSi formed during the delithiation. This increase in the formation of a-Li_xSi might be caused by a morphological change of the silicon during aging resulting in an increase in active silicon surface [53]. Further research is necessary to explain the mechanisms leading to the change in silicon delithiation behavior.

The absolute difference between the mean delithiation OCP curve obtained from the pristine anode samples and the mean of the aged anode samples is shown in Fig. 3(g). The standard deviation between the single OCP curves used to calculate the average curve is shown as shaded areas. The decrease in OCP at SOC below approximately 15 % SOC, between 18 and 40 % SOC and between 52 and 65 % SOC significantly exceeds the standard deviation between the samples taken from one electrode. The changes are probably due to the fact that the SOC where individual phase transitions are reached shifts to lower values due to the decrease in relative silicon capacity.

3.4. Change in the silicon–graphite lithiation open-circuit potential curve during cycle aging

The quasi-stationary OCP during lithiation of the anode samples is displayed in Fig. 3(b), the corresponding normalized DV is shown in Fig. 3(d). The features of the curve in Fig. 3(d) are similar to the features of the DV during delithiation: There are five peaks (G_1–G_5) corresponding to graphite phases. Peak G_5 corresponds to stage 2 while peaks G_1–G_4 correspond to graphite phases with lower lithiation degree. Peaks G_1-G_5 shift to lower SOC as cell aging progresses, which is probably due to the decrease in the silicon contribution to the electrode capacity [28,48]. In comparison to the DV curves during delithiation, the peaks exhibit a smaller left-shift for the lithiation case. The most probable reason for this is that the OCP of silicon shows a pronounced hysteresis and lies at lower potentials for the lithiation in

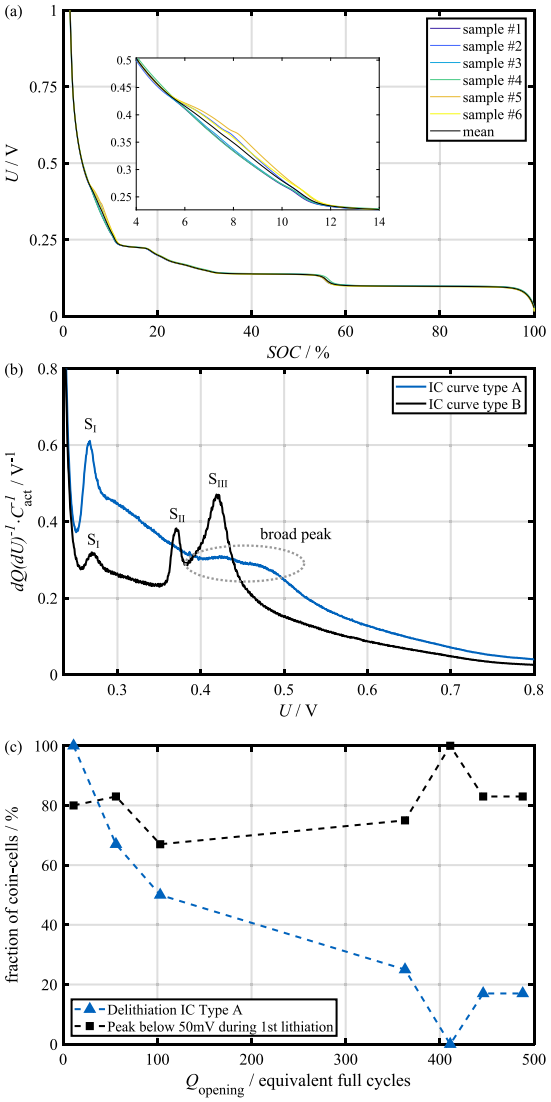

Fig. 5. (a) Voltage of silicon–graphite samples harvested from full-cell #7 (446 EFC) vs. Li/Li$^+$ during quasi-stationary delithiation as a function of the SOC of the individual coin-cells. In addition to the voltage of the individual samples, the arithmetic mean retrieved at different SOC interpolation points is indicated. The inset shows an enlarged section of the SOC region where the curves obtained from different samples exhibit significant differences. (b) Normalized incremental capacity vs. cell voltage (vs. Li/Li$^+$) during delithiation for two coin-cells containing silicon–graphite samples. The two samples exhibit the qualitatively different incremental capacity curves 'type A' (extracted from full-cell #1) and 'type B' (extracted from full-cell #7). (c) Fraction of silicon–graphite samples exhibiting an incremental capacity curve of type A during the first delithiation at different aging stages and fraction of silicon–graphite samples exhibiting an incremental capacity peak below 50 mV vs. Li/Li$^+$ during the first lithiation after the coin-cell assembly at different aging stages.

comparison to the delithiation [54]. So even though a major part of the silicon capacity is lithiated at the beginning of the lithiation step [49], there should also be a significant fraction of the silicon capacity being lithiated in parallel with the graphite at potentials < 0.2 V. Still, most of the silicon capacity is probably accessed at potentials > 0.2 V [49] and therefore the left-shift of peaks G_1-G_5 can be attributed to the relative decrease in the silicon capacity.

Peaks S_1 and S_2 are associated with phases of silicon [8,37]. Both peaks exhibit a shift to lower SOC during aging, which can be explained by the decrease in relative silicon capacity. S_2 is only weakly pronounced. Still, these peaks appear much more clearly during lithiation than during delithiation for all aging stages because the curves obtained from the single samples differ less in this SOC region. The phenomenon of large differences in silicon features between the individual samples which is observed during delithiation is not as pronounced as during lithiation. A possible explanation for this is that the lithiation process might be more homogeneous than the delithiation process, possibly because graphite and silicon are lithiated to a greater extent in parallel than they get delithiated due to the large hysteresis of silicon [54]. There is an additional peak S_C in Fig. 3(d) which is not observable during delithiation. This peak probably corresponds to the highly lithiated, crystalline phase c-$Li_{15}Si_4$ which is formed during lithiation at potentials < 0.05 V vs. Li/Li^+ [50].

In Fig. 3(f) the phase transitions during lithiation are analyzed via ICA. The most pronounced peaks G_I–G_{VI} can be assigned to the graphite phase transitions, with the main graphite phase transitions occurring around 0.080 V (G_I), around 0.114 V (G_{II}), and around 0.204 V (G_{VI}) [49]. They do not exhibit clear trends in their height and position for the different aging stages, indicating that the graphite-related reactions stay the same during aging. Peak G_I exhibits comparably large deviations between the different aging stages, but without showing a specific trend. This is probably due to the comparably large difference between the single samples during lithiation at SOC > 30%. There is a small peak observable between 0.28 V and 0.29 V which can be attributed to a silicon phase transition [50]. The silicon-induced IC peak around 0.1 V reported by some authors [50,52] is not visible, probably because it is superimposed with the graphite features. Around 0.026 V there is a distinct peak S_C which corresponds to the formation of crystalline lithiated silicon c-$Li_{15}Si_4$ [50]. Both silicon-related peaks decrease in height with progressing aging which is a sign of the decrease in the relative contribution of silicon to the overall electrode capacity. In addition to that, the level of normalized IC of the curves above 0.22 V, where most of the lithiation of the silicon occurs [49], is lower, indicating a reduced contribution of silicon to the electrode capacity. The fraction of the capacity accessed at potentials above 0.22 V during lithiation is indicated in Fig. 4 for different aging stages. As for the delithiation case, there is a significant decrease in the fraction of the capacity accessed at higher potentials. The fraction of the capacity accessed above 0.22 V decreases from 8.7% to 7.2% which is a decrease by 16.7%. Both the absolute numbers of the capacity fraction accessed in the chosen potential window and the relative decrease during aging are smaller than for the delithiation case. This is probably due to the fact that the lithiation of graphite and silicon occurs to a higher degree in parallel at lower potentials and a separation of the capacity contributions using this method is difficult.

In Fig. 3(h) the absolute difference in the averaged lithiation OCP curves between pristine and aged SiG samples is shown as solid lines and the standard deviation between the coin-cells as shaded areas. In between 5 and 30% SOC the average voltage is lower for aged cells because the phases of graphite and silicon are reached at lower electrode SOC due to the lower silicon capacity. Above 30% SOC both the standard deviation increases and the absolute of the voltage difference decreases. The trend towards lower voltages for aged cells visible below 30% SOC is not observed at higher SOC.

Our general finding of a lower OCP vs. electrode SOC for aged SiG anodes is consistent with the literature [29], and we conclude that the changes are due to a predominant degradation of silicon in comparison to graphite [28,29,48,54,55]. Possible degradation mechanisms of the silicon are the ionic and electric isolation of silicon particles [28,48,54] and change in the local structure, electrode morphology, and mechanical properties during cycling [28,54]. This does not mean that there is no degradation of the graphite, but the capacity provided by the silicon decreases at a higher rate than the capacity provided by the graphite. The individual degradation rates of graphite and silicon most probably depend on the operating conditions used for the full-cell cycling. In this study, the cell is discharged to the lowest voltage recommended by the manufacturer, which probably enhances silicon utilization and therefore silicon degradation [54,56]. Such deep cycles only rarely occur in real-world applications. The change in anode OCP due to selective silicon degradation might therefore be smaller in applications compared to our results. On the other hand, the comparably high current rate during the cycling period could lead to a reduced silicon utilization [56] compared to the usually lower average current rates used for example in automotive applications. However, the influence of the current rate on selective silicon degradation is probably smaller than the influence of the voltage window.

Besides the change in graphite to silicon capacity ratio we do not observe the formation or disappearance of phases giving rise to a change in the shape of the OCP curve which is consistent with the literature [29]. The only exception are the subtle changes in silicon-related IC features during delithiation which need to be investigated in more detail in future studies.

3.5. Change in the cathode open-circuit potential curve during cycle aging

The average quasi-stationary OCP of the cells containing cathode samples at different aging stages is displayed in Fig. 6(a) for charging (delithiation of the NMC) and in Fig. 6(b) for discharging (lithiation of the NMC). The normalized DV during delithiation is shown in Fig. 6(c). The DV during delithiation exhibits three peaks indicating NMC phases [36] (C_1–C_3). The exact position and height of the peaks show some variation for the different aging stages but there is no significant trend in position or height with the progress of aging. In Fig. 6(e) the normalized IC during delithiation is shown. The IC exhibits four peaks (C_I–C_{IV}) corresponding to phase transitions of the NMC at 3.56 V, 3.74 V, 4.01 V, and 4.18 V. No specific trend with aging can be observed for the height and position of the IC peaks.

The normalized DV during lithiation of the cathode samples shown in Fig. 6(d) exhibits three peaks (C_1–C_3) similar to the delithiation case. Peak C_1 and the valley left to it exhibit a subtle shift towards lower SOC during aging while peak C_2 does not change with aging. Peak C_3 is very broad during lithiation which makes it difficult to detect aging-related trends. The most pronounced change during aging is the left-shift of the steep ascend towards the end of the lithiation process for aged cells in comparison with the less aged cells #1 and 2. Still, it has to be noted that the SOC position of the DV ascend does not follow an aging-related trend for cells #3–8. As for the delithiation case, the normalized IC during lithiation shown in Fig. 3(f) has four peaks. They are located at 3.54 V (C_I), 3.73 V (C_{II}), 4.00 V (C_{III}), and 4.17 V (C_{IV}). There are some differences between the curves of the less aged cells #1 and 2 and the other cells. The most prominent difference is that peak C_I is distinctively pronounced only for cells #1 and 2 while it is smeared out for the more aged cells. This feature corresponds to the left-shifted and less sharp decrease in voltage towards the end of the lithiation for the more aged cells shown in Fig. 6(b), which has also been reported in the literature [33]. Additionally, both slopes of peak C_{IV} are slightly left-shifted for cells #3-8 in comparison to cells #1 and 2. This corresponds to the faster decrease in voltage at the beginning of the lithiation depicted in Fig. 6(b). Apart from these subtle differences, there is no significant change in the overall shape of the lithiation IC curves during aging.

Our results show that the shape of the OCP curve of NMC-811 does not change significantly during cycle aging, even though the material most probably degrades. The formation of a resistive, electrochemically inactive layer on the surface of the primary particles [32,57,58], which leads to electrode capacity decrease [57] and severe increase in the charge transfer resistance [32,57], as well as cracking of secondary particles [29,32] has been reported to occur in nickel-rich NMC during prolonged cycling. Another aging mechanism is the formation of

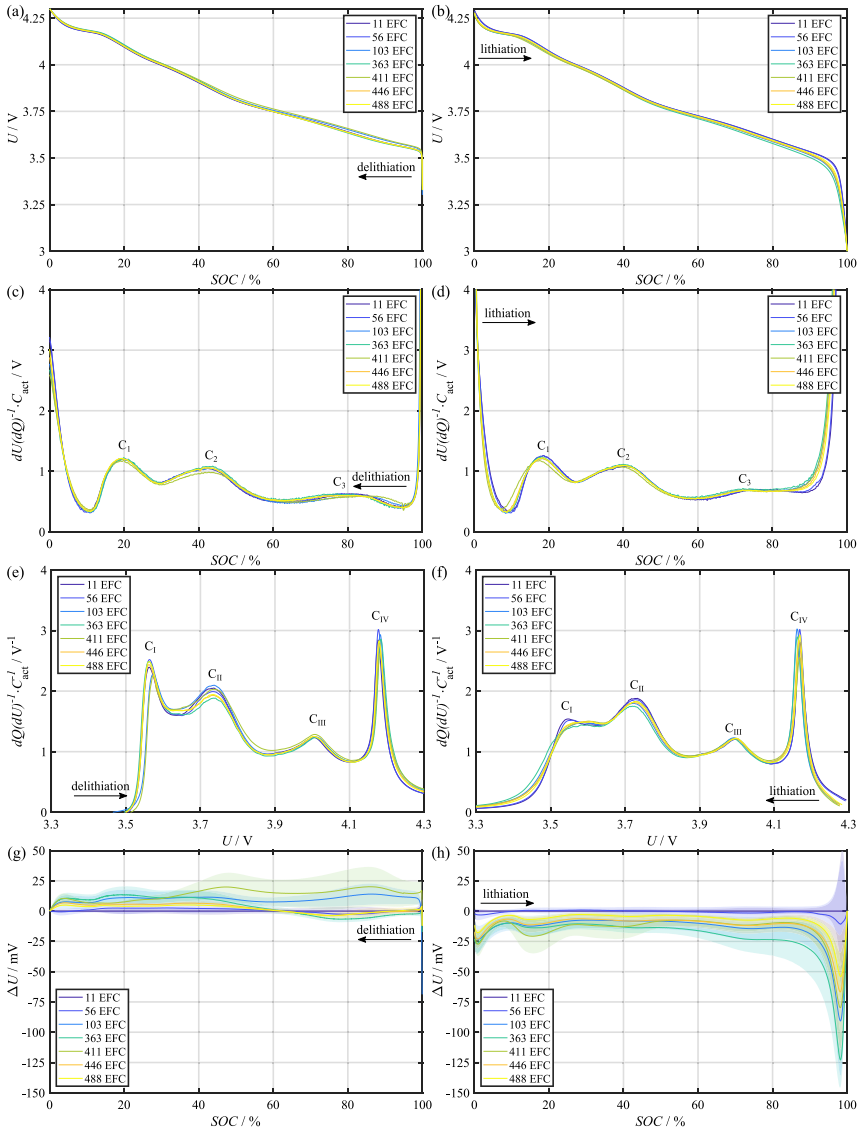

Fig. 6. First row: Mean quasi-stationary OCP vs. Li/Li^+ during (a) delithiation and (b) lithiation of the NMC samples extracted from full-cells that have been cycled for the number of equivalent full cycles indicated in the legend. Second row: Differential voltage during (c) delithiation and (d) lithiation of the NMC samples calculated based on the averaged OCP curves. The differential voltage values are normalized by multiplying with the actual capacity during the respective (dis-)charging step C_{act} and smoothed using a moving average filter. Third row: Incremental capacity during (e) delithiation and (f) lithiation of the NMC samples calculated based on the averaged OCP curves and plotted against cell voltage vs. Li/Li^+. The incremental capacity values are normalized by multiplying with the inverse of the actual capacity during the respective (dis-)charging step C_{act} and smoothed using a moving average filter. Fourth row: Difference between mean OCP of aged NMC samples and mean OCP of pristine NMC samples during (g) delithiation and (h) lithiation. The standard deviation between the OCP of the single samples harvested from the same electrode is shown as shaded area.

a fatigued bulk phase, which can only be partly delithiated under regular cycling conditions due to kinetic limitations [32,58]. While these mechanisms probably also occur in the NMC electrodes in this study, we want to emphasize that the shape of the OCP curve is not significantly altered by them. This is in accordance with the literature. Jung et al. showed that the mean discharge voltage and the shape of the OCP curve of NMC-811 that was not exposed to ambient air does not significantly change during cycle aging [31]. Friedrich et al. showed that the charge-averaged mean discharge voltage of NMC-811 does not change significantly if a low current rate is used [57]. Former studies investigating the cycle performance of commercial cells of the same type as the ones used in this study also do not report changes in the shape of the OCP curve of the cathode material [29,39,59]. There are some reports of a shift in the voltage position of the IC peaks of nickel-rich NMC during cycle aging, but the current rates used in these studies to obtain the IC curves are significantly higher than in our measurements [32,60], and it cannot be excluded that the shift in the voltage position of the peaks is due to an increase in the overpotential.

The invariance of the shape of the OCP curve suggests that the electrochemically active phases that are formed during delithiation and

lithiation do not change during cycle aging. This is in accordance with the literature as the bulk structure of NMC has been reported to stay the same during prolonged cycling [29,57,58]. The surface layer that is probably formed on the primary particles [57] does not affect the OCP curve as it is electrochemically inactive. We do not detect signs of an additional fatigued bulk phase towards the end of delithiation [32,58], but this does not mean that this phase does not exist. It has been reported that the fatigued phase can be almost completely delithiated during a prolonged CV phase giving enough time for the delithiation even though the kinetics are lower than for the pristine material [32]. As the quasi-stationary OCP is measured at a very low current rate of approximately C/90 in our experiments, the fatigued phase can probably be fully delithiated regardless of its low kinetics.

In Fig. 6(g) the difference between the mean quasi-stationary OCP during the delithiation of the aged cathode samples and the pristine cathode samples harvested from cell #1 is shown. The charge-averaged mean voltage during delithiation does not exhibit a clear trend with full-cell cycle aging and it is generally only slightly higher (< 14 mV) for the aged electrodes in comparison to pristine electrodes. The voltage difference during lithiation is presented in Fig. 6(h). The charge-averaged mean voltage during the lithiation of the aged samples is slightly lower (< 21 mV) in comparison to the pristine samples, even though there is no clear trend with aging. The subtle shift of the average voltage during delithiation and lithiation is probably due to an increase in the electrode impedance [29,32,57,61]. This increase in impedance probably leads to higher overpotentials even at the low current rate used for the measurement. An increase in electrode impedance is probably also the reason for the earlier and less sharp decrease in voltage towards the end of the lithiation [29].

Overall, we observe that there are no significant aging-induced changes in the shape of the OCP curve of the NMC-811, even though the material most probably degrades. For the development of model-based algorithms for SOH estimation, it is therefore appropriate to assume the shape of the half-cell OCP of NMC-811 to be invariant during cycle aging. The deviations of the absolute voltage vs. electrode SOC measured during low current (de-)lithiation are most probably due to an increase in electrode impedance. Such changes should therefore be considered by a change in the model elements or parameters describing the electrode impedance in a model describing the electrical behavior of an aged cell rather than by a change in the shape of the OCP curve.

4. Conclusion

We show that the shape of the OCP curve of silicon–graphite half-cells significantly changes during cycle aging of a full-cell containing these electrodes as anodes. Using DVA and ICA, we attribute these changes to a decrease in the relative contribution of the silicon to the electrode capacity. On the component level of this blended electrode, we observe a change in silicon-related features in the IC delithiation curve. Further research is necessary to understand the underlying mechanisms of this finding. In contrast to the changes in the SiG OCP curve, the shape of the OCP curve of NMC-811, which is used as cathode in the full-cells, exhibits only minor deviations as full-cell degradation progresses. This means that even though the NMC-811 probably degrades, it is appropriate to regard the shape of its OCP curve to be invariant in electrical cell models during cycle aging. The slight deviations between the quasi-stationary OCP curves of pristine and cycle aged cathode samples we observe are probably due to an increase in electrode impedance.

Another finding is that there are differences in the quasi-stationary OCP curve of individual coin-cells containing samples taken from nearby positions on the same electrode. We therefore use averaged OCP curves from several coin-cells for our analysis. Our recommendation for future studies using coin-cells containing harvested electrode samples is to build and measure several coin-cells containing material from the same electrode and use averaged measurement values in order to reduce possible influences of the coin-cell manufacturing process and to obtain representative results for the whole electrode. Especially for the SiG during delithiation we find differences in the OCP curves of individual coin-cells, which are probably caused by inhomogeneity of the SiG electrode.

Our main conclusion is that in electrical battery models the shape of the OCP curve of NMC-811 can be regarded as fairly invariant during full-cell cycle aging while this does not apply to the shape of SiG half-cells. As anodes containing significant proportions of silicon are increasingly used in applications, it becomes more and more important to consider these changes in battery aging diagnostics and state estimation algorithms. While the results provided in this study concentrate on the aging-related changes on the half-cell OCP, we will investigate the impact of these changes on the full-cell OCP during aging in our future research. We will also investigate methods that make it possible to include the changes in half-cell OCP of blended SiG electrodes into electrical battery models.

CRediT authorship contribution statement

Julius Schmitt: Conceptualization, Methodology, Validation, Formal analysis, Investigation, Writing - original draft, Writing - review & editing, Visualization. **Markus Schindler:** Conceptualization, Methodology, Investigation, Writing - review & editing. **Andreas Jossen:** Writing - review & editing, Supervision, Project administration, Funding acquisition.

Declaration of competing interest

The authors declare that they have no known competing financial interests or personal relationships that could have appeared to influence the work reported in this paper.

Acknowledgments

This work was supported by the German Federal Ministry for Economic Affairs and Energy (grant number 03ETE019F) and by AUDI AG in the scope of an INI.TUM project. The responsibility for this publication lies with the authors.

References

[1] S.F. Schuster, T. Bach, E. Fleder, J. Müller, M. Brand, G. Sextl, A. Jossen, Nonlinear aging characteristics of lithium-ion cells under different operational conditions, J. Energy Storage 1 (2015) 44–53, http://dx.doi.org/10.1016/j.est.2015.05.003.

[2] P. Keil, A. Jossen, Calendar aging of NCA lithium-ion batteries investigated by differential voltage analysis and coulomb tracking, J. Electrochem. Soc. 164 (1) (2016) A6066–A6074, http://dx.doi.org/10.1149/2.0091701jes.

[3] P. Keil, S.F. Schuster, J. Wilhelm, J. Travi, A. Hauser, R.C. Karl, A. Jossen, Calendar aging of lithium-ion batteries, J. Electrochem. Soc. 163 (9) (2016) A1872–A1880, http://dx.doi.org/10.1149/2.0411609jes.

[4] J. Schmitt, A. Maheshwari, M. Heck, S. Lux, M. Vetter, Impedance change and capacity fade of lithium nickel manganese cobalt oxide-based batteries during calendar aging, J. Power Sources 353 (2017) 183–194, http://dx.doi.org/10.1016/j.jpowsour.2017.03.090.

[5] M. Naumann, M. Schimpe, P. Keil, H.C. Hesse, A. Jossen, Analysis and modeling of calendar aging of a commercial $LiFePO_4$/graphite cell, J. Energy Storage 17 (2018) 153–169, http://dx.doi.org/10.1016/j.est.2018.01.019.

[6] A. Maheshwari, M. Heck, M. Santarelli, Cycle aging studies of lithium nickel manganese cobalt oxide-based batteries using electrochemical impedance spectroscopy, Electrochim. Acta 273 (2018) 335–348, http://dx.doi.org/10.1016/j.electacta.2018.04.045.

[7] Y. Gao, J. Jiang, C. Zhang, W. Zhang, Y. Jiang, Aging mechanisms under different state-of-charge ranges and the multi-indicators system of state-of-health for lithium-ion battery with $Li(NiMnCo)O_2$ cathode, J. Power Sources 400 (2018) 641–651, http://dx.doi.org/10.1016/j.jpowsour.2018.07.018.

[8] I. Zilberman, J. Sturm, A. Jossen, Reversible self-discharge and calendar aging of 18650 nickel-rich, silicon–graphite lithium-ion cells, J. Power Sources 425 (2019) 217–226, http://dx.doi.org/10.1016/j.jpowsour.2019.03.109.

[9] J. Schmitt, B. Kraft, J.P. Schmidt, B. Meir, K. Elian, D. Ensling, G. Keser, A. Jossen, Measurement of gas pressure inside large-format prismatic lithium-ion cells during operation and cycle aging, J. Power Sources 478 (2020) 228661, http://dx.doi.org/10.1016/j.jpowsour.2020.228661.

[10] P. Liu, J. Wang, J. Hicks-Garner, E. Sherman, S. Soukiazian, M. Verbrugge, H. Tataria, J. Musser, P. Finamore, Aging mechanisms of $LiFePO_4$ batteries deduced by electrochemical and structural analyses, J. Electrochem. Soc. 157 (4) (2010) A499, http://dx.doi.org/10.1149/1.3294790.

[11] M. Dubarry, C. Truchot, B.Y. Liaw, Synthesize battery degradation modes via a diagnostic and prognostic model, J. Power Sources 219 (2012) 204–216, http://dx.doi.org/10.1016/j.jpowsour.2012.07.016.

[12] I. Bloom, J.P. Christophersen, D.P. Abraham, K.L. Gering, Differential voltage analyses of high-power lithium-ion cells, J. Power Sources 157 (1) (2006) 537–542, http://dx.doi.org/10.1016/j.jpowsour.2005.07.054.

[13] A. Marongiu, N. Nlandi, Y. Rong, D.U. Sauer, On-board capacity estimation of lithium iron phosphate batteries by means of half-cell curves, J. Power Sources 324 (2016) 158–169, http://dx.doi.org/10.1016/j.jpowsour.2016.05.041.

[14] Z. Ma, Z. Wang, R. Xiong, J. Jiang, A mechanism identification model based state-of-health diagnosis of lithium-ion batteries for energy storage applications, J. Clean. Prod. 193 (2018) 379–390, http://dx.doi.org/10.1016/j.jclepro.2018.05.074.

[15] I. Zilberman, S. Ludwig, M. Schiller, A. Jossen, Online aging determination in lithium-ion battery module with forced temperature gradient, J. Energy Storage 28 (2020) 101170, http://dx.doi.org/10.1016/j.est.2019.101170.

[16] S. Wang, J. Wang, L. Vu, J. Purewal, S. Soukiazian, J. Graetz, On line battery capacity estimation based on half-cell open circuit voltages, J. Electrochem. Soc. 161 (12) (2014) A1788–A1793, http://dx.doi.org/10.1149/2.0271412jes.

[17] S. Dey, Y. Shi, K. Smith, A. Colclasure, X. Li, From battery cell to electrodes: Real-time estimation of charge and health of individual battery electrodes, IEEE Trans. Ind. Electron. 67 (3) (2020) 2167–2175, http://dx.doi.org/10.1109/TIE.2019.2907514.

[18] L. Ungurean, G. Cârstoiu, M.V. Micea, V. Groza, Battery state of health estimation: A structured review of models, methods and commercial devices, Int. J. Energy Res. 41 (2) (2017) 151–181, http://dx.doi.org/10.1002/er.3598.

[19] Z. Li, J. Huang, B.Y. Liaw, J. Zhang, On state-of-charge determination for lithium-ion batteries, J. Power Sources 348 (2017) 281–301, http://dx.doi.org/10.1016/j.jpowsour.2017.03.001.

[20] C. Campestrini, S. Kosch, A. Jossen, Influence of change in open circuit voltage on the state of charge estimation with an extended Kalman filter, J. Energy Storage 12 (2017) 149–156, http://dx.doi.org/10.1016/j.est.2017.04.011.

[21] A. Marongiu, D. Sauer, On-board aging estimation using half-cell voltage curves for $LiFePO_4$ cathode-based lithium-ion battery for electric vehicle application, World Electr. Veh. J. 7 (1) (2015) 14–24, http://dx.doi.org/10.3390/wevj7010014.

[22] S. Lee, J.B. Siegel, A.G. Stefanopoulou, J.-W. Lee, T.-K. Lee, Electrode state of health estimation for lithium ion batteries considering half-cell potential change due to aging, J. Electrochem. Soc. 167 (9) (2020) 090531, http://dx.doi.org/10.1149/1945-7111/ab8c83.

[23] S. Lee, P. Mohtat, J.B. Siegel, A.G. Stefanopoulou, J.-W. Lee, T.-K. Lee, Estimation error bound of battery electrode parameters with limited data window, IEEE Trans. Ind. Inf. 16 (5) (2020) 3376–3386, http://dx.doi.org/10.1109/TII.2019.2952066.

[24] C.R. Birkl, M.R. Roberts, E. McTurk, P.G. Bruce, D.A. Howey, Degradation diagnostics for lithium ion cells, J. Power Sources 341 (2017) 373–386, http://dx.doi.org/10.1016/j.jpowsour.2016.12.011.

[25] I. Zilberman, J. Schmitt, S. Ludwig, M. Naumann, A. Jossen, Simulation of voltage imbalance in large lithium-ion battery packs influenced by cell-to-cell variations and balancing systems, J. Energy Storage 32 (2020) 101828, http://dx.doi.org/10.1016/j.est.2020.101828.

[26] J.P. Schmidt, H.Y. Tran, J. Richter, E. Ivers-Tiffée, M. Wohlfahrt-Mehrens, Analysis and prediction of the open circuit potential of lithium-ion cells, J. Power Sources 239 (2013) 696–704, http://dx.doi.org/10.1016/j.jpowsour.2012.11.101.

[27] M. Wetjen, D. Pritzl, R. Jung, S. Solchenbach, R. Ghadimi, H.A. Gasteiger, Differentiating the degradation phenomena in silicon–graphite electrodes for lithium-ion batteries, J. Electrochem. Soc. 164 (12) (2017) A2840–A2852, http://dx.doi.org/10.1149/2.1921712jes.

[28] W.M. Dose, M.J. Piernas-Muñoz, V.A. Maroni, S.E. Trask, I. Bloom, C.S. Johnson, Capacity fade in high energy silicon–graphite electrodes for lithium-ion batteries, Chem. Commun. 54 (29) (2018) 3586–3589, http://dx.doi.org/10.1039/c8cc00456k.

[29] X. Li, A.M. Colclasure, D.P. Finegan, D. Ren, Y. Shi, X. Feng, L. Cao, Y. Yang, K. Smith, Degradation mechanisms of high capacity 18650 cells containing Si-graphite anode and nickel-rich NMC cathode, Electrochim. Acta 297 (2019) 1109–1120, http://dx.doi.org/10.1016/j.electacta.2018.11.194.

[30] D. Anseán, G. Baure, M. González, I. Cameán, A.B. García, M. Dubarry, Mechanistic investigation of silicon–graphite/$LiNi_{0.8}Mn_{0.1}Co_{0.1}O_2$ commercial cells for non-intrusive diagnosis and prognosis, J. Power Sources 459 (2020) 227882, http://dx.doi.org/10.1016/j.jpowsour.2020.227882.

[31] R. Jung, R. Morasch, P. Karayaylali, K. Phillips, F. Maglia, C. Stinner, Y. Shao-Horn, H.A. Gasteiger, Effect of ambient storage on the degradation of Ni-rich positive electrode materials (NMC811) for Li-ion batteries, J. Electrochem. Soc. 165 (2) (2018) A132–A141, http://dx.doi.org/10.1149/2.0401802jes.

[32] S. Schweidler, L. de Biasi, G. Garcia, A. Mazilkin, P. Hartmann, T. Brezesinski, J. Janek, Investigation into mechanical degradation and fatigue of high-Ni NCM cathode material: A long-term cycling study of full cells, ACS Appl. Energy Mater. 2 (10) (2019) 7375–7384, http://dx.doi.org/10.1021/acsaem.9b01354.

[33] X. Jia, C. Zhang, Y. Le Wang, L. Zhang, W. Zhang, The degradation characteristics and mechanism of $Li[Ni_{0.5}Co_{0.2}Mn_{0.3}]O_2$ batteries at different temperatures and discharge current rates, J. Electrochem. Soc. 167 (2) (2020) 020503, http://dx.doi.org/10.1149/1945-7111/ab61e9.

[34] F.M. Kindermann, A. Noel, S.V. Erhard, A. Jossen, Long-term equalization effects in Li-ion batteries due to local state of charge inhomogeneities and their impact on impedance measurements, Electrochim. Acta 185 (2015) 107–116, http://dx.doi.org/10.1016/j.electacta.2015.10.108.

[35] J. Sieg, M. Storch, J. Fath, A. Nuhic, J. Bandlow, B. Spier, D.U. Sauer, Local degradation and differential voltage analysis of aged lithium-ion pouch cells, J. Energy Storage 30 (2020) 101582, http://dx.doi.org/10.1016/j.est.2020.101582.

[36] J. Sturm, A. Rheinfeld, I. Zilberman, F.B. Spingler, S. Kosch, F. Frie, A. Jossen, Modeling and simulation of inhomogeneities in a 18650 nickel-rich, silicon–graphite lithium-ion cell during fast charging, J. Power Sources 412 (2019) 204–223, http://dx.doi.org/10.1016/j.jpowsour.2018.11.043.

[37] M. Schindler, J. Sturm, S. Ludwig, J. Schmitt, A. Jossen, Evolution of initial cell-to-cell variations during a three-year production cycle, eTransportation 14 (165) (2021) 100102, http://dx.doi.org/10.1016/j.etran.2020.100102.

[38] I. Zilberman, S. Ludwig, A. Jossen, Cell-to-cell variation of calendar aging and reversible self-discharge in 18650 nickel-rich, silicon–graphite lithium-ion cells, J. Energy Storage 26 (2019) 100900, http://dx.doi.org/10.1016/j.est.2019.100900.

[39] M. Schindler, J. Sturm, S. Ludwig, A. Durdel, A. Jossen, Comprehensive analysis of the aging behavior of nickel-rich, silicon–graphite lithium-ion cells subject to varying temperature and charging profiles, J. Electrochem. Soc. (2021) http://dx.doi.org/10.1149/1945-7111/ac03f6.

[40] A.U. Schmid, M. Kurka, K.P. Birke, Reproducibility of Li-ion cell reassembling processes and their influence on coin cell aging, J. Energy Storage 24 (2019) 100732, http://dx.doi.org/10.1016/j.est.2019.04.006.

[41] D. Allart, M. Montaru, H. Gualous, Model of lithium intercalation into graphite by potentiometric analysis with equilibrium and entropy change curves of graphite electrode, J. Electrochem. Soc. 165 (2) (2018) A380–A387, http://dx.doi.org/10.1149/2.1251802jes.

[42] J.R. Dahn, Phase diagram of LixC6, Phys. Rev. B 44 (17) (1991) 9170–9177, http://dx.doi.org/10.1103/PhysRevB.44.9170.

[43] D. Billaud, F.X. Henry, M. Lelaurain, P. Willmann, Revisited structures of dense and dilute stage II lithium–graphite intercalation compounds, J. Phys. Chem. Solids 57 (6–8) (1996) 775–781, http://dx.doi.org/10.1016/0022-3697(95)00348-7.

[44] T. Ohzuku, Y. Iwakoshi, K. Sawai, Formation of lithium–graphite intercalation compounds in nonaqueous electrolytes and their application as a negative electrode for a lithium ion (shuttlecock) cell, J. Electrochem. Soc. 140 (9) (1993) 2490–2498, http://dx.doi.org/10.1149/1.2220849.

[45] D. Billaud, F.X. Henry, Structural studies of the stage III lithium–graphite intercalation compound, Solid State Commun. 124 (8) (2002) 299–304, http://dx.doi.org/10.1016/S0038-1098(02)00469-6.

[46] S. Schweidler, L. de Biasi, A. Schiele, P. Hartmann, T. Brezesinski, J. Janek, Volume changes of graphite anodes revisited: A combined operando X-ray diffraction and in situ pressure analysis study, J. Phys. Chem. C 122 (16) (2018) 8829–8835, http://dx.doi.org/10.1021/acs.jpcc.8b01873.

[47] M.P. Mercer, C. Peng, C. Soares, H.E. Hoster, D. Kramer, Voltage hysteresis during lithiation/delithiation of graphite associated with meta-stable carbon stackings, J. Mater. Chem. A 9 (1) (2021) 492–504, http://dx.doi.org/10.1039/D0TA10403E.

[48] M. Klett, J.A. Gilbert, S.E. Trask, B.J. Polzin, A.N. Jansen, D.W. Dees, D.P. Abraham, Electrode behavior RE-visited: Monitoring potential windows, capacity loss, and impedance changes in $Li_{1.03}(Ni_{0.5}Co_{0.2}Mn_{0.3})$ 0.97 O_2/silicon–graphite full cells, J. Electrochem. Soc. 163 (6) (2016) A875–A887, http://dx.doi.org/10.1149/2.0271606jes.

[49] M. Klett, J.A. Gilbert, K.Z. Pupek, S.E. Trask, D.P. Abraham, Layered oxide, graphite and silicon–graphite electrodes for lithium-ion cells: Effect of electrolyte composition and cycling windows, J. Electrochem. Soc. 164 (1) (2017) A6095–A6102, http://dx.doi.org/10.1149/2.0131701jes.

[50] M.N. Obrovac, L. Christensen, Structural changes in silicon anodes during lithium insertion/extraction, J. Power Sources 7 (5) (2004) A93, http://dx.doi.org/10.1149/1.1652421.

[51] J.W. Wang, Y. He, F. Fan, X.H. Liu, S. Xia, Y. Liu, C.T. Harris, H. Li, J.Y. Huang, S.X. Mao, T. Zhu, Two-phase electrochemical lithiation in amorphous silicon, Nano Lett. 13 (2) (2013) 709–715, http://dx.doi.org/10.1021/nl304379k.

[52] A.Y.R. Prado, M.-T.F. Rodrigues, S.E. Trask, L. Shaw, D.P. Abraham, Electrochemical dilatometry of Si-bearing electrodes: Dimensional changes and experiment design, J. Electrochem. Soc. 167 (16) (2020) 160551, http://dx.doi.org/10.1149/1945-7111/abd465.

[53] Y. Jiang, G. Offer, J. Jiang, M. Marinescu, H. Wang, Voltage hysteresis model for silicon electrodes for lithium ion batteries, including multi-step phase transformations, crystallization and amorphization, J. Electrochem. Soc. 167 (13) (2020) 130533, http://dx.doi.org/10.1149/1945-7111/abbbba.

[54] M. Wetjen, S. Solchenbach, D. Pritzl, J. Hou, V. Tileli, H.A. Gasteiger, Morphological changes of silicon nanoparticles and the influence of cutoff potentials in silicon–graphite electrodes, J. Electrochem. Soc. 165 (7) (2018) A1503–A1514, http://dx.doi.org/10.1149/2.1261807jes.

[55] M.-T.F. Rodrigues, J.A. Gilbert, K. Kalaga, D.P. Abraham, Insights on the cycling behavior of a highly-prelithiated silicon–graphite electrode in lithium-ion cells, J. Phys. Energy 2 (2) (2020) 024002, http://dx.doi.org/10.1088/2515-7655/ab6b3a.

[56] P.-F. Lory, B. Mathieu, S. Genies, Y. Reynier, A. Boulineau, W. Hong, M. Chandesris, Probing silicon lithiation in silicon–carbon blended anodes with a multi-scale porous electrode model, J. Electrochem. Soc. 167 (12) (2020) 120506, http://dx.doi.org/10.1149/1945-7111/abaa69.

[57] F. Friedrich, B. Strehle, A.T.S. Freiberg, K. Kleiner, S.J. Day, C. Erk, M. Piana, H.A. Gasteiger, Editors' choice—Capacity fading mechanisms of NCM-811 cathodes in lithium-ion batteries studied by X-ray diffraction and other diagnostics, J. Electrochem. Soc. 166 (15) (2019) A3760–A3774, http://dx.doi.org/10.1149/2.0821915jes.

[58] C. Xu, K. Märker, J. Lee, A. Mahadevegowda, P.J. Reeves, S.J. Day, M.F. Groh, S.P. Emge, C. Ducati, B. Layla Mehdi, C.C. Tang, C.P. Grey, Bulk fatigue induced by surface reconstruction in layered Ni-rich cathodes for Li-ion batteries, Nature Mater. 20 (1) (2021) 84–92, http://dx.doi.org/10.1038/s41563-020-0767-8.

[59] T.M.M. Heenan, A. Jnawali, M.D.R. Kok, T.G. Tranter, C. Tan, A. Dimitrijevic, R. Jervis, D.J.L. Brett, P.R. Shearing, An advanced microstructural and electrochemical datasheet on 18650 Li-ion batteries with nickel-rich NMC811 cathodes and graphite–silicon anodes, J. Electrochem. Soc. 167 (14) (2020) 140530, http://dx.doi.org/10.1149/1945-7111/abc4c1.

[60] S.S. Zhang, Understanding of performance degradation of $LiNi_{0.80}Co_{0.10}Mn_{0.10}O_2$ cathode material operating at high potentials, J. Energy Chem. 41 (2020) 135–141, http://dx.doi.org/10.1016/j.jechem.2019.05.013.

[61] K. Kleiner, P. Jakes, S. Scharner, V. Liebau, H. Ehrenberg, Changes of the balancing between anode and cathode due to fatigue in commercial lithium-ion cells, J. Power Sources 317 (2016) 25–34, http://dx.doi.org/10.1016/j.jpowsour.2016.03.049.

4.2 Impact on the full-cell open-circuit voltage curve

In section 4.1, it is shown that there is a change in the shape of the OCP curve of SiC electrodes that is probably due to a faster degradation of the silicon capacity in comparison to the graphite capacity. These experimental results are expanded by two aspects in the study presented in this section.
First, the qualitative description of the change in the shape of the SiC OCP curve provided in section 4.1 is complemented by a quantitative description using a blend electrode model originally presented by Schmidt et al. [68] (see section 2.1.2). The blend electrode model allows to simulate a SiC blend electrode with varying capacity contributions of the individual components based on the OCP curves of the pure electrode active materials silicon and graphite. It is shown that measured half-cell OCP curves of SiC electrode samples at different aging states can be accurately fit by the blend electrode model. Thereby, the capacity contribution of silicon can be quantified as 9.5 % of the overall anode capacity for the pristine samples. The relative capacity contribution of silicon is found to decrease during cycle aging and reaches 5.6 % for the samples extracted from the most cycled cell (488 EFC).
Second, the impact of the change in the SiC half-cell OCP curve on the full-cell OCV curve is investigated. The mechanistic modeling approach described in section 2.2.2 is used to interpret the change in the shape of the full-cell OCV curve during aging. The full-cell quasi-stationary OCV curves are fit by half-cell OCP curves using three different types of OCP curves for the SiC anode: (a) the pristine half-cell OCP curve as it is usually done in the scope of full-cell OCV curve alignment (see section 2.2.3); (b) the measured half-cell OCP curves at different aging states and (c) synthetic half-cell OCP curves that are simulated using the blend electrode model. For the last case, the relative capacity contribution of the silicon is determined from the full-cell OCV curve via optimization. The results on the degradation modes are compared for the three different types of SiC half-cell curves. LAM_{an} and LLI are found to be the dominant degradation modes for all three types of anode half-cell curves. Still, lower values for LAM_{an} are determined if component-specific silicon degradation is considered either by using measured aged SiC OCP curves or by using synthetic OCP curves simulated with the blend electrode model. This finding is interpreted in a way that the shift of the graphite features corresponding to the 4L to 2L graphite stages towards lower SOC is erroneously interpreted to result solely from overall anode capacity loss if changes in the SiC half-cell OCP are neglected, while it is actually partly caused by component specific silicon degradation. In addition, slightly higher values for LAM_{cat} and LLI are obtained if changes in the SiC OCP curve are considered.
It is concluded that changes in the shape of the half-cell OCP curve of SiC blend electrodes should be considered in models that describe the full-cell OCV curve of cells containing this anode material during cycle aging. It is also concluded that, if degradation mode analysis based on full-cell OCV curves (see section 2.2.3) of SiC containing cells is performed, the LAM_{an} can get overestimated while LAM_{cat} and LLI can get underestimated if changes in the anode half-cell OCP are neglected. Still, the quantitative difference in the identified degradation modes is only in the order of a few percentage points, at least for the cell type and the aging scenario investigated in this study. However, with increasing silicon contents in anodes of lithium-ion batteries, modeling of component-specific silicon degradation might become more important in the future and the method presented in this study could be a valuable tool for analyzing the degradation of cells containing SiC anodes.

Publication notes

The article titled *Determination of degradation modes of lithium-ion batteries considering aging-induced changes in the half-cell open-circuit potential curve of silicon–graphite* is presented in the following. The article was published in the Journal of Power Sources [47]. Parts of the results have been presented as an online presentation titled *Non-Destructive Degradation Diagnostics of Lithium-Ion Cells considering Aging-Related Changes in the Shape of the Half-Cell Open Circuit Potential Curve of Silicon-Graphite* in the scope of the 240th ECS Meeting in October 2021.

Author contribution

The concept of the study was developed by Julius Schmitt. The experimental design was developed by Julius Schmitt and Markus Schindler. Markus Schindler conducted the experiments on full-cell level. Andreas Oberbauer and Julius Schmitt conducted the half-cell OCP measurements of graphite. The experimental data was analyzed and visualized by Julius Schmitt. The proposed method for degradation mode estimation considering anode component specific degradation was developed and implemented by Julius Schmitt. Andreas Jossen supervised the related research project as well as the scientific work presented in the article. The manuscript was written by Julius Schmitt and was edited by all authors. All authors discussed the data and commented on the results.

Determination of degradation modes of lithium-ion batteries considering aging-induced changes in the half-cell open-circuit potential curve of silicon–graphite

Julius Schmitt, Markus Schindler, Andreas Oberbauer and Andreas Jossen.

Journal of Power Sources 532 (9) (2022), p. 231296, DOI: 10.1016/j.jpowsour.2022.231296

Permanent weblink:
https://doi.org/10.1016/j.jpowsour.2022.231296

Journal of Power Sources 532 (2022) 231296

Contents lists available at ScienceDirect

Journal of Power Sources

journal homepage: www.elsevier.com/locate/jpowsour

Determination of degradation modes of lithium-ion batteries considering aging-induced changes in the half-cell open-circuit potential curve of silicon–graphite

Julius Schmitt [a,*], Markus Schindler [a], Andreas Oberbauer [a], Andreas Jossen [a,b]

[a] Technical University of Munich, School of Engineering and Design, Department of Energy and Process Engineering, Chair for Electrical Energy Storage Technology, Arcisstraße 21, 80333 Munich, Germany
[b] Technical University of Munich, Munich School of Engineering, Lichtenbergstraße 4a, 85748 Garching, Germany

HIGHLIGHTS

- Aging-induced change in SiC OCP curve is analyzed using a blend electrode model.
- Aged full-cell OCV curves are reconstructed using measured aged SiC OCP curves.
- Full-cell OCV curves are reconstructed using simulated SiC OCP curves.
- Degradation modes are estimated with higher validity avoiding misinterpretations.
- Destruction-free estimation method for component degradation in SiC is presented.

ARTICLE INFO

Keywords:
Lithium-ion battery
Cycle aging
Half-cell open-circuit potential
Silicon–graphite
Degradation modes

ABSTRACT

The shape of the open-circuit potential (OCP) curve of silicon–graphite blend electrodes changes during cycle aging due to the faster degradation of the silicon in comparison to the graphite. In this study, the impact of these changes on the open-circuit voltage (OCV) curve of full-cells is investigated. Reconstructing the OCV curve of aged cells by shifting and linearly scaling pristine half-cell OCP curves is an established diagnostic method of determining the degradation modes occurring in lithium-ion cells. We reconstruct the full-cell OCV curves of cycle-aged commercial cells with silicon–graphite anodes using both pristine and aged silicon–graphite OCP curves. Lower estimates are obtained for the loss of anode active material and higher estimates for the loss of both cathode active material and lithium inventory, when aging-induced changes in the shape of the silicon–graphite OCP are considered. Aging-induced changes in the shape of silicon–graphite OCP curves are integrated in the diagnostic method by using a blend electrode OCP model. This not only improves the validity of the determined degradation modes, but also enables the non-destructive estimation of the anode capacity fraction provided by silicon, based on full-cell OCV measurements.

1. Introduction

The capacity and power that can be provided by a lithium-ion cell decreases during long-term operation [1–3] and storage [4–6]. A vast number of degradation mechanisms have been identified as possible causes of the decrease in cell performance during aging [7]. Most methods used to identify individual degradation mechanisms are complex and necessitate the destruction of the cell during post-mortem analysis, rendering them unusable for onboard application and also limiting their applicability in research. Therefore, rather than analyzing individual mechanisms, the degradation of lithium-ion cells is often analyzed in terms of degradation modes. Degradation modes are clusters of various degradation mechanisms that result in the same observable changes on the cell level [7,8].

Dubarry et al. established a model that describes aging-induced changes in the full-cell open-circuit voltage (OCV) curve, based on three main degradation modes: loss of active material of the anode (LAM_{an}), loss of active material of the cathode (LAM_{cat}), and loss of lithium inventory (LLI) [8]. The model enables degradation modes to be determined based on the cell voltage during low-current charging or discharging, by aligning the open-circuit potential (OCP) curves of both electrodes to the full-cell OCV curve until the difference between the OCP curves fits the measured full-cell OCV curve. Many different

* Corresponding author.
E-mail address: julius.schmitt@tum.de (J. Schmitt).

https://doi.org/10.1016/j.jpowsour.2022.231296
Received 4 January 2022; Received in revised form 23 February 2022; Accepted 7 March 2022
Available online 31 March 2022

Table 1
Nominal cycles during the cycling period and full-cell charging capacity of cells at different aging states.

Cycles	Q_{tot}/EFC	C_{full}/Ah	ΔC/%
0	9	3.40	0
50	54	3.35	1.5
100	101	3.30	2.9
400	361	3.01	11.6
450	410	3.06	10.0
500	444	2.99	11.9
550	486	2.91	14.3

variants of this diagnostic method have been developed and used in recent years [9–21]. The definition and number of observed degradation modes differs between the various studies, as does the model used to simulate the full-cell OCV curve.

The shape of the OCP curve of the individual electrodes is generally regarded to be invariant during battery aging in the models used for analyzing degradation modes based on the full-cell OCV. This means that the OCP curve of an aged electrode can be obtained by linear scaling of the OCP curve of a pristine electrode. Some recent studies consider changes in the shape of the electrode OCP curves. Lee et al. propose an algorithm for adapting the shape of the OCP curve of lithium nickel manganese cobalt oxide (NMC) cathodes during aging [21]. Jia et al. show that the OCV of aged cells can be reconstructed with higher accuracy if the OCP curves of aged electrodes are used [19]. Schindler et al. propose modeling non-uniform electrode degradation using state of charge (SOC) dependent scaling of the half-cell curves [16].

In a recent study [22], we showed that the shape of the OCP curve of NMC-811 does not change significantly when cycled in the full-cell configuration. In contrast, we detected aging-induced changes in the shape of the OCP curve of silicon–graphite. We interpret these changes as being the result of the faster degradation of silicon than graphite during cycling. This affects the relative capacity contribution of both components and, in turn, the shape of the OCP curve of the blend electrode [22]. Increased degradation of the silicon in silicon–graphite blend electrodes in comparison to the graphite has also been reported by other authors [23–26]. It is attributed to increased electric and ionic contact loss of the silicon due to its pronounced expansion and contraction during lithiation and delithiation [23] and morphological changes during cycling [27]. The influence of such changes in the relative capacity contribution of silicon and graphite on the full-cell OCV curve during aging has been described using a blend electrode model [28].

This study expands on our previous findings [22] and investigates the influence of aging-induced changes in the shape of the silicon–graphite OCP curve on the full-cell OCV curve. To our knowledge, this is the first study, in which silicon–graphite half-cell OCP curves measured for cells at a series of aging states are used to reconstruct the full-cell OCV curve at the corresponding aging state. We analyze how changes in the shape of the silicon–graphite OCP influence the degradation modes determined from full-cell OCV curves and propose an extension of the diagnostic method presented by Dubarry et al. [8] that considers changes in the silicon–graphite OCP curve by using the blend electrode model presented by Schmidt et al. [9]. This approach of using a synthetic half-cell OCP curve calculated from pristine pure silicon and graphite OCP curves for the reconstruction of measured aged full-cell OCV curves has, to our knowledge, not been presented in the literature before. It enables the anode capacity fraction provided by the silicon to be estimated based on full-cell OCV curves and half-cell OCP curves of pristine electrode components, without the need for opening up aged cells and performing measurements on aged electrode samples.

2. Experimental

The experimental procedure used for cycling and characterizing commercial full-cells and harvested electrode samples was reported on in our previous work [22]. For this reason, we only provide a summary of the experimental procedure here. For further details, the reader is referred to the original work [22].

This study investigates commercially available cells of the type INR18650-MJ1 (MJ1) made by LG Chem. The cell format is 18 650 and the nominal minimum capacity is 3.35 Ah. The anode active material of this cell consists of a blend of graphite in the shape of ellipsoidal flakes with an average diameter of 15 µm [29] and particles of silicon-based compounds (SiO_x where x is equal to 0, 1, or 2, etc.) that have the shape of sharp-edged shards with an average diameter of 3 µm [29]. Different values for the mass ratio of silicon inside the anode material of this cell type are reported in the literature ranging from 1 wt.% to 5 wt.% [26,29–31]. NMC-811 is used for the cathode active material [29,31]. Full-cell C-rates used in this work refer to a nominal capacity of 3.35 Ah. One equivalent full cycle (EFC) refers to a charge throughput of twice the nominal capacity, which is 6.7 Ah.

The cells were first characterized using a series of procedures that are internally standardized at our institute to determine the long-term evolution of cell characteristics of this type of commercial cell [1,32,33]. A capacity checkup was then conducted comprising two constant current constant voltage (CCCV) cycles. The quasi-stationary OCV of the cells in the pristine state was then measured using low-current CCCV discharging and subsequent CCCV charging between 2.5 V and 4.2 V. The current rate during the constant current (CC) phases was C/30, and a cut-off current of C/1000 was used as the termination criterion for the constant voltage (CV) phase.

The cells were subsequently cycled for up to 550 cycles using CCCV charging and CC discharging at 25 °C. A current rate of C/2 was used for charging, while 1 C was used for discharging. The number of cycles after which the procedure was terminated differed for each cell so as to provoke different levels of degradation (see Table 1).

After the cycling, the quasi-stationary OCV of the aged cells was measured using the procedure described above, and the cells were finally discharged to 3 V using CCCV discharging. The cells were then opened up in an argon-filled glove box and samples from both electrodes were extracted. One cell was not cycled but discharged directly and opened up after characterization to measure the quasi-stationary OCP in the pristine state. The electrode samples were weighed using an analytical scale (Quintix 224-1S, Sartorius Mechatronics), and the quasi-stationary OCP was determined using coin-cell measurements with lithium metal foil as the counter electrode. A low current rate of approximately C/90 was used for the measurement. Details of the coin-cell measurement procedure can be found in Ref. [22].

In addition to the experiments described in Ref. [22], the quasi-stationary OCP of graphite was also measured in this study. Round samples with a diameter of 14 mm were punched out of a sheet of commercially available natural graphite with a mass loading of 13.0 mg cm^{-2}. The sheet was made up of a copper conductor with a graphite coating on both sides. The coating was removed on one side before the samples were obtained. Coin-cells containing a graphite sample and a piece of lithium metal foil as a counter electrode were subsequently constructed. The coin-cells were produced in the same way as described in Ref. [22]. Five formation cycles were applied as follows: CCCV lithiation with a current rate of C/10, a cut-off voltage of 0.01 V, and a cut-off current of C/50 followed by CC delithiation with a current rate of C/10 and a cut-off voltage of 1.7 V. There was a one-hour rest period between each lithiation and delithiation step. The C-rates for these coin-cells refer to a nominal capacity of 5.43 mAh.

The graphite was subsequently CCCV delithiated using a current rate of C/10, a cut-off voltage of 1.7 V, and a cut-off current of C/100. After a rest time of 100 s, the graphite was lithiated at a current rate of C/100 until a cut-off voltage of 0.01 V to measure the quasi-stationary OCP during lithiation. Both formation and OCP measurements were conducted at 25 °C inside an ESPEC LU-123 climatic chamber and using a BaSyTec CTS battery test system.

3. Model and methodology

3.1. Full-cell open-circuit voltage model and degradation diagnosis

The model and method for quantifying degradation modes presented in the following is based on the concept presented by Dubarry et al. [8]. The OCV of a full-cell U_{full} at a certain full-cell SOC x_{full} is calculated as:

$$U_{full}(x_{full}) = U_{cat}(x_{cat}) - U_{an}(x_{an}), \tag{1}$$

where $U_{cat}(x_{cat})$ is the cathode OCP at this full-cell SOC and $U_{an}(x_{an})$ is the anode OCP at this full-cell SOC. The measured potential curves for the anode $U_{an}(x_{an})$ and cathode $U_{cat}(x_{cat})$ are defined as functions of the electrode SOC x_{an} or x_{cat}. The electrode SOC of the anode x_{an} is defined as the amount of lithium inserted into the anode divided by the total amount of lithium inserted into the anode during a lithiation from 1.7 V to 0.01 V. Its value is therefore between 0 and 1, where 1 corresponds to the lithiated state. The electrode SOC of the cathode x_{cat} is defined as the amount of lithium extracted from the cathode divided by the total amount of lithium extracted from the cathode during a delithiation from 3.0 V to 4.3 V. Its value is therefore between 0 and 1, where 1 corresponds to the delithiated state at $U_{cat} = 4.3$ V.

The half-cell voltage limits are chosen as suggested in Ref. [31] to cover at least the lithiation window in which the electrodes are operated in the full-cell configuration throughout the aging. In principle, wider operating limits could be chosen for the half-cells, but we assume for the definition of electrode SOC and capacity that the half-cells should only be operated in the respective voltage windows due to the following considerations: Further delithiation of silicon–graphite would not lead to a significant capacity increase, as it already reaches a virtually fully delithiated state at 1.7 V vs. Li/Li$^+$ [34]. Any further lithiation would lead to a high risk of lithium plating. The NMC-811 is virtually fully lithiated at 3.0 V vs. Li/Li$^+$ [35,36] and any further delithiation above 4.3 V vs. Li/Li$^+$ would lead to increased degradation due to the formation of a surface rock-salt type layer [37].

Calculating the full-cell OCV curve requires a description of both electrode potentials as a function of the full-cell SOC. This can be obtained by aligning the half-cell curves with the full-cell curve as shown in Fig. 1(a). In this figure, both normalized half-cell curves are linearly scaled and shifted with respect to the SOC-axis in order to fit the full-cell curve. This linear scaling and shifting of the electrode OCP curves resembles a transformation of the electrode SOC into the corresponding full-cell SOC. For the anode SOC, this transformation is defined as:

$$x_{full} = \alpha_{an} \cdot x_{an} + \beta_{an}, \tag{2}$$

where α_{an} is the factor by which the anode OCP curve is scaled to fit the full-cell curve and β_{an} is the value by which the anode curve is shifted towards higher full-cell SOC to fit the full-cell curve. α_{an} can be interpreted as the factor by which the anode capacity is oversized in comparison to the full-cell capacity. The cathode SOC in the coordinate system of the full-cell is described by:

$$x_{full} = \alpha_{cat} \cdot x_{cat} + \beta_{cat}, \tag{3}$$

where α_{cat} is the linear scaling factor and β_{cat} is the shift of the cathode OCP curve towards higher SOC. In this model, the point of origin for the scaling of the half-cell OCP is always 0 % electrode SOC, which corresponds to the delithiated state for the anode and the lithiated state for the cathode. As both electrode curves need to have their origin at or below 0 % full-cell SOC, β_{an} and β_{cat} are always negative, which means that the curves are left-shifted in the full-cell coordinate system. By rearranging Eqs. (2) and (3), the respective electrode SOC can be calculated from the full-cell SOC:

$$x_{an} = (x_{full} - \beta_{an})/\alpha_{an}, \tag{4}$$

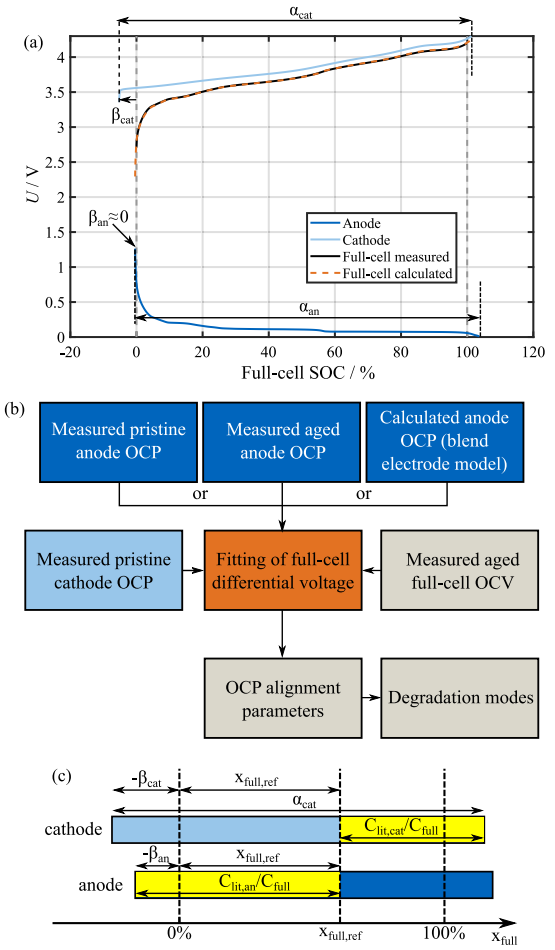

Fig. 1. (a) Reconstruction of a pristine full-cell OCV curve by linear scaling and shifting of pristine half-cell OCP curves. (b) Flowchart describing the method applied in this study for analyzing the impact of changes in the anode half-cell OCP curve on the determination of degradation modes. (c) Schematic representation of the definition of the lithium inventory.

$$x_{cat} = (x_{full} - \beta_{cat})/\alpha_{cat}. \tag{5}$$

Substituting Eqs. (4) and (5) into Eq. (1) yields a description of the full-cell voltage as a function of full-cell SOC:

$$U_{full}(x_{full}) = U_{cat}((x_{full} - \beta_{cat})/\alpha_{cat}) - U_{an}((x_{full} - \beta_{an})/\alpha_{an}). \tag{6}$$

This model enables full-cell OCV curves at different aging states to be described based on measured half-cell curves by adjusting the alignment parameters (α_{an}, α_{cat}, β_{an} and β_{cat}) until the reconstructed full-cell curve fits the measured curve. The alignment parameters can be used to determine the remaining capacity of the individual electrodes, the remaining lithium inventory in the electrodes, and the cell balancing.

The degradation modes are calculated based on the best fit for the alignment parameters. The anode capacity C_{an} at a certain aging state is calculated as the remaining full-cell capacity C_{full} multiplied by the anode scaling factor α_{an} at this aging state. The relative LAM_{an} at a certain aging state is then defined as:

$$LAM_{an} = \frac{C_{an,ini} - C_{an}}{C_{an,ini}}, \tag{7}$$

where $C_{an,ini}$ is the anode capacity in the pristine state. The relative LAM_{cat} is defined in a similar way. The lithium inventory C_{lit} is the lithium available for delithiation in both electrodes [20] starting from an arbitrary reference SOC $x_{full,ref}$ within the voltage limits of the full-cell. The lithium inventory in the electrodes is calculated by:

$$C_{lit} = C_{lit,an}(x_{full,ref}) + C_{lit,cat}(x_{full,ref}), \tag{8}$$

where $C_{lit,an}(x_{full,ref})$ is the capacity of the available lithium in the anode and $C_{lit,cat}(x_{full,ref})$ the capacity of the available lithium in the cathode when the full-cell is at the reference SOC $x_{full,ref}$. The term available lithium refers to the amount that can be potentially delithiated until the half-cell upper cut-off voltage of the respective electrode is reached. Regarding the capacity of the available lithium in the anode, the following applies:

$$C_{lit,an}(x_{full,ref}) = C_{full} \cdot (x_{full,ref} - \beta_{an}), \tag{9}$$

as the capacity of the available lithium in the anode is $C_{full} \cdot x_{full,ref}$ plus the portion of the anode capacity below 0 % full-cell SOC, which is equal to $C_{full} \cdot (-\beta_{an})$. The negative sign is necessary, as β_{an} is defined as negative for a left-shifted anode curve. The capacity of the available lithium in the cathode is given by:

$$C_{lit,cat}(x_{full,ref}) = C_{full} \cdot (\alpha_{cat} - x_{full,ref} + \beta_{cat}), \tag{10}$$

as it is the complete cathode capacity ($C_{full} \cdot \alpha_{cat}$) minus the delithiated part below $x_{full,ref}$. The concept of this definition for C_{lit} is shown as a schematic in Fig. 1(c). Substituting Eqs. (9) and (10) into Eq. (8) yields:

$$C_{lit} = [(x_{full,ref} - \beta_{an}) + (\alpha_{cat} - x_{full,ref} + \beta_{cat})] \cdot C_{full}. \tag{11}$$

It should be noted that $x_{full,ref}$ cancels out in Eq. (11), as the lithium inventory does not depend on the chosen reference SOC. The relative LLI is defined as

$$LLI = \frac{C_{lit,ini} - C_{lit}}{C_{lit,ini}}. \tag{12}$$

The following algorithm is used for the alignment of half-cell and full-cell curves. Both half-cell and full-cell curves are normalized, i.e., the measured charge throughput during charging of the full-cell, lithiation of the anode, or delithiation of the cathode, is divided by the charge throughput at the end of the procedure. A full-cell OCV curve is then calculated using Eq. (6) with an initial estimate of the alignment parameters. Next, the differential voltage (DV):

$$\left.\frac{dU}{dQ}\right|_{x_{full}} = \frac{U_{full}(x_{full} + \Delta x) - U_{full}(x_{full})}{\Delta x} \tag{13}$$

is calculated at 2001 equally spaced interpolation points between $x_{full} = 0$ and $x_{full} = 1$ for both the calculated and the measured full-cell OCV curve. Interpolating at this number of points, in our case, yields a sufficiently high resolution of the DV curve in the SOC dimension while the optimization can be executed in an appropriate time. Δx is a small fraction (0.2 %) of the SOC range for which the OCV curve is linearly approximated to calculate the local differential voltage. Then, the difference between the DV of the calculated and the measured OCV is evaluated at each interpolation point to obtain a measure of the fitting of both curves. The *lsqnonlin* function using the trust-region-reflective algorithm implemented in MATLAB® is used to minimize the sum of squared differences between the DV curves by varying the alignment parameters. The difference between the DV curves is used instead of the absolute OCV difference as an objective function for optimization, in order to align the features of the DV curves that represent the phases and phase transitions of the active materials and to minimize the influence of absolute offsets of the OCV curves. The difference between the DV curves at the edges of the full-cell SOC range (1 % at each side) is excluded to avoid the optimization being dominated by the steep slope of the OCV curves near the edges.

The influence of aging-induced changes in the shape of the anode OCP curve, i.e., a change in the function $U_{an}(x_{an})$, is investigated as follows: The quasi-stationary full-cell OCV, measured during low-current charging of the cells at different aging states just before they are opened up, is fitted with half-cell OCP curves according to the method described above. In the case of the cathode OCP, the half-cell curve measured with material extracted from the pristine full-cell is always used, because the shape of the curve does not change significantly during cycle aging [22]. Three different anode curves are used: the curve measured for material extracted from the pristine full-cell, the curve measured for the aged anode material extracted from the respective cell following the full-cell OCV measurement, and a synthetic curve calculated using a blend electrode model as described in Section 3.2. The measured OCP curves are averaged from multiple samples [22] and smoothed with a moving average filter before fitting.

A set of alignment parameters is thus obtained for each investigated aging state and for all three types of anode OCP curves. Finally, the degradation modes are calculated based on the different sets of alignment parameters. A schematic of the approach used in this study is shown in Fig. 1(b).

3.2. Silicon–graphite blend open-circuit potential model and determination of component degradation

We model the OCP curve of the silicon–graphite blend electrode using the following model, which was described by Schmidt et al. for a generic blend electrode [9]. The fraction of the capacity that can be inserted into a component of the silicon–graphite blend during lithiation until a potential U is reached is denoted as $Q_{Si}(U)$ for the silicon and $Q_G(U)$ for the graphite. The fraction of the blend anode capacity that is lithiated at this voltage is then given by:

$$Q_{blend}(U) = \gamma_{Si} \cdot Q_{Si}(U) + (1 - \gamma_{Si}) \cdot Q_G(U), \tag{14}$$

where γ_{Si} is the fraction of the total anode capacity provided by the silicon. At the lower cut-off voltage U_{min}, both $Q_{Si}(U)$ and $Q_G(U)$ are equal to one by definition, and therefore $Q_{blend}(U)$ is also one. $Q_{Si}(U)$ and $Q_G(U)$ are obtained by taking the inverse of the OCP curve of the respective component as a function of normalized charge. The OCP of the blend anode as a function of normalized charge or electrode SOC Q_{blend} can then be obtained from:

$$U_{OCV,blend}(Q_{blend}) = f^{-1}(Q_{blend}(U)). \tag{15}$$

The shape of $U_{OCV,blend}(Q_{blend})$ is affected by the value of γ_{Si}. The blend OCP curve is similar to that of graphite for small values of γ_{Si} and similar to that of silicon for large values of γ_{Si}. Fig. 2(a) shows OCP curves for graphite and silicon. The graphite curve is measured as described in the experimental section. Small local minima (<1 mV) in the voltage curve occurring during lithiation, which are most probably measurement artifacts, are removed to enable inversion of the curve. The lithiation curve of pure silicon is taken from Li et al. [38].

This model is used to determine the capacity fraction of the silicon component of a silicon–graphite anode, by constructing blend OCP curves for various values of γ_{Si} and minimizing the difference between the DV curves of the calculated and measured OCP curves. The optimization procedure is the same as the one used for fitting the full-cell OCV curves with half-cell OCP curves. Again, 1 % of the electrode SOC range are excluded at both edges of the voltage window during the optimization.

We also use synthetic OCP curves calculated with the blend electrode model to reconstruct measured full-cell OCV curves. To do this, a silicon–graphite OCP curve is first calculated using the blend electrode model. Then, the full-cell OCV curve is reconstructed by aligning both the synthetic anode OCP and the pristine cathode OCP. The silicon capacity fraction γ_{Si} used to calculate the anode OCP is then optimized along with the four alignment parameters.

If the gravimetric specific capacities of both components are known, an estimate for the mass fraction of the pristine anode that consists of silicon can be calculated, based on γ_{Si}. The silicon mass fraction can be obtained as a function of γ_{Si} by:

$$\frac{m_{Si}}{M_{blend}} = \frac{\gamma_{Si} \cdot c_G}{c_{Si} - \gamma_{Si} \cdot (c_{Si} - c_G)}, \tag{16}$$

where m_{Si} is the silicon mass, M_{blend} the total mass of the active blend material, c_{Si} the gravimetric specific capacity of silicon, and c_G the gravimetric specific capacity of graphite. The derivation of Eq. (16) can be found in the Appendix.

4. Results and discussion

As reported in our previous work [22], the investigated cells are at different aging states following cycling periods of varying duration. Table 1 lists the total charge throughput Q_{tot}, i.e., the number of equivalent full-cycles applied to the cells until the quasi-stationary OCV measurement prior to cell opening. In this study, the charge throughput during low-current charging after cycling and prior to cell opening is taken as the value of the remaining full-cell capacity C_{full}. Table 1 also lists the remaining full-cell capacities of the individual cells along with the relative capacity losses ΔC. In this section, we will analyze the degradation modes occurring during cell cycling.

4.1. Changes in the silicon–graphite open-circuit potential curve

To illustrate the calculation of a silicon–graphite OCP curve using the blend electrode model, Fig. 2(a) shows the measured and calculated OCP curves of a pristine blend electrode using γ_{Si} = 9.52%, which is obtained by optimization. The calculated curve fits the measured curve well. The right-shift of the graphite features in comparison to the pure graphite curve can be simulated particularly well with the model. The root-mean-square error (RMSE) between the measured and the calculated OCP curve is 6.6 mV.

In our previous work [22], we show that the shape of the OCP curve of the silicon–graphite used in the investigated cell type changes during cycle aging. The most prominent changes are a left-shift of both the graphite and silicon DV peaks towards a lower electrode SOC. This change is most probably caused by a decrease in the fraction of the electrode capacity provided by the silicon. The blend electrode model is capable of simulating OCP curves of electrodes with varying capacity contributions of the components and is therefore used here to describe the changes in the shape of the silicon–graphite OCP curves. The silicon–graphite OCP curves measured at different aging states are fitted using the model. As an example, the measured and calculated OCP curves of both the pristine silicon–graphite and the silicon–graphite cycled for 488 EFC in the full-cell configuration are shown in Fig. 2(b). The model is able to capture the aging-induced changes in the curve shape. The model captures the reduced charge inserted between 0.3 V and 0.2 V due to reduced silicon capacity and the shift of voltage slopes associated with graphite stages 4L to 2L towards lower SOC particularly. The RMSE between the calculated and the measured OCP curve is below 6.9 mV for all aging states, which shows that the model is suitable for fitting OCP curves of aged cells. This finding has two implications: First, it supports the theory that the change in the silicon–graphite OCP is caused by a faster capacity decrease of the silicon compared to the graphite [22]. Second, fitting aged OCP curves of silicon–graphite with the blend electrode model serves as a diagnostic tool for obtaining an estimate of the capacity fraction provided by both electrode components during cell aging.

Fig. 2(c) shows the fitting results of the relative capacity contribution of silicon γ_{Si} for the different aging states. There is a clear trend towards a lower capacity contribution of silicon as aging progresses. Predominant degradation of the silicon in silicon–graphite has also been reported in the literature [23–25,39]. The deviation of single data points from this trend is probably due to intrinsic cell variations, leading to differences in the aging behavior of the individual cells [1,33]. The fraction of the electrode capacity provided by the silicon for the electrode to which the most cycles (488 EFC) are applied is estimated at 5.55 %, which is only about 58 % of the initial value.

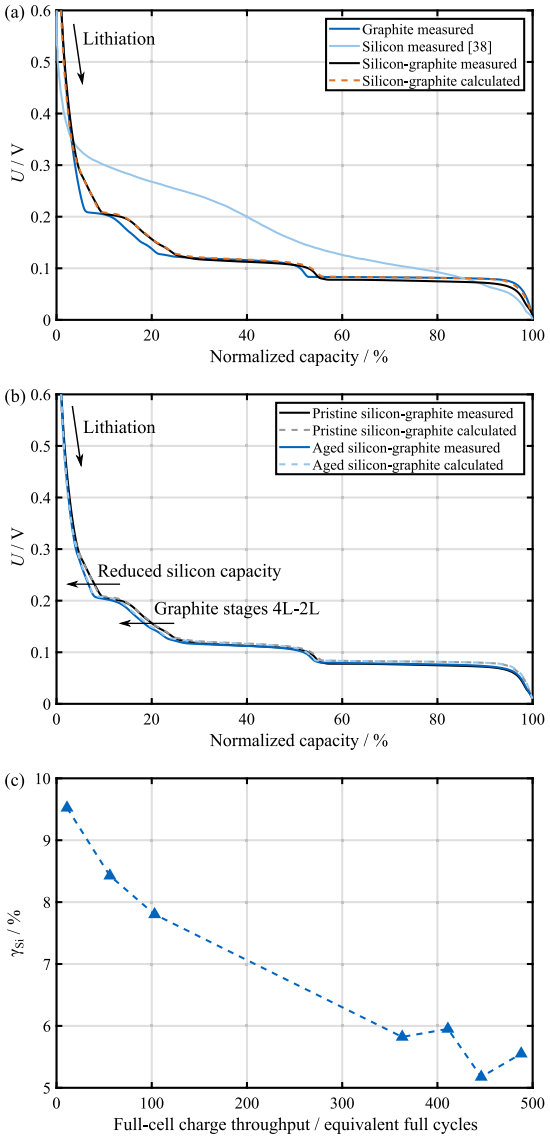

Fig. 2. (a) Reconstruction of the measured pristine silicon–graphite OCP curve based on the normalized lithiation curves of the electrode components using the blend electrode model. The lithiation curve of silicon is obtained from Ref. [38]. (b) Measurement and model calculation of a pristine and a cycle aged (488 EFC) silicon–graphite electrode. (c) Fraction of the silicon–graphite electrode capacity provided by silicon determined by fitting silicon–graphite half-cell curves at different aging states with the blend electrode model.

Using the theoretical values of the gravimetric specific capacities c_{Si} = 3579 mAh g^{-1} [25,38] and c_G = 372 mAh g^{-1} [40], in Eq. (16), the mass fraction of electrochemically active silicon as part of the silicon–graphite blend is determined to be 1.08 %. If it is assumed

that 5 wt.% of the anode material is made up of binder and carbon black, electrochemically active silicon should comprise 1.03 % of the total anode mass for pristine electrodes of this type. The total amount of silicon in the anode is probably higher, as higher values of the mass fraction of silicon have been reported in the literature for this cell type, but part of the silicon might be electrochemically inactive. Approximately 3.5 wt.% silicon was determined by inductively coupled plasma-optical emission spectroscopy (ICP-OES) [31], approximately 4.5 wt.% using energy-dispersive X-ray spectroscopy (EDS) [26] and approximately 3–4 wt.% using X-ray computed tomography (CT) [29]. It should also be noted that the precise composition of this commercial cell type has changed in recent years and the relative silicon content of the anode is lower for cells that were produced later, due to a change in the composition used by the manufacturer [32]. Therefore, the cells investigated in this study probably also contain less total silicon than those whose silicon content was reported in Refs. [26,29,31], even though they are of the same type.

To check the plausibility of our estimate of the electrochemically active silicon mass, we will now compare the calculated and measured absolute capacities of the pristine coin-cell samples. The average mass of the anode samples, including current collectors, is 35.9 mg. Subtracting an estimated mass for the current collector of 15.2 mg [31] yields an average electrode mass of 20.8 mg corresponding to a mass loading of 13.5 mg cm^{-2}. We assume that 5 % of the electrode mass comprises inactive components and 3.5 % [29,31] of the electrode mass consists of silicon, but only 1.03 % of the electrode mass is electrochemically active silicon and the remaining part is electrochemically inactive. The remaining 91.5 wt.% of the electrode mass is assumed to be graphite. Using these estimates and the theoretical gravimetric specific capacities, the absolute coin-cell capacity is calculated as 7.84 mAh. The average measured capacity during lithiation of the pristine silicon–graphite samples is 7.40 mAh. The calculated and measured capacities thus differ by less than 6 %, which leads us to the conclusion that our estimate of the capacity fraction provided by the silicon is plausible. If the entire 3.5 wt.% silicon were electrochemically active, the calculated coin-cell capacity would be 9.55 mAh, which clearly exceeds the measured value of 7.40 mAh. Our conclusion is therefore that a significant part of the silicon in the anode is electrochemically inactive which explains the discrepancy between our estimate regarding the silicon mass fraction and the results for the total silicon mass fraction provided in the literature [26,29,31]. Besides, a silicon capacity fraction of 10 % was also reported for a commercial silicon–graphite electrode with 3–4 wt.% silicon in Ref. [28]. The diagnostic method used to determine the capacity fraction provided by the silicon presented in our study might be an even better indicator of the practically usable silicon capacity than estimations based on the measured total silicon mass fraction, because the method only considers electrochemically active silicon, which might only be a fraction of the present silicon and also might change during cell aging.

4.2. Changes in the full-cell open-circuit voltage curve

Fig. 3(a) displays the quasi-stationary OCV during low-current charging for cells that have undergone different numbers of cycles. As a general trend, the absolute voltage at the same SOC increases with cycling. This is probably due to LLI leading to a shift in cell balancing such that the cathode is in a more delithiated state at the same full-cell SOC during full-cell charging [23]. In addition, the positions of the features of the OCV curve change, as analyzed on the basis of the DV curves. In Fig. 3(b), the normalized DV is plotted against the SOC. The peaks in the DV plot correspond to lithiation phases of the anode or the cathode. The minima correspond to phase transition regimes where two lithiation phases coexist. In Fig. 3(b), the peaks are associated with lithiation phases based on Refs. [4,37,41].

Changes in the shape of the OCV curve are evident during cycle aging. The peaks of the DV curve are at a lower SOC for aged cells, which means that the lithiation phases are reached earlier on in the charging process. There are two changes in the curve features that can be attributed to the cathode: The broad central peak between approximately 50 % and 60 % SOC corresponding to the monoclinic M-phase of NMC-811 [37] shifts to the left during cycling. This peak is not clearly visible for the pristine and mildly aged cells, as it is superimposed with the stage 2 peak of the graphite. Due to the left-shift, this peak becomes discernible for cells cycled for ≥361 EFC. The peak around 80 % SOC corresponding to the hexagonal H2-phase of NMC-811 [37] also shifts to the left during cycling. Both of these peak shifts are probably due to a change in the balancing between the two electrodes. As cyclable lithium is lost, the cathode becomes more delithiated during charging of the full-cell. The cathode half-cell curve therefore shifts to the left in comparison to the anode half-cell curve [16]. For this cell type, the anode is always limiting at 0 % full-cell SOC, as will be shown in Section 4.3. Therefore, this relative shift of the cathode OCP curve results in a left-shift of the cathode peaks in the full-cell DV curve.

In addition to the changes related to the cathode, there are also changes that can be attributed to the anode. The peaks corresponding to the partly lithiated graphite stages between 4L and 2L around 20 % SOC [41] shift to a lower SOC during aging. The peaks below 10 % SOC corresponding to silicon phases [4] are also located at a lower SOC for the cells that have been cycled for a longer period. There are two possible explanations for this observation: The traditional explanation, neglecting changes in the shape of the electrode OCP, would be that there is a higher relative loss of anode active material compared to the loss of cathode active material. This corresponds to a compression of the anode curve in the model. As the anode is limiting at 0 % SOC, compression of the anode OCP curve leads to a left-shift of the anode features in the full-cell OCV. But taking into account the results from our analysis on the electrode level, this shift of silicon and graphite peaks in the full-cell DV curve could also be caused by the changes in the shape of the anode half-cell OCP curve due to silicon degradation being faster than graphite degradation. As both effects would lead to the same results with regard to the full-cell OCV, the left-shift of the anode peaks in the full-cell DV can be misinterpreted as resulting solely from an overall anode active material loss. In fact, at least some of the left-shift of the anode peaks is most likely due to changes in the silicon–graphite half-cell curve caused by the faster degradation of silicon.

The central peak corresponding to stage 2 graphite exhibits some variation and decreases in height during aging, but there is no clear trend in its position. The decrease in the height of this peak is probably caused by an increase in the inhomogeneity of the anode [42–44].

4.3. Reconstruction of full-cell open-circuit voltage curves

The aging-induced changes in the quasi-stationary OCV curve during full-cell charging are analyzed quantitatively using the OCV model and the fitting procedure described in Section 3.1. In order to investigate the influence of changes in the shape of the silicon–graphite OCP during aging, the full-cell OCV curves are reconstructed using the pristine anode OCP curve, the aged anode OCP curve, i.e., the anode OCP measured at the same aging state as the full-cell OCV, and an OCP curve calculated using the blend electrode OCP model. As an example, the reconstruction of the OCV curve of the cell cycled for 486 EFC is shown in Fig. 4. The different interpretations of the changes in anode features in the full-cell OCV, depending on whether changes in anode half-cell OCP are considered, are visible here. In Fig. 4(a), the pristine anode half-cell curve is used to reconstruct the full-cell curve. The anode features in the full-cell curve, in particular the voltage slope associated with the 4L to 2L stages of graphite, are shifted to the left with respect to the pristine full-cell OCV. To obtain this left-shift in the reconstructed curve, the anode curve is compressed. This compression is interpreted as a loss of anode active material. Consequently, at 100 %

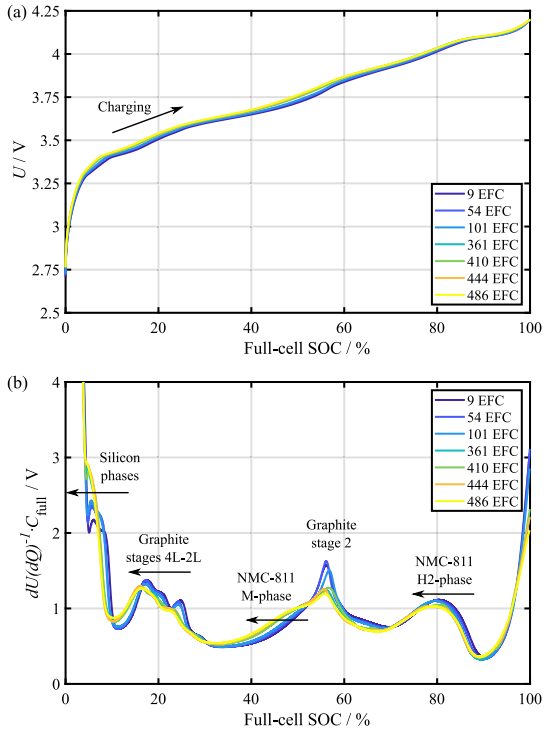

Fig. 3. (a) Quasi-stationary OCV curve of full-cells at different aging states during low-current (C/30) charging. (b) Normalized differential voltage of cells at different aging states during low-current charging.

full-cell SOC, the anode potential has already left the voltage plateau corresponding to the transition between graphite stage 2 and 1, and the anode potential is a limiting factor for reaching the upper full-cell cut-off voltage at the end of charging. In Fig. 4(b), the same aged full-cell OCV is reconstructed using the aged anode half-cell curve. This curve already exhibits a left-shift of the features related to anode lithiation phases on the half-cell level. Therefore, the anode curve is compressed less during the reconstruction of the full-cell curve. The same applies to the reconstruction of the full-cell curve using an anode curve simulated with the blend electrode OCP model shown in Fig. 4(c): Here, the left-shift of the anode features in the full-cell OCV is partly realized at the half-cell level by reducing the capacity contribution of silicon, and less compression of the whole anode curve is required compared to using the pristine anode curve. If changes in the half-cell OCP are considered, the anode is not identified as limiting at the end of charge, as the anode potential at 100 % full-cell SOC is still within the voltage plateau.

Fig. 5 shows the RMSE between the measured and the calculated full-cell OCV curve at different aging states for the three types of anode OCP curves. There is a general trend of increase in the RMSE with cell cycling. This might be due to an increase in electrode inhomogeneity during cycle aging [43,44], which also affects the OCV curve and is not considered in the model. Still, as the RMSE is always below 12 mV, a good agreement between the measured and the constructed curve is obtained for all three types of anode curves and at all aging states. Therefore, aging-related changes in the full-cell OCV curve can be accurately described with the model regardless of whether changes in the anode half-cell OCP are considered. But while having a small impact on fit accuracy, the consideration of changes in the half-cell OCP shape influences the quantitative results for the alignment parameters and therefore the interpretation of the changes in the full-cell OCV.

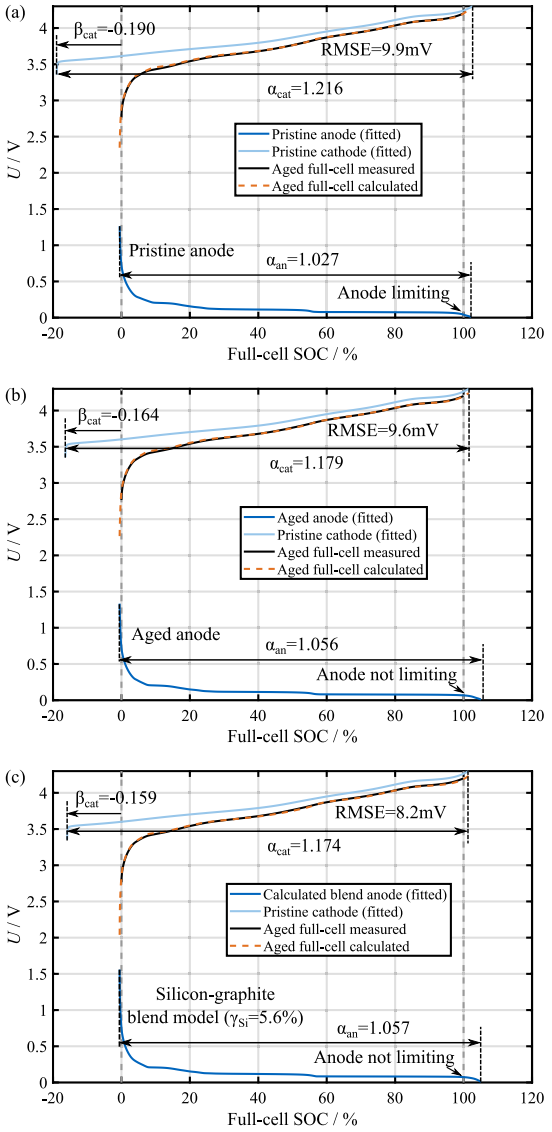

Fig. 4. Reconstruction of the quasi-stationary OCV during charging of a full-cell cycled for 486 EFC using (a) the anode half-cell curve of the pristine material, (b) the anode half-cell curve of the aged material, and (c) a synthetic anode OCP curve representing the half-cell curve of aged material calculated with the blend electrode model.

Fig. 6 contains plots of the four alignment parameters obtained at different aging states. The results are shown for all three types of anode curves. The progression of the anode scaling factor α_{an} is shown in Fig. 6(a). In the pristine state, the anode capacity is approximately 4 % larger than the full-cell capacity. An almost complete use of the anode has also been reported in the literature for this cell type [31]. Different trends for the progression of α_{an} are found, depending on whether changes in the anode half-cell OCP are considered. If the pristine anode OCP is used to reconstruct the aged full-cell OCV curves, there is a decreasing trend in α_{an} during aging. As discussed above, the left-shift of the anode features in the full-cell OCV curve is obtained by compressing the anode curve when the pristine anode OCP is used.

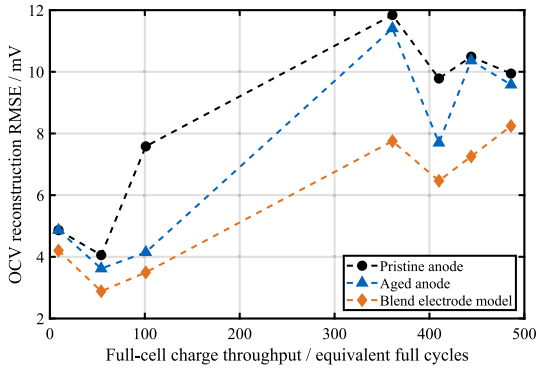

Fig. 5. Root-mean-square error for the reconstruction of the full-cell OCV at different aging states. The RMSE is plotted for using the pristine anode OCP, the aged anode OCP at a certain aging state, and synthetic OCP curves calculated with the blend electrode model.

A different result is obtained when changes in the anode half-cell OCP are considered: Regardless of whether the aged anode half-cell curves or the OCP curves calculated with the blend electrode model are used, α_{an} tends to increase during aging. However, this does not mean that there is an increase in absolute anode capacity. Rather, it should be interpreted such that less of the anode capacity is used within the voltage limits of the full-cell due to LLI.

The results of the anode offset β_{an} during aging are plotted in Fig. 6(b). The anode offset is close to zero ($|\beta_{an}| < 0.6\,\%$) throughout aging and for all types of anode curves. This means that the anode is always limiting the usable full-cell capacity at the lower cut-off voltage. There are small deviations (<0.12 percentage points) between the values of β_{an} obtained with the different types of anode curves, but these are probably due to the fitting and have no physical significance.

Fig. 6(c) shows plots of the progression of the cathode scaling factor α_{cat} during aging. For the pristine cell, the cathode capacity within the half-cell voltage limits is approximately 7 % larger than the full-cell capacity. Similar results have previously been reported for this cell type [31]. The cathode scaling factor increases during cycling, which means that a smaller fraction of the cathode capacity is used with ongoing aging, probably caused by LLI. The values of α_{cat} obtained for the heavily aged cells (≥361 EFC) are more than 2 percentage points smaller if changes in the anode half-cell curve are considered in the reconstruction process.

The cathode offset β_{cat} at different aging states is shown in Fig. 6(d). The cathode offset is estimated to be approximately −5 % for the pristine cell, which means that the cathode is not fully lithiated at the lower cut-off voltage of the full-cell. During aging, β_{cat} decreases further, corresponding to a left-shift of the cathode OCP curve. A relative left-shift of the cathode curve corresponds to LLI leading to a change in the balancing between the electrodes [16]. The decrease in β_{cat} is found to be smaller where changes in the shape of the anode OCP are considered.

4.4. Estimation of the silicon capacity based on full-cell open-circuit voltage curves

In Section 4.3 the influence of changes in the shape of the silicon–graphite OCP curve on the full-cell OCV curve during aging is analyzed by using measured aged silicon–graphite OCP curves and synthetic silicon–graphite OCP curves calculated with the blend electrode model to reconstruct aged full-cell OCV curves. While the first approach allows the impact of changes in the half-cell OCP on the degradation modes observable in the full-cell OCV curves to be analyzed on the basis of experimental results, the latter approach is particularly suitable as a diagnostic method in research and applications as it requires less experimental effort. The measurement of aged half-cell OCP curves is not necessary with this procedure. Instead, the blend anode OCP curve is calculated based on the OCP curves of pristine pure graphite and pristine pure silicon. The anode capacity fraction provided by silicon γ_{Si} is obtained by optimization, i.e., variation of γ_{Si} and the four alignment parameters to minimize the difference between the DV of the measured and that of the reconstructed full-cell OCV. Using this procedure enhances the validity of the results of the degradation modes in comparison to using the pristine silicon–graphite curve for the reconstruction of the full-cell OCV. It also enables the capacity fraction of the anode provided by the silicon to be estimated, without necessitating the measurement of the half-cell OCP curves of aged cells.

The results obtained for the anode capacity fraction provided by silicon are shown in Fig. 7. The results we obtain by reconstructing the aged full-cell OCV curves are similar to those we obtain for the reconstruction of the aged half-cell curves presented in Section 4.1. Both sets of values are shown in Fig. 7. The difference between the estimation based on full-cell curves and the one based on half-cell curves is below 0.8 percentage points for all aging states. The results for γ_{Si} obtained by reconstructing the full-cell curves are slightly higher than those obtained by fitting the half-cell curves. Like the results based on half-cell curves, γ_{Si} determined from full-cell curves tends to decrease during aging. The anode capacity fraction provided by silicon is estimated at 10.3 % for the pristine cell and 5.6 % for the cell cycled for 486 EFC. Using Eq. (16) and assuming the theoretical gravimetric specific capacities for silicon and graphite, the silicon mass fraction of the pristine anode material is estimated at 1.1 %.

The method we propose here may be useful for determining changes in the component balancing of composite electrodes. In addition to being non-destructive and easy to execute, the method has further possible advantages: Unlike methods that quantify total silicon mass such as ICP-OES [31] or EDS [26], this method only determines the capacity of the electrochemically active part of the silicon. In an application context, this quantity might be even more relevant than the total silicon mass. It also enables the degradation of the silicon to be analyzed, which is not possible with methods that determine total silicon mass, as the quantity does not change during aging [26], even though the usable capacity of the silicon decreases.

4.5. Determination of degradation modes

The degradation modes occurring during the cycling are calculated using the results of the alignment parameters for aged cells and the changes in full-cell capacity listed in Table 1. Fig. 8(a) shows LAM_{an}, which displays an increasing trend during cell cycling. As discussed above, a lower anode capacity loss is determined if the aged anode curves or anode curves calculated with the blend electrode model are used than when using the pristine anode curve, because the left-shift of the anode features in the full-cell OCV curve is obtained in part from the changes in the shape of the anode curve rather than solely from compression of the anode curve. The values obtained for LAM_{an} with aged anode curves are very similar to those obtained using synthetic curves calculated with the blend electrode model. If changes in the silicon–graphite OCP are considered, the LAM_{an} after 486 EFC is estimated at 13.1 %. In contrast, the LAM_{an} is estimated at 15.5 % if the pristine silicon–graphite OCP is used. Regardless of whether or not changes in the silicon–graphite OCP are considered, the LAM_{an} is identified as an important degradation mode for this cell type and under these operation conditions. Significant degradation by LAM_{an} has also been reported by other authors [4,26,44] for this cell. Still, the loss of anode material is probably overestimated by something in the order of a few percentage points if no changes in the shape of the silicon–graphite OCP are considered.

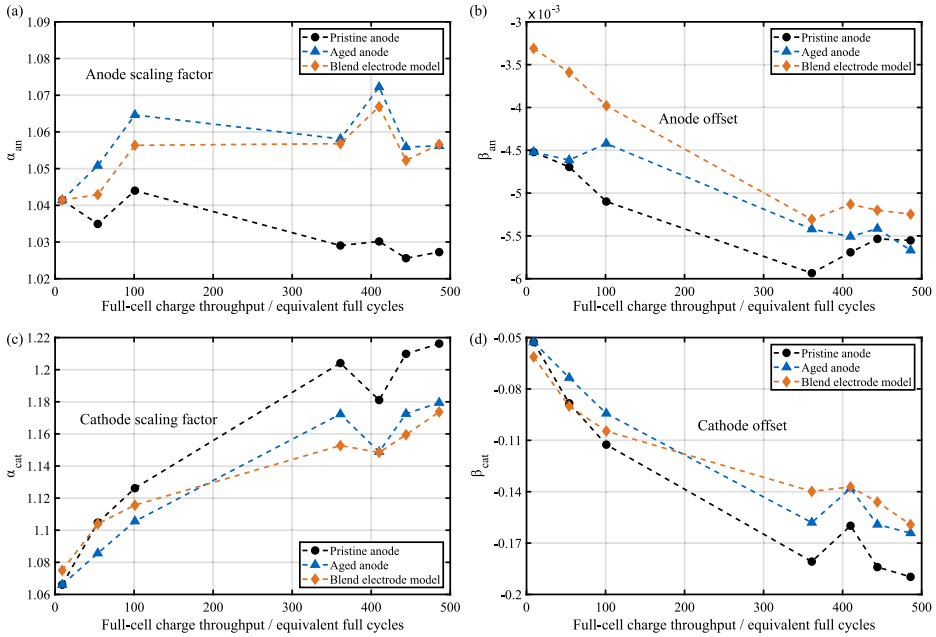

Fig. 6. Alignment parameters obtained by reconstructing the full-cell OCV curve at different aging states using different types of anode half-cell curves: (a) anode scaling factor, (b) anode offset, (c) cathode scaling factor, (d) cathode offset.

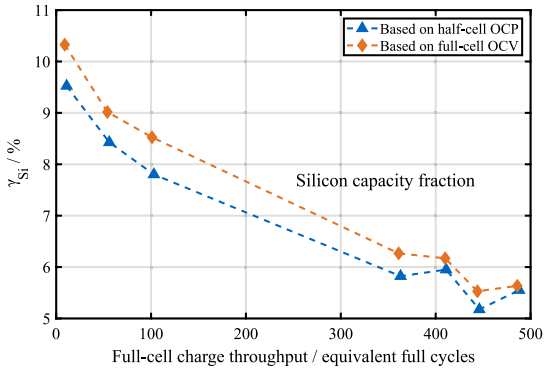

Fig. 7. Estimate of the fraction of anode capacity provided by the silicon at different aging states. Results obtained by reconstruction of half-cell OCP curves of silicon–graphite and full-cell OCV curves are shown.

LAM_{cat} during cycling is shown in Fig. 8(b). During the first 100 EFC, the estimated values for LAM_{cat} are negative, which corresponds to a slight increase in cathode capacity. The capacity increase is more pronounced if the pristine anode half-cell curve is used. After 100 EFC, LAM_{cat} starts to increase. Using aged anode curves yields similar values for the more aged cells (≥361 EFC) to those obtained with the blend electrode model. Using the pristine anode curve results in values for the LAM_{cat} of cells cycled for more than 361 EFC that are approximately 3 percentage points lower. The drop in cathode capacity might therefore be slightly underestimated, when changes in the shape of the anode curve are neglected. Overall, the loss of cathode active material is much lower than LAM_{an}, which is in accordance with the literature [29,43,44], regardless of whether changes in the silicon–graphite OCP are considered or not. For example, if the measured aged anode curves are used, 5.3 % LAM_{cat} and 15.5 % LAM_{an} are estimated for the cell cycled for 486 EFC.

Fig. 8(c) shows the LLI for different aging states. The LLI exhibits an increasing trend during cycling. The estimate for the LLI is very similar to the relative capacity loss of the cells listed in Table 1. At all aging states, the amount of available lithium in the electrodes that could be delithiated up to the upper electrode cut-off voltage is only slightly higher than the amount of lithium used within the voltage limits of the full-cell. This means that there is significant LLI throughout aging. The estimated LLI is up to 1.1 percentage points higher if changes in the silicon–graphite OCP are considered.

Summing up the results regarding the degradation modes, the capacity loss observed for this cell type under these operating conditions is caused by both LAM_{an} and LLI. Considering aging-induced changes in the shape of the anode half-cell curve leads to lower estimates for LAM_{an} and higher estimates for LAM_{cat} and LLI, and improves the validity of the estimates for the individual degradation modes.

5. Conclusion

Expanding on the results of our previous study regarding the changes in the shape of the OCP curve of silicon–graphite during full-cell cycling [22], we show that these changes in the OCP curve can be described by a blend electrode model. Fitting OCP curves of cycle-aged silicon–graphite with the model enables the capacity fraction contributed by the individual electrode components to be estimated. We deduce from the half-cell OCP measurements that the capacity fraction provided by the silicon is approximately 9.5 % for a pristine electrode decreasing to 5.5 % for an electrode cycled for 488 EFC in the full-cell configuration. The silicon therefore degrades faster than the graphite under the operating conditions used in our study.

An accurate reconstruction of aged full-cell OCV curves can be obtained by shifting and scaling half-cell OCP curves regardless of whether aging-related changes in the shape of the silicon–graphite OCP are considered or not. Still, the validity of the degradation mode

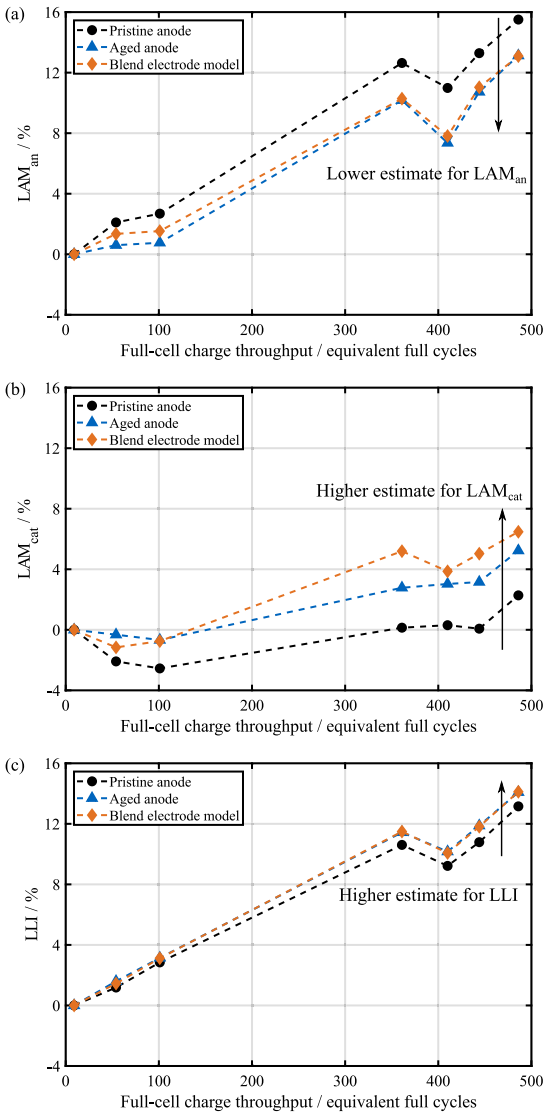

Fig. 8. (a) Loss of active material of the anode, (b) loss of active material of the cathode, and (c) loss of lithium inventory for cells cycled for a different number of equivalent full-cycles estimated via reconstruction of full-cell quasi-stationary OCV curves. The results obtained using the pristine anode half-cell curve, aged anode half-cell curves, and synthetic anode half-cell curves calculated with the blend electrode model are shown.

estimates obtained with this diagnostic method can be improved by considering aging-induced changes in the shape of the silicon–graphite OCP curve. For the investigated cell, the loss of anode active material is probably slightly overestimated, while the loss of cathode active material and the LLI are slightly underestimated if changes in the silicon–graphite OCP are neglected.

In addition, expanding the diagnostic method by using synthetic anode curves calculated with a blend electrode model, as proposed in this study, enables an estimation of the anode capacity fraction provided by the individual electrode components. The estimates that we obtain for the anode capacity fraction provided by the silicon based on low-current full-cell charging curves are similar to those that we obtain from silicon–graphite half-cell lithiation measurements. The method proposed in this study can be used for the destruction-free estimation of the component specific degradation of silicon–graphite.

Besides analyzing low-current charging curves measured under laboratory conditions, this diagnostic method might also be applied to the analysis of cell degradation based on measurements obtained during typical charging phases of applications. Further research is necessary to investigate how the proposed method performs using only partial charging curves or charging curves obtained at higher current rates.

Table of abbreviations

CC	Constant current
CCCV	Constant current constant voltage
CT	X-ray computed tomography
CV	Constant voltage
DV	Differential voltage
EDS	Energy-dispersive X-ray spectroscopy
EFC	Equivalent full cycle
ICP-OES	Inductively coupled plasma-optical emission spectroscopy
LAM$_{an}$	Loss of active material of the anode
LAM$_{cat}$	Loss of active material of the cathode
LLI	Loss of lithium inventory
MJ1	LG Chem INR18650-MJ1 (cell type)
NMC	Lithium nickel manganese cobalt oxide
OCP	(Half-cell) open-circuit potential
OCV	(Full-cell) open-circuit voltage
RMSE	Root-mean-square error
SOC	State of charge

CRediT authorship contribution statement

Julius Schmitt: Conceptualization, Methodology, Validation, Formal analysis, Investigation, Writing – original draft, Writing – review & editing, Visualization. **Markus Schindler:** Writing – review & editing. **Andreas Oberbauer:** Investigation, Writing – review & editing. **Andreas Jossen:** Writing – review & editing, Supervision, Project administration, Funding acquisition.

Declaration of competing interest

The authors declare that they have no known competing financial interests or personal relationships that could have appeared to influence the work reported in this paper.

Acknowledgments

This work was supported by the German Federal Ministry for Economic Affairs and Energy (grant number 03ETE019F). The responsibility for this publication lies with the authors. The fruitful discussions with Alexander Karger and Sebastian Ludwig are gratefully acknowledged. We would like to thank Fabian Oehler, Axel Durdel, Marco Fischer, Ilya Zilberman and Jan Philipp Schmidt for proofreading the manuscript.

Appendix. Derivation of formula for silicon mass fraction

Absolute silicon capacity C_{Si} is calculated as a fraction of the total capacity of the blend C_{blend}:

$$C_{Si} = \gamma_{Si} \cdot C_{blend}. \tag{A.1}$$

Silicon capacity can also be calculated as:

$$C_{Si} = m_{Si} \cdot c_{Si}, \tag{A.2}$$

where m_{Si} is the silicon mass and c_{Si} the gravimetric specific capacity of silicon. Similarly,

$$C_G = m_G \cdot c_G \tag{A.3}$$

applies to the graphite capacity C_G, with m_G being the graphite mass and c_G the gravimetric specific capacity of graphite. The total blend capacity is defined as:

$$C_{blend} = C_{Si} + C_G, \tag{A.4}$$

and the total mass of the active blend material M_{blend} is given by:

$$M_{blend} = m_{Si} + m_G. \tag{A.5}$$

Using the equality of the right-hand sides of Eqs. (A.1) and (A.2) yields:

$$\gamma_{Si} \cdot C_{blend} = m_{Si} \cdot c_{Si}, \tag{A.6}$$

and substituting Eq. (A.4) leads to:

$$\gamma_{Si} \cdot (C_{Si} + C_G) = m_{Si} \cdot c_{Si}. \tag{A.7}$$

Substituting Eqs. (A.3) and (A.2) leads to:

$$\gamma_{Si} \cdot (m_{Si} \cdot c_{Si} + m_G \cdot c_G) = m_{Si} \cdot c_{Si}. \tag{A.8}$$

Solving Eq. (A.5) for m_G and substituting into Eq. (A.8) results in:

$$\gamma_{Si} \cdot (m_{Si} \cdot c_{Si} + (M_{blend} - m_{Si}) \cdot c_G) = m_{Si} \cdot c_{Si}, \tag{A.9}$$

which can be rearranged to Eq. (16).

References

[1] M. Schindler, J. Sturm, S. Ludwig, A. Durdel, A. Jossen, Comprehensive analysis of the aging behavior of nickel-rich, silicon-graphite lithium-ion cells subject to varying temperature and charging profiles, J. Electrochem. Soc. (2021) http://dx.doi.org/10.1149/1945-7111/ac03f6.

[2] A. Maheshwari, M. Heck, M. Santarelli, Cycle aging studies of lithium nickel manganese cobalt oxide-based batteries using electrochemical impedance spectroscopy, Electrochim. Acta 273 (2018) 335–348, http://dx.doi.org/10.1016/j.electacta.2018.04.045.

[3] J. Schmitt, B. Kraft, J.P. Schmidt, B. Meir, K. Elian, D. Ensling, G. Keser, A. Jossen, Measurement of gas pressure inside large-format prismatic lithium-ion cells during operation and cycle aging, J. Power Sources 478 (2020) 228661, http://dx.doi.org/10.1016/j.jpowsour.2020.228661.

[4] I. Zilberman, J. Sturm, A. Jossen, Reversible self-discharge and calendar aging of 18650 nickel-rich, silicon-graphite lithium-ion cells, J. Power Sources 425 (2019) 217–226, http://dx.doi.org/10.1016/j.jpowsour.2019.03.109.

[5] J. Schmitt, A. Maheshwari, M. Heck, S. Lux, M. Vetter, Impedance change and capacity fade of lithium nickel manganese cobalt oxide-based batteries during calendar aging, J. Power Sources 353 (2017) 183–194, http://dx.doi.org/10.1016/j.jpowsour.2017.03.090.

[6] P. Keil, S.F. Schuster, J. Wilhelm, J. Travi, A. Hauser, R.C. Karl, A. Jossen, Calendar aging of lithium-ion batteries, J. Electrochem. Soc. 163 (9) (2016) A1872–A1880, http://dx.doi.org/10.1149/2.0411609jes.

[7] J.S. Edge, S. O'Kane, R. Prosser, N.D. Kirkaldy, A.N. Patel, A. Hales, A. Ghosh, W. Ai, J. Chen, J. Yang, S. Li, M.-C. Pang, L. Bravo Diaz, A. Tomaszewska, M.W. Marzook, K.N. Radhakrishnan, H. Wang, Y. Patel, B. Wu, G.J. Offer, Lithium ion battery degradation: what you need to know, Phys. Chem. Chem. Phys. : PCCP 23 (14) (2021) 8200–8221, http://dx.doi.org/10.1039/d1cp00359c.

[8] M. Dubarry, C. Truchot, B.Y. Liaw, Synthesize battery degradation modes via a diagnostic and prognostic model, J. Power Sources 219 (2012) 204–216, http://dx.doi.org/10.1016/j.jpowsour.2012.07.016.

[9] J.P. Schmidt, H.Y. Tran, J. Richter, E. Ivers-Tiffée, M. Wohlfahrt-Mehrens, Analysis and prediction of the open circuit potential of lithium-ion cells, J. Power Sources 239 (2013) 696–704, http://dx.doi.org/10.1016/j.jpowsour.2012.11.101.

[10] X. Han, M. Ouyang, L. Lu, J. Li, Y. Zheng, Z. Li, A comparative study of commercial lithium ion battery cycle life in electrical vehicle: Aging mechanism identification, J. Power Sources 251 (2014) 38–54, http://dx.doi.org/10.1016/j.jpowsour.2013.11.029.

[11] K. Honkura, T. Horiba, Study of the deterioration mechanism of LiCoO2/graphite cells in charge/discharge cycles using the discharge curve analysis, J. Power Sources 264 (2014) 140–146, http://dx.doi.org/10.1016/j.jpowsour.2014.04.036.

[12] C.R. Birkl, E. McTurk, M.R. Roberts, P.G. Bruce, D.A. Howey, A parametric open circuit voltage model for lithium ion batteries, J. Electrochem. Soc. 162 (12) (2015) A2271–A2280, http://dx.doi.org/10.1149/2.0331512jes.

[13] A. Marongiu, N. Nlandi, Y. Rong, D.U. Sauer, On-board capacity estimation of lithium iron phosphate batteries by means of half-cell curves, J. Power Sources 324 (2016) 158–169, http://dx.doi.org/10.1016/j.jpowsour.2016.05.041.

[14] C.R. Birkl, M.R. Roberts, E. McTurk, P.G. Bruce, D.A. Howey, Degradation diagnostics for lithium ion cells, J. Power Sources 341 (2017) 373–386, http://dx.doi.org/10.1016/j.jpowsour.2016.12.011.

[15] C.R. Birkl, E. McTurk, S. Zekoll, F.H. Richter, M.R. Roberts, P.G. Bruce, D.A. Howey, Degradation diagnostics for commercial lithium-ion cells tested at −10°C, J. Electrochem. Soc. 164 (12) (2017) A2644–A2653, http://dx.doi.org/10.1149/2.1401712jes.

[16] S. Schindler, M.A. Danzer, A novel mechanistic modeling framework for analysis of electrode balancing and degradation modes in commercial lithium-ion cells, J. Power Sources 343 (2017) 226–236, http://dx.doi.org/10.1016/j.jpowsour.2017.01.026.

[17] Y. Gao, J. Jiang, C. Zhang, W. Zhang, Y. Jiang, Aging mechanisms under different state-of-charge ranges and the multi-indicators system of state-of-health for lithium-ion battery with Li(NiMnCo)O2 cathode, J. Power Sources 400 (2018) 641–651, http://dx.doi.org/10.1016/j.jpowsour.2018.07.018.

[18] Z. Ma, Z. Wang, R. Xiong, J. Jiang, A mechanism identification model based state-of-health diagnosis of lithium-ion batteries for energy storage applications, J. Clean. Prod. 193 (2018) 379–390, http://dx.doi.org/10.1016/j.jclepro.2018.05.074.

[19] X. Jia, C. Zhang, Y. Le Wang, L. Zhang, W. Zhang, The degradation characteristics and mechanism of Li[Ni 0.5 Co 0.2 Mn 0.3]o 2 batteries at different temperatures and discharge current rates, J. Electrochem. Soc. 167 (2) (2020) 020503, http://dx.doi.org/10.1149/1945-7111/ab61e9.

[20] S. Lee, P. Mohtat, J.B. Siegel, A.G. Stefanopoulou, J.-W. Lee, T.-K. Lee, Estimation error bound of battery electrode parameters with limited data window, IEEE Trans. Ind. Inform. 16 (5) (2020) 3376–3386, http://dx.doi.org/10.1109/TII.2019.2952066.

[21] S. Lee, J.B. Siegel, A.G. Stefanopoulou, J.-W. Lee, T.-K. Lee, Electrode state of health estimation for lithium ion batteries considering half-cell potential change due to aging, J. Electrochem. Soc. 167 (9) (2020) 090531, http://dx.doi.org/10.1149/1945-7111/ab8c83.

[22] J. Schmitt, M. Schindler, A. Jossen, Change in the half-cell open-circuit potential curves of silicon–graphite and nickel-rich lithium nickel manganese cobalt oxide during cycle aging, J. Power Sources 506 (1) (2021) 230240, http://dx.doi.org/10.1016/j.jpowsour.2021.230240.

[23] M. Klett, J.A. Gilbert, S.E. Trask, B.J. Polzin, A.N. Jansen, D.W. Dees, D.P. Abraham, Electrode behavior RE-visited: Monitoring potential windows, capacity loss, and impedance changes in Li 1.03 (Ni 0.5 Co 0.2 Mn 0.3) 0.97 O 2 /silicon-graphite full cells, J. Electrochem. Soc. 163 (6) (2016) A875–A887, http://dx.doi.org/10.1149/2.0271606jes.

[24] M. Wetjen, D. Pritzl, R. Jung, S. Solchenbach, R. Ghadimi, H.A. Gasteiger, Differentiating the degradation phenomena in silicon-graphite electrodes for lithium-ion batteries, J. Electrochem. Soc. 164 (12) (2017) A2840–A2852, http://dx.doi.org/10.1149/2.1921712jes.

[25] W.M. Dose, M.J. Piernas-Muñoz, V.A. Maroni, S.E. Trask, I. Bloom, C.S. Johnson, Capacity fade in high energy silicon-graphite electrodes for lithium-ion batteries, Chem. Commun. (Cambr. Engl.) 54 (29) (2018) 3586–3589, http://dx.doi.org/10.1039/c8cc00456k.

[26] X. Li, A.M. Colclasure, D.P. Finegan, D. Ren, Y. Shi, X. Feng, L. Cao, Y. Yang, K. Smith, Degradation mechanisms of high capacity 18650 cells containing Si-graphite anode and nickel-rich NMC cathode, Electrochim. Acta 297 (2019) 1109–1120, http://dx.doi.org/10.1016/j.electacta.2018.11.194.

[27] M. Wetjen, S. Solchenbach, D. Pritzl, J. Hou, V. Tileli, H.A. Gasteiger, Morphological changes of silicon nanoparticles and the influence of cutoff potentials in silicon-graphite electrodes, J. Electrochem. Soc. 165 (7) (2018) A1503–A1514, http://dx.doi.org/10.1149/2.1261807jes.

[28] D. Anseán, G. Baure, M. González, I. Cameán, A.B. García, M. Dubarry, Mechanistic investigation of silicon-graphite/LiNi0.8Mn0.1Co0.1O2 commercial cells for non-intrusive diagnosis and prognosis, J. Power Sources 459 (2020) 227882, http://dx.doi.org/10.1016/j.jpowsour.2020.227882.

[29] T.M.M. Heenan, A. Jnawali, M.D.R. Kok, T.G. Tranter, C. Tan, A. Dimitrijevic, R. Jervis, D.J.L. Brett, P.R. Shearing, An advanced microstructural and electrochemical datasheet on 18650 Li-ion batteries with nickel-rich NMC811 cathodes and graphite-silicon anodes, J. Electrochem. Soc. 167 (14) (2020) 140530, http://dx.doi.org/10.1149/1945-7111/abc4c1.

[30] H. Popp, N. Zhang, M. Jahn, M. Arrinda, S. Ritz, M. Faber, D.U. Sauer, P. Azais, I. Cendoya, Ante-mortem analysis, electrical, thermal, and ageing testing of state-of-the-art cylindrical lithium-ion cells, E I Elektrotech. Inform. 137 (4–5) (2020) 169–176, http://dx.doi.org/10.1007/s00502-020-00814-9.

[31] J. Sturm, A. Rheinfeld, I. Zilberman, F.B. Spingler, S. Kosch, F. Frie, A. Jossen, Modeling and simulation of inhomogeneities in a 18650 nickel-rich, silicon-graphite lithium-ion cell during fast charging, J. Power Sources 412 (2019) 204–223, http://dx.doi.org/10.1016/j.jpowsour.2018.11.043.

[32] M. Schindler, J. Sturm, S. Ludwig, J. Schmitt, A. Jossen, Evolution of initial cell-to-cell variations during a three-year production cycle, ETransportation 14 (165) (2021) 100102, http://dx.doi.org/10.1016/j.etran.2020.100102.

[33] I. Zilberman, S. Ludwig, A. Jossen, Cell-to-cell variation of calendar aging and reversible self-discharge in 18650 nickel-rich, silicon–graphite lithium-ion cells, J. Energy Storage 26 (2019) 100900, http://dx.doi.org/10.1016/j.est.2019.100900.

[34] E. Moyassari, L. Streck, N. Paul, M. Trunk, R. Neagu, C.C. Chang, S.-C. Hou, B. Märkisch, R. Gilles, A. Jossen, Impact of silicon content within silicon-graphite anodes on performance and li concentration profiles of li-ion cells using neutron depth profiling, J. Electrochem. Soc. (2021) http://dx.doi.org/10.1149/1945-7111/abe1db.

[35] R. Jung, R. Morasch, P. Karayaylali, K. Phillips, F. Maglia, C. Stinner, Y. Shao-Horn, H.A. Gasteiger, Effect of ambient storage on the degradation of Ni-rich positive electrode materials (NMC811) for Li-ion batteries, J. Electrochem. Soc. 165 (2) (2018) A132–A141, http://dx.doi.org/10.1149/2.0401802jes.

[36] F. Friedrich, B. Strehle, A.T.S. Freiberg, K. Kleiner, S.J. Day, C. Erk, M. Piana, H.A. Gasteiger, Editors' choice—Capacity fading mechanisms of NCM-811 cathodes in lithium-ion batteries studied by X-ray diffraction and other diagnostics, J. Electrochem. Soc. 166 (15) (2019) A3760–A3774, http://dx.doi.org/10.1149/2.0821915jes.

[37] R. Jung, M. Metzger, F. Maglia, C. Stinner, H.A. Gasteiger, Oxygen release and its effect on the cycling stability of LiNi x Mn y Co z O 2 (NMC) cathode materials for li-ion batteries, J. Electrochem. Soc. 164 (7) (2017) A1361–A1377, http://dx.doi.org/10.1149/2.0021707jes.

[38] J. Li, J.R. Dahn, An in situ X-Ray diffraction study of the reaction of li with crystalline Si, Electrochem. Solid-State Lett. 154 (3) (2007) A156, http://dx.doi.org/10.1149/1.2409862.

[39] I. Zilberman, S. Ludwig, M. Schiller, A. Jossen, Online aging determination in lithium-ion battery module with forced temperature gradient, J. Energy Storage 28 (2020) 101170, http://dx.doi.org/10.1016/j.est.2019.101170.

[40] Y. Nishi, Lithium ion secondary batteries; past 10 years and the future, J. Power Sources 100 (1–2) (2001) 101–106, http://dx.doi.org/10.1016/S0378-7753(01)00887-4.

[41] S. Schweidler, L. de Biasi, A. Schiele, P. Hartmann, T. Brezesinski, J. Janek, Volume changes of graphite anodes revisited: A combined operando X-ray diffraction and in situ pressure analysis study, J. Phys. Chem. C 122 (16) (2018) 8829–8835, http://dx.doi.org/10.1021/acs.jpcc.8b01873.

[42] J. Sieg, M. Storch, J. Fath, A. Nuhic, J. Bandlow, B. Spier, D.U. Sauer, Local degradation and differential voltage analysis of aged lithium-ion pouch cells, J. Energy Storage 30 (2020) 101582, http://dx.doi.org/10.1016/j.est.2020.101582.

[43] E. Coron, S. Geniès, M. Cugnet, P.X. Thivel, Impact of lithium-ion cell condition on its second life viability, J. Electrochem. Soc. 167 (11) (2020) 110556, http://dx.doi.org/10.1149/1945-7111/aba703.

[44] E. Coron, S. Geniès, M. Cugnet, P.X. Thivel, High-energy li-ion cells: Impact of electrode ageing on second life viability, J. Electrochem. Soc. 168 (10) (2021) 100539, http://dx.doi.org/10.1149/1945-7111/ac3112.

5 State of health estimation based on partial charging processes

As elaborated on in section 2.3.1, a method for SOH estimation should ideally fulfill the following requirements:

1. It should work without a pre-parametrized aging model or a correlation between a measurable feature and the SOH.
2. It should be possible to measure the necessary input data frequently during regular operation.
3. It should be applicable for all relevant aging conditions.
4. It should allow capacity estimation with sufficient accuracy.

In this chapter, a method for SOH estimation that fulfills these requirements is presented. The method is physical model-based and uses the mechanistic model presented in section 2.2.2 to describe the electrical behaviour of the cell during charging. The model is parameterized at different states during aging by fitting voltage curves measured during CC charging with linearly scaled and shifted half-cell OCP curves (full-cell OCV curve alignment) as conceptually described in section 2.2.3. The remaining full-cell capacity is then calculated as the capacity of the part of the reconstructed OCV curve between the voltage limits used for full-cell operation. No prior information on battery degradation is required as the model can be parameterized solely based on the data that is measured during the CC part of charging phases and current pulses, which are occasionally needed to obtain an updated estimate for the internal resistance. In this way, the first of the aforementioned requirements is fulfilled by the algorithm.
As described in section 2.2.3, this type of model parametrization is typically performed based on complete charging or discharging curves measured at low current rates, which are usually not observable in applications under operating conditions. Although charging phases in general can be regularly observed in most applications, these are typically not conducted at low current rates nor do they comprise a complete charging of the battery from 0 % to 100 % SOC, which is usually the case for the input data used for full-cell OCV curve alignment. In order to fulfill the second requirement, the method should therefore also be applicable to partial charging phases and charging phases that are conducted at higher current rates. The focus of the study presented in this chapter therefore lies on analyzing the accuracy of capacity and degradation mode estimation based on partial charging curves and charging curves measured at higher current rates.
In the study presented in this chapter, an algorithm for full-cell OCV curve alignment that is suitable to be applied to partial charging curves and that considers overpotentials at higher current rates is described. The accuracy of the algorithm output for different input data is then systematically analyzed by applying it to different parts of low-current charging curves measured for cells at different aging states and which are aged under a variety of conditions. The accuracy of the algorithm output is also analyzed for scenarios in which complete and partial charging curves measured at higher current rates and at different aging states are used as input. The input data used for this analysis was measured in the scope of an experimental campaign in which commercial cells of the type INR18650-MJ1 built by

LG Chem were aged under different conditions.
The results indicate that the degradation modes and the remaining cell capacity can be accurately estimated based on partial low-current charging curves throughout aging, if the part of the charging curve between 20% and 70% SOC is available. It is also shown that the remaining capacity can be estimated with an accuracy of 2% of the nominal capacity, if partial charging curves between 10% and 80% SOC measured at approximately C/4 are used as input for the algorithm. The presented algorithm therefore enables accurate SOH estimation under application-relevant conditions and without the need for a pre-parametrized aging model or a known correlation between a measurable feature and the remaining cell capacity. Provided that a charging curve comprising a suitable SOC window is used as input, also the accuracy of the SOH estimation should be sufficient for most applications. If accurate estimates for the degradation mode analysis are additionally required, charging curves measured at current rates below C/15 should be used.
An additional finding of the experimental aging campaign presented in this chapter is that the aging conditions only have a limited impact on the degradation modes as a function of the remaining cell capacity. We interpret this in a way that while the different aging conditions lead to different rates of cell degradation, the degradation modes occur in a similar ratio regardless of the aging conditions.

Publication notes

The article titled *Capacity and degradation mode estimation for lithium-ion batteries based on partial charging curves at different current rates* is presented in the following. The article was submitted to the Journal of Energy Storage [272] and is currently under review. Parts of the results have been presented as a poster contribution titled *State of health estimation based on partial cell charging* in the scope of the Advanced Battery Power conference held in Münster (Germany) in March 2022.

Author contribution

The concept of the study was developed by Julius Schmitt. The experimental design was developed by Julius Schmitt and the experiments were conducted by Julius Schmitt. The experimental data was analyzed and visualized by Julius Schmitt. Julius Schmitt developed and implemented the presented algorithm for degradation mode analysis and SOH estimation. Mathias Rehm also contributed to the implementation of the algorithm. Julius Schmitt, Mathias Rehm and Alexander Karger carried out the literature review presented in the introduction of the article. Andreas Jossen supervised the related research project as well as the scientific work presented in the article. The manuscript was written by Julius Schmitt and was edited by all authors. All authors discussed the data and commented on the results.

Capacity and degradation mode estimation for lithium-ion batteries based on partial charging curves at different current rates

Julius Schmitt, Mathias Rehm, Alexander Karger and Andreas Jossen

Journal of Power Energy Storage 59 (3) (2023), p. 106517, DOI: 10.1016/j.est.2022.106517

Permanent weblink:
https://doi.org/10.1016/j.est.2022.106517

Journal of Energy Storage 59 (2023) 106517

Contents lists available at ScienceDirect

Journal of Energy Storage

journal homepage: www.elsevier.com/locate/est

Research papers

Capacity and degradation mode estimation for lithium-ion batteries based on partial charging curves at different current rates

Julius Schmitt [a,*], Mathias Rehm [a], Alexander Karger [a,b], Andreas Jossen [a]

[a] Technical University of Munich, School of Engineering and Design, Department of Energy and Process Engineering, Chair of Electrical Energy Storage Technology, Arcisstraße 21, 80333 Munich, Germany
[b] TWAICE Technologies GmbH, Joseph-Dollinger-Bogen 26, 80807 Munich, Germany

ARTICLE INFO

Dataset link: https://mediatum.ub.tum.de/1690455

Keywords:
Lithium-ion battery
State of health estimation
Degradation modes
OCV curve
Capacity estimation
Partial charging

ABSTRACT

The open circuit voltage (OCV) curve of a lithium-ion cell can be described as the difference between the half-cell open circuit potential curves of both electrodes. Fitting a reconstructed OCV curve to the OCV curve of an aged cell allows identification of degradation modes. In this study, we show that this method can also be applied to partial charging curves of a commercial cell with silicon–graphite and NMC-811 as electrode materials. Both the degradation modes and the remaining cell capacity can be determined from the reconstructed OCV curve. For the investigated cell, accurate OCV reconstruction and degradation mode estimation can be obtained from C/30 partial charging curves if the state of charge (SOC) window between 20 % and 70 % is available. We show that the method is also applicable to charging curves at higher current rates if the additional overpotential is considered by subtracting a constant voltage offset. Capacity estimation with an accuracy of 2 % of the nominal capacity is possible for current rates up to approximately C/4 if partial charging curves between 10 % and 80 % SOC are used, while a maximum current rate of C/15 should be used for accurate estimation of the degradation modes.

1. Introduction

One of the most important functions of a battery management system (BMS) for lithium-ion batteries is monitoring the remaining capacity of the battery over its lifetime in order to provide accurate estimates of the available energy and power. The fraction of the initial capacity that is still usable is often referred to as the state of health (SOH). The methods for SOH estimation for lithium-ion batteries that have been proposed in the literature can be categorized into three main categories:

1. Electrical model-based: the electrical behavior of the battery is described by a model. The model parameters are updated during aging by minimizing the difference between an estimated and measured model output, which is usually the terminal voltage. The obtained model parameters either directly include the SOH or indirectly allow its calculation [1–9].
2. Feature correlation-based: the correlation between a measurable feature and the SOH is established via lab experiments. In the application, the correlation is then used to calculate the SOH whenever it is possible to measure the feature [10–21].
3. Aging model-based: a pre-parameterized empirical aging model is used to calculate the SOH based on the operation history of a battery [22,23].

The main drawback of feature correlation-based and aging model-based methods is the necessity for tedious and costly aging studies for model parametrization. This is avoided by electrical model-based methods that do not require aging experiments during algorithm development except for validation purposes and can therefore be implemented more quickly with less effort.

One of the major challenges for electrical model-based SOH estimation is the change in the shape of the open circuit voltage (OCV) curve, i.e., the relationship between state of charge (SOC) and the OCV, during aging. Neglecting these changes leads to a significant decrease in the accuracy of electrical models during aging [24,25] so that methods to update the OCV curve are therefore needed [1]. The most commonly used framework to describe the OCV curve during aging is the mechanistic modeling approach introduced by Dubarry et al. [24] which has been used by many authors over the last decade [5,7,8,26–36]. In this framework, the OCV curve is modeled as the difference between the open circuit potential (OCP) curves of the cathode and

* Corresponding author.
E-mail address: julius.schmitt@tum.de (J. Schmitt).

https://doi.org/10.1016/j.est.2022.106517
Received 20 September 2022; Received in revised form 8 November 2022; Accepted 20 December 2022

the anode. Changes in the OCV curve are traced back to degradation modes, which are clusters of degradation mechanisms occurring at the cell components. The most important degradation modes are the loss of active material at the anode (LAM_{an}), the loss of active material at the cathode (LAM_{cat}) and the loss of lithium inventory (LLI) [24]. In many studies, additional degradation modes such as resistance increase [5,24], increase in inhomogeneity [30], and component specific degradation of silicon in silicon–graphite blend electrodes [33] are also considered. The degradation modes are usually quantified by fitting reconstructed OCV curves to low-current charging or discharging curves.

This framework can be used to develop algorithms for SOH estimation that take changes in the OCV curve into account [2,3,7,8,37], and which can be included in the class of electrical model-based methods. In this study, we present such an algorithm for both SOH and degradation mode estimation and systematically evaluate its performance when applied to partial charging curves and charging curves at higher current rates. These aspects are highly important for the practical applicability of the algorithm because batteries are usually only partially charged and/or charged at higher currents in applications.

There are some papers that report on the reconstruction of OCV curves based on partial cycles: Yang et al. applied degradation mode analysis to partial charging curves at a current rate of C/3 [37]. They reported that the method performs well for both capacity estimation and degradation mode analysis at this current rate, if the charging curves at least include the range between 20–70% SOC. Lee et al. studied the theoretical estimation uncertainty of electrode-alignment parameters based on partial OCV curves using Cramér–Rao bounds [8]. They found that the analytical error bound of alignment parameters decreases with increasing size of the SOC window used for the curve alignment and that the inclusion of regions with a high voltage slope is beneficial for an accurate alignment parameter estimation. Marongiu et al. reported that accurate capacity estimation for a LFP/graphite cell is possible if the length of the upper two full-cell OCV plateaus is observable [2,3].

Methods for OCV reconstruction and degradation mode estimation based on constant current phases at higher current rates have also been investigated: Chen et al. showed that the degradation modes can be determined from full and partial constant current (CC) discharging curves at 0.3 C using incremental capacity (IC) and differential voltage (DV) peak tracking [38]. In the work by Yang et al. the overpotential at higher current rates is compensated by adding an ohmic resistance term to the model used for calculating the terminal voltage and by using the weighted sum of the mean square deviation of both OCV and DV as a cost function for the OCV reconstruction [37]. Lu et al. investigated compensating the overpotential during charging/discharging measurements by adding a linearly SOC-dependent resistance term but did not achieve accurate results for OCV reconstruction using this approach [34]. Instead, they recommended using the lowest possible current rate for OCV and OCP measurements. Apart from this, there are papers in which partial charging curves or charging curves at higher current rates were used to directly estimate the remaining cell capacity via feature-correlation based methods for which a pre-parametrized model is needed [13,18,20,21,39,40].

In the scope of this work, an algorithm for SOH estimation and degradation mode estimation based on OCV reconstruction is presented and its accuracy is systematically evaluated for partial charging curves comprising different SOC ranges and for charging curves at different current rates. To the best of our knowledge, a systematic evaluation of the impact of the SOC range and the current rate of charging curves used as input data for OCV reconstruction has yet to be presented in the literature. We concentrate on CC charging curves as input as this type of data can be regularly measured in many applications. The algorithm could be applied to the analysis of field data or implemented in a BMS for on-board battery monitoring. No parametrization of an aging model or correlation of a feature with SOH is necessary. The algorithm is independent of SOC estimation and the updated OCV curve, which is obtained as an additional output, can be used for other BMS tasks that depend on an accurate OCV curve such as model-based SOC estimation [1,2,6,25,41].

2. Experimental

2.1. Overview

Commercially available cells of the type INR18650-MJ1 made by LG Chem were investigated in this study. The 18 650 format cells have a nominal minimum capacity (C_{nom}) of 3.35 Ah. C-rates used in this study refer to this capacity. The anode active material of the cells is a blend of silicon-based compounds and graphite. Different values for the mass ratio of silicon in the anode material within the range of 1 wt.% to 5 wt.% have been reported for this cell type [33,42–45]. The cathode active material is NMC-811 [43,44]. One equivalent full cycle (EFC) is defined as the charge throughput of twice the nominal capacity, which is 6.7 Ah. Whenever a constant voltage (CV) phase was applied, the cut-off current was 50 mA.

An overview of the conducted experiments is given in Fig. 1(a). The cells were operated at 25 °C ambient temperature inside a temperature chamber using a CTS battery test system from BaSyTec. An aging test sequence consisting of a capacity test, a pulse test, an application phase, a charging rate test and a continuous cycling phase was repeatedly applied to ten cells of the aforementioned type. This aging test sequence was applied up to 26 times with a total duration (t_{tot}) of 486 days or until a temperature of 60 °C (T_{max}) at the cell surface was exceeded at any point during the tests. After completion of the last iteration of the aging test sequence, another capacity test and pulse test were performed. 158 days after the aging test sequence was stopped, an extended charging rate test was conducted with some of the cells. Details on the aging test sequence and the extended charging rate test are presented below. An overview on the experimental procedures applied to the individual cells is provided in Table A.1 in the appendix. The experimental data measured in the scope of this study is made available in [46].

2.2. Aging test sequence

Capacity test. The cells were cycled two times using constant current constant voltage (CCCV) charging at a current rate of C/2 to 4.2 V and CCCV discharging with a current rate of C/5 to 2.5 V. The charge extracted during the CC part of the second discharging is denoted as $C_{C/5\ dch}$.

Pulse test. The cells were charged to 50% SOC and current pulses with a duration of 10 s and with current rates of C/3, 2C/3 and 1 C were applied in both the discharging and charging directions. There was a relaxation period of 30 min after setting the SOC and a 10 min relaxation period between the pulses.

Application phase. The application phase was designed to simulate the conditions in a battery electric vehicle. It contains dynamic operation with a profile based on the worldwide harmonized light vehicles test procedure (WLTP), CCCV charging procedures and rest times with several hours of duration. The vehicle model presented in [47] was used to convert the WLTP velocity profile to power requirements. The application phase has a total duration of three days. The measurement data recorded during the application phases is not further discussed within this work but might be used in future studies. We publish the measurement data recorded during the application phases at different aging states in [46]. Additional information on the application phase and the vehicle model is provided in Appendix B.

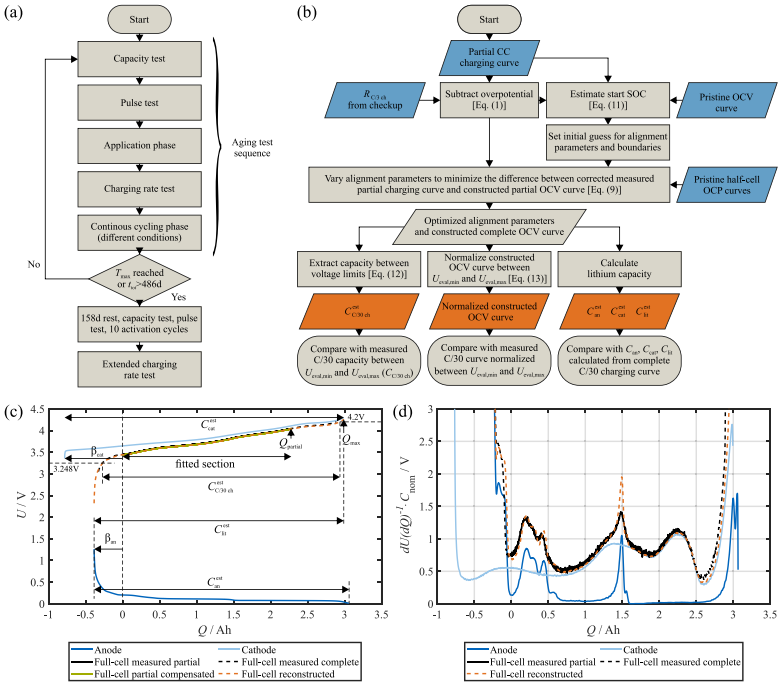

Fig. 1. (a) Flowchart describing the experimental procedure. (b) Flowchart describing the algorithm for capacity estimation, OCV reconstruction and degradation mode analysis based on partial charging curves. Inputs are highlighted in blue, outputs are highlighted in orange. (c) Example for fitting half-cell OCP curves to a partial charging curve (10–80% SOC) with compensation of the overpotential. A C/10 charging process is shown for a new cell and the X-axis indicates charge throughput with respect to the starting point of the partial curve used for the fitting. (d) Differential voltage of the curves shown in (c). (For interpretation of the references to color in this figure legend, the reader is referred to the web version of this article.)

Charging rate test. The cells were repeatedly CC-discharged to 2.5 V with a current rate of C/5 and then charged to 4.2 V using different rates. The procedure was executed using CCCV charging at 1 C, C/2 and 0.264 C and for constant power constant voltage (CPCV) charging at 3.183 W. Finally, the cells were CC discharged to 2.5 V at a current rate of C/5 and, after a relaxation period lasting 6 h, the cells were CC charged at a rate of C/30 until they reached a terminal voltage of 4.2 V. After another 6 h relaxation period, the cells were CC-discharged at a rate of C/30 until they reached a terminal voltage of 2.5 V.

The power of 3.183 W corresponds to the power at which each cell of a hypothetical battery pack consisting of 3456 cells (96s36p configuration, total nominal energy of 42 kWh) would be charged, if the total charging power was 11 kW, a value which is typical of home-installed AC charging stations. 0.264 C is the current rate corresponding to this power at the nominal cell voltage.

Continuous cycling phase. Two of the cells were kept under open circuit conditions for eight days after being CC charged at C/2 to 3.7 V. The remaining eight cells were continuously cycled for eight days under different conditions. Four sets of cycling conditions were used and two of the cells were cycled under each set of conditions. All of the cells were CCCV-charged at a rate of C/2. Different voltage limits and discharging procedures were used. They are listed in Table 1 along with the labels that are used to refer to the respective cells below. The cells labeled WLTP were discharged using the same dynamic discharging profile that was used in the application phase. The cells that were kept under open circuit conditions during this phase are denoted as "Only checkups" as they were only operated during the capacity, pulse and charging rate tests as well as the application phases but otherwise were only subject to calendar aging.

Table 1
Operation conditions applied during the continuous cycling phase.

Label	U_{min}	U_{max}	Discharge procedure
2.5 V–4.2 V	2.5 V	4.2 V	1 C CC
2.5 V–4.0 V	2.5 V	4.0 V	1 C CC
3.6 V–4.2 V	3.6 V	4.2 V	1 C CC
WLTP	2.5 V	4.2 V	WLTP profile

2.3. Extended charging rate test

Prior to the actual extended charging rate test, a capacity and a pulse test, ten activation cycles (1 C CC discharging to 2.5 V, C/2 CCCV charging to 4.2 V) and then another capacity and pulse test were applied. During the extended charging rate test, the cells were CCCV charged to 4.2 V using different current rates. The current rates during the charging phases were 0.264 C, C/6, C/8, C/10, C/12, C/15, C/20, C/25 and C/30. Between the charging phases, the cells were consistently CC discharged to 2.5 V at a current rate of C/5 with a subsequent 6 h relaxation phase. The extended charging rate test was conducted with the cells that had been aged under the conditions "3.6 V-4.2 V" and "Only checkups" as well as with two cells that had not been cycled before.

3. Algorithm and validation method

The algorithm for SOH and degradation mode estimation presented in this study is based on the mechanistic modeling framework introduced by Dubarry et al. [24]. The main aim of this study is to systematically evaluate its estimation accuracy for partial charging

curves and for charging curves at higher current rates. Therefore, the algorithm is implemented in such a way that it can be applied not only to complete charging curves, as is usually the case for degradation mode analysis, but also to partial charging curves without prior knowledge of the start and end SOC.

A flow chart representing the working principle of the algorithm is shown in Fig. 1(b). The main idea is to reconstruct the complete OCV curve based on a partial OCV curve. The cell capacity can then be estimated as the part of the reconstructed OCV curve that lies between the upper and lower cut-off voltage. In this study, we consider the charging curve at C/30 to be the reference for the OCV curve [38]. For those cases where charging curves at higher current rates are analyzed, an estimate for the additional overpotential in comparison to the C/30 charging curve is subtracted from the voltage data. The compensated partial charging curve $U_{\mathrm{OCV}}(Q)$ as a function of the charge throughput measured during the partial charging Q is calculated according to

$$U_{\mathrm{OCV}}(Q) = U_{\mathrm{meas}}(Q) - (I - I_{\mathrm{C/30}}) \cdot R_{\mathrm{C/3\ ch}} \tag{1}$$

where $U_{\mathrm{meas}}(Q)$ is the measured terminal voltage, I is the charging current, $I_{\mathrm{C/30}}$ is the current applied during C/30 charging and $R_{\mathrm{C/3\ ch}}$ is the resistance that is calculated from the C/3, 10 s charging pulse at 50% SOC during the pulse test preceding the respective charging rate test. $R_{\mathrm{C/3\ ch}}$ is calculated as

$$R_{\mathrm{C/3\ ch}} = \frac{\Delta U}{\Delta I} \tag{2}$$

where ΔU is the difference between the voltage measured at the end of the pulse and the voltage measured directly before the pulse. ΔI is the current amplitude of the pulse.

For the reconstruction of the full-cell OCV curve, the normalized pristine half-cell OCP curves which are functions of the electrode SOC

$$U_{\mathrm{cat}} = f_{\mathrm{cat}}(SOC_{\mathrm{cat}}) \tag{3}$$

$$U_{\mathrm{an}} = f_{\mathrm{an}}(SOC_{\mathrm{an}}) \tag{4}$$

need to be transformed into the coordinate system (Q) of the partial full-cell curve by linear scaling with the estimated electrode capacity ($C_{\mathrm{an}}^{\mathrm{est}}$, $C_{\mathrm{cat}}^{\mathrm{est}}$) and linear shifting by an offset (β_{an}, β_{cat}) [24,37]:

$$Q_{\mathrm{cat,full}} = C_{\mathrm{cat}}^{\mathrm{est}} \cdot (1 - f_{\mathrm{cat}}^{-1}(U_{\mathrm{cat}})) + \beta_{\mathrm{cat}} = f_{\mathrm{cat,full}}^{-1}(U_{\mathrm{cat}}, \theta) \tag{5}$$

$$Q_{\mathrm{an,full}} = C_{\mathrm{an}}^{\mathrm{est}} \cdot (f_{\mathrm{an}}^{-1}(U_{\mathrm{an}})) + \beta_{\mathrm{an}} = f_{\mathrm{an,full}}^{-1}(U_{\mathrm{an}}, \theta) \tag{6}$$

The alignment parameters used for scaling and shifting of the OCP curves are collectively denoted as

$$\theta = [C_{\mathrm{an}}^{\mathrm{est}}, C_{\mathrm{cat}}^{\mathrm{est}}, \beta_{\mathrm{an}}, \beta_{\mathrm{cat}}]. \tag{7}$$

$f_{\mathrm{cat,full}}(Q, \theta)$ and $f_{\mathrm{an,full}}(Q, \theta)$ then describe the OCP of the electrodes as a function of absolute charge in the coordinate system of the partial charging curve. The half-cell OCP curves are taken from [48] and are implemented as lookup tables. The full-cell OCV curve is reconstructed as the difference between the transformed half-cell curves

$$U_{\mathrm{OCV}}^{\mathrm{est}}(Q, \theta) = f_{\mathrm{cat,full}}(Q, \theta) - f_{\mathrm{an,full}}(Q, \theta). \tag{8}$$

The alignment parameters are obtained by minimizing the sum of square errors (SSE) between the measured partial OCV curve and the reconstructed OCV curve in the range between the beginning $Q = 0\,\mathrm{Ah}$ and the end of the partial charging curve $Q = Q_{\mathrm{partial}}$:

$$\arg\min_{\theta} \mathrm{SSE} = (U_{\mathrm{OCV}}^{\mathrm{est}}([0\,\mathrm{Ah}, Q_{\mathrm{partial}}], \theta) - U_{\mathrm{OCV}}([0\,\mathrm{Ah}, Q_{\mathrm{partial}}]))^2 \tag{9}$$

The nonlinear programming solver *fmincon* using the interior-point algorithm implemented in MATLAB® is used for the optimization. The optimization is performed subject to the constraint that the reconstructed OCV curve reaches at least a value of 4.2 V at the end of charging

$$U_{\mathrm{OCV}}^{\mathrm{est}}(Q_{\mathrm{max}}) \geq 4.2\,\mathrm{V}, \tag{10}$$

where Q_{max} is the end of the overlapping part of the transformed half-cell curves. A similar approach is suggested in [8]. A typical result of an OCV curve reconstruction based on a partial charging curve is shown in Fig. 1(c). The difference between absolute voltages is used as a cost function for the optimization in this study. The DV of the reconstructed OCV curve also fits the DV of the measured voltage well in cases where the fitting in the voltage domain is successful. An example of this is shown in Fig. 1(d).

The initial values and boundaries for the alignment parameter optimization are set according to Table 2. For the cases in which C/30 curves of aged cells from the aging test sequence are reconstructed, the results for the alignment parameters obtained for the preceding iteration are used as initial values [37] and the boundaries are chosen to allow 30% of variation from this value, as long as the absolute boundary values listed in Table 2 are not exceeded. As can be seen in Table 2, the initial values for β_{an} and β_{cat} depend on an estimate for the initial SOC of the partial charging curve. This estimated initial SOC ($SOC_{\mathrm{min}}^{\mathrm{est}}$) is calculated as

$$SOC_{\mathrm{min}}^{\mathrm{est}} = SOC(U_{\mathrm{OCV}}(0\,\mathrm{Ah})) \tag{11}$$

where $SOC(U)$ is an interpolation of the pristine SOC-OCV curve and $U_{\mathrm{OCV}}(0\,\mathrm{Ah})$ is the first voltage value contained in the partial charging curve compensated by the overpotential offset. The pristine SOC-OCV curve is calculated as the average of the normalized C/30 charging curves measured for the individual cells during the first charging rate test. We would like to emphasize that this estimate on the start SOC is solely used to set the initial values for β_{an} and β_{cat}. The final values for these parameters are obtained during the optimization step. A low estimation accuracy of $SOC_{\mathrm{min}}^{\mathrm{est}}$ therefore has no significant impact on the accuracy of the capacity and degradation mode estimation.

Based on the complete reconstructed OCV curve, the cell capacity $C_{\mathrm{C/30}}^{\mathrm{est}}$ can be calculated [8] according to

$$C_{\mathrm{C/30}}^{\mathrm{est}} = Q_{\mathrm{OCV}}^{\mathrm{est}}(U_{\mathrm{eval,max}}) - Q_{\mathrm{OCV}}^{\mathrm{est}}(U_{\mathrm{eval,min}}), \tag{12}$$

where $Q_{\mathrm{OCV}}^{\mathrm{est}}(U)$ is the inverse of the reconstructed OCV curve and $U_{\mathrm{eval,min}}$ and $U_{\mathrm{eval,max}}$ are the voltage limits between which the C/30 charging capacity is defined in this study. The definition of $C_{\mathrm{C/30}}^{\mathrm{est}}$ is shown diagrammatically in Fig. 1(c). $U_{\mathrm{eval,max}} = 4.2\,\mathrm{V}$ is the upper cut-off voltage during charging and was chosen according to the specifications of the cell manufacturer. For $U_{\mathrm{eval,min}}$ the value of 3.248 V is chosen based on the following consideration: during the experiments, the cells were CC discharged to 2.5 V prior to the C/30 charging procedure but the measured charging curves do not start at this value as the voltage relaxes towards higher values during the relaxation time before the charging phase. The minimum voltage value of the charging curve also generally increases with aging as the internal resistance and therefore the overpotential at the end of the discharging phase increases. In order to have a consistent measured reference for the cell capacity and the OCV (C/30) curve at all aging states, we use $U_{\mathrm{eval,min}} = 3.248\,\mathrm{V}$, the highest minimum value of all C/30 charging curves, as the starting point for the capacity calculation and reconstructed OCV curve evaluation. The reference capacity $C_{\mathrm{C/30\ ch}}$ is then calculated as the charge throughput measured between $U_{\mathrm{eval,min}}$ and $U_{\mathrm{eval,max}}$ during the C/30 charging phase.

The second output of the algorithm is the reconstructed OCV curve itself, which could for example be used to update the OCV curve used by a BMS for SOC estimation during aging. To decouple the evaluation of the accuracy of the shape of the reconstructed OCV curve from the accuracy of the capacity estimation, both the reference curve and the curve calculated with the algorithm are normalized in the charge dimension

$$U_{\mathrm{OCV,eval}}^{\mathrm{est}}(Q') = U_{\mathrm{OCV}}^{\mathrm{est}}([Q_{\mathrm{OCV}}^{\mathrm{est}}(U_{\mathrm{eval,min}}), Q_{\mathrm{OCV}}^{\mathrm{est}}(U_{\mathrm{eval,max}})]) \tag{13}$$

$$U_{\mathrm{OCV,eval}}(Q') = U_{\mathrm{OCV}}([Q_{\mathrm{OCV}}(U_{\mathrm{eval,min}}), Q_{\mathrm{OCV}}(U_{\mathrm{eval,max}})]) \tag{14}$$

Table 2
Initial values and boundaries for the alignment parameters.

Parameter	Initial value	Lower boundary	Upper boundary
C_{an}^{est}	3.45 Ah	2.21 Ah	3.67 Ah
C_{cat}^{est}	3.82 Ah	2.35 Ah	4.02 Ah
β_{an}	$(0.02 - SOC_{min}^{est}) \cdot 3.45$ Ah	−3.67 Ah	0 Ah
β_{cat}	$(0.13 - SOC_{min}^{est}) \cdot 3.82$ Ah	−4.02 Ah	0 Ah

where Q' is a vector of $n = 2000$ equally spaced interpolation points between 0 and 1 at which the difference between the reconstructed and measured curve is evaluated. As a measure for the accuracy of the reconstructed OCV curve we use the root mean square error (RMSE) between the reconstructed OCV curve and the measured C/30 charging curve in the voltage range between $U_{eval,min}$ and $U_{eval,max}$, denoted as ε_{OCV}:

$$\varepsilon_{OCV} = \sqrt{\frac{1}{n}(U_{OCV,eval}^{est}(Q') - U_{OCV,eval}(Q'))^2}. \quad (15)$$

Finally, the accuracy of the results in respect of the electrode capacities (C_{an}^{est}, C_{cat}^{est}) and the lithium inventory (C_{lit}^{est}) is evaluated. C_{an}^{est} and C_{cat}^{est} are direct output parameters of the optimization procedure, the lithium inventory is calculated as the difference in charge between the end of the cathode OCP curve where the cathode is delithiated and the beginning of the anode OCP curve where the anode is delithiated [33].

The algorithm is applied to parts of the C/30 charging curves measured during the aging test sequence. It is also applied to the CC charging curves at higher current rates measured during the extended charging rate test to study the accuracy of the method at higher charging rates. Before the charging data is processed by the algorithm, it is resampled at equidistant Q values corresponding to a sample frequency of 1 Hz (the original sampling was conducted in a voltage-based manner at a voltage change of 0.5 mV) and filtered by applying a Savitzky–Golay filter with polynomial order of five and a frame length of 71 data points three times. A section of the charging curve is cut out to simulate the scenario where only a part of the charging curve can be measured in an application. The actual capacity measured during the charging phase is used for calculating the SOCs for cutting out the partial curves. For the extended charging rate tests, this also includes the CV phase.

The RMSE of the algorithm output quantities (X^{est}) for all cells and all periods of the aging test sequence (until SOH = 80%) is used as a measure of the accuracy of the algorithm for different SOC windows. It is calculated according to

$$\mathrm{RMSE}(X^{est}) = \sqrt{\frac{1}{N}\sum_{i=1}^{n_{cell}}\sum_{j=1}^{n_{period}}(X_{i,j}^{est} - X_{i,j})^2}, \quad (16)$$

where $X_{i,j}^{est}$ is the estimate for the respective output quantity ($C_{C/30\ ch}^{est}$, C_{an}^{est}, C_{cat}^{est}, C_{lit}^{est}) of the ith cell in the jth period of the aging test sequence. $X_{i,j}$ is the corresponding reference value, i.e., the measured $C_{C/30\ ch}$ of the ith cell in the jth period or the respective value for C_{an}, C_{cat} or C_{lit} that is obtained from the complete C/30 charging curve of the ith cell in the jth period. $n_{cell} = 10$ is the total number of cells and n_{period} the total number of analyzed charging curves of each individual cell until SOH = 80%. N is the total number of analyzed charging curves for all cells. The RMS of ε_{OCV}

$$\mathrm{RMS}(\varepsilon_{OCV}) = \sqrt{\frac{1}{N}\sum_{i=1}^{n_{cell}}\sum_{j=1}^{n_{period}}(\varepsilon_{OCV,i,j})^2}, \quad (17)$$

where $\varepsilon_{OCV,i,j}$ is the RMSE of the reconstructed OCV curve of the ith cell in the jth period of the aging test sequence, is used as a measure of the accuracy of the OCV curve reconstruction throughout aging.

Similar measures are used to describe the accuracy of the algorithm for different SOC windows at higher charging rates with the difference that there are only six analyzed cells and that there is only one charging curve per cell, which is the curve obtained during the extended charging rate test.

Using the proposed algorithm in a BMS or for the analysis of field data would be possible by implementing the following additional steps: first, the CC charging phases need to be detected and cut out from the measurement data. This implies that measurement data of current and voltage during charging phases need to be temporally stored. Then, the current is integrated over the time of the charging process to generate the charge throughput vector that is provided to the algorithm along with the corresponding terminal voltage vector. A section at the begin of the charging phase would need to be discarded as discussed in Section 4.2. In addition, another algorithm for determining the resistance values from dynamic operation data, such as the one proposed by Ludwig et al. [49], would needed to be implemented. The updated resistance value at a middle SOC as well as the relevant section of the charging curve would then be provided to the algorithm and processed as described in this section.

4. Results and discussion

4.1. Aging analysis based on complete low-current charging curves

In this section, the results of the aging test sequence and the algorithm output for the reference case, where the complete C/30 charging curves are used as input, are presented and discussed.

The discharging capacity measured during the capacity tests ($C_{C/5\ dch}$) is plotted in Fig. 2(a) as a function of total charge throughput. The capacity decreases for all cells with significant differences in the rate of capacity decrease depending on the operating conditions during the continuous cycling periods. The capacity of the cells that are cycled in a limited voltage window (2.5 V-4.0 V and 3.6 V-4.2 V) decreases more slowly over equivalent full cycles when compared to the cells that are cycled in the full voltage range (2.5 V-4.2 V and WLTP). Schindler et al. also observed an extension of the cycle life upon limitation of the upper cut-off voltage for cells of this type [50]. They also measured a similar aging rate for cells of the same type cycled over the full voltage range. The internal pulse resistance $R_{C/3\ ch}$ measured during the pulse tests is shown in Fig. 2(b) as a function of total charge throughput. Analogously to the capacity decrease, the cells that are cycled over the full voltage range exhibit a quicker increase in internal resistance than the cells that are cycled within a limited voltage range.

The cells cycled over the full voltage range reach heavily degraded states during the experiments. The end of life (EOL) of a lithium-ion cell is usually defined as reached when the capacity-based SOH has dropped below 80%. In this study, we define the SOH as $C_{C/5\ dch}/C_{nom}$. As shown in Fig. 2(a), the cells cycled over the full voltage range reach this EOL definition after approximately 570 EFC. The algorithm is only applied to cases where the SOH is above 80% in this study. In principle, the proposed algorithm could also be applied to cells at SOH below 80%, but for the analysis of accuracy and impact of available SOC window and current rate, we concentrate on the case above 80% SOH, because this represents the most important scope of application, as heavily degraded cells at SOH below 80% would not continued to be used in most applications. All charging curves for which the SOH is below 80% are therefore excluded for the following analysis. The number of charging curves above 80% SOH for the individual cells are listed in Table A.1.

The C/30 charging capacity measured between 3.248 V and 4.2 V ($C_{C/30\ ch}$) is used as reference for the capacity estimation as explained in Section 3. The results for $C_{C/30\ ch}$ are shown in Fig. 2(c). The absolute values are lower than for $C_{C/5\ dch}$ because only the part of the capacity above 3.248 V is considered but the trends of the capacity decrease are the same as for $C_{C/5\ dch}$. Applying the algorithm presented in Section 3 to the complete C/30 charging curves at different aging states yields reconstructed OCV curves that are a good fit to the

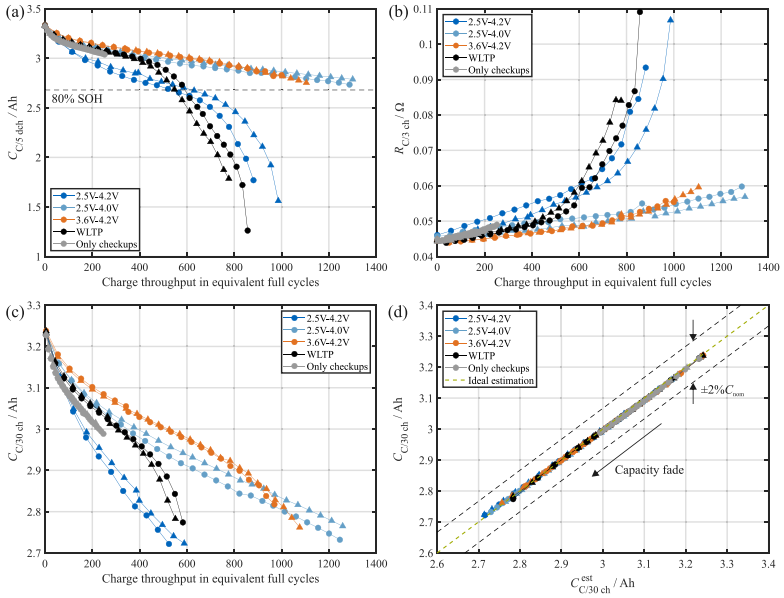

Fig. 2. (a) CC discharging capacity measured at C/5 during the capacity tests as part of the aging test sequence. The different symbols indicate results for the two cells tested under each aging condition. (b) C/3 charging pulse resistance (10 s pulse duration) at 50% SOC measured during the pulse tests. (c) C/30 charging capacity between 3.248 V and 4.2 V ($C_{\mathrm{C/30\ ch}}$) measured during the charging rate tests until 80% SOH. (d) Correlation between measured C/30 charging capacity and C/30 charging capacity estimated with the algorithm at different aging states for the case in which the complete C/30 charging curves are used as input.

measured curves. The RMS($\varepsilon_{\mathrm{OCV}}$) for all considered charging curves is 3.6 mV and $\varepsilon_{\mathrm{OCV}}$ is always below 7 mV. This means that the proposed OCV model is suitable for reproducing the shape of the OCV curve throughout aging and for different aging conditions. In Fig. 2(d), the correlation between the estimated and the measured C/30 charging capacity is shown. The RMSE($C^{\mathrm{est}}_{\mathrm{C/30\ ch}}$) for all cells and aging states is 0.2% C_{nom} and the capacity estimates shown in 2(d) are near to the ideal estimation line ($C^{\mathrm{est}}_{\mathrm{C/30\ ch}} = C_{\mathrm{C/30\ ch}}$). This means that the capacity can be accurately calculated with the proposed algorithm if the complete C/30 charging curves are available.

The degradation modes occurring during aging of the individual cells are calculated from the results for the electrode capacities and the lithium inventory as

$$\mathrm{LAM_{an}} = \frac{C_{\mathrm{an,ini}} - C_{\mathrm{an}}}{C_{\mathrm{an,ini}}} \tag{18}$$

$$\mathrm{LAM_{cat}} = \frac{C_{\mathrm{cat,ini}} - C_{\mathrm{cat}}}{C_{\mathrm{cat,ini}}} \tag{19}$$

$$\mathrm{LLI} = \frac{C_{\mathrm{lit,ini}} - C_{\mathrm{lit}}}{C_{\mathrm{lit,ini}}}, \tag{20}$$

where the subscript "ini" refers to the value obtained for the C/30 charging curve in the initial state. The results for $\mathrm{LAM_{an}}$ are shown in Fig. 3(a). The change in $\mathrm{LAM_{an}}$ as a function of charge throughput differs for the different aging conditions while the two cells aged under the same conditions show comparably similar results. The same applies to the $\mathrm{LAM_{cat}}$ shown in Fig. 3(c) and the LLI shown in Fig. 3(e). $\mathrm{LAM_{an}}$ and LLI are higher than $\mathrm{LAM_{cat}}$ for all aging conditions, which means that cell degradation is primarily driven by these two degradation modes. Similar results have previously been found for this cell type [33,45,51,52].

The shape of the half-cell OCP curves is considered invariant during aging in the algorithm presented in this study, even though it has been shown that this assumption is only approximately valid for silicon–graphite blend anodes [48]. The $\mathrm{LAM_{an}}$ is therefore probably overestimated by the order of a few percentage points while $\mathrm{LAM_{cat}}$ and LLI are probably underestimated by the order of a few percentage points [33]. The change in shape of the silicon–graphite OCP curve could theoretically be considered in the algorithm by using a blend electrode model and adding another optimization parameter describing the remaining anode capacity ratio provided by the silicon [33]. This is not done here, because adding another optimization parameter results in lower robustness of the fitting algorithm if partial charging curves are used as input, which would be a challenge in applications.

In Figs. 3(b), 3(d) and 3(f) the degradation modes are plotted with respect to the remaining cell capacity $C_{\mathrm{C/5\ dch}}$. This representation shows that the difference between the degradation modes for cells at the same SOH is always below 4 percentage points even though they are aged under different conditions. We interpret this finding in such a way that the different degradation modes are triggered in an approximately fixed ratio that is only slightly influenced by the applied aging conditions. Further research is needed to obtain quantitative results on this topic and to investigate whether this result can be generalized to other aging conditions and cells.

4.2. Accuracy of the method for partial charging curves

In this section, the accuracy of the estimated remaining cell capacity, OCV reconstruction and estimated degradation modes is analyzed for the case in which only parts of the C/30 charging curves measured during the aging test sequence are used as input for the algorithm.

Fig. 4(a) shows the RMSE($C^{\mathrm{est}}_{\mathrm{C/30\ ch}}$) for all cells and aging states for different SOC windows used for the OCV reconstruction. In this representation, each field of the matrix corresponds to a certain SOC window defined by the SOC at which the partial curve begins ($\mathrm{SOC_{min}}$, indicated on the X-axis) and the SOC at which the partial curve ends ($\mathrm{SOC_{max}}$, indicated on the Y-axis). The numeric value for the RMSE of the capacity estimation obtained from the OCV reconstruction based on a certain SOC window is indicated in the corresponding field of the matrix. The estimation accuracy is also visualized by a color code, where blue corresponds to high accuracy and yellow to low accuracy.

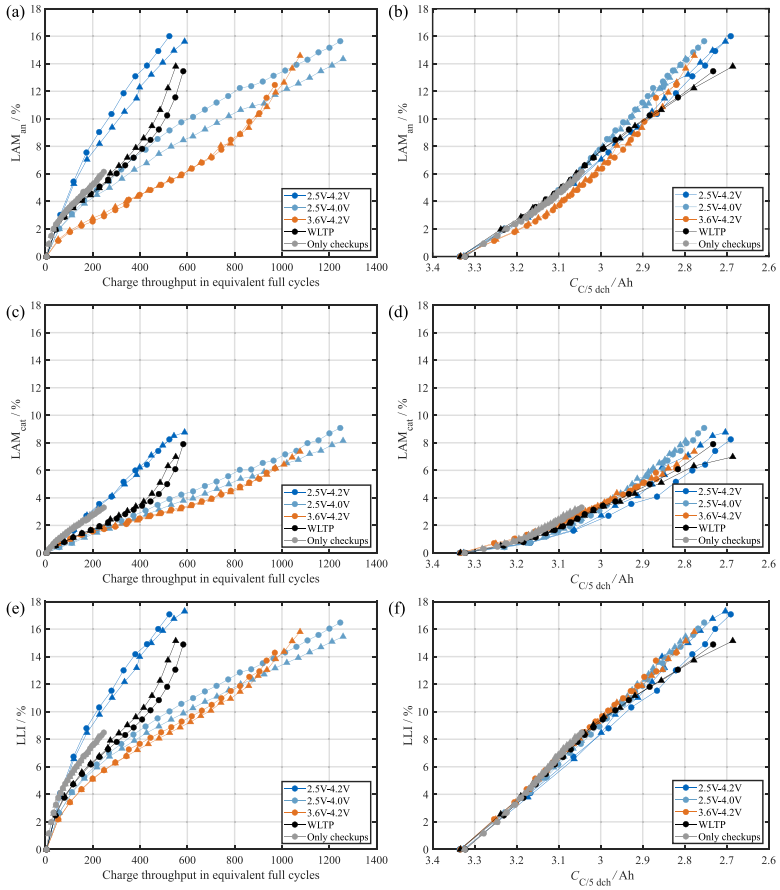

Fig. 3. Reference values for the degradation modes obtained from complete C/30 charging curves. The different symbols represent results for the two cells aged under the same conditions. (a) LAM_{an} as a function of total charge throughput. (b) LAM_{an} as a function of the remaining C/5 discharging capacity. (c) LAM_{cat} as a function of total charge throughput. (d) LAM_{cat} as a function of the remaining C/5 discharging capacity. (e) LLI as a function of total charge throughput. (f) LLI as a function of the remaining C/5 discharging capacity.

As visible in Fig. 4(a), the accuracy of the capacity estimation strongly depends on the SOC window of the partial charging curve provided to the algorithm. The position of the bluish area in Fig. 4(a) reveals that SOC_{min} needs to be less than or equal to 20% in order to obtain capacity estimates with high accuracy ($RMSE(C^{est}_{C/30\ ch}) \leq 2.0\%$). We assume that the reason for the algorithm failing at SOC_{min} above 20% is that the information on the position of the stage 2L graphite phase is necessary to obtain an accurate estimate for the anode capacity, which is also limiting for the full-cell capacity at low cell voltages. This can be seen in Fig. 4(c) where the DV of a pristine cell is shown and the peaks are associated with phases of the electrode materials [51,53,54]. If partial charging curves with SOC_{min} greater than 20% are used, the anode capacity, and as a consequence also the cell capacity, are heavily overestimated. Similar results were obtained by Yang et al. [37]. Also Marongiu et al. [2,3] reported that the length and position of voltage plateaus corresponding to the 2L-2 and 2–1 phase transitions of the graphite need to be observable in order to obtain accurate capacity estimation based on the reconstruction of partial charging curves.

In addition to starting at a low SOC_{min}, the partial charging curves should comprise at least 30% of the actual cell capacity to provide enough information for accurate capacity estimation. For cases where SOC_{min} is between 5% and 20%, the accuracy of the capacity estimation increases with an increase in the width of the SOC window used until SOC_{max} of approximately 60%. The proposed algorithm should therefore preferably be applied to charging curves comprising at least the window between 20% and 60% SOC to enable accurate capacity estimation throughout aging. As an example of the capacity estimation for cells aged under different conditions and at different aging stages, the correlation between estimated and measured capacity is shown in 4(d) for the case where partial charging curves in the SOC window between 15% and 75% are used. It can be seen that the deviation from the ideal estimation is smaller than 2% C_{nom} in most cases.

In Fig. 4(b), the $RMS(\varepsilon_{OCV})$ for all cells and aging states is shown as a measure of the accuracy of the reconstruction of the shape of the aged OCV curve from partial charging curves with different SOC windows. Analogous to the accuracy of the capacity estimation, the obtained accuracy of the reconstructed OCV curve shape strongly depends on the SOC window used. Reconstructed complete OCV curves with high accuracy ($RMS(\varepsilon_{OCV}) \leq 6.2$ mV) can be obtained if a window extending between 20% SOC and 70% SOC at least is used. As for the capacity estimation, the necessity for a $SOC_{min} \leq 20\%$ arises form the need to have at least a part of the 2L graphite stage inside the analyzed part of the charging curve in order to obtain accurate estimates on the anode capacity. The necessity of an $SOC_{max} \geq 70\%$ for accurate OCV construction differs from the requirements for the capacity estimation, where accurate estimates can also be obtained with a lower SOC_{max}.

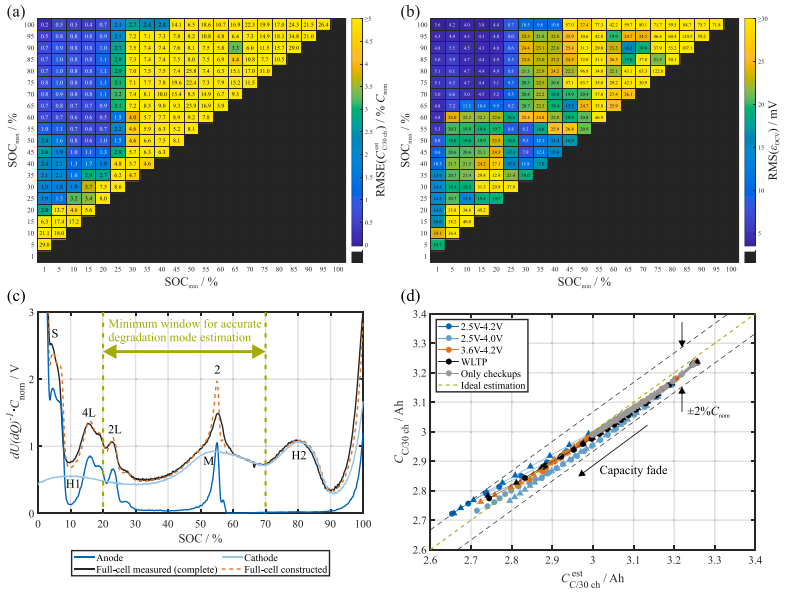

Fig. 4. (a) RMSE of the C/30 charging capacity estimates for all cells and aging states for partial curves with different SOC windows. (b) RMS of the RMSE of the reconstructed OCV curves (ε_{OCV}) for all cells and aging states for partial curves with different SOC windows. (c) Measured and reconstructed DV of a pristine cell. The peaks of the DV are associated with phases of the electrode materials: Graphite stages 4L, 2L and 2 [53], a silicon phase S [51] and NMC-811 phases H1, M and H2 [54]. (d) Correlation between measured C/30 charging capacity and C/30 charging capacity estimated using the algorithm based on partial C/30 charging curves between 15% and 75% SOC at different aging states. (For interpretation of the references to color in this figure legend, the reader is referred to the web version of this article.)

The RMSE of the estimated anode capacity, cathode capacity and lithium inventory based on partial charging curves with different SOC windows is shown in Figs. 5(a)–5(c). The estimation accuracy results are presented as a percentage of the respective mean value obtained for the complete charging curves in the pristine state ($C_{an,ini,mean}$, $C_{cat,ini,mean}$, $C_{lit,ini,mean}$). As for the reconstruction of the OCV curve, accurate estimates for the anode capacity (RMSE (C^{est}_{an}) $\leq 2.2\%\, C_{an,ini,mean}$) are obtained for $SOC_{min} \leq 20\%$ and $SOC_{max} \geq 70\%$. Estimation of the cathode capacity with high accuracy (RMSE (C^{est}_{cat}) $\leq 1.0\%\, C_{cat,ini,mean}$) is also only possible for cases where $SOC_{max} \geq 70\%$ but comparably accurate results on the cathode capacity can also be obtained if only the upper part of the SOC range, for example between 60% and 90% is available. Accurate estimation of the lithium inventory (RMSE (C^{est}_{lit}) $\leq 2.1\%\, C_{lit,ini,mean}$) can be obtained if SOC_{min} is not greater than 20% and if the width of the used SOC window is at least 25% of the actual cell capacity.

Accurate OCV reconstruction and electrode capacity estimation is only possible if $SOC_{max} \geq 70\%$. This means that even though accurate capacity estimates can be obtained for $SOC_{max} \leq 70\%$, the reconstruction of the complete curve is only performed correctly if the middle SOC range, where the graphite stage 2 and the NMC-811 M phase are located (see Fig. 4(c)), is included in the analyzed partial charging curve. If this is not the case, the cathode capacity is increasingly underestimated and the anode capacity is increasingly overestimated during aging. Nevertheless, the estimation of the lithium inventory is comparably accurate as can be seen in Fig. 5(c). This is because the cathode is identified as limiting the cell capacity at 100% SOC with cathode capacity reserves below 0% SOC and the anode is identified as limiting the cell capacity at 0% SOC with anode capacity reserves above 100% SOC as shown in Fig. 5(d). Neither the overestimated part of the anode capacity nor the underestimated part of the cathode capacity contribute to the cell capacity or the lithium inventory, therefore an erroneous estimation of these quantities does not lead to a huge error in the full-cell capacity estimation.

Another phenomenon that can be observed is that in some cases the estimation accuracy of the cell capacity and the electrode capacities, as well as the OCV reconstruction accuracy is slightly reduced if the SOC range between 5% and 15% is included in the algorithm input. This results from an underestimation of both anode and cathode capacity for aged cells if this SOC range is included. A possible reason for this phenomenon is that the OCV model that is used by the algorithm might be less accurate for aged silicon–graphite at low lithiation because the probable increase in inhomogeneous lithiation [30] and a change in the capacity contribution of silicon [33,48] are not considered in the model. The algorithm still tries to align the measured and simulated full-cell OCV curves in this SOC region, which leads to a reduced overall estimation accuracy. Reduced estimation accuracy is not observed if the begin of charge is also included in the algorithm input, as the fitting is dominated by the steep increase of the OCV curve at the begin of charge in this case.

Summing up the results concerning the accuracy of OCV reconstruction based on partial C/30 CC charging curves, it can be stated that for the investigated cell type, accurate capacity estimation and estimation of the lithium inventory is possible throughout aging if the charging curve starts at or below 20% SOC and lasts for at least 30% of the actual cell capacity. Accurate reconstruction of the OCV curve and estimation of the electrode capacities is only possible under the additional condition that the cell is charged up to an SOC of at least 70%. Similar results were reported by Yang et al. who used a similar algorithm and found that SOH estimation with a relative error of ±2.5% is possible as long as the partial charging curve contains the SOC range from 20% to 70% [37]. It should be noted that in real applications, a partial charging curve is not obtained as a segment of a complete charging curve but measured during an actual partial charging process,

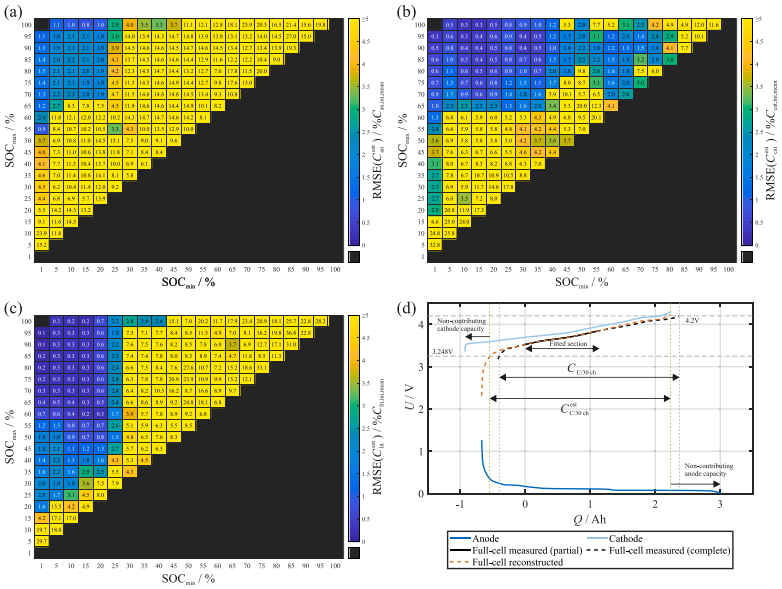

Fig. 5. (a) RMSE of the estimated anode capacity for all cells and aging states based on partial C/30 charging curves with different SOC windows as input. (b) RMSE of the estimated cathode capacity for all cells and aging states based on partial C/30 charging curves with different SOC windows as input. (c) RMSE of the estimated lithium inventory for all cells and aging states based on partial C/30 charging curves with different SOC windows as input. (d) Result for fitting a charging curve between 15% and 55% SOC of an aged cell (cycled between 3.6 V-4.2 V up to 82.9% SOH).

in which the overpotential builds up at the start of the charging. Findings have demonstrated that the section of the charging curve in which the overpotential builds up, should be discarded from the input for OCV reconstruction [21,37]. Consequently, a lower SOC_{min} than indicated by our results is probably needed in applications to compensate for the discarded section.

In this study, we investigate charging phases where the cells have been at rest at the begin of charge. In principle, the algorithm should also be applicable to charging phases where the cell had not been at rest at the begin of charge. In this case, the section at the begin of charge in which the terminal voltage is significantly influenced by overpotentials resulting from the operation prior to the charging phase has to be excluded from the algorithm input.

4.3. Accuracy of the method at higher charging rates

In this section, the accuracy of the capacity estimation, OCV reconstruction and degradation mode estimation is evaluated for the case, where charging rates higher than C/30 from the extended charging rate test are used as input. There are two general problems for applying OCV reconstruction to charging curves at higher rates: first, the overpotential that builds up during the charging process is higher than for the low-current case and can therefore not be neglected. In this study we consider this overpotential by subtracting a constant voltage offset from the charging curves as described in Section 3. Using this simple electrical model for overpotential compensation has the advantage of simple parametrization. In our case, it is sufficient to extract a pulse resistance at a middle SOC from time to time to update the scalar value of $R_{C/3\ ch}$, which we consider to be feasible in most applications. The determination of an SOC-dependent resistance would be significantly more complex. Another advantage of using an SOC-independent resistance value for polarization compensation is that the shape of the measured charging curve is not affected by the compensation. Using an SOC-dependent resistance could introduce additional features to the compensated charging curve that are not contained in the measured curve. Contrary to this, using an SOC-dependent resistance value could possibly improve the accuracy of the overpotential compensation in SOC regions where the resistance significantly differs from the value at 50% SOC. For the investigated cell type, this would mainly apply to the region below 20% SOC [55].

The second main problem is that the lithiation/delithiation of the electrodes is increasingly inhomogeneous at higher charging rates which hinders the determination of the electrode capacities. The DV of the CC charging procedures at different rates as part of the extended charging rate test performed on a pristine cell is shown in Fig. 6(a). The inhomogeneous lithiation of the anode at higher charging rates results in a broadening of the anode DV peaks as can be seen in Fig. 6(a). The central anode DV peak corresponding to the graphite stage 2 is not visible if the cells are charged at 0.264 C. Similarly, Marongiu et al. reported that the graphite phase transitions are not clearly distinguishable from charging curves measured at current rates above 0.3 C [3].

In Fig. 6(b) the results for $C^{est}_{C/30\ ch}$ estimated from complete CC charging curves with different rates are shown for three sample cells at different SOH and with different aging history. The estimated capacities differ increasingly from the measured reference if higher charging rates are used. A capacity estimation with an error of less than 2% C_{nom} is obtained for current rates up to C/6 for the pristine cell. For the cell cycled until an SOH of 84.2%, this accuracy is only obtained for current rates up to C/15. The negative influence of higher current rates on the accuracy of the method therefore increases with cell aging. Detailed results for the capacity estimation accuracy obtained for all cells that were subject to the extended charging rate test are listed in Table 3.

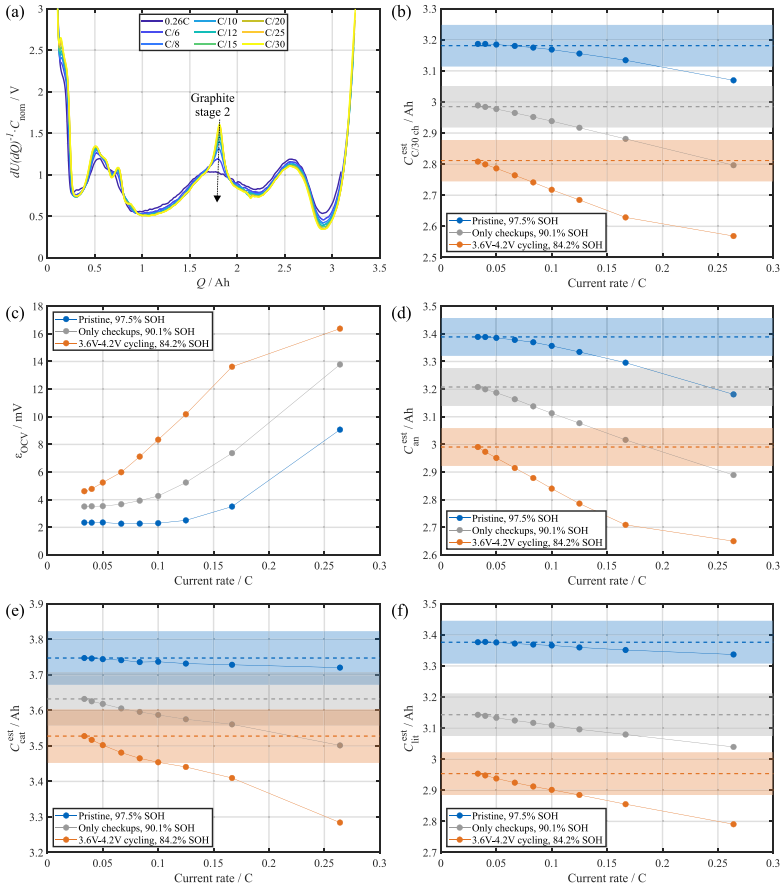

Fig. 6. (a) DV of CC charging curves at different current rates for a pristine cell. (b) Capacities of three sample cells at different aging states estimated using the algorithm including overpotential compensation based on complete charging curves at different current rates. The measured reference values for $C_{C/30\ ch}$ are indicated as dashed horizontal lines. The shaded areas indicate the 2% C_{nom} error range. (c) RMSE of the reconstructed OCV curves, (d) anode capacities, (e) cathode capacities and (f) lithium inventory of the three sample cells estimated using the algorithm including overpotential compensation based on complete charging curves at different current rates. The reference values obtained from the complete C/30 charging curves are indicated as dashed horizontal lines in (d-f) and error ranges corresponding to 2% of $C_{an,ini,mean}/C_{cat,ini,mean}/C_{lit,ini,mean}$ are shown as shaded areas.

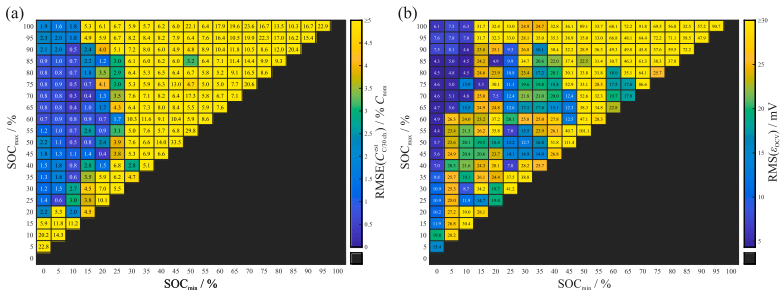

Fig. 7. (a) RMSE of the capacity estimates for six cells (two each at approx. 97%, 90% and 83% SOH) calculated from partial charging curves at C/10 with different SOC windows using overpotential compensation. (b) RMS of the RMSE of the reconstructed OCV curves for the six cells calculated from partial charging curves at C/10 with different SOC windows using overpotential compensation.

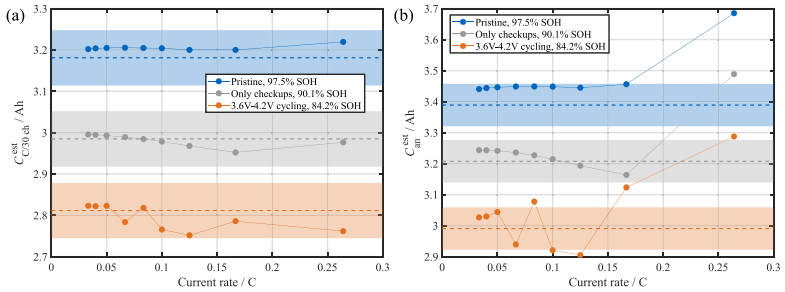

Fig. 8. (a) Capacities of three sample cells at different aging states estimated with the proposed algorithm including overpotential compensation based on partial charging curves (10–80% SOC) at different current rates. The measured values for $C_{\mathrm{C/30\ ch}}$ which are used as reference are indicated as dashed horizontal lines. The shaded areas indicate the 2% C_{nom} error range. (b) Anode capacities of the three cells at different aging states estimated with the algorithm including overpotential compensation based on partial charging curves (10–80% SOC) at different current rates. The anode capacities values obtained from the complete C/30 charging curves which are used as reference are indicated as dashed horizontal lines. The shaded areas indicate the 2% $C_{\mathrm{an,ini,mean}}$ error range.

Table 3
Capacity estimation error based on complete charging curves at different current rates measured during the extended charging rate test. The results are obtained using overpotential compensation.

Charging rate/C		1/30	1/25	1/20	1/15	1/12	1/10	1/8	1/6	0.264
Cell	SOH/%	Capacity estimation error/% C_{nom}								
Pristine #1	97.5	0.2	0.2	0.1	0.0	0.2	0.4	0.8	1.4	3.3
Pristine #2	97.5	0.1	0.1	0.1	0.0	0.2	0.4	0.7	1.3	3.3
Only checkups #1	90.1	0.1	0.0	0.2	0.6	1.0	1.4	2.0	3.1	5.6
Only checkups #2	90.4	0.1	0.0	0.2	0.6	1.0	1.3	2.0	3.0	5.5
3.6 V–4.2 V #1	82.5	0.1	0.4	0.8	1.6	2.4	3.2	4.3	5.9	7.7
3.6 V–4.2 V #2	84.2	0.1	0.4	0.7	1.4	2.1	2.8	3.8	5.5	7.2

Table 4
Capacity estimation error based on partial charging curves (10–80% SOC) at different current rates measured during the extended charging rate test. The results are obtained using overpotential compensation.

Charging rate/C		1/30	1/25	1/20	1/15	1/12	1/10	1/8	1/6	0.264
Cell	SOH/%	Capacity estimation error/% C_{nom}								
Pristine #1	97.5	0.6	0.7	0.7	0.7	0.7	0.7	0.6	0.6	1.1
Pristine #2	97.5	0.6	0.7	0.7	0.7	0.7	0.7	0.6	0.7	1.2
Only checkups #1	90.1	0.3	0.3	0.2	0.1	0.0	0.2	0.5	1.0	0.2
Only checkups #2	90.4	0.3	0.3	0.3	0.2	0.0	0.1	0.4	0.8	0.1
3.6 V–4.2 V #1	82.5	0.3	0.3	0.2	0.8	0.1	0.1	0.4	0.9	2.0
3.6 V–4.2 V #2	84.2	0.3	0.3	0.3	0.8	0.2	1.4	1.8	0.8	1.5

The accuracy of the OCV estimation $\varepsilon_{\mathrm{OCV}}$ is shown in Fig. 6(c). Again, the accuracy decreases both with the increase in current rate and cell degradation, but highly accurate OCV reconstruction ($\varepsilon_{\mathrm{OCV}} \leq 6\,\mathrm{mV}$) is possible for the C/6 charging curve of the pristine cell.

As already mentioned, a probable reason for the reduced accuracy of the algorithm results at higher current rates is the increasingly inhomogeneous lithiation of the anode, which hinders the detection of the graphite stages (see Fig. 6(a)) and thus the estimation of the anode capacity. Another reason might be that for higher current rates, the curve alignment gets dominated by a comparably steep voltage increase at the end of charging, which is erroneously interpreted as complete lithiation of the anode but is probably at least partly due to overpotentials that are not correctly compensated by the model. The second aspect can be avoided by leaving out the SOC range above 85% as discussed below.

As visible in Figs. 6(d)–6(f), the accuracy of the estimation of electrode capacities and lithium inventory is also lower at higher current rates, especially for aged cells. The results suggest that accurate anode capacity estimation ($|C_{\mathrm{an}}^{\mathrm{est}} - C_{\mathrm{an}}| \leq 2\%\, C_{\mathrm{an,ini,mean}}$) is possible for charging rates up to C/8 for the pristine cell but only for charging rates up to C/20 for the aged cell. The estimation of the cathode capacity is less sensitive to increased current rates and an accuracy of $|C_{\mathrm{cat}}^{\mathrm{est}} - C_{\mathrm{cat}}| \leq 2\%\, C_{\mathrm{cat,ini,mean}}$ can be obtained even at 0.264 C for the pristine cell and for current rates up to C/10 for the cell at 84.2% SOH. Similar results are obtained for the accuracy of the estimation of C_{lit}, where $|C_{\mathrm{lit}}^{\mathrm{est}} - C_{\mathrm{lit}}| \leq 2\%\, C_{\mathrm{lit,ini,mean}}$ is reached for current rates up to 0.264 C for the pristine cell and for current rates up to C/8 for the cell at 84.2% SOH. The systematic underestimation of the electrode capacities at higher current rates in comparison to the reference obtained at C/30 might be due to a limited rate capability of the electrodes which also increases with aging [36]. Typical results for one of the cells for each aging history are shown in Figs. 6(b)–6(f) as the results for the respective second cell with the same aging history are similar to the examples shown.

The requirements on the current rate for both capacity estimation and degradation mode analysis are probably different for other cell types. With a nominal volumetric energy density of approximately 696 Whl^{-1}, the investigated cells are optimized towards high energy and have therefore comparably thick electrode coatings (anode $\approx$ 85 µm, cathode $\approx$ 72 µm [43]). This probably results in a comparably inhomogeneous lithiation/delithiation of the electrodes which hinders the OCV reconstruction even at moderate charging rates. Thus, the

charging rate limits might be higher for cell types that are more optimized towards high power.

A comparison between the algorithm results obtained with and without using the overpotential compensation is provided in Fig. C.1 in the appendix. This comparison shows that using the proposed overpotential compensation increases the accuracy of the capacity estimation, the OCV reconstruction and the estimation of $C_{\mathrm{lit}}^{\mathrm{est}}$ in most cases, while it reduces the accuracy of the electrode capacity estimation in most cases.

The combined influence of using both a limited part of the charging curve and a higher current rate is shown in Fig. 7(a). The RMSE ($C_{\mathrm{C/30\ ch}}^{\mathrm{est}}$) calculated based on the C/10 charging curves of the six cells that underwent the extended charging rate test is shown here as a function of the SOC window used. These results indicate that accurate capacity estimation (RMSE ($C_{\mathrm{C/30\ ch}}^{\mathrm{est}}$) $\leq 2\%\, C_{\mathrm{nom}}$) can be obtained if $\mathrm{SOC_{min}}$ is not higher than 10% and the width of the SOC window is greater than 20%. In addition to this, the capacity estimation accuracy is higher, if the upper 10% of the SOC window is excluded for the curve alignment. In this SOC region near the end of charging, the measured curves exhibit a steep increase, which is erroneously interpreted to be a feature of the anode OCP but is most probably caused by the overpotential due to the higher current.

In Fig. 7(b) the RMS($\varepsilon_{\mathrm{OCV}}$) for the six cells at different aging states is shown for different SOC windows. These results suggest that for accurate OCV reconstruction (RMS($\varepsilon_{\mathrm{OCV}}$) ≤ 6 mV), $\mathrm{SOC_{min}}$ needs to be $\leq 10\%$, and $70\% \leq \mathrm{SOC_{max}} \leq 85\%$. For $\mathrm{SOC_{min}} = 0\%$, accurate OCV reconstruction is possible for $45\% \leq \mathrm{SOC_{max}} \leq 85\%$. In comparison with the capacity estimation, the requirements on the SOC window are therefore stricter if OCV reconstruction and degradation mode analysis is additionally intended. This discrepancy arises from the same source as was found for the partial charging rates at C/30: if $\mathrm{SOC_{max}} < 70\%$, the electrode capacity estimation is erroneous but neither the underestimated part of the cathode capacity nor the overestimated part of the anode capacity contribute towards the lithium inventory and the cell capacity and therefore these two quantities are still estimated with reasonable accuracy (see Fig. 5(d)).

The sensitivity analysis shows that the window between 10% and 80% SOC is a suitable window for applying the proposed algorithm. In the following, results that can be obtained from charging curves of this example suitable window are discussed. In Fig. 8(a), the results for the capacity estimation based on this SOC window are shown for one example cell of each aging history and for different current rates. If this SOC window is used, accurate capacity estimation with less than $2\%\, C_{\mathrm{nom}}$ deviation from the reference is achieved for current rates up to 0.264 C even for the aged cell at 84.2% SOH. Similar results are obtained for the other cells with the same aging history. Detailed results for the capacity estimation accuracy based on charging curves between 10–80% SOC at different charging rates are listed in Table 4.

In Fig. 8(b), $C_{\mathrm{an}}^{\mathrm{est}}$ calculated from partial charging curves between 10% SOC and 80% SOC is shown for different current rates for the sample cells. For the aged cell at 84.2% SOH, the estimated values differ by more than $2\%\, C_{\mathrm{an,ini,mean}}$ for current rates above C/15. At 0.264 C, the anode capacity cannot be accurately estimated even for the pristine cell. This is probably due to the lack of information on the anode phases in the charging curve at this current rate (see Fig. 6(a)).

The restrictions on the applicability of the proposed algorithm are therefore higher if not only the remaining cell capacity but also the degradation modes are to be extracted from partial charging curves at higher charging rates. The accuracy of the algorithm could probably be improved by using a more complex model to consider the overpotential [24,56], but our results show that even with a very simple and easily implementable electrical model, accurate results can be achieved under realistic charging conditions at least in respect of the capacity estimation.

5. Conclusion

We have presented an algorithm for capacity, OCV curve and degradation mode estimation based on CC charging curves that uses the concept of reconstructing OCV curves by fitting pristine half-cell OCP curves to charging curves. The algorithm is easily implemented and no parametrization of an aging model or a correlation between an observable feature and the capacity is necessary. The proposed algorithm is also independent of SOC estimation. We have evaluated the applicability of the algorithm to both partial charging curves and charging curves at higher current rates. For the investigated cell type, the algorithm yields accurate results when applied to partial low-current (C/30) charging curves if the used SOC window comprises at least the range between 20% and 70% SOC.

For the OCV reconstruction based on CC charging curves at higher current rates, the overpotential is compensated by subtracting a constant voltage offset. The accuracy for capacity and degradation mode estimation decreases both with the increase in current rate and with cell degradation. Nevertheless, the algorithm presented in this study yields accurate capacity estimates based on charging curves at current rates up to approximately C/4 even for aged cells if a suitable part of the charging curve (10–80% SOC) is used as input. For an accurate estimation of the degradation modes, charging curves at lower current rates (≤C/15) are necessary for the investigated cell type. The results show that accurate SOH estimation based on partial charging phases at application-relevant current rates is possible with the presented algorithm for cells at different aging states and which are aged under different conditions. The influence of the charging current amplitude on estimation accuracy probably depends on the cell design which should be further investigated in the future.

Furthermore, we show that for the investigated cell, the aging conditions only have a limited impact on the degradation modes as a function of remaining cell capacity. The different aging conditions lead to different rates of cell degradation but the degradation modes occur in a similar ratio for all investigated aging conditions. Further research is required to investigate whether this finding can be generalized to other aging conditions and cell types.

CRediT authorship contribution statement

Julius Schmitt: Conceptualization, Methodology, Software, Validation, Formal analysis, Investigation, Data curation, Writing – original draft, Visualization, Funding acquisition. **Mathias Rehm:** Software, Writing – review & editing. **Alexander Karger:** Writing – review & editing. **Andreas Jossen:** Writing – review & editing, Supervision, Project administration, Funding acquisition.

Declaration of competing interest

The authors declare the following financial interests/personal relationships which may be considered as potential competing interests: Alexander Karger reports a relationship with TWAICE Technologies GmbH that includes: employment.

Data availability

Datasets related to this article can be found at https://mediatum.ub.tum.de/1690455, hosted at the Technical University of Munich [46].

Acknowledgments

This work was supported by the German Federal Ministry for Economic Affairs and Climate Action (grant number 03ETE019F). The responsibility for this publication lies with the authors. Fruitful discussions with Marcel Rogge, Andreas Graule, Julius Bahrke, Marco Fischer and Sven Friedrich are gratefully acknowledged. We would like to thank Lucas Koltermann for the support during the development of the battery electric vehicle profile.

Appendix A. Experimental procedures applied to individual cells

See Table A.1.

Table A.1
Experimental procedures applied to the individual cells. n_{total} is the number of iterations the aging test sequence was applied to an individual cell. n_{period} is the number of charging rate tests at which the SOH is above 80% and that are analyzed in the scope of this study.

Cell	n_{total}	n_{period}	Aging test sequence (applied repeatedly)					Extended charging rate test
Test type			Capacity test	Pulse test	Application phase	Charging rate test	Continuous cycling phase	
2.5 V–4.2 V #1	19	11	Yes	Yes	Yes	Yes	Yes (2.5 V–4.2 V)	No
2.5 V–4.2 V #2	22	13	Yes	Yes	Yes	Yes	Yes (2.5 V–4.2 V)	No
2.5 V–4.0 V #1	26	26	Yes	Yes	Yes	Yes	Yes (2.5 V–4.0 V)	No
2.5 V–4.0 V #2	26	26	Yes	Yes	Yes	Yes	Yes (2.5 V–4.0 V)	No
3.6 V–4.2 V #1	26	26	Yes	Yes	Yes	Yes	Yes (3.6 V–4.2 V)	Yes
3.6 V–4.2 V #2	24	24	Yes	Yes	Yes	Yes	Yes (3.6 V–4.2 V)	Yes
WLTP #1	26	17	Yes	Yes	Yes	Yes	Yes (WLTP)	No
WLTP #2	24	17	Yes	Yes	Yes	Yes	Yes (WLTP)	No
Only checkups #1	26	26	Yes	Yes	Yes	Yes	No (storage)	Yes
Only checkups #2	23	23	Yes	Yes	Yes	Yes	No (storage)	Yes
Pristine #1	0	0	No	No	No	No	No	Yes
Pristine #2	0	0	No	No	No	No	No	Yes

Appendix B. Description of the application phase and the vehicle model

The application phase is designed to simulate typical conditions of battery usage in a battery electric vehicle. The measurement data obtained during the application phase is not discussed in the scope of this study but could for example be used for testing methods for SOC and SOH estimation with dynamic data recorded for cells at different aging states and aged under different conditions.

In each application phase test, the cells were initially fully charged using CCCV charging to 4.2 V with a cut-off current of 50 mA. Afterwards, the application phase with a total duration of three days was started. The application phase contains sections with three types of operating conditions: extended rest times under open-circuit conditions simulating times in which the vehicle is not used (“Rest”); dynamic operation according to a power profile that simulates conditions during driving and regenerative breaking based on one of the WLTP phases (“Low”, “Medium”, “High” and “Extra high”); CCCV charging at C/2 to 4.2 V with a cut-off current of 50 mA simulating charging of the vehicle. The sequence in which these sections are combined in the application phase is described in Table B.1. The idea behind this sequence is to have several discharging phases with different depth and SOC window, charging phases with different SOC window and rest times with realistic duration at different SOC level combined in one measurement sequence. An example of the current and voltage measurements obtained during an application phase of a pristine cell is shown in Fig. B.1. Dynamic operation accounts for approximately 12% of the duration of the application phase, while charging accounts for approximately 7% and resting for approximately 81% of the duration.

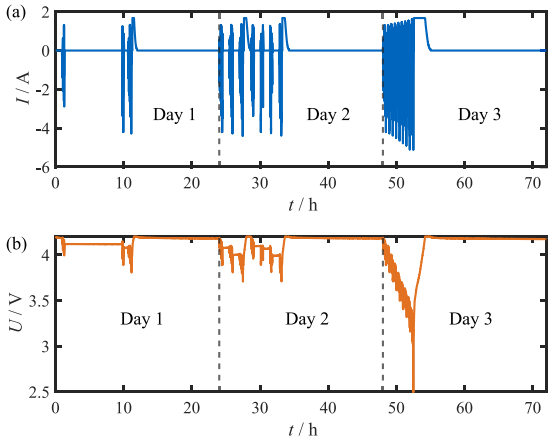

Fig. B.1. Exemplary measurement values obtained during the application phase applied to a pristine cell: (a) applied current, (b) terminal voltage.

The vehicle model that is used to convert the velocity profile of the world harmonized light duty test cycle (WLTC) into a power profile is described in [47, p. 77 ff.]. The implementation of the model used for this study is based on [57]. The parameters used for the vehicle model are described in Table B.2.

Table B.1
Sequence of sections contained in the application phase.

Day	Section	Duration
1	Rest	1 h
	Low	590 s
	Medium	432 s
	Rest	8.5 h
	High	455 s
	Extra high	323 s
	Rest	40 min
	Low	590 s
	Medium	432 s
	High	455 s
	Extra high	323 s
	Rest	5 min
	Charging	approx. 44 min
	Rest	Until a total duration of 24 h is reached
2	Low	590 s
	Medium	432 s
	High	455 s
	Extra high	323 s
	Rest	1 h
	Low	590 s
	Medium	432 s
	High	455 s
	Extra high	323 s
	Rest	1 h
	Low	590 s
	Medium	432 s
	High	455 s
	Extra high	323 s
	Rest	5 min
	Charging	approx. 1 h
	Rest	5 min
	Low	590 s
	Medium	432 s
	High	455 s
	Rest	1 h
	Extra high	323 s
	Low	590 s
	Medium	432 s
	Rest	1 h
	High	455 s
	Extra high	323 s
	Low	590 s
	Rest	1 h
	Medium	432 s
	High	455 s
	Extra high	323 s
	Rest	5 min
	Charging	approx. 1 h
	Rest	Until a total duration of 48 h is reached
3	Low, Medium, High, Extra high	Repeatedly applied until 2.5 V is reached
	Rest	5 min
	Charging	approx. 2.5 h
	Rest	Until a total duration of 72 h is reached

Table B.2
Parameters of the vehicle model used to generate power profiles based on the WLTP velocity profiles.

Parameter	Value
Gravitation	9.81 ms^{-2}
Density of air	1.184 kg m^{-3}
Vehicle mass including battery	1345 kg
Additional mass	100 kg
Air drag coefficient	0.29
Vehicle front area	2.38 m^2
Tire roll resistance factor	0.015
Rotational mass factor	1.05
Additional consumption	1000 W
Motor efficiency	91%
Inverter efficiency	96%

(*continued on next page*)

Table B.2 (*continued*).

Parameter	Value
Efficiency factor transmission	90%
Recuperation efficiency	70%
Maximum motor power	125 kW
Maximum recuperation power	50 kW
Number of cells	3456

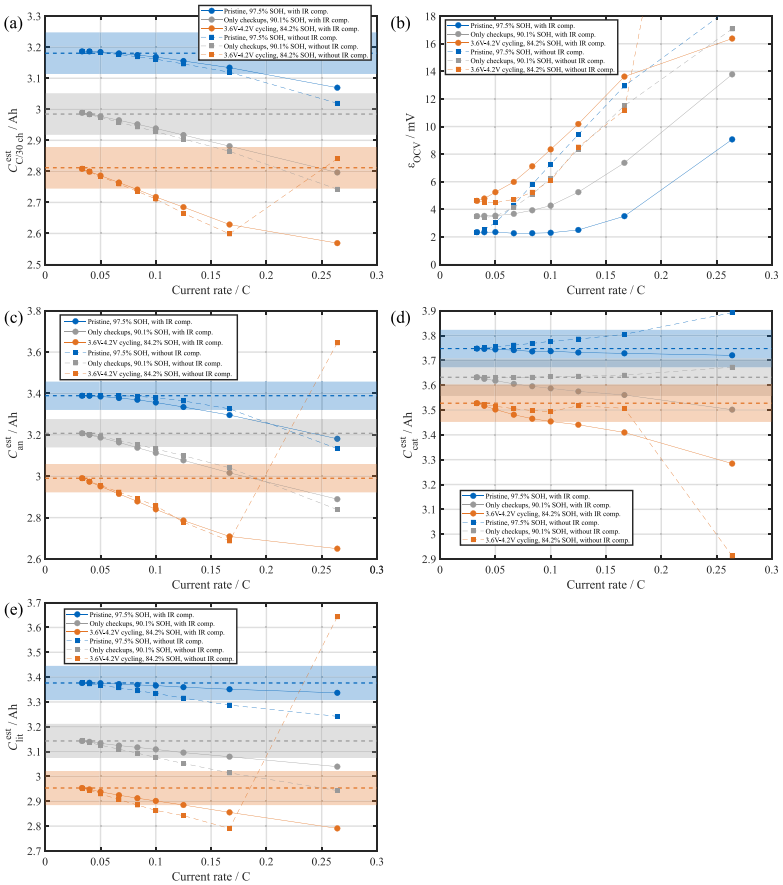

Fig. C.1. (a) Capacities of three sample cells at different aging states estimated using the algorithm with and without overpotential (IR) compensation based on complete charging curves at different current rates. The measured reference values for $C_{\mathrm{C/30\ ch}}$ are indicated as dashed horizontal lines. The shaded areas indicate the 2% C_{nom} error range. (b) RMSE of the reconstructed OCV curves. The data points outside the plotted range are at 0.26C/52 mV ('3.6 V–4.2 V cycling without IR comp.') and 0.26C/18.7 mV ('Pristine without IR comp.'). (c) Anode capacities, (d) cathode capacities and (e) lithium inventory of the three sample cells estimated using the algorithm with and without overpotential compensation based on complete charging curves at different current rates. The reference values obtained from the complete C/30 charging curves are indicated as dashed horizontal lines in (c-e) and error ranges corresponding to 2% of $C_{\mathrm{an,ini,mean}}/C_{\mathrm{cat,ini,mean}}/C_{\mathrm{lit,ini,mean}}$ are shown as shaded areas.

Appendix C. Comparison of algorithm results with and without overpotential compensation

See Fig. C.1.

References

[1] S. Tong, M.P. Klein, J.W. Park, On-line optimization of battery open circuit voltage for improved state-of-charge and state-of-health estimation, J. Power Sources 293 (2015) 416–428, http://dx.doi.org/10.1016/j.jpowsour.2015.03.157.

[2] A. Marongiu, D.U. Sauer, On-board aging estimation using half-cell voltage curves for LiFePO4 cathode-based lithium-ion batteries for EV applications, Int. J. Automot. Technol. 17 (3) (2016) 465–472, http://dx.doi.org/10.1007/s12239-016-0048-3.

[3] A. Marongiu, N. Nlandi, Y. Rong, D.U. Sauer, On-board capacity estimation of lithium iron phosphate batteries by means of half-cell curves, J. Power Sources 324 (2016) 158–169, http://dx.doi.org/10.1016/j.jpowsour.2016.05.041.

[4] N. Wassiliadis, J. Adermann, A. Frericks, M. Pak, C. Reiter, B. Lohmann, M. Lienkamp, Revisiting the dual extended Kalman filter for battery state-of-charge

and state-of-health estimation: A use-case life cycle analysis, J. Energy Storage 19 (2018) 73–87, http://dx.doi.org/10.1016/j.est.2018.07.006.

[5] Z. Ma, Z. Wang, R. Xiong, J. Jiang, A mechanism identification model based state-of-health diagnosis of lithium-ion batteries for energy storage applications, J. Clean. Prod. 193 (2018) 379–390, http://dx.doi.org/10.1016/j.jclepro.2018.05.074.

[6] X. Li, Z. Wang, L. Zhang, Co-estimation of capacity and state-of-charge for lithium-ion batteries in electric vehicles, Energy 174 (2019) 33–44, http://dx.doi.org/10.1016/j.energy.2019.02.147.

[7] S. Lee, J.B. Siegel, A.G. Stefanopoulou, J.-W. Lee, T.-K. Lee, Electrode state of health estimation for lithium ion batteries considering half-cell potential change due to aging, J. Electrochem. Soc. 167 (9) (2020) 090531, http://dx.doi.org/10.1149/1945-7111/ab8c83.

[8] S. Lee, P. Mohtat, J.B. Siegel, A.G. Stefanopoulou, J.-W. Lee, T.-K. Lee, Estimation error bound of battery electrode parameters with limited data window, IEEE Trans. Ind. Inform. 16 (5) (2020) 3376–3386, http://dx.doi.org/10.1109/TII.2019.2952066.

[9] S. Dey, Y. Shi, K. Smith, A. Colclasure, X. Li, From battery cell to electrodes: Real-time estimation of charge and health of individual battery electrodes, IEEE Trans. Ind. Electr. 67 (3) (2020) 2167–2175, http://dx.doi.org/10.1109/TIE.2019.2907514.

[10] M. Dubarry, M. Berecibar, A. Devie, D. Anseán, N. Omar, I. Villarreal, State of health battery estimator enabling degradation diagnosis: Model and algorithm description, J. Power Sources 360 (2017) 59–69, http://dx.doi.org/10.1016/j.jpowsour.2017.05.121.

[11] J. Yang, B. Xia, W. Huang, Y. Fu, C. Mi, Online state-of-health estimation for lithium-ion batteries using constant-voltage charging current analysis, Appl. Energy 212 (2018) 1589–1600, http://dx.doi.org/10.1016/j.apenergy.2018.01.010.

[12] Y. Li, C. Zou, M. Berecibar, E. Nanini-Maury, J.C.-W. Chan, P. van den Bossche, J. van Mierlo, N. Omar, Random forest regression for online capacity estimation of lithium-ion batteries, Appl. Energy 232 (2018) 197–210, http://dx.doi.org/10.1016/j.apenergy.2018.09.182.

[13] R.R. Richardson, C.R. Birkl, M.A. Osborne, D.A. Howey, Gaussian process regression for in situ capacity estimation of lithium-ion batteries, IEEE Trans. Ind. Inf. 15 (1) (2019) 127–138, http://dx.doi.org/10.1109/TII.2018.2794997.

[14] S. Shen, M. Sadoughi, X. Chen, M. Hong, C. Hu, A deep learning method for online capacity estimation of lithium-ion batteries, J. Energy Storage 25 (2) (2019) 100817, http://dx.doi.org/10.1016/j.est.2019.100817.

[15] J. Schmitt, B. Kraft, J.P. Schmidt, B. Meir, K. Elian, D. Ensling, G. Keser, A. Jossen, Measurement of gas pressure inside large-format prismatic lithium-ion cells during operation and cycle aging, J. Power Sources 478 (2020) 228661, http://dx.doi.org/10.1016/j.jpowsour.2020.228661.

[16] I. Zilberman, S. Ludwig, M. Schiller, A. Jossen, Online aging determination in lithium-ion battery module with forced temperature gradient, J. Energy Storage 28 (2020) 101170, http://dx.doi.org/10.1016/j.est.2019.101170.

[17] X. Feng, C. Weng, X. He, X. Han, L. Lu, D. Ren, M. Ouyang, Online state-of-health estimation for Li-Ion battery using partial charging segment based on support vector machine, IEEE Trans. Veh. Technol. 68 (9) (2019) 8583–8592, http://dx.doi.org/10.1109/TVT.2019.2927120.

[18] J. Tian, R. Xiong, W. Shen, F. Sun, Electrode ageing estimation and open circuit voltage reconstruction for lithium ion batteries, Energy Storage Mater. 37 (2021) 283–295, http://dx.doi.org/10.1016/j.ensm.2021.02.018.

[19] Q. Zhang, X. Li, C. Zhou, Y. Zou, Z. Du, M. Sun, Y. Ouyang, D. Yang, Q. Liao, State-of-health estimation of batteries in an energy storage system based on the actual operating parameters, J. Power Sources 506 (2021) 230162, http://dx.doi.org/10.1016/j.jpowsour.2021.230162.

[20] S. Jenu, A. Hentunen, J. Haavisto, M. Pihlatie, State of health estimation of cycle aged large format lithium-ion cells based on partial charging, J. Energy Storage 46 (2022) 103855, http://dx.doi.org/10.1016/j.est.2021.103855.

[21] B. Jiang, H. Dai, X. Wei, Incremental capacity analysis based adaptive capacity estimation for lithium-ion battery considering charging condition, Appl. Energy 269 (2020) 115074, http://dx.doi.org/10.1016/j.apenergy.2020.115074.

[22] A. Nuhic, T. Terzimehic, T. Soczka-Guth, M. Buchholz, K. Dietmayer, Health diagnosis and remaining useful life prognostics of lithium-ion batteries using data-driven methods, J. Power Sources 239 (2013) 680–688, http://dx.doi.org/10.1016/j.jpowsour.2012.11.146.

[23] N. Omar, M.A. Monem, Y. Firouz, J. Salminen, J. Smekens, O. Hegazy, H. Gaulous, G. Mulder, P. van den Bossche, T. Coosemans, J. van Mierlo, Lithium iron phosphate based battery – Assessment of the aging parameters and development of cycle life model, Appl. Energy 113 (2014) 1575–1585, http://dx.doi.org/10.1016/j.apenergy.2013.09.003.

[24] M. Dubarry, C. Truchot, B.Y. Liaw, Synthesize battery degradation modes via a diagnostic and prognostic model, J. Power Sources 219 (2012) 204–216, http://dx.doi.org/10.1016/j.jpowsour.2012.07.016.

[25] C. Campestrini, S. Kosch, A. Jossen, Influence of change in open circuit voltage on the state of charge estimation with an extended Kalman filter, J. Energy Storage 12 (2017) 149–156, http://dx.doi.org/10.1016/j.est.2017.04.011.

[26] K. Kleiner, P. Jakes, S. Scharner, V. Liebau, H. Ehrenberg, Changes of the balancing between anode and cathode due to fatigue in commercial lithium-ion cells, J. Power Sources 317 (2016) 25–34, http://dx.doi.org/10.1016/j.jpowsour.2016.03.049.

[27] C.R. Birkl, M.R. Roberts, E. McTurk, P.G. Bruce, D.A. Howey, Degradation diagnostics for lithium ion cells, J. Power Sources 341 (2017) 373–386, http://dx.doi.org/10.1016/j.jpowsour.2016.12.011.

[28] C.R. Birkl, E. McTurk, S. Zekoll, F.H. Richter, M.R. Roberts, P.G. Bruce, D.A. Howey, Degradation diagnostics for commercial lithium-ion cells tested at - 10 °C, J. Electrochem. Soc. 164 (12) (2017) A2644–A2653, http://dx.doi.org/10.1149/2.1401712jes.

[29] Y. Gao, J. Jiang, C. Zhang, W. Zhang, Y. Jiang, Aging mechanisms under different state-of-charge ranges and the multi-indicators system of state-of-health for lithium-ion battery with Li(NiMnCo)O2 cathode, J. Power Sources 400 (2018) 641–651, http://dx.doi.org/10.1016/j.jpowsour.2018.07.018.

[30] J.P. Fath, D. Dragicevic, L. Bittel, A. Nuhic, J. Sieg, S. Hahn, L. Alsheimer, B. Spier, T. Wetzel, Quantification of aging mechanisms and inhomogeneity in cycled lithium-ion cells by differential voltage analysis, J. Energy Storage 25 (2019) 100813, http://dx.doi.org/10.1016/j.est.2019.100813.

[31] Y. Gao, S. Yang, J. Jiang, C. Zhang, W. Zhang, X. Zhou, The mechanism and characterization of accelerated capacity deterioration for lithium-ion battery with Li(NiMnCo) O 2 cathode, J. Electrochem. Soc. 166 (8) (2019) A1623–A1635, http://dx.doi.org/10.1149/2.1001908jes.

[32] X. Jia, C. Zhang, Y. Le Wang, L. Zhang, W. Zhang, The degradation characteristics and mechanism of Li[Ni 0.5 Co 0.2 Mn 0.3]O 2 batteries at different temperatures and discharge current rates, J. Electrochem. Soc. 167 (2) (2020) 020503, http://dx.doi.org/10.1149/1945-7111/ab61e9.

[33] J. Schmitt, M. Schindler, A. Oberbauer, A. Jossen, Determination of degradation modes of lithium-ion batteries considering aging-induced changes in the half-cell open-circuit potential curve of silicon–graphite, J. Power Sources 532 (9) (2022) 231296, http://dx.doi.org/10.1016/j.jpowsour.2022.231296.

[34] D. Lu, M. Scott Trimboli, G. Fan, R. Zhang, G.L. Plett, Implementation of a physics-based model for half-cell open-circuit potential and full-cell open-circuit voltage estimates: Part II. Processing full-cell data, J. Electrochem. Soc. 168 (7) (2021) 070533, http://dx.doi.org/10.1149/1945-7111/ac11a5.

[35] K. Mergo Mbeya, N. Damay, G. Friedrich, C. Forgez, M. Juston, Off-line method to determine the electrode balancing of Li-ion batteries, Math. Comput. Simul. 183 (10) (2021) 34–47, http://dx.doi.org/10.1016/j.matcom.2020.02.013.

[36] M. Dubarry, D. Beck, Perspective on mechanistic modeling of Li-Ion batteries, Account. Mater. Res. 1 (5) (2022) 242, http://dx.doi.org/10.1021/accountsmr.2c00082.

[37] S. Yang, C. Zhang, J. Jiang, W. Zhang, Y. Gao, L. Zhang, A voltage reconstruction model based on partial charging curve for state-of-health estimation of lithium-ion batteries, J. Energy Storage 35 (2021) 102271, http://dx.doi.org/10.1016/j.est.2021.102271.

[38] J. Chen, M.N. Marlow, Q. Jiang, B. Wu, Peak-tracking method to quantify degradation modes in lithium-ion batteries via differential voltage and incremental capacity, J. Energy Storage 45 (2022) 103669, http://dx.doi.org/10.1016/j.est.2021.103669.

[39] C. Qian, B. Xu, L. Chang, B. Sun, Q. Feng, D. Yang, Y. Ren, Z. Wang, Convolutional neural network based capacity estimation using random segments of the charging curves for lithium-ion batteries, Energy 227 (6058) (2021) 120333, http://dx.doi.org/10.1016/j.energy.2021.120333.

[40] M. Maures, A. Capitaine, J.-Y. Delétage, J.-M. Vinassa, O. Briat, Lithium-ion battery SoH estimation based on incremental capacity peak tracking at several current levels for online application, Microelectron. Reliab. 114 (23) (2020) 113798, http://dx.doi.org/10.1016/j.microrel.2020.113798.

[41] V. Pop, H.J. Bergveld, P.P.L. Regtien, J.H.G. Op het Veld, D. Danilov, P.H.L. Notten, Battery aging and its influence on the electromotive force, J. Electrochem. Soc. 154 (8) (2007) A744, http://dx.doi.org/10.1149/1.2742296.

[42] H. Popp, N. Zhang, M. Jahn, M. Arrinda, S. Ritz, M. Faber, D.U. Sauer, P. Azais, I. Cendoya, Ante-mortem analysis, electrical, thermal, and ageing testing of state-of-the-art cylindrical lithium-ion cells, e & i, Elektrotech. Inf. tech. 137 (4–5) (2020) 169–176, http://dx.doi.org/10.1007/s00502-020-00814-9.

[43] T.M.M. Heenan, A. Jnawali, M.D.R. Kok, T.G. Tranter, C. Tan, A. Dimitrijevic, R. Jervis, D.J.L. Brett, P.R. Shearing, An advanced microstructural and electrochemical datasheet on 18650 Li-Ion batteries with nickel-rich NMC811 cathodes and graphite-silicon anodes, J. Electrochem. Soc. 167 (14) (2020) 140530, http://dx.doi.org/10.1149/1945-7111/abc4c1.

[44] J. Sturm, A. Rheinfeld, I. Zilberman, F.B. Spingler, S. Kosch, F. Frie, A. Jossen, Modeling and simulation of inhomogeneities in a 18650 nickel-rich, silicon-graphite lithium-ion cell during fast charging, J. Power Sources 412 (2019) 204–223, http://dx.doi.org/10.1016/j.jpowsour.2018.11.043.

[45] X. Li, A.M. Colclasure, D.P. Finegan, D. Ren, Y. Shi, X. Feng, L. Cao, Y. Yang, K. Smith, Degradation mechanisms of high capacity 18650 cells containing Si-graphite anode and nickel-rich NMC cathode, Electrochim. Acta 297 (2019) 1109–1120, http://dx.doi.org/10.1016/j.electacta.2018.11.194.

[46] J. Schmitt, M. Rehm, A. Karger, A. Jossen, Aging data, charging curves and battery electric vehicle application profiles of a nickel-rich NMC / silicon-graphite high-energy lithium-ion cell, 2022, http://dx.doi.org/10.14459/2022mp1690455, URL https://mediatum.ub.tum.de/1690455.

[47] E. Kirchner, Leistungsübertragung in Fahrzeuggetrieben: Grundlagen der Auslegung, Entwicklung und Validierung von Fahrzeuggetrieben und deren Komponenten, VDI-Buch, Springer Berlin Heidelberg, Berlin, Heidelberg, 2007.

[48] J. Schmitt, M. Schindler, A. Jossen, Change in the half-cell open-circuit potential curves of silicon–graphite and nickel-rich lithium nickel manganese cobalt oxide during cycle aging, J. Power Sources 506 (1) (2021) 230240, http://dx.doi.org/10.1016/j.jpowsour.2021.230240.

[49] S. Ludwig, I. Zilberman, A. Oberbauer, M. Rogge, M. Fischer, M. Rehm, A. Jossen, Adaptive method for sensorless temperature estimation over the lifetime of lithium-ion batteries, J. Power Sources 521 (2022) 230864, http://dx.doi.org/10.1016/j.jpowsour.2021.230864.

[50] M. Schindler, J. Sturm, S. Ludwig, A. Durdel, A. Jossen, Comprehensive analysis of the aging behavior of nickel-rich, silicon-graphite lithium-ion cells subject to varying temperature and charging profiles, J. Electrochem. Soc. (2021) http://dx.doi.org/10.1149/1945-7111/ac03f6.

[51] I. Zilberman, J. Sturm, A. Jossen, Reversible self-discharge and calendar aging of 18650 nickel-rich, silicon-graphite lithium-ion cells, J. Power Sources 425 (2019) 217–226, http://dx.doi.org/10.1016/j.jpowsour.2019.03.109.

[52] E. Coron, S. Geniès, M. Cugnet, P.X. Thivel, High-energy Li-Ion cells: Impact of electrode ageing on second life viability, J. Electrochem. Soc. 168 (10) (2021) 100539, http://dx.doi.org/10.1149/1945-7111/ac3112.

[53] S. Schweidler, L. de Biasi, A. Schiele, P. Hartmann, T. Brezesinski, J. Janek, Volume changes of graphite anodes revisited: A combined operando X-ray diffraction and in situ pressure analysis study, J. Phys. Chem. C 122 (16) (2018) 8829–8835, http://dx.doi.org/10.1021/acs.jpcc.8b01873.

[54] R. Jung, M. Metzger, F. Maglia, C. Stinner, H.A. Gasteiger, Oxygen release and its effect on the cycling stability of LiNi x Mn y Co z O 2 (NMC) cathode materials for Li-Ion batteries, J. Electrochem. Soc. 164 (7) (2017) A1361–A1377, http://dx.doi.org/10.1149/2.0021707jes.

[55] I. Zilberman, J. Schmitt, S. Ludwig, M. Naumann, A. Jossen, Simulation of voltage imbalance in large lithium-ion battery packs influenced by cell-to-cell variations and balancing systems, J. Energy Storage 32 (2020) 101828, http://dx.doi.org/10.1016/j.est.2020.101828.

[56] S. Schindler, G. Baure, M.A. Danzer, M. Dubarry, Kinetics accommodation in Li-ion mechanistic modeling, J. Power Sources 440 (23) (2019) 227117, http://dx.doi.org/10.1016/j.jpowsour.2019.227117.

[57] C. Campestrini, M.F. Horsche, I. Zilberman, T. Heil, T. Zimmermann, A. Jossen, Validation and benchmark methods for battery management system functionalities: State of charge estimation algorithms, J. Energy Storage 7 (2016) 38–51, http://dx.doi.org/10.1016/j.est.2016.05.007.

6 Discussion, conclusion and outlook

Discussion The studies presented in the scope of this thesis are novel contributions to two related fields of research: the results presented in chapter 4 contribute to the field of understanding and modeling of battery degradation while the results presented in chapters 3 and 5 mainly contribute to the field of methods for the quantification of degradation effects during operation, also known as SOH estimation. Many methods for SOH estimation have been described in the literature [22–24]. As discussed in section 2.3.1, they can be categorized into the three main categories of aging model-based, feature correlation-based and physical model-based methods. Both a feature correlation-based method and a physical model-based method have been developed in the scope of this thesis.

In chapter 3, a novel method for SOH estimation based on measurements of the internal gas pressure inside prismatic lithium-ion cells is presented. The method is feature correlation-based and uses the approximately linear correlation between the increase in internal gas pressure and the decrease in cell capacity during cycle aging. This correlation was empirically observed during long-term cycling experiments using large-format prismatic NMC-111/graphite cells that were equipped with a sensor for measuring the gas pressure inside the cell case. In addition to the increase in pressure during aging, the dependence of the internal gas pressure on SOC and temperature was also investigated in this study. It was found that the pressure exhibits a non-linear, non-monotonic dependence on SOC that is caused by the non-linear expansion and contraction of the electrodes upon lithiation and delithiation. The pressure also increases non-linearly with temperature. In an application, the gas pressure could be measured during rest phases. Then, the influence of a difference in SOC and temperature could be compensated using the determined SOC and temperature dependencies. Finally, the empirically determined correlation between pressure increase and capacity fade could be used to estimate the remaining cell capacity and thus the SOH.
The results presented in chapter 3 represent the proof-of-concept for internal gas pressure-based SOH estimation. While an approximately linear correlation between pressure increase and capacity fade is observed for all investigated cells, the proportionality factor of this correlation differs for the individual cells. It is likely, that this difference between the individual cells arises from the fact that the cells were manually manufactured prototypes with higher cell-to-cell variations than would be expected for cells produced with a higher degree of automation. A high cell-to-cell variation of the proportionality between pressure increase and capacity fade, as observed in this experimental study, would be a problem for applying the proposed SOH estimation algorithm. In this case, the correlation between pressure increase and capacity faded needed to be determined individually for every cell, which is not feasible. Apart from this, it has to be stated that in the study presented in chapter 3, only a limited number of degradation scenarios could be tested. Before the algorithm for SOH estimation could be applied, the correlation between pressure rise and impedance fade needed to be investigated for all relevant operation conditions, in order to investigate whether there is an influence of the operating conditions on the correlation.
There are also some drawbacks of the proposed method that need to be considered: as all feature correlation-based methods, a pre-parameterized correlation between feature and SOH is needed. Ap-

plying the method to a new cell type is thus connected with considerable effort as the correlation needs to be parameterized for this new cell type via laboratory experiments. Another problem might be that the correlation between pressure increase and capacity fade is only reasonably linear after approximately 100 cycles. A last aspect to be considered is that the integration of an additional sensor for pressure measurement leads to additional effort and costs.
Still, SOH estimation based on gas pressure measurements could be applied in addition to voltage and current measurement-based methods in critical systems, in order to provide redundancy. Apart from this, measuring the internal gas pressure could be used for the detection of safety critical states as has been presented in [273]. Finally, additional value of the study presented in chapter 3 should be seen in the systematic investigation of the influence of SOC, temperature and aging on the gas pressure inside prismatic lithium-ion cells. To the author's knowledge, this has been the first study in which all of these three aspects have been investigated for a large-size prismatic cell. The obtained insights on the mechanical behavior of lithium-ion cells might be useful in the context of cell and battery system design.

The second method for SOH estimation developed in the scope of this thesis, presented in chapter 5, is a physical model-based method. A problem for models describing the electrical behavior of lithium-ion cells is that the shape of the OCV curve needs to be adapted during aging [77; 206]. In the method proposed in this chapter, this is solved by parametrizing a model describing the full-cell OCV curve by minimizing the error between measured and simulated partial charging curves. The mechanistic cell model [25], which provides a physics-based interpretation for the change in the full-cell OCV curve and links the change in the curve shape to the degradation modes LAM_{an}, LAM_{cat} and LLI, is used for this purpose. The remaining cell capacity and estimates for the degradation modes can be calculated based on the determined model parameters.
The main contribution of the study presented in chapter 5 is the expansion of the scope of application of the diagnostic method of full-cell OCV curve alignment (see section 2.2.3) to application realistic input data, i.e., partial charging processes at higher current rates that could be observable in an application. Using a systematic investigation of the capacity and degradation mode estimation accuracy obtained for partial charging curves of different SOC windows as algorithm input, it was found that accurate estimates for the remaining capacity (RMSE $\leq$ 2%) can be obtained from low-current (C/30) partial charging curves as long as the SOC range in between 20% and 70% SOC is contained in the input data. The investigation of the performance of the method for charging data measured at higher current rates revealed that a capacity estimation with RMSE $\leq$ 2% can be obtained even for charging at approximately C/4 if a suitable SOC window, e.g. 10-80% SOC, is chosen as input data. These results implicate that full-cell OCV curve alignment as a method for remaining capacity estimation can be applied to charging phases frequently observed in applications as the charging process neither needs to contain the complete SOC range nor does it need to be recorded at a very low current. An example application are BEV charging processes which are carried out using a typical 11 kW home-installed AC charging station, where current rates below C/4 can be expected. In the scope of the study, the method is comprehensively validated with measurement data obtained for cells aged under different conditions and thus the universal applicability at different aging conditions is shown.
A direct comparison between different methods for SOH estimation is difficult as the requirements on SOH estimation are always application-specific and the performance of different methods usually also depends on the cell type they are applied to (see section 2.3.1). Still, it can be stated that the method presented in chapter 5 of this work combines a number of advantages, many methods that can be found in the literature are missing: as a physical model-based method, it does not require a pre-parameterized aging model or correlation between a feature and the SOH, which makes it comparably

easy to be implemented with limited parametrization effort. The change in the full-cell OCV curve shape is explicitly considered, which allows the estimation of degradation modes, providing a deeper insight into battery degradation beyond a scalar capacity-based SOH. In addition, the updated OCV curve that is obtained during aging can be used for other tasks such as model-based SOC estimation [77]. Another advantage is that the method is independent of accurate SOC estimation. Furthermore, the situations in which the algorithm can be applied, i.e., partial charging processes, are likely to occur frequently in many applications [274] and the performance of the algorithm has been validated for a variety of aging conditions. The transferability of the method to other cell types is in principle possible. Due to these reasons, this algorithm is advantageous in many aspects and thus comprises a useful addition to the methods for SOH estimation described in the literature.

The topics of battery aging, battery modeling and SOH estimation are closely interlinked, at least for physical model-based SOH estimation methods. Due to this, also more fundamental topics indirectly connected with SOH estimation have been investigated in this work. The shape of the half-cell OCP curves, which is an important parameter of electrical cell models, is mainly assumed to be invariant during battery degradation [25; 26; 86]. In the study, presented in section 4.1, this assumption is confirmed for NMC-811 but significant changes in the half-cell OCP curve shape of SiC are observed. This change in the OCP curve shape is probably due the comparably fast degradation of the Silicon leading to a reduction of the relative capacity contribution of the Silicon in comparison to the graphite. This result is in accordance with the existing literature [41; 50; 91; 275; 276] but to the author's knowledge it represents the first experimental study showing this effect for commercial cells cycled in full-cell configuration. The change in the half-cell OCP curve shape can be modeled by the blend electrode model proposed by Schmidt et al. [68], which is shown in the study presented in section 4.2.
Apart from this, in this second study it is also investigated how the aging-induced change in the half-cell OCP curve of SiC influences the results on degradation modes obtained from full-cell OCV curve alignment. It is shown that neglecting the change in the SiC OCP curve shape can lead to a misinterpretation of the change in the full-cell OCV curve shape. For the investigated cell type, neglecting the SiC half-cell OCP curve change leads to an overestimation of the LAM_{an} and an underestimation of the LAM_{cat} and the LLI. The errors on the degradation mode estimates induced by this effect are in the order of a few percentage points. It is further shown that the change in the relative capacity contribution of the silicon can be considered by replacing the aging-invariant SiC OCP curve with an OCP curve that is simulated using the blend electrode model. The relative capacity contribution of silicon becomes an additional optimization parameter for the curve alignment process in this case. This approach improves the accuracy of the degradation mode estimates and additionally allows an online estimation of the remaining component capacities of silicon and graphite. Modeling the change in the OCP curve of SiC during aging had been proposed before [70], but to the author's knowledge the study presented in section 4.2 represents the first report of applying this model approach for SiC in a diagnostic context, i.e., to determine the remaining silicon capacity based on experimental charging/discharging curves. It thus comprises a useful addition to the non-invasive diagnostic methods available for analyzing the degradation of lithium-ion batteries.

During the research on SOH estimation based on partial charging curves at higher currents that resulted in the study presented in chapter 5, it was observed that the aforementioned method for the estimation of the remaining silicon capacity contribution can not directly be applied to partial charging curves. Especially in cases in which the low SOC region is not contained in the input charging curves,

no reasonable separation of the anode component capacities is possible. This might be due to the fact that the silicon is primarily active in this SOC region. The applicability of the proposed method for the estimation of the individual capacity of silicon and graphite in its present form is thus restricted to complete, low-current charging curves obtained in the scope of laboratory test. The model extension to the component level is thus not applied in the SOH estimation method presented in chapter 5 and changes in the shape of the OCP curve of SiC are neglected in this study. The algorithms still yields accurate results for the capacity estimation which means that extending the OCV model to the component level is not necessary for the investigated cell type and scenario, in order to obtain accurate capacity estimates with this algorithm. Modeling of component-specific silicon degradation might probably become more important in the future, as cells with even higher silicon ratios in the anode might be commercialized.

Conclusion The main goal of this work was the development of two novel methods for SOH estimation for lithium-ion batteries. Following the discussion of the presented results, the main conclusions of this thesis are: the SOH, i.e., the remaining capacity, can be estimated with sufficient accuracy from partial charging curves at application-relevant currents with the method presented in chapter 5, if charging curves of a suitable SOC window are available. The main advantages of the proposed method are that no pre-parameterized aging model or feature correlation is needed and that the shape of the full-cell OCV curve can be updated during aging.
The method is based on the mechanistic cell model that links changes in the shape of the full-cell OCV curve to degradation modes. The shape of the half-cell OCP curves is usually regarded to be aging-invariant in this type of models. In this work it is shown that this assumption does not hold true for SiC anodes as the silicon degrades faster than the graphite resulting in a change of the half-cell OCP curve. Still, for the investigated cell type with approximately 10 % of the anode capacity provided by silicon, SOH estimation with sufficient accuracy can be obtained by fitting the full-cell OCV model to partial charging curves even if the changes on the half-cell level are neglected. Incorporating component-specific silicon degradation in models used for SOH estimation might become more important in the future as the silicon content used in anodes for lithium-ion batteries is expected to increase.
In addition to this, it was found that the internal gas pressure inside prismatic lithium-ion cells can in principle be used as a feature for SOH estimation, but due to the discussed advantages, physical model-based methods such as the one presented in chapter 5 should be preferred.

Outlook There are several future research objectives expanding on the results obtained in the scope of this thesis. One of these objectives could be the applicability of physical model-based estimation methods to the analysis of field data. Especially algorithms such as the one presented in chapter 5 of this work that additionally allow the estimation of degradation modes have the potential to extract new insights on battery degradation from large sets of field data. In this way, for example empirical aging models on the degradation model level (see section 2.2.2) could possibly be parameterized. Such models could then be used for the optimization of the operation strategy for battery systems.
A possible next step for the further improvement of the method for SOH estimation based on charging curves could be an investigation of the impact of changes in temperature on the estimation accuracy, and, if necessary, the development of compensation strategies. Another aspect could be expanding

the method by using a more complex model describing the overpotential during charging. In order to expand the scope of application of the method, it should also be investigated, whether the method can be applied to constant-power charging, fast charging profiles or dynamic discharging.
Another, more general aspect that was found to be insufficiently covered in the scientific literature is the standardization of the validation methods for SOH estimation algorithms. Direct comparison of the performance of different methods presented in the literature is difficult, which could be improved by introducing standardized validation methods.
The diagnostic method for the estimation of the remaining active silicon capacity could be applied for a systematic investigation of the silicon degradation depending on the operation conditions. The blend electrode model and the associated diagnostic method could also be further improved by considering component specific overpotentials.

References

[1] United Nations Framework Convention on Climate Change: *Paris Agreement*. 2015. URL: https://treaties.un.org/doc/Treaties/2016/02/20160215%2006-03%20PM/Ch_XXVII-7-d.pdf (visited on 11/14/2022).

[2] Council of the European Union: *Submission to the UNFCCC on behalf of the European Union and its Member States on the update of the nationally determined contribution of the European Union and its Member States*. 2020. URL: https://data.consilium.europa.eu/doc/document/ST-14222-2020-REV-1/en/pdf (visited on 12/12/2022).

[3] European Council: *European Council meeting (12 December 2019) – Conclusions*. 2019. URL: https://www.consilium.europa.eu/media/41768/12-euco-final-conclusions-en.pdf (visited on 09/19/2022).

[4] European Parliament and Council of the European Union: *Directive (EU) 2018/2002 of the European Parliament and of the Council of 11 December 2018 amending Directive 2012/ 27/EU on energy efficiency*. 2018. URL: https://eur-lex.europa.eu/legal-content/EN/TXT/PDF/?uri=CELEX:32018L2002&rid=7 (visited on 09/19/2022).

[5] European Parliament and Council of the European Union: *Directive (EU) 2018/2001 of the European Parliament and of the Council of 11 December 2018 on the promotion of the use of energy from renewable sources*. 2018. URL: https://eur-lex.europa.eu/legal-content/EN/TXT/PDF/?uri=CELEX:32018L2001 (visited on 09/19/2022).

[6] Council of the European Union: *Vorschlag für eine Richtlinie der europäischen Parlaments und der Rates zur Änderung der Richtlinie (EU) 2018/2001 des Europäischen Parlaments und des Rates, der Verordnung (EU) 2018/1999 des Europäischen Parlaments und des Rates und der Richtlinie 98/70/EG des Europäischen Parlaments und des Rates im Hinblick auf die Förderung von Energie aus erneuerbaren Quellen und zur Aufhebung der Richtlinie (EU) 2015/652 des Rates*. 2022. URL: https://data.consilium.europa.eu/doc/document/ST-10488-2022-INIT/de/pdf (visited on 09/19/2022).

[7] European Parliament and Council of the European Union: *Regulation (EU) 2019/631 of the European Parliament and of the Council of 17 April 2019 setting CO2 emission performance standards for new passenger cars and for new light commercial vehicles, and repealing Regulations (EC) No 443/2009 and (EU) No 510/2011*. 2019. URL: https://eur-lex.europa.eu/legal-content/EN/TXT/PDF/?uri=CELEX:32019R0631&from=EN (visited on 12/12/2022).

[8] European Environment Agency: *New registrations of electric vehicles in Europe*. 2022. URL: https://www.eea.europa.eu/ims/new-registrations-of-electric-vehicles (visited on 12/19/2022).

[9] International Energy Agency: *Global Electric Vehicle Outlook 2022*. 2022. URL: https://iea.blob.core.windows.net/assets/ad8fb04c-4f75-42fc-973a-6e54c8a4449a/GlobalElectricVehicleOutlook2022.pdf (visited on 12/12/2022).

[10] European Commission: *Vorschlag für eine Verordnung des europäischen Parlaments und des Rates zur Änderung der Verordnung (EU) 2019/631 im Hinblick auf eine Verschärfung der CO2-Emissionsnormen für neue Personenkraftwagen und für neue leichte Nutzfahrzeuge im Einklang mit den ehrgeizigeren Klimazielen der Union*. 2021. URL: https://eur-lex.europa.eu/resource.html?uri=cellar:870b365e-eecc-11eb-a71c-01aa75ed71a1.0015.02/DOC_1&format=PDF (visited on 09/20/2022).

[11] Muratori, M. et al.: *The rise of electric vehicles—2020 status and future expectations*. In: *Progress in Energy* 3 (2) (2021), p. 022002. DOI: 10.1088/2516-1083/abe0ad.

[12] Muralidharan, N., Self, E. C., Dixit, M., Du, Z., Essehli, R., Amin, R., Nanda, J., and Belharouak, I.: *Next–Generation Cobalt–Free Cathodes – A Prospective Solution to the Battery Industry's Cobalt Problem*. In: *Advanced Energy Materials* 12 (9) (2022), p. 2103050. DOI: 10.1002/aenm.202103050.

[13] Ralon Pablo, Taylor, M., Ilas, A., Diaz-Bone, H., and Kairies, K.-P.: *Electricity storage and renewables: Costs and markets to 2030*. Abu Dhabi: International Renewable Energy Agency, 2017. ISBN: 978-92-9260-038-9.

[14] Andrey, C., Barberi, P., Lacombe, L., van Nuffel, L., Gérard, F., Dedecca, J. G., Rademaekers, K., El Idrissi, Y., and Crenes, M.: *Study on energy storage: Contribution to the security of the electricity supply in Europe*. Luxembourg: Publications Office of the European Union, 2020. ISBN: 978-92-76-03377-6. DOI: 10.2833/077257.

[15] Figgener, J. et al.: *The development of stationary battery storage systems in Germany – A market review*. In: *Journal of Energy Storage* 29 (2020), p. 101153. DOI: 10.1016/j.est.2019.101153.

[16] Figgener, J., Hecht, C., Haberschusz, D., Bors, J., Spreuer, K. G., Kairies, K.-P., Stenzel, P., and Sauer, D. U.: *The development of battery storage systems in Germany - A market review (status 2022)*. 2022. DOI: 10.48550/arXiv.2203.06762. URL: https://arxiv.org/abs/2203.06762 (visited on 12/12/2022).

[17] Vetter, J. et al.: *Ageing mechanisms in lithium-ion batteries*. In: *Journal of Power Sources* 147 (1-2) (2005), pp. 269–281. DOI: 10.1016/j.jpowsour.2005.01.006.

[18] Edge, J. S. et al.: *Lithium ion battery degradation: what you need to know*. In: *Physical chemistry chemical physics : PCCP* 23 (14) (2021), pp. 8200–8221. DOI: 10.1039/d1cp00359c.

[19] Vermeer, W., Chandra Mouli, G. R., and Bauer, P.: *A Comprehensive Review on the Characteristics and Modeling of Lithium-Ion Battery Aging*. In: *IEEE Transactions on Transportation Electrification* 8 (2) (2022), pp. 2205–2232. DOI: 10.1109/TTE.2021.3138357.

[20] Han, X., Lu, L., Zheng, Y., Feng, X., Li, Z., Li, J., and Ouyang, M.: *A review on the key issues of the lithium ion battery degradation among the whole life cycle*. In: *eTransportation* 1 (1–2) (2019), p. 100005. DOI: 10.1016/j.etran.2019.100005.

[21] Krause, F. C., Ruiz, J. P., Jones, S. C., Brandon, E. J., Darcy, E. C., Iannello, C. J., and Bugga, R. V.: *Performance of Commercial Li-Ion Cells for Future NASA Missions and Aerospace Applications*. In: *Journal of The Electrochemical Society* 168 (4) (2021), p. 040504. DOI: 10.1149/1945-7111/abf05f.

[22] Yang, S., Zhang, C., Jiang, J., Zhang, W., Zhang, L., and Wang, Y.: *Review on state-of-health of lithium-ion batteries: Characterizations, estimations and applications*. In: *Journal of Cleaner Production* 314 (2021), p. 128015. DOI: 10.1016/j.jclepro.2021.128015.

[23] Ungurean, L., Cârstoiu, G., Micea, M. V., and Groza, V.: *Battery state of health estimation: A structured review of models, methods and commercial devices*. In: *International Journal of Energy Research* 41 (2) (2017), pp. 151–181. DOI: 10.1002/er.3598.

[24] Waag, W., Fleischer, C., and Sauer, D. U.: *Critical review of the methods for monitoring of lithium-ion batteries in electric and hybrid vehicles*. In: *Journal of Power Sources* 258 (2014), pp. 321–339. DOI: 10.1016/j.jpowsour.2014.02.064.

[25] Dubarry, M., Truchot, C., and Liaw, B. Y.: *Synthesize battery degradation modes via a diagnostic and prognostic model*. In: *Journal of Power Sources* 219 (2012), pp. 204–216. DOI: 10.1016/j.jpowsour.2012.07.016.

[26] Dubarry, M. and Beck, D.: *Perspective on Mechanistic Modeling of Li-Ion Batteries*. In: *Accounts of Materials Research* 1 (5) (2022), p. 242. DOI: 10.1021/accountsmr.2c00082.

[27] Whittingham, M. S.: *Lithium batteries and cathode materials*. In: *Chemical reviews* 104 (10) (2004), pp. 4271–4301. DOI: 10.1021/cr020731c.

[28] Newman, J. and Balsara, N. P.: *Electrochemical systems*. Fourth edition. ECS, the Electrochemical Society series. Hoboken, NJ: Wiley, 2021. ISBN: 9781119514596.

[29] Guyomard, D. and Tarascon, J.-M.: *Rocking-chair or lithium-ion rechargeable lithium batteries*. In: *Advanced Materials* 6 (5) (1994), pp. 408–412. DOI: 10.1002/adma.19940060516.

[30] Hausbrand, R., Cherkashinin, G., Ehrenberg, H., Gröting, M., Albe, K., Hess, C., and Jaegermann, W.: *Fundamental degradation mechanisms of layered oxide Li-ion battery cathode materials: Methodology, insights and novel approaches*. In: *Materials Science and Engineering: B* 192 (16) (2015), pp. 3–25. DOI: 10.1016/j.mseb.2014.11.014.

[31] Korthauer, R., ed.: *Handbuch Lithium-Ionen-Batterien*. Berlin, Heidelberg: Springer Vieweg, 2013. ISBN: 978-3-642-30653-2. DOI: 10.1007/978-3-642-30653-2.

[32] Winter, M., Besenhard, J. O., Spahr, M. E., and Novák, P.: *Insertion Electrode Materials for Rechargeable Lithium Batteries*. In: *Advanced Materials* 10 (10) (1998), pp. 725–763. DOI: 10.1002/(SICI)1521-4095(199807)10:10<725::AID-ADMA725>3.0.CO;2-Z.

[33] Nishi, Y.: *Lithium ion secondary batteries; past 10 years and the future*. In: *Journal of Power Sources* 100 (1-2) (2001), pp. 101–106. DOI: 10.1016/S0378-7753(01)00887-4.

[34] Ohzuku, T., Iwakoshi, Y., and Sawai, K.: *Formation of Lithium–Graphite Intercalation Compounds in Nonaqueous Electrolytes and Their Application as a Negative Electrode for a Lithium Ion (Shuttlecock) Cell*. In: *Journal of The Electrochemical Society* 140 (9) (1993), pp. 2490–2498. DOI: 10.1149/1.2220849.

[35] Schweidler, S., Biasi, L. de, Schiele, A., Hartmann, P., Brezesinski, T., and Janek, J.: *Volume Changes of Graphite Anodes Revisited: A Combined Operando X-ray Diffraction and In Situ Pressure Analysis Study*. In: *The Journal of Physical Chemistry C* 122 (16) (2018), pp. 8829–8835. DOI: 10.1021/acs.jpcc.8b01873.

[36] Allart, D., Montaru, M., and Gualous, H.: *Model of Lithium Intercalation into Graphite by Potentiometric Analysis with Equilibrium and Entropy Change Curves of Graphite Electrode*. In: *Journal of the Electrochemical Society* 165 (2) (2018), A380–A387. DOI: 10.1149/2.1251802jes.

[37] Dahn, J. R.: *Phase diagram of LixC6*. In: *Physical review. B, Condensed matter* 44 (17) (1991), pp. 9170–9177. DOI: 10.1103/PhysRevB.44.9170.

[38] Billaud, D., Henry, F. X., Lelaurain, M., and Willmann, P.: *Revisited structures of dense and dilute stage II lithium-graphite intercalation compounds*. In: *Journal of Physics and Chemistry of Solids* 57 (6-8) (1996), pp. 775–781. DOI: 10.1016/0022-3697(95)00348-7.

[39] Billaud, D. and Henry, F.: *Structural studies of the stage III lithium–graphite intercalation compound*. In: *Solid State Communications* 124 (8) (2002), pp. 299–304. DOI: 10.1016/S0038-1098(02)00469-6.

[40] Mercer, M. P., Peng, C., Soares, C., Hoster, H. E., and Kramer, D.: *Voltage hysteresis during lithiation/delithiation of graphite associated with meta-stable carbon stackings*. In: *Journal of Materials Chemistry A* 9 (1) (2021), pp. 492–504. DOI: 10.1039/D0TA10403E.

[41] Dose, W. M., Piernas-Muñoz, M. J., Maroni, V. A., Trask, S. E., Bloom, I., and Johnson, C. S.: *Capacity fade in high energy silicon-graphite electrodes for lithium-ion batteries*. In: *Chemical communications* 54 (29) (2018), pp. 3586–3589. DOI: 10.1039/c8cc00456k.

[42] Wu, J., Cao, Y., Zhao, H., Mao, J., and Guo, Z.: *The critical role of carbon in marrying silicon and graphite anodes for high–energy lithium–ion batteries*. In: *Carbon Energy* 1 (1) (2019), pp. 57–76. DOI: 10.1002/cey2.2.

[43] Jerliu, B., Hüger, E., Dörrer, L., Seidlhofer, B.-K., Steitz, R., Oberst, V., Geckle, U., Bruns, M., and Schmidt, H.: *Volume Expansion during Lithiation of Amorphous Silicon Thin Film Electrodes Studied by In-Operando Neutron Reflectometry*. In: *The Journal of Physical Chemistry C* 118 (18) (2014), pp. 9395–9399. DOI: 10.1021/jp502261t.

[44] Moyassari, E., Roth, T., Kücher, S., Chang, C.-C., Hou, S.-C., Spingler, F. B., and Jossen, A.: *The Role of Silicon in Silicon-Graphite Composite Electrodes Regarding Specific Capacity, Cycle Stability, and Expansion*. In: *Journal of The Electrochemical Society* 169 (1) (2022), p. 010504. DOI: 10.1149/1945-7111/ac4545.

[45] Heenan, T. M. M., Jnawali, A., Kok, M. D. R., Tranter, T. G., Tan, C., Dimitrijevic, A., Jervis, R., Brett, D. J. L., and Shearing, P. R.: *An Advanced Microstructural and Electrochemical Datasheet on 18650 Li-Ion Batteries with Nickel-Rich NMC811 Cathodes and Graphite-Silicon Anodes*. In: *Journal of The Electrochemical Society* 167 (14) (2020), p. 140530. DOI: 10.1149/1945-7111/abc4c1.

[46] Schmitt, J., Schindler, M., and Jossen, A.: *Change in the half-cell open-circuit potential curves of silicon–graphite and nickel-rich lithium nickel manganese cobalt oxide during cycle aging*. In: *Journal of Power Sources* 506 (1) (2021), p. 230240. DOI: 10.1016/j.jpowsour.2021.230240.

[47] Schmitt, J., Schindler, M., Oberbauer, A., and Jossen, A.: *Determination of degradation modes of lithium-ion batteries considering aging-induced changes in the half-cell open-circuit potential curve of silicon–graphite*. In: *Journal of Power Sources* 532 (9) (2022), p. 231296. DOI: 10.1016/j.jpowsour.2022.231296.

[48] Popp, H., Zhang, N., Jahn, M., Arrinda, M., Ritz, S., Faber, M., Sauer, D. U., Azais, P., and Cendoya, I.: *Ante-mortem analysis, electrical, thermal, and ageing testing of state-of-the-art cylindrical lithium-ion cells*. In: *e & i Elektrotechnik und Informationstechnik* 137 (4-5) (2020), pp. 169–176. DOI: 10.1007/s00502-020-00814-9.

[49] Sturm, J., Rheinfeld, A., Zilberman, I., Spingler, F. B., Kosch, S., Frie, F., and Jossen, A.: *Modeling and simulation of inhomogeneities in a 18650 nickel-rich, silicon-graphite lithium-ion cell during fast charging*. In: *Journal of Power Sources* 412 (2019), pp. 204–223. DOI: 10.1016/j.jpowsour.2018.11.043.

[50] Li, X., Colclasure, A. M., Finegan, D. P., Ren, D., Shi, Y., Feng, X., Cao, L., Yang, Y., and Smith, K.: *Degradation mechanisms of high capacity 18650 cells containing Si-graphite anode and nickel-rich NMC cathode*. In: *Electrochimica Acta* 297 (2019), pp. 1109–1120. DOI: 10.1016/j.electacta.2018.11.194.

[51] Campestrini, C., Heil, T., Kosch, S., and Jossen, A.: *A comparative study and review of different Kalman filters by applying an enhanced validation method*. In: *Journal of Energy Storage* 8 (2016), pp. 142–159. DOI: 10.1016/j.est.2016.10.004.

[52] Chandesris, M., Caliste, D., Jamet, D., and Pochet, P.: *Thermodynamics and Related Kinetics of Staging in Intercalation Compounds*. In: *The Journal of Physical Chemistry C* 123 (38) (2019), pp. 23711–23720. DOI: 10.1021/acs.jpcc.9b05298.

[53] Noh, H.-J., Youn, S., Yoon, C. S., and Sun, Y.-K.: *Comparison of the structural and electrochemical properties of layered Li[NixCoyMnz]O2 (x = 1/3, 0.5, 0.6, 0.7, 0.8 and 0.85) cathode material for lithium-ion batteries*. In: *Journal of Power Sources* 233 (2013), pp. 121–130. DOI: 10.1016/j.jpowsour.2013.01.063.

[54] Jung, R., Metzger, M., Maglia, F., Stinner, C., and Gasteiger, H. A.: *Oxygen Release and Its Effect on the Cycling Stability of LiNi x Mn y Co z O 2 (NMC) Cathode Materials for Li-Ion Batteries*. In: *Journal of the Electrochemical Society* 164 (7) (2017), A1361–A1377. DOI: 10.1149/2.0021707jes.

[55] Smith, R. B., Khoo, E., and Bazant, M. Z.: *Intercalation Kinetics in Multiphase-Layered Materials*. In: *The Journal of Physical Chemistry C* 121 (23) (2017), pp. 12505–12523. DOI: 10.1021/acs.jpcc.7b00185.

[56] Zhang, Q., Guo, Q., and White, R. E.: *A New Kinetic Equation for Intercalation Electrodes*. In: *Journal of the Electrochemical Society* 153 (2) (2006), A301. DOI: 10.1149/1.2142287.

[57] Birkl, C. R., McTurk, E., Roberts, M. R., Bruce, P. G., and Howey, D. A.: *A Parametric Open Circuit Voltage Model for Lithium Ion Batteries*. In: *Journal of The Electrochemical Society* 162 (12) (2015), A2271–A2280. DOI: 10.1149/2.0331512jes.

[58] Verbrugge, M., Baker, D., and Xiao, X.: *Formulation for the Treatment of Multiple Electrochemical Reactions and Associated Speciation for the Lithium-Silicon Electrode*. In: *Journal of the Electrochemical Society* 163 (2) (2016), A262–A271. DOI: 10.1149/2.0581602jes.

[59] Verbrugge, M., Baker, D., Koch, B., Xiao, X., and Gu, W.: *Thermodynamic Model for Substitutional Materials: Application to Lithiated Graphite, Spinel Manganese Oxide, Iron Phosphate, and Layered Nickel-Manganese-Cobalt Oxide*. In: *Journal of the Electrochemical Society* 164 (11) (2017), E3243–E3253. DOI: 10.1149/2.0341708jes.

[60] Lu, D., Scott Trimboli, M., Fan, G., Zhang, R., and Plett, G. L.: *Implementation of a Physics-Based Model for Half-Cell Open-Circuit Potential and Full-Cell Open-Circuit Voltage Estimates: Part I. Processing Half-Cell Data*. In: *Journal of The Electrochemical Society* 168 (7) (2021), p. 070532. DOI: 10.1149/1945-7111/ac11a4.

[61] Karthikeyan, D. K., Sikha, G., and White, R. E.: *Thermodynamic model development for lithium intercalation electrodes*. In: *Journal of Power Sources* 185 (2) (2008), pp. 1398–1407. DOI: 10.1016/j.jpowsour.2008.07.077.

[62] Lavigne, L., Sabatier, J., Francisco, J. M., Guillemard, F., and Noury, A.: *Lithium-ion Open Circuit Voltage (OCV) curve modelling and its ageing adjustment*. In: *Journal of Power Sources* 324 (2016), pp. 694–703. DOI: 10.1016/j.jpowsour.2016.05.121.

[63] Verbrugge, M. W. and Koch, B. J.: *Modeling Lithium Intercalation of Single–Fiber Carbon Microelectrodes*. In: *Journal of the Electrochemical Society* 143 (2) (1996), pp. 600–608. DOI: 10.1149/1.1836486.

[64] Plett, G. L.: *Extended Kalman filtering for battery management systems of LiPB-based HEV battery packs*. In: *Journal of Power Sources* 134 (2) (2004), pp. 262–276. DOI: 10.1016/j.jpowsour.2004.02.032.

[65] Barai, A., Widanage, W. D., Marco, J., McGordon, A., and Jennings, P.: *A study of the open circuit voltage characterization technique and hysteresis assessment of lithium-ion cells*. In: *Journal of Power Sources* 295 (2015), pp. 99–107. DOI: 10.1016/j.jpowsour.2015.06.140.

[66] Ai, W., Kirkaldy, N., Jiang, Y., Offer, G., Wang, H., and Wu, B.: *A composite electrode model for lithium-ion batteries with silicon/graphite negative electrodes*. In: *Journal of Power Sources* 527 (1) (2022), p. 231142. DOI: 10.1016/j.jpowsour.2022.231142.

[67] Zilberman, I., Rheinfeld, A., and Jossen, A.: *Uncertainties in entropy due to temperature path dependent voltage hysteresis in Li-ion cells*. In: *Journal of Power Sources* 395 (2018), pp. 179–184. DOI: 10.1016/j.jpowsour.2018.05.052.

[68] Schmidt, J. P., Tran, H. Y., Richter, J., Ivers-Tiffée, E., and Wohlfahrt-Mehrens, M.: *Analysis and prediction of the open circuit potential of lithium-ion cells*. In: *Journal of Power Sources* 239 (2013), pp. 696–704. DOI: 10.1016/j.jpowsour.2012.11.101.

[69] Jung, S.: *Mathematical model of lithium-ion batteries with blended-electrode system*. In: *Journal of Power Sources* 264 (2014), pp. 184–194. DOI: 10.1016/j.jpowsour.2014.04.072.

[70] Anseán, D., Baure, G., González, M., Cameán, I., García, A. B., and Dubarry, M.: *Mechanistic investigation of silicon-graphite/LiNi0.8Mn0.1Co0.1O2 commercial cells for non-intrusive diagnosis and prognosis*. In: *Journal of Power Sources* 459 (2020), p. 227882. DOI: 10.1016/j.jpowsour.2020.227882.

[71] Yao, K. P. C., Okasinski, J. S., Kalaga, K., Almer, J. D., and Abraham, D. P.: *Operando Quantification of (De)Lithiation Behavior of Silicon-Graphite Blended Electrodes for Lithium-Ion Batteries*. In: *Advanced Energy Materials* 9 (8) (2019), p. 1803380. DOI: 10.1002/aenm.201803380.

[72] Klett, M., Gilbert, J. A., Pupek, K. Z., Trask, S. E., and Abraham, D. P.: *Layered Oxide, Graphite and Silicon-Graphite Electrodes for Lithium-Ion Cells: Effect of Electrolyte Composition and Cycling Windows*. In: *Journal of the Electrochemical Society* 164 (1) (2017), A6095–A6102. DOI: 10.1149/2.0131701jes.

[73] Jiang, Y., Offer, G., Jiang, J., Marinescu, M., and Wang, H.: *Voltage Hysteresis Model for Silicon Electrodes for Lithium Ion Batteries, Including Multi-Step Phase Transformations, Crystallization and Amorphization*. In: *Journal of The Electrochemical Society* 167 (13) (2020), p. 130533. DOI: 10.1149/1945-7111/abbbba.

[74] Li, J. and Dahn, J. R.: *An In Situ X-Ray Diffraction Study of the Reaction of Li with Crystalline Si*. In: *Electrochemical and Solid-State Letters* 154 (3) (2007), A156. DOI: 10.1149/1.2409862.

[75] Lu, D., Scott Trimboli, M., Fan, G., Zhang, R., and Plett, G. L.: *Implementation of a Physics-Based Model for Half-Cell Open-Circuit Potential and Full-Cell Open-Circuit Voltage Estimates: Part II. Processing Full-Cell Data*. In: *Journal of The Electrochemical Society* 168 (7) (2021), p. 070533. DOI: 10.1149/1945-7111/ac11a5.

[76] Campestrini, C., Horsche, M. F., Zilberman, I., Heil, T., Zimmermann, T., and Jossen, A.: *Validation and benchmark methods for battery management system functionalities: State of charge estimation algorithms*. In: *Journal of Energy Storage* 7 (2016), pp. 38–51. DOI: 10.1016/j.est.2016.05.007.

[77] Campestrini, C., Kosch, S., and Jossen, A.: *Influence of change in open circuit voltage on the state of charge estimation with an extended Kalman filter*. In: *Journal of Energy Storage* 12 (2017), pp. 149–156. DOI: 10.1016/j.est.2017.04.011.

[78] Weng, C., Sun, J., and Peng, H.: *A unified open-circuit-voltage model of lithium-ion batteries for state-of-charge estimation and state-of-health monitoring*. In: *Journal of Power Sources* 258 (2014), pp. 228–237. DOI: 10.1016/j.jpowsour.2014.02.026.

[79] Pattipati, B., Balasingam, B., Avvari, G. V., Pattipati, K. R., and Bar-Shalom, Y.: *Open circuit voltage characterization of lithium-ion batteries*. In: *Journal of Power Sources* 269 (2014), pp. 317–333. DOI: 10.1016/j.jpowsour.2014.06.152.

[80] Zheng, F., Xing, Y., Jiang, J., Sun, B., Kim, J., and Pecht, M.: *Influence of different open circuit voltage tests on state of charge online estimation for lithium-ion batteries*. In: *Applied Energy* 183 (2016), pp. 513–525. DOI: 10.1016/j.apenergy.2016.09.010.

[81] Kirkaldy, N., Samieian, M. A., Offer, G. J., Marinescu, M., and Patel, Y.: *Lithium-Ion Battery Degradation: Measuring Rapid Loss of Active Silicon in Silicon-Graphite Composite Electrodes*. In: *ACS Applied Energy Materials* 5 (11) (2022), pp. 13367–13376. DOI: 10.1021/acsaem.2c02047.

[82] Lory, P.-F., Mathieu, B., Genies, S., Reynier, Y., Boulineau, A., Hong, W., and Chandesris, M.: *Probing Silicon Lithiation in Silicon-Carbon Blended Anodes with a Multi-Scale Porous Electrode Model*. In: *Journal of The Electrochemical Society* 167 (12) (2020), p. 120506. DOI: 10.1149/1945-7111/abaa69.

[83] Zilberman, I., Sturm, J., and Jossen, A.: *Reversible self-discharge and calendar aging of 18650 nickel-rich, silicon-graphite lithium-ion cells*. In: *Journal of Power Sources* 425 (2019), pp. 217–226. DOI: 10.1016/j.jpowsour.2019.03.109.

[84] Gao, Y., Yang, S., Jiang, J., Zhang, C., Zhang, W., and Zhou, X.: *The Mechanism and Characterization of Accelerated Capacity Deterioration for Lithium-Ion Battery with Li(NiMnCo) O 2 Cathode*. In: *Journal of the Electrochemical Society* 166 (8) (2019), A1623–A1635. DOI: 10.1149/2.1001908jes.

[85] Lee, S., Siegel, J. B., Stefanopoulou, A. G., Lee, J.-W., and Lee, T.-K.: *Electrode State of Health Estimation for Lithium Ion Batteries Considering Half-cell Potential Change Due to Aging*. In: *Journal of The Electrochemical Society* 167 (9) (2020), p. 090531. DOI: 10.1149/1945-7111/ab8c83.

[86] Yang, S., Zhang, C., Jiang, J., Zhang, W., Gao, Y., and Zhang, L.: *A voltage reconstruction model based on partial charging curve for state-of-health estimation of lithium-ion batteries*. In: *Journal of Energy Storage* 35 (2021), p. 102271. DOI: 10.1016/j.est.2021.102271.

[87] Li, Y., Abdel-Monem, M., Gopalakrishnan, R., Berecibar, M., Nanini-Maury, E., Omar, N., van den Bossche, P., and van Mierlo, J.: *A quick on-line state of health estimation method for Li-ion battery with incremental capacity curves processed by Gaussian filter*. In: *Journal of Power Sources* 373 (2018), pp. 40–53. DOI: 10.1016/j.jpowsour.2017.10.092.

[88] Prosser, R., Offer, G., and Patel, Y.: *Lithium-Ion Diagnostics: The First Quantitative In-Operando Technique for Diagnosing Lithium Ion Battery Degradation Modes under Load with Realistic Thermal Boundary Conditions*. In: *Journal of The Electrochemical Society* 168 (3) (2021), p. 030532. DOI: 10.1149/1945-7111/abed28.

[89] Lui, Y. H. et al.: *Physics-based prognostics of implantable-grade lithium-ion battery for remaining useful life prediction*. In: *Journal of Power Sources* 485 (6273) (2021), p. 229327. DOI: 10.1016/j.jpowsour.2020.229327.

[90] Dubarry, M. and Baure, G.: *Perspective on Commercial Li-ion Battery Testing, Best Practices for Simple and Effective Protocols*. In: *Electronics* 9 (1) (2020), p. 152. DOI: 10.3390/electronics9010152.

[91] Klett, M., Gilbert, J. A., Trask, S. E., Polzin, B. J., Jansen, A. N., Dees, D. W., and Abraham, D. P.: *Electrode Behavior RE-Visited: Monitoring Potential Windows, Capacity Loss, and Impedance Changes in Li 1.03 (Ni 0.5 Co 0.2 Mn 0.3) 0.97 O 2 /Silicon-Graphite Full Cells*. In: *Journal of the Electrochemical Society* 163 (6) (2016), A875–A887. DOI: 10.1149/2.0271606jes.

[92] Jung, R., Morasch, R., Karayaylali, P., Phillips, K., Maglia, F., Stinner, C., Shao-Horn, Y., and Gasteiger, H. A.: *Effect of Ambient Storage on the Degradation of Ni-Rich Positive Electrode Materials (NMC811) for Li-Ion Batteries*. In: *Journal of the Electrochemical Society* 165 (2) (2018), A132–A141. DOI: 10.1149/2.0401802jes.

[93] Chen, J., Marlow, M. N., Jiang, Q., and Wu, B.: *Peak-tracking method to quantify degradation modes in lithium-ion batteries via differential voltage and incremental capacity*. In: *Journal of Energy Storage* 45 (2022), p. 103669. DOI: 10.1016/j.est.2021.103669.

[94] Schmid, A. U., Kurka, M., and Birke, K. P.: *Reproducibility of Li-ion cell reassembling processes and their influence on coin cell aging*. In: *Journal of Energy Storage* 24 (2019), p. 100732. DOI: 10.1016/j.est.2019.04.006.

[95] Tian, J., Xu, R., Wang, Y., and Chen, Z.: *Capacity attenuation mechanism modeling and health assessment of lithium-ion batteries*. In: *Energy* 221 (15) (2021), p. 119682. DOI: 10.1016/j.energy.2020.119682.

[96] Jia, X., Zhang, C., Le Wang, Y., Zhang, L., and Zhang, W.: *The Degradation Characteristics and Mechanism of Li[Ni 0.5 Co 0.2 Mn 0.3]O 2 Batteries at Different Temperatures and Discharge Current Rates*. In: *Journal of The Electrochemical Society* 167 (2) (2020), p. 020503. DOI: 10.1149/1945-7111/ab61e9.

[97] Birkl, C. R., Roberts, M. R., McTurk, E., Bruce, P. G., and Howey, D. A.: *Degradation diagnostics for lithium ion cells*. In: *Journal of Power Sources* 341 (2017), pp. 373–386. DOI: 10.1016/j.jpowsour.2016.12.011.

[98] Birkl, C. R., McTurk, E., Zekoll, S., Richter, F. H., Roberts, M. R., Bruce, P. G., and Howey, D. A.: *Degradation Diagnostics for Commercial Lithium-Ion Cells Tested at − 10°C*. In: *Journal of the Electrochemical Society* 164 (12) (2017), A2644–A2653. DOI: 10.1149/2.1401712jes.

[99] Jones, E. M. C., Çapraz, Ö. Ö., White, S. R., and Sottos, N. R.: *Reversible and Irreversible Deformation Mechanisms of Composite Graphite Electrodes in Lithium-Ion Batteries*. In: *Journal of The Electrochemical Society* 163 (9) (2016), A1965–A1974. DOI: 10.1149/2.0751609jes.

[100] Bauer, M., Wachtler, M., Stöwe, H., Persson, J. V., and Danzer, M. A.: *Understanding the dilation and dilation relaxation behavior of graphite-based lithium-ion cells*. In: *Journal of Power Sources* 317 (2016), pp. 93–102. DOI: 10.1016/j.jpowsour.2016.03.078.

[101] Rieger, B., Schlueter, S., Erhard, S. V., Schmalz, J., Reinhart, G., and Jossen, A.: *Multi-scale investigation of thickness changes in a commercial pouch type lithium-ion battery*. In: *Journal of Energy Storage* 6 (2016), pp. 213–221. DOI: 10.1016/j.est.2016.01.006.

[102] Koyama, Y., Tanaka, I., Adachi, H., Makimura, Y., and Ohzuku, T.: *Crystal and electronic structures of superstructural Li1−x[Co1/3Ni1/3Mn1/3]O2 (0≤x≤1)*. In: *Journal of Power Sources* 119-121 (2003), pp. 644–648. DOI: 10.1016/S0378-7753(03)00194-0.

[103] Yoon, W.-S., Chung, K. Y., McBreen, J., and Yang, X.-Q.: *A comparative study on structural changes of LiCo1/3Ni1/3Mn1/3O2 and LiNi0.8Co0.15Al0.05O2 during first charge using in situ XRD*. In: *Electrochemistry Communications* 8 (8) (2006), pp. 1257–1262. DOI: 10.1016/j.elecom.2006.06.005.

[104] Yabuuchi, N., Makimura, Y., and Ohzuku, T.: *Solid-State Chemistry and electrochemistry of LiCo1/3Ni1/3Mn1/3O2 for Advanced Lithium-Ion Batteries*. In: *Journal of Power Sources* 154 (4) (2007), A314. DOI: 10.1149/1.2455585.

[105] Märker, K., Reeves, P. J., Xu, C., Griffith, K. J., and Grey, C. P.: *Evolution of Structure and Lithium Dynamics in LiNi 0.8 Mn 0.1 Co 0.1 O 2 (NMC811) Cathodes during Electrochemical Cycling*. In: *Chemistry of Materials* 31 (7) (2019), pp. 2545–2554. DOI: 10.1021/acs.chemmater.9b00140.

[106] Bitzer, B. and Gruhle, A.: *A new method for detecting lithium plating by measuring the cell thickness*. In: *Journal of Power Sources* 262 (2014), pp. 297–302. DOI: 10.1016/j.jpowsour.2014.03.142.

[107] Cannarella, J. and Arnold, C. B.: *Stress evolution and capacity fade in constrained lithium-ion pouch cells*. In: *Journal of Power Sources* 245 (2014), pp. 745–751. DOI: 10.1016/j.jpowsour.2013.06.165.

[108] Cannarella, J. and Arnold, C. B.: *State of health and charge measurements in lithium-ion batteries using mechanical stress*. In: *Journal of Power Sources* 269 (2014), pp. 7–14. DOI: 10.1016/j.jpowsour.2014.07.003.

[109] Zhou, S., Wang, G., Xiao, Y., Li, Q., Yang, D., and Yan, K.: *Influence of charge status on the stress safety properties of Li(Ni 1/3 Co 1/3 Mn 1/3)O 2 cells*. In: *RSC Advances* 6 (68) (2016), pp. 63378–63389. DOI: 10.1039/C6RA08774D.

[110] Willenberg, L. K., Dechent, P., Fuchs, G., Sauer, D. U., and Figgemeier, E.: *High-Precision Monitoring of Volume Change of Commercial Lithium-Ion Batteries by Using Strain Gauges*. In: *Sustainability* 12 (2) (2020), p. 557. DOI: 10.3390/su12020557.

[111] Willenberg, L., Dechent, P., Fuchs, G., Teuber, M., Eckert, M., Graff, M., Kürten, N., Sauer, D. U., and Figgemeier, E.: *The Development of Jelly Roll Deformation in 18650 Lithium-Ion Batteries at Low State of Charge*. In: *Journal of The Electrochemical Society* 167 (12) (2020), p. 120502. DOI: 10.1149/1945-7111/aba96d.

[112] Matasso, A., Wetz, D., and Liu, F.: *The Effects of Internal Pressure Evolution on the Aging of Commercial Li-Ion Cells*. In: *Journal of The Electrochemical Society* 162 (1) (2015), A92–A97. DOI: 10.1149/2.0611501jes.

[113] Schiele, A., Hatsukade, T., Berkes, B. B., Hartmann, P., Brezesinski, T., and Janek, J.: *High-Throughput in Situ Pressure Analysis of Lithium-Ion Batteries*. In: *Analytical chemistry* 89 (15) (2017), pp. 8122–8128. DOI: 10.1021/acs.analchem.7b01760.

[114] Pastor-Fernández, C., Yu, T. F., Widanage, W. D., and Marco, J.: *Critical review of non-invasive diagnosis techniques for quantification of degradation modes in lithium-ion batteries*. In: *Renewable and Sustainable Energy Reviews* 109 (2019), pp. 138–159. DOI: 10.1016/j.rser.2019.03.060.

[115] Yang, X.-G., Leng, Y., Zhang, G., Ge, S., and Wang, C.-Y.: *Modeling of lithium plating induced aging of lithium-ion batteries: Transition from linear to nonlinear aging*. In: *Journal of Power Sources* 360 (2017), pp. 28–40. DOI: 10.1016/j.jpowsour.2017.05.110.

[116] Kleiner, K., Jakes, P., Scharner, S., Liebau, V., and Ehrenberg, H.: *Changes of the balancing between anode and cathode due to fatigue in commercial lithium-ion cells*. In: *Journal of Power Sources* 317 (2016), pp. 25–34. DOI: 10.1016/j.jpowsour.2016.03.049.

[117] Lüders, C. von, Keil, J., Webersberger, M., and Jossen, A.: *Modeling of lithium plating and lithium stripping in lithium-ion batteries*. In: *Journal of Power Sources* 414 (2019), pp. 41–47. DOI: 10.1016/j.jpowsour.2018.12.084.

[118] Dubarry, M. and Beck, D.: *Big data training data for artificial intelligence-based Li-ion diagnosis and prognosis*. In: *Journal of Power Sources* 479 (3) (2020), p. 228806. DOI: 10.1016/j.jpowsour.2020.228806.

[119] Billy, E., Joulié, M., Laucournet, R., Boulineau, A., Vito, E. de, and Meyer, D.: *Dissolution Mechanisms of LiNi1/3Mn1/3Co1/3O2 Positive Electrode Material from Lithium-Ion Batteries in Acid Solution*. In: *ACS applied materials & interfaces* 10 (19) (2018), pp. 16424–16435. DOI: 10.1021/acsami.8b01352.

[120] Friedrich, F., Strehle, B., Freiberg, A. T. S., Kleiner, K., Day, S. J., Erk, C., Piana, M., and Gasteiger, H. A.: *Editors' Choice—Capacity Fading Mechanisms of NCM-811 Cathodes in Lithium-Ion Batteries Studied by X-ray Diffraction and Other Diagnostics*. In: *Journal of the Electrochemical Society* 166 (15) (2019), A3760–A3774. DOI: 10.1149/2.0821915jes.

[121] Schweidler, S., Biasi, L. de, Garcia, G., Mazilkin, A., Hartmann, P., Brezesinski, T., and Janek, J.: *Investigation into Mechanical Degradation and Fatigue of High-Ni NCM Cathode Material: A Long-Term Cycling Study of Full Cells*. In: *ACS Applied Energy Materials* 2 (10) (2019), pp. 7375–7384. DOI: 10.1021/acsaem.9b01354.

[122] Xu, C. et al.: *Bulk fatigue induced by surface reconstruction in layered Ni-rich cathodes for Li-ion batteries*. In: *Nature materials* 20 (1) (2021), pp. 84–92. DOI: 10.1038/s41563-020-0767-8.

[123] Matasso, A., Wong, D., Wetz, D., and Liu, F.: *Correlation of Bulk Internal Pressure Rise and Capacity Degradation of Commercial LiCoO2 Cells*. In: *Journal of the Electrochemical Society* 161 (14) (2014), A2031–A2035. DOI: 10.1149/2.0221414jes.

[124] Kim, Y.: *Mechanism of gas evolution from the cathode of lithium-ion batteries at the initial stage of high-temperature storage*. In: *Journal of Materials Science* 48 (24) (2013), pp. 8547–8551. DOI: 10.1007/s10853-013-7673-2.

[125] Mao, Z., Farkhondeh, M., Pritzker, M., Fowler, M., and Chen, Z.: *Calendar Aging and Gas Generation in Commercial Graphite/NMC-LMO Lithium-Ion Pouch Cell*. In: *Journal of the Electrochemical Society* 164 (14) (2017), A3469–A3483. DOI: 10.1149/2.0241714jes.

[126] Matasso, A., Wong, D., Wetz, D., and Liu, F.: *Effects of High-Rate Cycling on the Bulk Internal Pressure Rise and Capacity Degradation of Commercial LiCoO2 Cells*. In: *Journal of the Electrochemical Society* 162 (6) (2015), A885–A891. DOI: 10.1149/2.0461506jes.

[127] Self, J., Aiken, C. P., Petibon, R., and Dahn, J. R.: *Survey of Gas Expansion in Li-Ion NMC Pouch Cells*. In: *Journal of the Electrochemical Society* 162 (6) (2015), A796–A802. DOI: 10.1149/2.0081506jes.

[128] Aiken, C. P., Xia, J., Wang, D. Y., Stevens, D. A., Trussler, S., and Dahn, J. R.: *An Apparatus for the Study of In Situ Gas Evolution in Li-Ion Pouch Cells*. In: *Journal of the Electrochemical Society* 161 (10) (2014), A1548–A1554. DOI: 10.1149/2.0151410jes.

[129] Xia, J., Aiken, C. P., Ma, L., Kim, G. Y., Burns, J. C., Chen, L. P., and Dahn, J. R.: *Combinations of Ethylene Sulfite (ES) and Vinylene Carbonate (VC) as Electrolyte Additives in Li(Ni 1/3 Mn 1/3 Co 1/3)O 2 /Graphite Pouch Cells*. In: *Journal of the Electrochemical Society* 161 (6) (2014), A1149–A1157. DOI: 10.1149/2.108406jes.

[130] Ma, Y., Feng, L., Tang, C.-Y., Ouyang, J.-H., and Dillon, S. J.: *Effects of Commonly Evolved Solid-Electrolyte-Interphase (SEI) Reaction Product Gases on the Cycle Life of Li-Ion Full Cells*. In: *Journal of the Electrochemical Society* 165 (13) (2018), A3084–A3094. DOI: 10.1149/2.0691813jes.

[131] Matasso, A., Wetz, D., and Liu, F.: *The Effects of Internal Pressure Evolution on the Aging of Commercial Li-Ion Cells*. In: *ECS Transactions* 58 (46) (2014), pp. 37–44. DOI: 10.1149/05846.0037ecst.

[132] O'Kane, S. E. J. et al.: *Lithium-ion battery degradation: how to model it*. In: *Physical chemistry chemical physics : PCCP* 24 (13) (2022), pp. 7909–7922. DOI: 10.1039/d2cp00417h.

[133] Keil, J. and Jossen, A.: *Electrochemical Modeling of Linear and Nonlinear Aging of Lithium-Ion Cells*. In: *Journal of The Electrochemical Society* 167 (11) (2020), p. 110535. DOI: 10.1149/1945-7111/aba44f.

[134] Li, J., Adewuyi, K., Lotfi, N., Landers, R. G., and Park, J.: *A single particle model with chemical/mechanical degradation physics for lithium ion battery State of Health (SOH) estimation*. In: *Applied Energy* 212 (2018), pp. 1178–1190. DOI: 10.1016/j.apenergy.2018.01.011.

[135] Jana, A., Shaver, G. M., and García, R. E.: *Physical, on the fly, capacity degradation prediction of LiNiMnCoO2-graphite cells*. In: *Journal of Power Sources* 422 (2019), pp. 185–195. DOI: 10.1016/j.jpowsour.2019.02.073.

[136] Lee, S., Mohtat, P., Siegel, J. B., Stefanopoulou, A. G., Lee, J.-W., and Lee, T.-K.: *Estimation Error Bound of Battery Electrode Parameters With Limited Data Window*. In: *IEEE Transactions on Industrial Informatics* 16 (5) (2020), pp. 3376–3386. DOI: 10.1109/TII.2019.2952066.

[137] Christensen, J. and Newman, J.: *Effect of Anode Film Resistance on the Charge/Discharge Capacity of a Lithium-Ion Battery*. In: *Journal of the Electrochemical Society* 150 (11) (2003), A1416. DOI: 10.1149/1.1612501.

[138] Christensen, J. and Newman, J.: *Cyclable Lithium and Capacity Loss in Li-Ion Cells*. In: *Journal of the Electrochemical Society* 152 (4) (2005), A818. DOI: 10.1149/1.1870752.

[139] Gao, Y., Jiang, J., Zhang, C., Zhang, W., and Jiang, Y.: *Aging mechanisms under different state-of-charge ranges and the multi-indicators system of state-of-health for lithium-ion battery with Li(NiMnCo)O2 cathode*. In: *Journal of Power Sources* 400 (2018), pp. 641–651. DOI: 10.1016/j.jpowsour.2018.07.018.

[140] Han, X., Ouyang, M., Lu, L., Li, J., Zheng, Y., and Li, Z.: *A comparative study of commercial lithium ion battery cycle life in electrical vehicle: Aging mechanism identification.* In: *Journal of Power Sources* 251 (2014), pp. 38–54. DOI: 10.1016/j.jpowsour.2013.11.029.

[141] Ma, Z., Wang, Z., Xiong, R., and Jiang, J.: *A mechanism identification model based state-of-health diagnosis of lithium-ion batteries for energy storage applications.* In: *Journal of Cleaner Production* 193 (2018), pp. 379–390. DOI: 10.1016/j.jclepro.2018.05.074.

[142] Marongiu, A. and Sauer, D. U.: *On-board aging estimation using half-cell voltage curves for LiFePO4 cathode-based lithium-ion batteries for EV applications.* In: *International Journal of Automotive Technology* 17 (3) (2016), pp. 465–472. DOI: 10.1007/s12239-016-0048-3.

[143] Marongiu, A., Nlandi, N., Rong, Y., and Sauer, D. U.: *On-board capacity estimation of lithium iron phosphate batteries by means of half-cell curves.* In: *Journal of Power Sources* 324 (2016), pp. 158–169. DOI: 10.1016/j.jpowsour.2016.05.041.

[144] Schindler, S. and Danzer, M. A.: *A novel mechanistic modeling framework for analysis of electrode balancing and degradation modes in commercial lithium-ion cells.* In: *Journal of Power Sources* 343 (2017), pp. 226–236. DOI: 10.1016/j.jpowsour.2017.01.026.

[145] Tian, J., Xiong, R., Shen, W., and Sun, F.: *Electrode ageing estimation and open circuit voltage reconstruction for lithium ion batteries.* In: *Energy Storage Materials* 37 (2021), pp. 283–295. DOI: 10.1016/j.ensm.2021.02.018.

[146] Fath, J. P., Dragicevic, D., Bittel, L., Nuhic, A., Sieg, J., Hahn, S., Alsheimer, L., Spier, B., and Wetzel, T.: *Quantification of aging mechanisms and inhomogeneity in cycled lithium-ion cells by differential voltage analysis.* In: *Journal of Energy Storage* 25 (2019), p. 100813. DOI: 10.1016/j.est.2019.100813.

[147] Dubarry, M., Baure, G., and Devie, A.: *Durability and Reliability of EV Batteries under Electric Utility Grid Operations: Path Dependence of Battery Degradation.* In: *Journal of the Electrochemical Society* 165 (5) (2018), A773–A783. DOI: 10.1149/2.0421805jes.

[148] Dubarry, M., Truchot, C., Devie, A., and Liaw, B. Y.: *State-of-Charge Determination in Lithium-Ion Battery Packs Based on Two-Point Measurements in Life.* In: *Journal of the Electrochemical Society* 162 (6) (2015), A877–A884. DOI: 10.1149/2.0201506jes.

[149] Dubarry, M., Truchot, C., and Liaw, B. Y.: *Cell degradation in commercial LiFePO4 cells with high-power and high-energy designs.* In: *Journal of Power Sources* 258 (2014), pp. 408–419. DOI: 10.1016/j.jpowsour.2014.02.052.

[150] Zilberman, I., Schmitt, J., Ludwig, S., Naumann, M., and Jossen, A.: *Simulation of voltage imbalance in large lithium-ion battery packs influenced by cell-to-cell variations and balancing systems.* In: *Journal of Energy Storage* 32 (2020), p. 101828. DOI: 10.1016/j.est.2020.101828.

[151] Dubarry, M. and Beck, D.: *Analysis of Synthetic Voltage vs. Capacity Datasets for Big Data Li-ion Diagnosis and Prognosis.* In: *Energies* 14 (9) (2021), p. 2371. DOI: 10.3390/en14092371.

[152] Devie, A., Dubarry, M., and Liaw, B. Y.: *Overcharge Study in Li 4 Ti 5 O 12 Based Lithium-Ion Pouch Cell.* In: *Journal of the Electrochemical Society* 162 (6) (2015), A1033–A1040. DOI: 10.1149/2.0941506jes.

[153] Sieg, J., Storch, M., Fath, J., Nuhic, A., Bandlow, J., Spier, B., and Sauer, D. U.: *Local degradation and differential voltage analysis of aged lithium-ion pouch cells.* In: *Journal of Energy Storage* 30 (2020), p. 101582. DOI: 10.1016/j.est.2020.101582.

[154] Coron, E., Geniès, S., Cugnet, M., and Thivel, P. X.: *Impact of Lithium-Ion Cell Condition on Its Second Life Viability*. In: *Journal of The Electrochemical Society* 167 (11) (2020), p. 110556. DOI: 10.1149/1945-7111/aba703.

[155] Liu, P., Wang, J., Hicks-Garner, J., Sherman, E., Soukiazian, S., Verbrugge, M., Tataria, H., Musser, J., and Finamore, P.: *Aging Mechanisms of LiFePO[sub 4] Batteries Deduced by Electrochemical and Structural Analyses*. In: *Journal of the Electrochemical Society* 157 (4) (2010), A499. DOI: 10.1149/1.3294790.

[156] Bloom, I., Christophersen, J. P., Abraham, D. P., and Gering, K. L.: *Differential voltage analyses of high-power lithium-ion cells*. In: *Journal of Power Sources* 157 (1) (2006), pp. 537–542. DOI: 10.1016/j.jpowsour.2005.07.054.

[157] Wetjen, M., Pritzl, D., Jung, R., Solchenbach, S., Ghadimi, R., and Gasteiger, H. A.: *Differentiating the Degradation Phenomena in Silicon-Graphite Electrodes for Lithium-Ion Batteries*. In: *Journal of the Electrochemical Society* 164 (12) (2017), A2840–A2852. DOI: 10.1149/2.1921712jes.

[158] Honkura, K., Takahashi, K., and Horiba, T.: *Capacity-fading prediction of lithium-ion batteries based on discharge curves analysis*. In: *Journal of Power Sources* 196 (23) (2011), pp. 10141–10147. DOI: 10.1016/j.jpowsour.2011.08.020.

[159] Downey, A., Lui, Y.-H., Hu, C., Laflamme, S., and Hu, S.: *Physics-based prognostics of lithium-ion battery using non-linear least squares with dynamic bounds*. In: *Reliability Engineering & System Safety* 182 (2) (2019), pp. 1–12. DOI: 10.1016/j.ress.2018.09.018.

[160] Bloom, I., Jansen, A. N., Abraham, D. P., Knuth, J., Jones, S. A., Battaglia, V. S., and Henriksen, G. L.: *Differential voltage analyses of high-power, lithium-ion cells*. In: *Journal of Power Sources* 139 (1-2) (2005), pp. 295–303. DOI: 10.1016/j.jpowsour.2004.07.021.

[161] Zilberman, I., Ludwig, S., Schiller, M., and Jossen, A.: *Online aging determination in lithium-ion battery module with forced temperature gradient*. In: *Journal of Energy Storage* 28 (2020), p. 101170. DOI: 10.1016/j.est.2019.101170.

[162] Keil, P. and Jossen, A.: *Calendar Aging of NCA Lithium-Ion Batteries Investigated by Differential Voltage Analysis and Coulomb Tracking*. In: *Journal of The Electrochemical Society* 164 (1) (2016), A6066–A6074. DOI: 10.1149/2.0091701jes.

[163] Keil, P. and Jossen, A.: *Charging protocols for lithium-ion batteries and their impact on cycle life—An experimental study with different 18650 high-power cells*. In: *Journal of Energy Storage* 6 (2016), pp. 125–141. DOI: 10.1016/j.est.2016.02.005.

[164] Keil, P., Schuster, S. F., Wilhelm, J., Travi, J., Hauser, A., Karl, R. C., and Jossen, A.: *Calendar Aging of Lithium-Ion Batteries*. In: *Journal of the Electrochemical Society* 163 (9) (2016), A1872–A1880. DOI: 10.1149/2.0411609jes.

[165] Schindler, M., Sturm, J., Ludwig, S., Schmitt, J., and Jossen, A.: *Evolution of Initial Cell-to-Cell Variations During a Three-Year Production Cycle*. In: *eTransportation* 14 (165) (2021), p. 100102. DOI: 10.1016/j.etran.2020.100102.

[166] Zilberman, I., Ludwig, S., and Jossen, A.: *Cell-to-cell variation of calendar aging and reversible self-discharge in 18650 nickel-rich, silicon–graphite lithium-ion cells*. In: *Journal of Energy Storage* 26 (2019), p. 100900. DOI: 10.1016/j.est.2019.100900.

[167] Safari, M. and Delacourt, C.: *Aging of a Commercial Graphite/LiFePO4 Cell*. In: *Journal of the Electrochemical Society* 158 (10) (2011), A1123. DOI: 10.1149/1.3614529.

[168] Barai, A., Uddin, K., Dubarry, M., Somerville, L., McGordon, A., Jennings, P., and Bloom, I.: *A comparison of methodologies for the non-invasive characterisation of commercial Li-ion cells*. In: *Progress in Energy and Combustion Science* 72 (2019), pp. 1–31. DOI: 10.1016/j.pecs.2019.01.001.

[169] Dubarry, M., Truchot, C., Liaw, B. Y., Gering, K., Sazhin, S., Jamison, D., and Michelbacher, C.: *Evaluation of commercial lithium-ion cells based on composite positive electrode for plug-in hybrid electric vehicle applications. Part II. Degradation mechanism under 2C cycle aging*. In: *Journal of Power Sources* 196 (23) (2011), pp. 10336–10343. DOI: 10.1016/j.jpowsour.2011.08.078.

[170] Dubarry, M., Berecibar, M., Devie, A., Anseán, D., Omar, N., and Villarreal, I.: *State of health battery estimator enabling degradation diagnosis: Model and algorithm description*. In: *Journal of Power Sources* 360 (2017), pp. 59–69. DOI: 10.1016/j.jpowsour.2017.05.121.

[171] Simolka, M., Heger, J.-F., Traub, N., Kaess, H., and Friedrich, K. A.: *Influence of Cycling Profile, Depth of Discharge and Temperature on Commercial LFP/C Cell Ageing: Cell Level Analysis with ICA, DVA and OCV Measurements*. In: *Journal of The Electrochemical Society* 167 (11) (2020), p. 110502. DOI: 10.1149/1945-7111/ab9cd1.

[172] Feng, X., Sun, J., Ouyang, M., He, X., Lu, L., Han, X., Fang, M., and Peng, H.: *Characterization of large format lithium ion battery exposed to extremely high temperature*. In: *Journal of Power Sources* 272 (2) (2014), pp. 457–467. DOI: 10.1016/j.jpowsour.2014.08.094.

[173] Feng, X. et al.: *A reliable approach of differentiating discrete sampled-data for battery diagnosis*. In: *eTransportation* 3 (7490) (2020), p. 100051. DOI: 10.1016/j.etran.2020.100051.

[174] Dubarry, M. and Anseán, D.: *Best practices for incremental capacity analysis*. In: *Frontiers in Energy Research* 10 (2022), p. 227882. DOI: 10.3389/fenrg.2022.1023555.

[175] Ouyang, M., Feng, X., Han, X., Lu, L., Li, Z., and He, X.: *A dynamic capacity degradation model and its applications considering varying load for a large format Li-ion battery*. In: *Applied Energy* 165 (2016), pp. 48–59. DOI: 10.1016/j.apenergy.2015.12.063.

[176] Ouyang, M., Chu, Z., Lu, L., Li, J., Han, X., Feng, X., and Liu, G.: *Low temperature aging mechanism identification and lithium deposition in a large format lithium iron phosphate battery for different charge profiles*. In: *Journal of Power Sources* 286 (2015), pp. 309–320. DOI: 10.1016/j.jpowsour.2015.03.178.

[177] Yan, D., Lu, L., Li, Z., Feng, X., Ouyang, M., and Jiang, F.: *Durability comparison of four different types of high-power batteries in HEV and their degradation mechanism analysis*. In: *Applied Energy* 179 (2016), pp. 1123–1130. DOI: 10.1016/j.apenergy.2016.07.054.

[178] Rumberg, B., Epding, B., Stradtmann, I., and Kwade, A.: *Identification of Li ion battery cell aging mechanisms by half-cell and full-cell open-circuit-voltage characteristic analysis*. In: *Journal of Energy Storage* 25 (2019), p. 100890. DOI: 10.1016/j.est.2019.100890.

[179] Pan, B., Dong, D., Wang, J., Nie, J., Liu, S., Cao, Y., and Jiang, Y.: *Aging mechanism diagnosis of lithium ion battery by open circuit voltage analysis*. In: *Electrochimica Acta* 362 (2020), p. 137101. DOI: 10.1016/j.electacta.2020.137101.

[180] Honkura, K., Honbo, H., Koishikawa, Y., and Horiba, T.: *State Analysis of Lithium-Ion Batteries Using Discharge Curves*. In: *ECS Transactions* 13 (19) (2008), pp. 61–73. DOI: 10.1149/1.3018750.

[181] Hahn, S. L., Storch, M., Swaminathan, R., Obry, B., Bandlow, J., and Birke, K. P.: *Quantitative validation of calendar aging models for lithium-ion batteries*. In: *Journal of Power Sources* 400 (3) (2018), pp. 402–414. DOI: 10.1016/j.jpowsour.2018.08.019.

[182] Wang, S., Wang, J., Vu, L., Purewal, J., Soukiazian, S., and Graetz, J.: *On Line Battery Capacity Estimation Based on Half-Cell Open Circuit Voltages*. In: *Journal of The Electrochemical Society* 161 (12) (2014), A1788–A1793. DOI: 10.1149/2.0271412jes.

[183] Lu, T., Luo, Y., Zhang, Y., Luo, W., Yan, L., and Xie, J.: *Degradation Analysis of Commercial Lithium-Ion Battery in Long-Term Storage*. In: *Journal of the Electrochemical Society* 164 (4) (2017), A775–A784. DOI: 10.1149/2.1321704jes.

[184] Ando, K., Matsuda, T., and Imamura, D.: *Degradation diagnosis of lithium-ion batteries with a LiNi0.5Co0.2Mn0.3O2 and LiMn2O4 blended cathode using dV/dQ curve analysis*. In: *Journal of Power Sources* 390 (2018), pp. 278–285. DOI: 10.1016/j.jpowsour.2018.04.043.

[185] Fathi, R., Burns, J. C., Stevens, D. A., Ye, H., Hu, C., Jain, G., Scott, E., Schmidt, C., and Dahn, J. R.: *Ultra High-Precision Studies of Degradation Mechanisms in Aged LiCoO 2 /Graphite Li-Ion Cells*. In: *Journal of the Electrochemical Society* 161 (10) (2014), A1572–A1579. DOI: 10.1149/2.0321410jes.

[186] Gantenbein, S., Schönleber, M., Weiss, M., and Ivers-Tiffée, E.: *Capacity Fade in Lithium-Ion Batteries and Cyclic Aging over Various State-of-Charge Ranges*. In: *Sustainability* 11 (23) (2019), p. 6697. DOI: 10.3390/su11236697.

[187] Dose, W. M., Xu, C., Grey, C. P., and Volder, M. F. de: *Effect of Anode Slippage on Cathode Cutoff Potential and Degradation Mechanisms in Ni-Rich Li-Ion Batteries*. In: *Cell Reports Physical Science* 1 (11) (2020), p. 100253. DOI: 10.1016/j.xcrp.2020.100253.

[188] Mergo Mbeya, K., Damay, N., Friedrich, G., Forgez, C., and Juston, M.: *Off-line method to determine the electrode balancing of Li-ion batteries*. In: *Mathematics and Computers in Simulation* 183 (10) (2021), pp. 34–47. DOI: 10.1016/j.matcom.2020.02.013.

[189] Schmitt, J., Maheshwari, A., Heck, M., Lux, S., and Vetter, M.: *Impedance change and capacity fade of lithium nickel manganese cobalt oxide-based batteries during calendar aging*. In: *Journal of Power Sources* 353 (2017), pp. 183–194. DOI: 10.1016/j.jpowsour.2017.03.090.

[190] Naumann, M., Spingler, F. B., and Jossen, A.: *Analysis and modeling of cycle aging of a commercial LiFePO4/graphite cell*. In: *Journal of Power Sources* 451 (14) (2020), p. 227666. DOI: 10.1016/j.jpowsour.2019.227666.

[191] Spotnitz, R.: *Simulation of capacity fade in lithium-ion batteries*. In: *Journal of Power Sources* 113 (1) (2003), pp. 72–80. DOI: 10.1016/S0378-7753(02)00490-1.

[192] Attia, P. M. et al.: *Review—"Knees" in Lithium-Ion Battery Aging Trajectories*. In: *Journal of The Electrochemical Society* 169 (6) (2022), p. 060517. DOI: 10.1149/1945-7111/ac6d13.

[193] Schimpe, M., Kuepach, M. E. von, Naumann, M., Hesse, H. C., Smith, K., and Jossen, A.: *Comprehensive Modeling of Temperature-Dependent Degradation Mechanisms in Lithium Iron Phosphate Batteries*. In: *Journal of the Electrochemical Society* 165 (2) (2018), A181–A193. DOI: 10.1149/2.1181714jes.

[194] Naumann, M., Schimpe, M., Keil, P., Hesse, H. C., and Jossen, A.: *Analysis and modeling of calendar aging of a commercial LiFePO 4 /graphite cell*. In: *Journal of Energy Storage* 17 (2018), pp. 153–169. DOI: 10.1016/j.est.2018.01.019.

[195] E. Peled: *The Electrochemical Behavior of Alkali and Alkaline Earth Metals in Nonaqueous Battery Systems—The Solid Electrolyte Interphase Model*. In: *Journal of The Electrochemical Society* 126 (12) (1979), p. 2047. DOI: 10.1149/1.2128859.

[196] Park, S. W., Lee, H., and Won, Y. S.: *A novel aging parameter method for online estimation of Lithium-ion battery states of charge and health*. In: *Journal of Energy Storage* 48 (1) (2022), p. 103987. DOI: 10.1016/j.est.2022.103987.

[197] Bian, X., Wei, Z., He, J., Yan, F., and Liu, L.: *A Novel Model-Based Voltage Construction Method for Robust State-of-Health Estimation of Lithium-Ion Batteries*. In: *IEEE Transactions on Industrial Electronics* 68 (12) (2021), pp. 12173–12184. DOI: 10.1109/TIE.2020.3044779.

[198] Hamar, J., Zoerr, C., Erhard, S. V., and Jossen, A.: *Anode Potential Estimation in Lithium-Ion Batteries Using Data-Driven Models for Online Applications*. In: *Journal of The Electrochemical Society* (2021). DOI: 10.1149/1945-7111/abe721.

[199] He, Z., Shen, X., Sun, Y., Zhao, S., Fan, B., and Pan, C.: *State-of-health estimation based on real data of electric vehicles concerning user behavior*. In: *Journal of Energy Storage* 41 (Feb) (2021), p. 102867. DOI: 10.1016/j.est.2021.102867.

[200] Cai, L., Meng, J., Stroe, D.-I., Luo, G., and Teodorescu, R.: *An evolutionary framework for lithium-ion battery state of health estimation*. In: *Journal of Power Sources* 412 (2019), pp. 615–622. DOI: 10.1016/j.jpowsour.2018.12.001.

[201] Nuhic, A., Terzimehic, T., Soczka-Guth, T., Buchholz, M., and Dietmayer, K.: *Health diagnosis and remaining useful life prognostics of lithium-ion batteries using data-driven methods*. In: *Journal of Power Sources* 239 (2013), pp. 680–688. DOI: 10.1016/j.jpowsour.2012.11.146.

[202] Yang, J., Xia, B., Huang, W., Fu, Y., and Mi, C.: *Online state-of-health estimation for lithium-ion batteries using constant-voltage charging current analysis*. In: *Applied Energy* 212 (2018), pp. 1589–1600. DOI: 10.1016/j.apenergy.2018.01.010.

[203] Yang, D., Zhang, X., Pan, R., Wang, Y., and Chen, Z.: *A novel Gaussian process regression model for state-of-health estimation of lithium-ion battery using charging curve*. In: *Journal of Power Sources* 384 (2018), pp. 387–395. DOI: 10.1016/j.jpowsour.2018.03.015.

[204] Berecibar, M., Devriendt, F., Dubarry, M., Villarreal, I., Omar, N., Verbeke, W., and van Mierlo, J.: *Online state of health estimation on NMC cells based on predictive analytics*. In: *Journal of Power Sources* 320 (2016), pp. 239–250. DOI: 10.1016/j.jpowsour.2016.04.109.

[205] Wassiliadis, N., Adermann, J., Frericks, A., Pak, M., Reiter, C., Lohmann, B., and Lienkamp, M.: *Revisiting the dual extended Kalman filter for battery state-of-charge and state-of-health estimation: A use-case life cycle analysis*. In: *Journal of Energy Storage* 19 (2018), pp. 73–87. DOI: 10.1016/j.est.2018.07.006.

[206] Li, X., Wang, Z., and Zhang, L.: *Co-estimation of capacity and state-of-charge for lithium-ion batteries in electric vehicles*. In: *Energy* 174 (2019), pp. 33–44. DOI: 10.1016/j.energy.2019.02.147.

[207] Plett, G. L.: *Extended Kalman filtering for battery management systems of LiPB-based HEV battery packs*. In: *Journal of Power Sources* 134 (2) (2004), pp. 277–292. DOI: 10.1016/j.jpowsour.2004.02.033.

[208] Wang, L., Pan, C., Liu, L., Cheng, Y., and Zhao, X.: *On-board state of health estimation of LiFePO4 battery pack through differential voltage analysis*. In: *Applied Energy* 168 (2016), pp. 465–472. DOI: 10.1016/j.apenergy.2016.01.125.

[209] Wang, Z., Zeng, S., Guo, J., and Qin, T.: *State of health estimation of lithium-ion batteries based on the constant voltage charging curve*. In: *Energy* 167 (2019), pp. 661–669. DOI: 10.1016/j.energy.2018.11.008.

[210] Wei, J., Dong, G., and Chen, Z.: *Remaining Useful Life Prediction and State of Health Diagnosis for Lithium-Ion Batteries Using Particle Filter and Support Vector Regression*. In: *IEEE Transactions on Industrial Electronics* 65 (7) (2018), pp. 5634–5643. DOI: 10.1109/TIE.2017.2782224.

[211] Yu, J.: *Health Degradation Detection and Monitoring of Lithium-Ion Battery Based on Adaptive Learning Method*. In: *IEEE Transactions on Instrumentation and Measurement* 63 (7) (2014), pp. 1709–1721. DOI: 10.1109/TIM.2013.2293234.

[212] Zhang, L., Mu, Z., and Sun, C.: *Remaining Useful Life Prediction for Lithium-Ion Batteries Based on Exponential Model and Particle Filter*. In: *IEEE Access* 6 (2018), pp. 17729–17740. DOI: 10.1109/ACCESS.2018.2816684.

[213] Zheng, L., Zhu, J., Lu, D. D.-C., Wang, G., and He, T.: *Incremental capacity analysis and differential voltage analysis based state of charge and capacity estimation for lithium-ion batteries*. In: *Energy* 150 (2018), pp. 759–769. DOI: 10.1016/j.energy.2018.03.023.

[214] Li, X., Wang, Z., and Yan, J.: *Prognostic health condition for lithium battery using the partial incremental capacity and Gaussian process regression*. In: *Journal of Power Sources* 421 (2019), pp. 56–67. DOI: 10.1016/j.jpowsour.2019.03.008.

[215] Lin, H.-T., Liang, T.-J., and Chen, S.-M.: *Estimation of Battery State of Health Using Probabilistic Neural Network*. In: *IEEE Transactions on Industrial Informatics* 9 (2) (2013), pp. 679–685. DOI: 10.1109/TII.2012.2222650.

[216] Goh, T., Park, M., Seo, M., Kim, J. G., and Kim, S. W.: *Capacity estimation algorithm with a second-order differential voltage curve for Li-ion batteries with NMC cathodes*. In: *Energy* 135 (2017), pp. 257–268. DOI: 10.1016/j.energy.2017.06.141.

[217] Huang, S.-C., Tseng, K.-H., Liang, J.-W., Chang, C.-L., and Pecht, M.: *An Online SOC and SOH Estimation Model for Lithium-Ion Batteries*. In: *Energies* 10 (4) (2017), p. 512. DOI: 10.3390/en10040512.

[218] Li, X., Wang, Z., Zhang, L., Zou, C., and Dorrell, D. D.: *State-of-health estimation for Li-ion batteries by combing the incremental capacity analysis method with grey relational analysis*. In: *Journal of Power Sources* 410-411 (2019), pp. 106–114. DOI: 10.1016/j.jpowsour.2018.10.069.

[219] Li, Y., Zou, C., Berecibar, M., Nanini-Maury, E., Chan, J. C.-W., van den Bossche, P., van Mierlo, J., and Omar, N.: *Random forest regression for online capacity estimation of lithium-ion batteries*. In: *Applied Energy* 232 (2018), pp. 197–210. DOI: 10.1016/j.apenergy.2018.09.182.

[220] Liu, C., Wang, Y., and Chen, Z.: *Degradation model and cycle life prediction for lithium-ion battery used in hybrid energy storage system*. In: *Energy* 166 (2019), pp. 796–806. DOI: 10.1016/j.energy.2018.10.131.

[221] Song, Y., Liu, D., Yang, C., and Peng, Y.: *Data-driven hybrid remaining useful life estimation approach for spacecraft lithium-ion battery*. In: *Microelectronics Reliability* 75 (2017), pp. 142–153. DOI: 10.1016/j.microrel.2017.06.045.

[222] Tang, X., Zou, C., Yao, K., Chen, G., Liu, B., He, Z., and Gao, F.: *A fast estimation algorithm for lithium-ion battery state of health.* In: *Journal of Power Sources* 396 (2018), pp. 453–458. DOI: 10.1016/j.jpowsour.2018.06.036.

[223] dos Reis, G., Strange, C., Yadav, M., and Li, S.: *Lithium-ion battery data and where to find it.* In: *Energy and AI* 5 (4) (2021), p. 100081. DOI: 10.1016/j.egyai.2021.100081.

[224] Yang, F., Song, X., Dong, G., and Tsui, K.-L.: *A coulombic efficiency-based model for prognostics and health estimation of lithium-ion batteries.* In: *Energy* 171 (2019), pp. 1173–1182. DOI: 10.1016/j.energy.2019.01.083.

[225] Hu, C., Youn, B. D., and Chung, J.: *A multiscale framework with extended Kalman filter for lithium-ion battery SOC and capacity estimation.* In: *Applied Energy* 92 (2012), pp. 694–704. DOI: 10.1016/j.apenergy.2011.08.002.

[226] Petit, M., Prada, E., and Sauvant-Moynot, V.: *Development of an empirical aging model for Li-ion batteries and application to assess the impact of Vehicle-to-Grid strategies on battery lifetime.* In: *Applied Energy* 172 (2016), pp. 398–407. DOI: 10.1016/j.apenergy.2016.03.119.

[227] Shen, P., Ouyang, M., Lu, L., Li, J., and Feng, X.: *The Co-estimation of State of Charge, State of Health, and State of Function for Lithium-Ion Batteries in Electric Vehicles.* In: *IEEE Transactions on Vehicular Technology* 67 (1) (2018), pp. 92–103. DOI: 10.1109/TVT.2017.2751613.

[228] You, G.-w., Park, S., and Oh, D.: *Real-time state-of-health estimation for electric vehicle batteries: A data-driven approach.* In: *Applied Energy* 176 (2016), pp. 92–103. DOI: 10.1016/j.apenergy.2016.05.051.

[229] You, G.-w., Park, S., and Oh, D.: *Diagnosis of Electric Vehicle Batteries Using Recurrent Neural Networks.* In: *IEEE Transactions on Industrial Electronics* 64 (6) (2017), pp. 4885–4893. DOI: 10.1109/TIE.2017.2674593.

[230] Bartlett, A., Marcicki, J., Onori, S., Rizzoni, G., Yang, X. G., and Miller, T.: *Electrochemical Model-Based State of Charge and Capacity Estimation for a Composite Electrode Lithium-Ion Battery.* In: *IEEE Transactions on Control Systems Technology* (2015), p. 1. DOI: 10.1109/TCST.2015.2446947.

[231] Xiong, R., Li, L., Li, Z., Yu, Q., and Mu, H.: *An electrochemical model based degradation state identification method of Lithium-ion battery for all-climate electric vehicles application.* In: *Applied Energy* 219 (2018), pp. 264–275. DOI: 10.1016/j.apenergy.2018.03.053.

[232] Xiong, R., Sun, F., Chen, Z., and He, H.: *A data-driven multi-scale extended Kalman filtering based parameter and state estimation approach of lithium-ion polymer battery in electric vehicles.* In: *Applied Energy* 113 (2014), pp. 463–476. DOI: 10.1016/j.apenergy.2013.07.061.

[233] Xiong, R., Tian, J., Mu, H., and Wang, C.: *A systematic model-based degradation behavior recognition and health monitoring method for lithium-ion batteries.* In: *Applied Energy* 207 (2017), pp. 372–383. DOI: 10.1016/j.apenergy.2017.05.124.

[234] Xiong, R., Zhang, Y., Wang, J., He, H., Peng, S., and Pecht, M.: *Lithium-Ion Battery Health Prognosis Based on a Real Battery Management System Used in Electric Vehicles.* In: *IEEE Transactions on Vehicular Technology* 68 (5) (2019), pp. 4110–4121. DOI: 10.1109/TVT.2018.2864688.

[235] Deng, Z., Yang, L., Cai, Y., Deng, H., and Sun, L.: *Online available capacity prediction and state of charge estimation based on advanced data-driven algorithms for lithium iron phosphate battery*. In: *Energy* 112 (2016), pp. 469–480. DOI: 10.1016/j.energy.2016.06.130.

[236] Hu, X., Jiang, J., Cao, D., and Egardt, B.: *Battery Health Prognosis for Electric Vehicles Using Sample Entropy and Sparse Bayesian Predictive Modeling*. In: *IEEE Transactions on Industrial Electronics* (2015), p. 1. DOI: 10.1109/TIE.2015.2461523.

[237] Li, S., Pischinger, S., He, C., Liang, L., and Stapelbroek, M.: *A comparative study of model-based capacity estimation algorithms in dual estimation frameworks for lithium-ion batteries under an accelerated aging test*. In: *Applied Energy* 212 (2018), pp. 1522–1536. DOI: 10.1016/j.apenergy.2018.01.008.

[238] Ma, Z., Yang, R., and Wang, Z.: *A novel data-model fusion state-of-health estimation approach for lithium-ion batteries*. In: *Applied Energy* 237 (2019), pp. 836–847. DOI: 10.1016/j.apenergy.2018.12.071.

[239] Tian, J., Xiong, R., and Yu, Q.: *Fractional-Order Model-Based Incremental Capacity Analysis for Degradation State Recognition of Lithium-Ion Batteries*. In: *IEEE Transactions on Industrial Electronics* 66 (2) (2019), pp. 1576–1584. DOI: 10.1109/TIE.2018.2798606.

[240] Torai, S., Nakagomi, M., Yoshitake, S., Yamaguchi, S., and Oyama, N.: *State-of-health estimation of LiFePO 4 /graphite batteries based on a model using differential capacity*. In: *Journal of Power Sources* 306 (2016), pp. 62–69. DOI: 10.1016/j.jpowsour.2015.11.070.

[241] Zou, Y., Hu, X., Ma, H., and Li, S. E.: *Combined State of Charge and State of Health estimation over lithium-ion battery cell cycle lifespan for electric vehicles*. In: *Journal of Power Sources* 273 (2015), pp. 793–803. DOI: 10.1016/j.jpowsour.2014.09.146.

[242] Eddahech, A., Briat, O., Bertrand, N., Delétage, J.-Y., and Vinassa, J.-M.: *Behavior and state-of-health monitoring of Li-ion batteries using impedance spectroscopy and recurrent neural networks*. In: *International Journal of Electrical Power & Energy Systems* 42 (1) (2012), pp. 487–494. DOI: 10.1016/j.ijepes.2012.04.050.

[243] Wang, Q.-K., He, Y.-J., Shen, J.-N., Ma, Z.-F., and Zhong, G.-B.: *A unified modeling framework for lithium-ion batteries: An artificial neural network based thermal coupled equivalent circuit model approach*. In: *Energy* 138 (2017), pp. 118–132. DOI: 10.1016/j.energy.2017.07.035.

[244] Wei, Z., Zhao, J., Ji, D., and Tseng, K. J.: *A multi-timescale estimator for battery state of charge and capacity dual estimation based on an online identified model*. In: *Applied Energy* 204 (2017), pp. 1264–1274. DOI: 10.1016/j.apenergy.2017.02.016.

[245] Zou, C., Manzie, C., Nešić, D., and Kallapur, A. G.: *Multi-time-scale observer design for state-of-charge and state-of-health of a lithium-ion battery*. In: *Journal of Power Sources* 335 (2016), pp. 121–130. DOI: 10.1016/j.jpowsour.2016.10.040.

[246] Gholizadeh, M. and Salmasi, F. R.: *Estimation of State of Charge, Unknown Nonlinearities, and State of Health of a Lithium-Ion Battery Based on a Comprehensive Unobservable Model*. In: *IEEE Transactions on Industrial Electronics* 61 (3) (2014), pp. 1335–1344. DOI: 10.1109/TIE.2013.2259779.

[247] Hu, X., Yuan, H., Zou, C., Li, Z., and Zhang, L.: *Co-Estimation of State of Charge and State of Health for Lithium-Ion Batteries Based on Fractional-Order Calculus*. In: *IEEE Transactions on Vehicular Technology* 67 (11) (2018), pp. 10319–10329. DOI: 10.1109/TVT.2018.2865664.

[248] Hu, C., Jain, G., Zhang, P., Schmidt, C., Gomadam, P., and Gorka, T.: *Data-driven method based on particle swarm optimization and k-nearest neighbor regression for estimating capacity of lithium-ion battery*. In: *Applied Energy* 129 (2014), pp. 49–55. DOI: 10.1016/j.apenergy.2014.04.077.

[249] Vichard, L., Ravey, A., Venet, P., Harel, F., Pelissier, S., and Hissel, D.: *A method to estimate battery SOH indicators based on vehicle operating data only*. In: *Energy* 225 (6) (2021), p. 120235. DOI: 10.1016/j.energy.2021.120235.

[250] Wei, Z., Meng, S., Xiong, B., Ji, D., and Tseng, K. J.: *Enhanced online model identification and state of charge estimation for lithium-ion battery with a FBCRLS based observer*. In: *Applied Energy* 181 (2016), pp. 332–341. DOI: 10.1016/j.apenergy.2016.08.103.

[251] Jiang, B., Dai, H., and Wei, X.: *Incremental capacity analysis based adaptive capacity estimation for lithium-ion battery considering charging condition*. In: *Applied Energy* 269 (2020), p. 115074. DOI: 10.1016/j.apenergy.2020.115074.

[252] Richardson, R. R., Birkl, C. R., Osborne, M. A., and Howey, D. A.: *Gaussian Process Regression for In Situ Capacity Estimation of Lithium-Ion Batteries*. In: *IEEE Transactions on Industrial Informatics* 15 (1) (2019), pp. 127–138. DOI: 10.1109/TII.2018.2794997.

[253] Shen, S., Sadoughi, M., Chen, X., Hong, M., and Hu, C.: *A deep learning method for online capacity estimation of lithium-ion batteries*. In: *Journal of Energy Storage* 25 (2) (2019), p. 100817. DOI: 10.1016/j.est.2019.100817.

[254] Guo, P., Cheng, Z., and Yang, L.: *A data-driven remaining capacity estimation approach for lithium-ion batteries based on charging health feature extraction*. In: *Journal of Power Sources* 412 (2019), pp. 442–450. DOI: 10.1016/j.jpowsour.2018.11.072.

[255] Eddahech, A., Briat, O., and Vinassa, J.-M.: *Determination of lithium-ion battery state-of-health based on constant-voltage charge phase*. In: *Journal of Power Sources* 258 (2014), pp. 218–227. DOI: 10.1016/j.jpowsour.2014.02.020.

[256] Zhu, J. et al.: *Data-driven capacity estimation of commercial lithium-ion batteries from voltage relaxation*. In: *Nature communications* 13 (1) (2022), p. 2261. DOI: 10.1038/s41467-022-29837-w.

[257] Schuster, S. F., Brand, M. J., Campestrini, C., Gleissenberger, M., and Jossen, A.: *Correlation between capacity and impedance of lithium-ion cells during calendar and cycle life*. In: *Journal of Power Sources* 305 (2016), pp. 191–199. DOI: 10.1016/j.jpowsour.2015.11.096.

[258] Popp, H., Koller, M., Jahn, M., and Bergmann, A.: *Mechanical methods for state determination of Lithium-Ion secondary batteries: A review*. In: *Journal of Energy Storage* 32 (7) (2020), p. 101859. DOI: 10.1016/j.est.2020.101859.

[259] Wu, Y. and Jossen, A.: *Entropy-induced temperature variation as a new indicator for state of health estimation of lithium-ion cells*. In: *Electrochimica Acta* 276 (2018), pp. 370–376. DOI: 10.1016/j.electacta.2018.04.203.

[260] Zheng, Y., Wang, J., Qin, C., Lu, L., Han, X., and Ouyang, M.: *A novel capacity estimation method based on charging curve sections for lithium-ion batteries in electric vehicles*. In: *Energy* 185 (5) (2019), pp. 361–371. DOI: 10.1016/j.energy.2019.07.059.

[261] Meng, J., Cai, L., Stroe, D.-I., Luo, G., Sui, X., and Teodorescu, R.: *Lithium-ion battery state-of-health estimation in electric vehicle using optimized partial charging voltage profiles*. In: *Energy* 185 (2019), pp. 1054–1062. DOI: 10.1016/j.energy.2019.07.127.

[262] Berecibar, M., Garmendia, M., Gandiaga, I., Crego, J., and Villarreal, I.: *State of health estimation algorithm of LiFePO4 battery packs based on differential voltage curves for battery management system application.* In: *Energy* 103 (2016), pp. 784–796. DOI: 10.1016/j.energy.2016.02.163.

[263] Tong, S., Klein, M. P., and Park, J. W.: *On-line optimization of battery open circuit voltage for improved state-of-charge and state-of-health estimation.* In: *Journal of Power Sources* 293 (2015), pp. 416–428. DOI: 10.1016/j.jpowsour.2015.03.157.

[264] Cui, Y., Zuo, P., Du, C., Gao, Y., Yang, J., Cheng, X., Ma, Y., and Yin, G.: *State of health diagnosis model for lithium ion batteries based on real-time impedance and open circuit voltage parameters identification method.* In: *Energy* 144 (2018), pp. 647–656. DOI: 10.1016/j.energy.2017.12.033.

[265] Bian, X., Liu, L., Yan, J., Zou, Z., and Zhao, R.: *An open circuit voltage-based model for state-of-health estimation of lithium-ion batteries: Model development and validation.* In: *Journal of Power Sources* 448 (5) (2020), p. 227401. DOI: 10.1016/j.jpowsour.2019.227401.

[266] Dey, S., Shi, Y., Smith, K., Colclasure, A., and Li, X.: *From Battery Cell to Electrodes: Real-Time Estimation of Charge and Health of Individual Battery Electrodes.* In: *IEEE Transactions on Industrial Electronics* 67 (3) (2020), pp. 2167–2175. DOI: 10.1109/TIE.2019.2907514.

[267] Couto, L. D., Schorsch, J., Job, N., Léonard, A., and Kinnaert, M.: *State of health estimation for lithium ion batteries based on an equivalent-hydraulic model: An iron phosphate application.* In: *Journal of Energy Storage* 21 (2019), pp. 259–271. DOI: 10.1016/j.est.2018.11.001.

[268] Hu, X., Cao, D., and Egardt, B.: *Condition Monitoring in Advanced Battery Management Systems: Moving Horizon Estimation Using a Reduced Electrochemical Model.* In: *IEEE/ASME Transactions on Mechatronics* 23 (1) (2018), pp. 167–178. DOI: 10.1109/TMECH.2017.2675920.

[269] Park, M.-S., Lee, J.-W., Choi, W., Im, D., Doo, S.-G., and Park, K.-S.: *On the surface modifications of high-voltage oxide cathodes for lithium-ion batteries: new insight and significant safety improvement.* In: *Journal of Materials Chemistry* 20 (34) (2010), pp. 7208–7213. DOI: 10.1039/c0jm00617c.

[270] Lanz, P., Sommer, H., Schulz-Dobrick, M., and Novák, P.: *Oxygen release from high-energy xLi2MnO3 · (1−x)LiMO2 (M=Mn, Ni, Co): Electrochemical, differential electrochemical mass spectrometric, in situ pressure, and in situ temperature characterization.* In: *Electrochimica Acta* 93 (2013), pp. 114–119. DOI: 10.1016/j.electacta.2013.01.105.

[271] Schmitt, J., Kraft, B., Schmidt, J. P., Meir, B., Elian, K., Ensling, D., Keser, G., and Jossen, A.: *Measurement of gas pressure inside large-format prismatic lithium-ion cells during operation and cycle aging.* In: *Journal of Power Sources* 478 (2020), p. 228661. DOI: 10.1016/j.jpowsour.2020.228661.

[272] Schmitt, J., Rehm, M., Karger, A., and Jossen, A.: *Capacity and degradation mode estimation for lithium-ion batteries based on partial charging curves at different current rates.* In: *Journal of Energy Storage* 59 (3) (2023), p. 106517. DOI: 10.1016/j.est.2022.106517.

[273] Schmitt, J., Kraft, B., Schmidt, J. P., Elian, K., Keser, G., Behne, S., Meir, B., Ensling, D., and Jossen, A.: *In-situ measurement of gas pressure inside prismatic lithium ion cells during operation and abuse scenarios.* Batterieforum Deutschland, Berlin, 2019.

[274] Smart, J., Powell, W., and Schey, S.: *Extended Range Electric Vehicle Driving and Charging Behavior Observed Early in the EV Project*. In: *SAE technical paper series* (2013). DOI: 10.4271/2013-01-1441.

[275] Wetjen, M., Solchenbach, S., Pritzl, D., Hou, J., Tileli, V., and Gasteiger, H. A.: *Morphological Changes of Silicon Nanoparticles and the Influence of Cutoff Potentials in Silicon-Graphite Electrodes*. In: *Journal of the Electrochemical Society* 165 (7) (2018), A1503–A1514. DOI: 10.1149/2.1261807jes.

[276] Rodrigues, M.-T. F., Gilbert, J. A., Kalaga, K., and Abraham, D. P.: *Insights on the cycling behavior of a highly-prelithiated silicon–graphite electrode in lithium-ion cells*. In: *Journal of Physics: Energy* 2 (2) (2020), p. 024002. DOI: 10.1088/2515-7655/ab6b3a.

List of publications

Peer-reviewed journal paper contributions (lead author)

I **Schmitt, J.**, Rehm, M., Karger, A., Jossen, A.: *Capacity and degradation mode estimation for lithium-ion batteries based on partial charging curves at different current rates.* In: *Journal of Energy Storage* 59 (2023), p. 106517, DOI: 10.1016/j.est.2022.106517

II **Schmitt, J.**, Schindler, M., Oberbauer, A., Jossen, A.: *Determination of degradation modes of lithium-ion batteries considering aging-induced changes in the half-cell open-circuit potential curve of silicon–graphite.* In: *Journal of Power Sources* 532 (2022), p. 231296, DOI: 10.1016/j.jpowsour.2022.231296

III **Schmitt, J.**, Schindler, M., Jossen, A.: *Change in the half-cell open-circuit potential curves of silicon–graphite and nickel-rich lithium nickel manganese cobalt oxide during cycle aging.* In: *Journal of Power Sources* 506 (2021), p. 230240, DOI: 10.1016/j.jpowsour.2021.230240

IV **Schmitt, J.**, Kraft, B., Schmidt, J. P., Meir, B., Elian, K., Ensling D., Keser, G., Jossen, A.: *Measurement of gas pressure inside large-format prismatic lithium-ion cells during operation and cycle aging.* In: *Journal of Power Sources* 478 (2020), p. 228661, DOI: 10.1016/j.jpowsour.2020.228661

Peer-reviewed journal paper contributions (co-author)

I Schindler, M., Sturm, J., Ludwig, S., **Schmitt, J.**, Jossen, A.: *Evolution of Initial Cell-to-Cell Variations During a Three-Year Production Cycle.* In: *eTransportation* 7 (2021), p. 100102, DOI: 10.1016/j.etran.2020.100102

II Zilberman, I., **Schmitt, J.**, Ludwig, S., Naumann, M., Jossen, A.: *Simulation of voltage imbalance in large lithium-ion battery packs influenced by cell-to-cell variations and balancing systems.* In: *Journal of Energy Storage* 32 (2020), p. 101828, DOI: 10.1016/j.est.2020.101828

Conference contributions (lead author)

I **Schmitt, J.**, Jossen, A.: *State of health estimation based on partial cell charging.* In: *Advanced Battery Power*, Münster, Poster, 2022

II **Schmitt, J.**, Schindler, M., Jossen, A.: *Non-Destructive Degradation Diagnostics of Lithium-Ion Cells considering Aging-Related Changes in the Shape of the Half-Cell Open Circuit Potential Curve of Silicon-Graphite.* In: *240th ECS Meeting*, Orlando (Florida, US) / online, Presentation, 2021

III **Schmitt, J.**, Schindler, M., Jossen, A.: *Experimental investigation of the aging invariance of electrode open circuit voltage curves.* In: *Advanced Battery Power*, Aachen / online, Presentation, 2021

IV **Schmitt, J.**, Zilberman, I., Ludwig, S., Jossen, A.: *Influence of Intrinsic Cell Variations, Temperature Gradients and Balancing on the Long-Term Performance of Lithium-Ion Battery Packs.* In: *Batterieforum Deutschland*, Berlin, Poster, 2021

V **Schmitt, J.**, Jossen, A.: *Influence of State of Charge, Temperature and Aging on the Gas Pressure inside Prismatic Lithium Ion Cells.* In: *Batterieforum Deutschland*, Berlin, Poster, 2020

VI **Schmitt, J.**, Schmidt, J. P., Kraft, B., Meir, B., Keser, G., Jossen, A.: *Change of Gas Pressure inside Prismatic Lithium Ion Cells during Aging.* In: *Advanced Battery Power*, Aachen, Poster, 2019

VII **Schmitt, J.**, Kraft, B., Schmidt, J. P., Elian, K., Keser, G., Behne, S., Meir, B., Ensling, D., Jossen, A.: *In-situ measurement of gas pressure inside prismatic lithium ion cells during operation and abuse scenarios.* In: *Batterieforum Deutschland*, Berlin, Poster, 2019

VIII **Schmitt, J.**, Campestrini, C., Jossen, A.: *Software partitioning of distributed battery management systems for intelligent battery cells.* In: *Batterieforum Deutschland*, Berlin, Poster, 2018

Conference contributions (co-author)

I Ludwig, S., **Schmitt, J.**, Zilberman, I., Wendel, S., Jossen, A.: *New Method for Analyzing Ultrasonic based Measurements for Lithium-ion Batteries.* In: *Advanced Battery Power*, Aachen, Presentation, 2019

Acknowledgment

This thesis is the result of my time as a research associate at the Chair of Electrical Energy Storage Technology at the Technical University of Munich. First of all, I would like to express my gratitude to my supervisor Prof. Dr.-Ing. Andreas Jossen. Thank you very much for giving me the opportunity of working in your group, for the continuous support and guidance, and for your valuable feedback on my research.

Furthermore, I would like to thank Prof. Dr.-Ing. Jan Philipp Schmidt for mentoring me throughout the last years. You were always a source of inspiration and motivation for me and I really enjoyed our regular exchange on my research and the field of battery technology in general.

I would like to thank Prof. Dr. rer. nat. Dirk Uwe Sauer for acting as second examiner of this thesis and Prof. Dr. rer. pol. Christoph Goebel for being the chairman of the examination committee. I am very thankful to both of you for doing everything necessary to finish this project right on time before the birth of my first child.

Thank you very much to all co-authors of my papers. It was a great experience working with you. Special thanks go to my office colleagues Dr.-Ing. Markus Schindler and Andreas Graule for the joyful days at the end of the corridor on the first floor.

I would like to thank my colleagues from team Battery Management Systems for all the fruitful discussions, your valuable support and the fun it was working with you. I especially thank Dr.-Ing. Ilya Zilberman for his support as team lead during my first year at the chair. Furthermore, I would like to thank Sebastian Ludwig, Alexander Karger, and Mathias Rehm for proofreading the manuscript of this thesis.

I thank Dr. rer. nat. Gudrun Rahn-Koltermann for managing the organizational aspects of the research projects I was involved in and for the great collaboration during writing project proposals. I would also like to thank Carolin Nierwetberg and the administrative team for their support. I thank Korbinian Schmidt and Jens Dietrich for their valuable help concerning all aspects of working in the lab. Thank you to all my colleagues at the Chair of Electrical Energy Storage Technology for all of your help and the great time I had with you. I would also like to thank all partners from the research projects MiBZ and LImeS for the great collaboration.

Many thanks to my family and friends, on which I could always rely on. I would like to especially thank my parents Renate and Franz-Josef Schmitt for everything they did for me and for always believing in me. Last but not least, I am deeply grateful to my wonderful wife Ina Oppelt. Thank you for moving to Munich with me and for motivating me throughout this whole project. Thank you very much for all the support you gave me and for being always by my side. This thesis is dedicated to you.